



University
of Glasgow

Alsayednoor, Jafar (2013) *Modelling and characterisation of porous materials*. PhD thesis.

<http://theses.gla.ac.uk/4808/>

Copyright and moral rights for this thesis are retained by the author

A copy can be downloaded for personal non-commercial research or study, without prior permission or charge

This thesis cannot be reproduced or quoted extensively from without first obtaining permission in writing from the Author

The content must not be changed in any way or sold commercially in any format or medium without the formal permission of the Author

When referring to this work, full bibliographic details including the author, title, awarding institution and date of the thesis must be given

Modelling and Characterisation of Porous Materials

Jafar Alsayednoor

A thesis for the degree of Doctor of Philosophy (PhD)

Submitted to the School of Engineering,

College of Science and Engineering,

University of Glasgow

October 2013

DECLARATION

I declare that this thesis is a record of the original work carried out by myself under the supervision of Dr. Philip Harrison in the School of Engineering at the University of Glasgow, United Kingdom. The copyright of this thesis therefore belongs to the author under the terms of the United Kingdom Copyright acts. Due acknowledgement must always be made of the use of any material contained in, or derived from, this thesis. The thesis has not been presented elsewhere in consideration for a higher degree.

Signature  _____

Printed name: Mr Jafar Alsayednoor

Signature _____

Printed name: Dr. Philip Harrison

Abstract

Porous materials possessing random microstructures exist in both organic (e.g. polymer foam, bone) and in-organic (e.g. silica aerogels) forms. Foams and aerogels are two such materials with numerous engineering and scientific applications such as light-weight cores in sandwich structures, packaging, impact and crash structures, filters, catalysts and thermal and electrical insulators. As such, design and manufacture using these materials is an important task that can benefit significantly from the use of computer aided engineering tools. With the increase in computational power, multi-scale modelling is fast becoming a powerful and increasingly relevant computational technique. Ultimately, the aim is to employ this technique to decrease the time and cost of experimental mechanical characterisation and also to optimise material microstructures. Both these goals can be achieved through the use of multi-scale modelling to predict the macro-mechanical behaviour of porous materials from their microstructural morphologies, and the constituent materials from which they are made. The aim of this work is to create novel software capable of generating realistic randomly micro-structured material models, for convenient import into commercial finite element software. An important aspect is computational efficiency and all techniques are developed paying close attention to the computation time required by the final finite element simulations. Existing methods are reviewed and where required, new techniques are devised. The research extensively employs the concept of the Representative Volume Element (RVE), and a Periodic Boundary Condition (PBC) is used in conjunction with the RVEs to obtain a volume-averaged mechanical response of the bulk material from the micro-scale. Numerical methods such as Voronoi, Voronoi-Laguerre and Diffusion Limited Cluster-Cluster Aggregation are all employed in generating the microstructures, and where necessary, enhanced in order to create a wide variety of realistic microstructural morphologies, including mono-disperse, polydisperse and isotropic microstructures (relevant to gas-expanded foam materials) as well as diffusion-based microstructures (relevant for aerogels). Methods of performing large strain simulations of foams microstructures, up to and beyond the onset strain of

densification are developed and the dependence of mechanical response on the size of an RVE is considered. Both mechanical and morphological analysis of the RVEs is performed in order to investigate the relationship between mechanical response and internal microstructural morphology of the RVE. The majority of the investigation is limited to 2-d models though the work culminates in extending the methods to consider 3-d microstructures.

Acknowledgments

This work is dedicated to HUJJAT IBN ALHASAN ALASKARI

First of all, I would like to express my great thanks to Dr Philip Harrison. A truly gentleman who was not only my supervisor, he was, and indeed he is my best teacher. Even more thanks to him for his endless clever ideas and friendly advices which made me always relax and happy to work with him. Unfortunately, the words are not enough to appreciate him more.

Also, I like to thank Dr Zaoyang Guo, my second supervisor and MSc lecturer, who provide me with this opportunity to undertake PhD program.

Many thanks to my lovely friends who helped and encouraged me a lot during these years: Omid, Shayan, Mr Hashemi, Shahin, Mr Ebadi (also known as Mr Bawi), Qader, Rana, Ahmad, Haj Agha Nilforoushan and Mustafa.

Special thanks to my darling Fatemeh, although she joined me at the end of this rout, but her presence was a great support and motivation to finish my work.

I also would like to thank Dr Damien McGrouther for setting FIB experiment and providing X-aerogel images within University of Glasgow.

Many thanks to Dr Richard Green for his kindness, Professor Tanner and Dr Coupaud for helping me improve my presentation skills.

Finally I would like to acknowledge the EPSRC for their financial support for this PhD course.

Table of Contents

ABSTRACT	I
ACKNOWLEDGMENTS.....	III
LIST OF SYMBOLS.....	VII
CHAPTER 1 . INTRODUCTION	1—1
1.1 CLASSIFICATION OF POROUS MATERIALS.....	1—1
1.1.1 <i>Lattice materials</i>	1—2
1.1.2 <i>Random cellular materials</i>	1—3
1.1.3 <i>Aerogel materials</i>	1—4
1.2 MULTI-SCALE MODELLING OF POROUS MATERIALS	1—6
1.2.1 <i>Representative volume element</i>	1—7
1.2.2 <i>Repeat unit cell approach</i>	1—7
1.3 BOUNDARY CONDITION ON RVE	1—8
1.4 GENERATION OF POROUS RVES	1—9
1.5 OBJECTIVES.....	1—11
1.6 THESIS OVERVIEW	1—11
CHAPTER 2 . TWO DIMENSIONAL MODELLING OF POROUS MICROSTRUCTURES.....	2—13
2.1 TWO DIMENSIONAL MODELLING OF FOAMS	2—13
2.1.1 <i>Generation of two-dimensional beam-based Representative Volume Element (RVE)</i>	2—13
2.1.2 <i>Two-dimensional beam-based RVE generation for mono-disperse cellular structure</i>	2—15
2.1.3 <i>Two-dimensional beam-based RVE generation for poly-disperse cellular structures</i>	2—19
2.1.4 <i>Mono-disperse foam-like RVE generation by employing the Lloyd's relaxation algorithm</i>	2—26
2.2 TWO-DIMENSIONAL MODELLING OF AEROGELS	2—28
2.2.1 <i>Introduction</i>	2—28
2.2.2 <i>Two-dimensional particle-based RVE generation methods</i>	2—29
2.2.3 <i>Generation of 2-d periodic aerogel model by DLCA</i>	2—33
2.2.4 <i>Converting lattice-based RVE to beam-based</i>	2—36
2.3 CONCLUSIONS OF CHAPTER 2.....	2—37
CHAPTER 3 . MECHANICAL EVALUATION OF TWO-DIMENSIONAL RVES.....	3—39
3.1 INTRODUCTION	3—39
3.2 MONO-DISPERSE MICROSTRUCTURE CREATED USING THE MODIFIED ZHU ALGORITHM	3—42
3.2.1 <i>RVE design</i>	3—42
3.2.2 <i>Boundary condition on periodic 2-d RVE</i>	3—43
3.2.3 <i>Equivalent shell-based RVEs</i>	3—44
3.2.4 <i>Size and computational resource considerations</i>	3—46
3.2.5 <i>Large strain response results</i>	3—49
3.3 POLY-DISPERSE RVE MICROSTRUCTURE GENERATED USING THE DROP AND ROLL METHOD.....	3—57
3.4 CONCLUSIONS OF CHAPTER 3.....	3—62
CHAPTER 4 . ORIENTATION DEPENDENT COMPRESSIVE RESPONSE OF TWO-DIMENSIONAL REPRESENTATIVE VOLUME ELEMENTS.....	4—64

4.1 INTRODUCTION	4—64
4.2 LITERATURE REVIEW	4—66
4.2.1 Directional response of honeycomb structures.....	4—66
4.2.2 Analytical predictions of honeycomb response.....	4—66
4.2.3 Modelling of two-dimensional random foam microstructures using a numerical RVE approach.	4—69
4.3 BEAM-BASED RVE PREPARATION FOR FE ANALYSIS.....	4—72
4.3.1 Application of PBC on RVE for Compression in an Arbitrary Direction.....	4—72
4.4 MECHANICAL RESPONSE OF PERIODIC HONEYCOMB STRUCTURE WHEN COMPRESSED IN ARBITRARY DIRECTIONS	4—72
4.4.1 Finite element model for honeycomb structure.....	4—73
4.4.2 Method of determining mechanical response of honeycomb RVE in different loading directions.....	4—75
4.4.3 Mechanical response of honeycomb RVE in arbitrary loading direction for compressive strain less than 10%.....	4—80
4.4.4 Mechanical response of honeycomb RVE compressed in arbitrary loading directions for strains greater than 10%.....	4—85
4.5 MECHANICAL RESPONSE OF INCREASINGLY RANDOMISED RVEs GENERATED USING THE ENHANCED METHOD OF ZHU, WHEN COMPRESSED AT 0° , 45° AND 90°	4—88
4.6 GENERATING ISOTROPIC RVEs WITH REALISTIC MONO-DISPERSE MICROSTRUCTURES	4—95
4.7 MECHANICAL RESPONSE OF POLY-DISPERSE STRUCTURE WHEN COMPRESSED AT 0° , 45° AND 90°	4—99
4.9 CONCLUSIONS OF CHAPTER 4.....	4—103
CHAPTER 5 . ANALYSIS OF 2-D RVE MICROSTRUCTURAL MORPHOLOGIES.....	5—104
5.1 INTRODUCTION	5—104
5.2 LITERATURE REVIEW	5—105
5.2.1 Passive characterisation	5—105
5.2.2 Active characterisation	5—106
5.3 PASSIVE MORPHOLOGICAL CHARACTERISATION OF 2-D BEAM-BASED RVEs	5—106
5.3.1 Quantification of cellular anisotropy	5—107
5.3.2 Morphological Analysis of RVEs Generated using the Enhanced Method of Zhu	5—109
5.3.3 Morphological Analysis of RVEs Generated using a combination of the Enhanced Method of Zhu and the Lloyd's Relaxation Algorithm	5—122
5.3.4 Analysis of the Microstructural Morphology generated using the Drop and Roll method	5—128
5.4 ACTIVE MORPHOLOGICAL CHARACTERISATION OF 2-D BEAM-BASED RVEs	5—137
5.4.1 Morphological Evaluation of Mono-disperse Beam-Based RVE under Compressive Loading.....	5—137
5.4.2 Morphological Evaluation of Poly-Disperse Shell-Based RVE under Compressive Loading.....	5—145
<i>To study the evolution of cellular morphology of poly-disperse microstructures, RVEs with a degree of poly-dispersity of 0.1 have been generated. These RVEs have similar morphologies to those of higher poly-dispersity and are therefore assumed to be representative of this generic class of RVE, i.e those generated by the modified Drop and Roll method.</i>	<i>5—145</i>
5.5 CONCLUSIONS OF CHAPTER 5.....	5—154
CHAPTER 6 . CHARACTERISATION AND MODELLING OF 3-D FOAM MICROSTRUCTURES.....	6—156
6.1 INTRODUCTION	6—156
6.2 LITERATURE REVIEW	6—156
6.2.1 Plateau's law.....	6—156
6.2.2 Euler's law for convex polyhedral	6—157
6.2.3 Characterisation of Micro-Structure of Real 3-d Foams.....	6—157
6.2.4 Previous numerical-based modelling of 3-d foam microstructures.....	6—159
6.2.5 Mechanical evaluation of numerically generated microstructures.....	6—166
6.3 MORPHOLOGICAL CHARACTERISATION OF 3-D BEAM-BASED RVEs.....	6—168
6.3.1 Geometrical Study of 3-d RVEs.....	6—169

6.3.2 Geometrical Study of Poly-Disperse RVEs	6—175
6.4 CONCLUSIONS OF CHAPTER 6.....	6—190
CHAPTER 7 . CONCLUSIONS AND FUTURE WORK.....	7—192
7.1 CONCLUSIONS.....	7—192
7.2 FUTURE WORK	7—194
APPENDIX 1	7—197
REFERENCES:.....	7—199

List of symbols

A_0	Area of square region
A_L	Square Lattice area
A	Area of RVE
A'	Undeformed area of imaginary RVE
A_p	Area of closed polygon
a	Power law constant
b	Power law constant
D	Diffusion coefficient
D_c	Diffusion coefficient
D_{max}	Maximum diffusion coefficient
D'	Flexural rigidity
d_1	Dummy node 1
d_2	Dummy node 2
d_3	Dummy node 3
d_0	Minimum distance between seeds
d	Fractal dimensionality
d'_0	Minimum distance between adjacent seeds
E_f	Foam Young's modulus
\bar{E}_f	Reduced foam Young's modulus
E_S	Young's modulus of solid material
E	Young's modulus
E_1^*	Young's modulus in transverse direction
E_2^*	Young's modulus in perpendicular direction
E_{el}	Elastic Young's modulus of aerogels
f	Average number of faces per cell
f_L	Average number of faces per cell
f_E	Average number of faces per cell
GR	Growth rate
h_s	Shell thickness
H	Deformed RVE height
H_0	Undeformed RVE height
h	Side length of hexagonal cell
I	Second moment of inertia
I_{xx}	Second moment of inertia
I_{yy}	Second moment of inertia
I_{xy}	Second moment of inertia
K	Power law Young's modulus
L	Square lattice size
LH_0	Undeformed imaginary RVE height
LW_0	Undeformed imaginary RVE width
LH	Deformed imaginary RVE height
LW	Deformed imaginary RVE width

L_s	Shortest polygon axis
L_l	Longest polygon axis
L_t	Height of tetrakaidecahedron
l	Side length of hexagonal cell
l'	Length of element
m	Disk mean radius
m'	Aerogel power law constant
N	Number of cell
N_p	Number of non-overlapping particles in lattice
n	Number of seeds
n_e	Number of elements
n_r	Rotational stiffness at nodal connections
n_L	Average number of struts per faces
n_E	Average number of struts per faces
n_s	Average number of struts per faces
q	Load
r	Disk radius
r_{min}	Minimum allowable disk radius
r_{max}	Maximum allowable disk radius
S	Mass of cluster
t	Time
t_b	Thickness of beam
t_c	Cross sectional thickness
U	Dummy node displacement
u_{el}	Elastic deformation
V_i	Particle velocity
V_0	Volume of 3D RVE
W	Deformed RVE width
W_0	Undeformed RVE width
W_{el}	Elastic strain energy
X_i	Particle coordinates in space
x	Displacement
x_i^{-k}	Initial BCC seed distribution
x_c	Polygon centroid in x-coordinate
y_c	Polygon centroid in y-coordinate
α	Degree of irregularity
α_z	Degree of regularity
α'_z	Degree of regularity for 3D Zhu method
α'	Degree of irregularity
Δ	Range limit of random generated data
δ	Minimum allowable seed distance
δ_0	Minimum distance between seeds with regular honeycomb pattern
δ_L	Allowable lateral/vertical displacement
δ'	Minimum allowable distance between seeds
Φ	Sphere Packing density
φ_i^{-k}	Random variable generated from uniform distribution
φ	Fractal density
φ_c	Concentration of diffusing particles

ε_y	Yield strain of the material
ε	Strain
ε_1	Strain in transverse direction
ε_2	Strain in perpendicular direction
λ	Normalised strut length
λ_K	Normalised strut length from Kraynik simulations
λ_L	Normalised strut length from Lloyd's simulations
Π	Matrix of second moments of inertia
μ	Mean of data
η	Efficiency function
ρ	Density
ρ_p	Particle in lattice density
ρ_R	Relative density
ρ_S	Density of solid material
ρ^*	Density of porous material
σ	Normal stress
$\bar{\sigma}$	Reduced stress
$(\sigma_{el}^*)_2$	Non-linear elastic collapse stress in perpendicular direction
σ_{sd}	Standard deviation of data
v	Sound velocity
ν	Poisson's ratio
ν_{12}^*	Poisson's ratio
ν_{21}^*	Poisson's ratio
ν_s	Poisson's ratio of solid material
γ	Variance of the disk size
γ_F	Diffusion coefficient exponent
θ_0	Loading direction
θ_d	Drifting angle
θ	Beam angle
w	Shell/beam deflection

Chapter 1 . Introduction

1.1 Classification of porous materials

Porous materials are important in a wide range of applications including core materials in sandwich structures, impact energy absorbing materials in crash structures including helmets and automotive components, cushioning products designed to distribute pressure and thermally insulating materials [Banhart, 2001]. Some porous structures have smart behaviours, for example, shape memory polymers have been flagged for future use as a man-made self-healing structural foam [Patrick et al. 2012; John and Li, 2010], while cancellous bone can both adapt to loading conditions and self-repair. Porous materials can be classified using a variety of schemes. One possibility is to classify them based on the constituent material from which they are made, for example organic (e.g. polymeric foam) or inorganic (e.g. metallic and ceramic foams or silica aerogels). Another possible classification is related to their manufacture process, for example naturally occurring (e.g. cancellous bone, sponge) or man-made (polymer, metal or ceramic foams) and diffusion based materials such as aerogels. A third possible classification scheme is related to the materials internal morphological structure. Indeed, several investigations have studied the effect of manufacturing technique on the final microstructure [Woignier et al. 1989; Gibson and Ashby, 1997; Horrigan et al. 2009; Surace and Filippis, 2010; Malekjafarian et al. 2011; Bouakba et al. 2012]. In these investigations a typical goal is to understand the link between bulk mechanical response and microstructural properties such as porosity, pore size distribution, average cellular orientation and cell morphology. Since the main focus of this investigation is in understanding the relationship between the internal morphology of materials with randomly organised microstructures and the material's macroscopic mechanical behaviour (see Section 1.6), this particular classification scheme is elaborated further below.

1.1.1 Lattice materials

These are usually man-made networks containing a repeated unit cell throughout the material. Based upon engineering requirements, lattice structures can be manufactured in different geometrical forms such as a 3-d network of interconnected beams (see Figure 1-1a) or a 2-d lattice structure extruded in the out-of-plane direction, for example a honeycomb core (see Figure 1-1b) [Wadley et al. 2003]. Lattice structures can be manufactured with extremely high specific mechanical properties [Chen et al. 2013; Abramovitch et al. 2010]. For example, 2-d lattice structures such as honeycomb-cored sandwich panels are commonly used in engineering applications due to their high strength to weight ratio in the out-of-plane direction [Bitzer, 1997]. The topic of lattice structured porous materials is growing in importance due to increasingly viable manufacturing routes [Deshpande et al. 2001] and the design of novel internal architectures that can be optimised to provide unusual properties such as negative Poisson's ratios (auxetic materials) [Scarpa et al. 2004; Bianchi et al. 2010]. Honeycomb lattice structures are particularly relevant to this investigation as it has been popular practice in the past to study the in-plane mechanical properties of honeycomb as a first step towards understanding the more complex behaviour of random foam microstructures, e.g. [Gibson and Ashby, 1997].

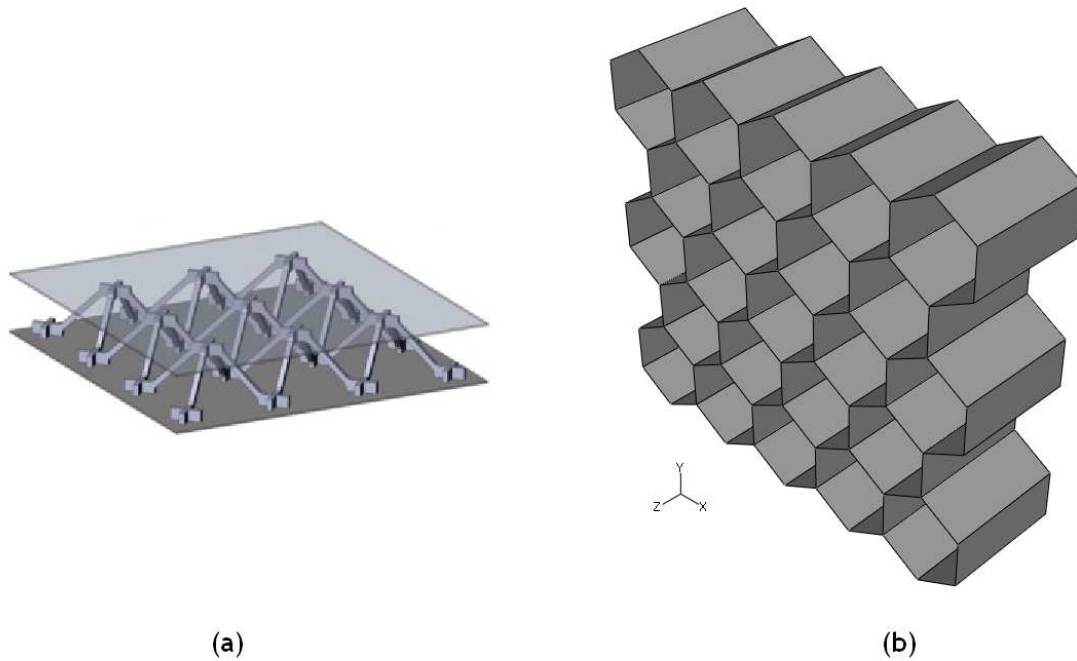


Figure 1-1: (a) Pyramidal lattice core [Zhang et al. 2013] (b) A honeycomb with hexagonal cell. Structure is extruded in out-plane direction (Z-axis).

1.1.2 Random cellular materials

These are the main focus of this investigation and are available as both man-made (e.g. polymer or metal foam) and natural (e.g. cancellous bone, sponge, coral) materials. Unlike lattice structured porous materials, cellular materials can be viewed as a 3-d network of connected cells, where each cell has its own unique geometry, i.e. there is no repeat unit cell within the internal structure. The porosity and type of constituent material within foam determine useful properties such as compressibility, density, specific mechanical properties and thermal/electrical conductivity. Based on the desired application and also the type of constituent material, different manufacturing techniques can be used to produce foam materials such as gas-expansion (e.g. polyurethane foam) or gas-injection methods (aluminium foam) [Jebur, 2013].

Foam materials can be further sub-classified according to their internal morphology into foams with cells connected together by solid struts or ribs (open-cell foams, see Figure 1-2a) and those connected with faces or windows (closed-cell foams, see Figure 1-2b). As a result, open cell foams are permeable whereas

closed cell foams are impermeable. Further, the microstructure can be described as either mono-disperse or poly-disperse. Mono-disperse foams are comprised of cells with a narrow range of cell volumes whereas poly-disperse foams contain cells with a wide range of volumes. The mechanical behaviour of foam can also be either isotropic or anisotropic. Mechanical anisotropy is generally related to internal microstructural anisotropy; a statistically significant degree of alignment of elongated cells along a preferred axis within the microstructure. The elongation of the cells usually results from the manufacture process [Huber and Gibson, 1988], and leads to transverse isotropy in the material's mechanical response [Tagarielli et al. 2005]. The mechanical properties of foams are strongly influenced by three distinct parameters: (i) the relative density of the foam, ρ_R , (ii) the mechanical properties of the constituent solid material and (iii) the generic cell morphology within the foam microstructure [Gibson and Ashby, 1997].

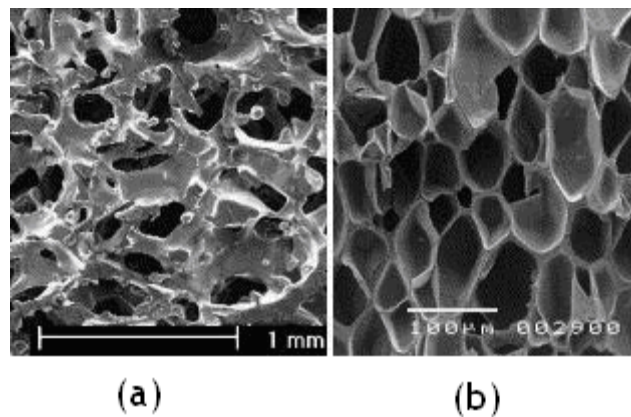
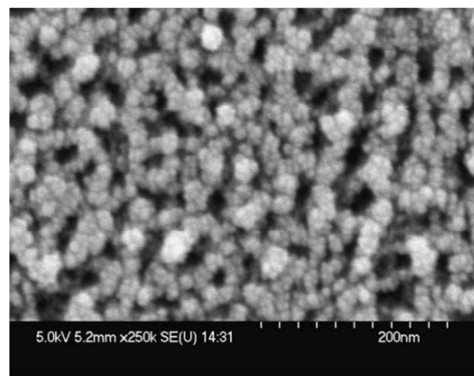


Figure 1-2: (a) an open cellular aluminum foam [San Marchi et al. 2004] (b) closed cell polymeric foams [Mills et al. 2003].

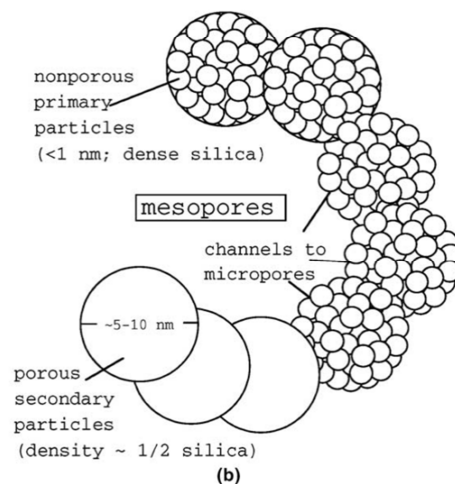
1.1.3 Aerogel materials

These are ultra low-density, highly porous materials, composed of a 3-d network of randomly interconnected nanoparticles. Like cellular materials, they can be classified as either organic or inorganic, based on the constituent material. An example of an organic aerogel is resorcinol formaldehyde aerogel whereas silica aerogel is an example of an inorganic aerogel. The pore size of aerogels is generally in the range of 0.1-100μm (see Figure 1-3) [Hench, 1998; Moner-Girona

et al. 2003], much smaller than most gas-expanded foams, which typically have pore diameters of between 100-500 μm [Kumar, 2007]. The fundamental difference between gas-expanded foam and aerogels is in their manufacture method; aerogels are created via a diffusion-based chemical synthesis process (Brinker and Scherer, 1990; Pierre, 1998; Dorcheh and Abbasi, 2008]. This results in their peculiar and unique particle-based internal structure. Conventional open-cellular foams can be idealised as a 3D network of interconnected beam-like elements (or ribs). Aerogels, on the other hand, have more complex internal structures. For example, silica aerogels, have a pearl necklace-like nanostructure whilst vanadium oxide aerogels have a worm-like morphology (see Figure 1-3 and 1-4). These differences mean that very different computational techniques are required to model the microstructures of aerogels and random cellular materials such as foam.



(a)



(b)

Figure 1-3: (a) SEM image of silica aerogel (b) proposed interior structure (Zhang et al. 2004).

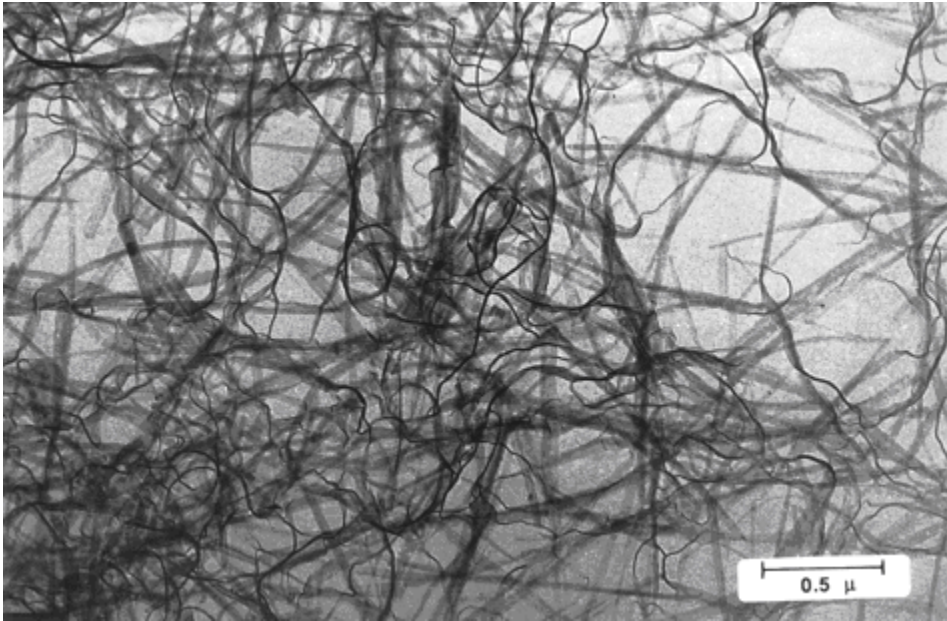


Figure 1-4: Electron microscopy image of vanadium pentoxide [Livage, 1991].

1.2 Multi-scale modelling of porous materials

An important goal is to evaluate the mechanical response of porous materials for subsequent engineering design purposes. The traditional method to accomplish this is by experimental characterisation. However, this approach can be difficult, time consuming (and therefore expensive) and provides little information with regard to the underlying deformation mechanisms occurring within the material's microstructure and consequently limited scope for microstructural optimisation. The exponential increase in computational power has made computational modelling an interesting alternative to experiments in evaluating the mechanical response of porous materials. As the microstructure is an important factor in determining the bulk mechanical response of porous materials, a large body of work has been dedicated to understanding the relationship between the microstructure and macro-scale properties [Miehe and Koch, 2002; Hohe and Becker, 2003; Kouznetsova et al., 2001; Smit et al. 1998; Swan, 1994].

1.2.1 Representative volume element

Due to the heterogeneous nature of foams, use of a Representative Volume Element (RVE) is generally considered to be a more powerful approach than the unit cell method to predicting the micro-to-macro response of porous materials, allowing the macroscopic response to be predicted from the material's underlying internal microstructural morphology [Gittus et al. 1987, Pavliotis and Stuart, 2008]. The concept of a RVE [Hill, 1963] is frequently used for microstructural design of heterogeneous media such as composites, ceramics, foams and granular materials [Kouznetsova et al. 2001]. Here, the volume averaged deformation gradient across the RVE is determined from the displacement of its surface, likewise the volume averaged nominal stress is computed in terms of the nominal stress on its surface. Once these volume averaged behaviours are determined they can be used either in parameter fitting for continuum-based constitutive models, or more directly, using a micro-to-macro simulation strategy [Miehe and Koch, 2002; Hohe and Becker, 2003]. The accuracy and practicality of computational homogenisation depends on the use of RVEs that are both realistic and computationally efficient, two criteria that are often at odds with one another [Swan, 1994; Smit et al. 1998; Kouznetsova et al., 2001]. The size of the RVE and its level of detail are two important considerations. For materials based on a regularly repeating micro or mesoscale structure, such as a honeycomb core or a woven textile, the choice of RVE size is usually trivial, and can be taken as the repeat unit cell within the material [Smit, 1998] (though this choice precludes the prediction of deformations with wavelengths longer than the size of the repeat unit cell). When it comes to materials possessing random microstructures, in general, the larger the RVE the more microstructural information it will contain. Ideally, an RVE model should be sufficiently large to be statistically representative of the composite [Drugan and Willis, 1996] while small in comparison to the larger structure.

1.2.2 Repeat unit cell approach

In repeat unit cell approach the microstructure of porous material is idealised as a network of connected regular cell with unique size and geometry (e.g. honeycomb and Kelvin structure for 2-d and 3-d idealisation, respectively). This approach is well suited to modelling lattice-structured porous materials (see Section 1.1)

[Warren and Kraynik, 1988; Zhu et al. 1997;] but is less appropriate for materials with randomly organised microstructures. Nevertheless, many studies have been performed to understand the mechanical behaviour of foam materials by considering the response of a unit hexagonal, cubic or Kelvin cell using both analytical and numerical approaches (see for example, Figure 1-1b) [Papka and Kyriakides, 1994; Gibson and Ashby, 1997; Zhu et al. 1997; Zhu et al. 2000]. In this case, the repeat unit cell method permits the prediction of mechanical behaviour when a foam is subjected to small strains and can produce reasonably accurate results [Gibson and Ashby, 1997; Zhu and Windle, 2002]. However, the use of a repeat unit cell in describing the internal microstructure of a foam is clearly a significant simplification and inevitably introduces errors that tend to become more significant as the applied strain increases [Zhu and Windle, 2002; Mills, 2007].

1.3 Boundary condition on RVE

In finite element applications, it is important to choose the most appropriate type of boundary condition. Mixed Boundary condition (MBC), Prescribed Displacement Boundary Condition (PDBC) and Periodic Boundary Condition (PBC) are the three most popular types of constraints that are imposed on the microstructures [Chen et al. 1999]. By considering imaginary 2-d square shape RVE, in the MBC, the normal displacement is imposed on two non-opposite edges where the opposite pairs are fixed to perform rotational and translational displacement. In applications where the average bulk behaviour is desired a Periodic Boundary Condition (PBC) is usually employed with the RVE [Guedes and Kikuchi, 1990; Anthoine, 1995] in order to obtain a homogenised macro-response for a material's bulk behaviour. According to Chen et al. 1999, a PBC produces an intermediate response for the RVE stiffness, lower than that predicted using a Prescribed Displacement but higher than that predicted by a Mixed Boundary Condition, consequently a PBC has been adopted throughout the computational modelling of this investigation.

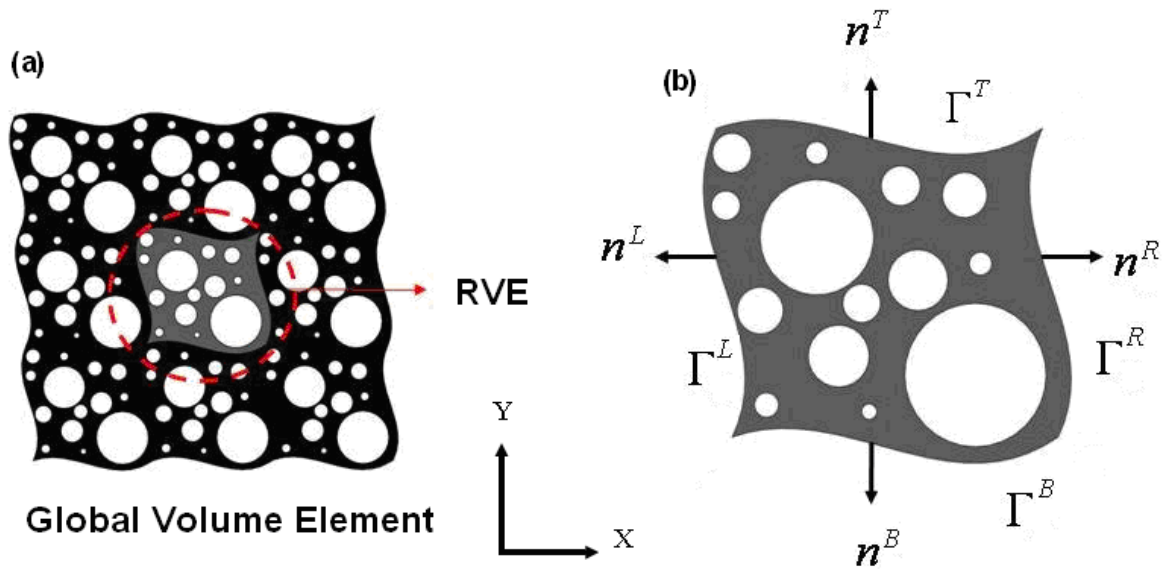


Figure 1-5: (a) Schematic representation of a 2-d material composed of a periodic microstructure consisting of a repeated RVE. (b) 2D RVE with applied PBC showing counterpart nodes on opposing faces.

The concepts of a RVE and a PBC are intrinsically linked [Smit et al. 1998]. To apply a PBC on any 2-d or 3-d RVE, the structure must be fully periodic. This means that a node on one boundary must have a counterpart at the same horizontal (sides) or vertical (top/bottom) position along the opposite boundary, (see Figure 1-5). Here the superscripts L, R, T and B indicate the left, right, top and bottom boundaries respectively. A two dimensional PBC requires that: (1) The motion of counterpart nodes on each pair of RVE boundaries are constrained to each other and (2) Stress continuity across boundaries is preserved. A full description of the method of applying a PBC in the FEM is given in Chapter 3.

1.4 Generation of porous RVEs

Imaged-based X-ray micro computed tomography (X-ray microCT) is a very powerful method for characterisation of foam microstructure and can provide significant detail about material deformation mechanisms [Montminy et al. 2001; Elliot et al. 2002; Elmoutaouakkil et al. 2002; Dillard et al. 2005; Youssef et al. 2005; McDonald et al. 2009]. X-ray microCT has previously been used to generate porous RVEs within the FEM by converting the image to a FE model. Various commercial software are currently available to perform such conversions (e.g. Simpleware, Mimics, AMIRA). For foams of medium to high relative density, this

usually involves the creation of an RVE using continuum finite elements. For open-cell foams with small relative density the interconnected network of straight beam (struts) can be idealised using structural finite elements (see Figure 1-6). In this case, it becomes possible to use beam or shell elements to determine the mechanical response of the RVE. This simplification can lead to significant improvements in computational efficiency. Nevertheless, the direct conversion of image-based structures into FE models usually leads to extremely high demands on computational resource because the RVE is not periodic and therefore very large models are required to create an RVE that is both statistically representative of the real material and is also relatively free from edge and therefore size effects [Elliot et al. 2002; Jebur et al., 2012]. For this reason, an alternative approach to image-based modelling is to generate periodic RVEs (see Section 1.2) using numerical algorithms. In order to generate the wide range of possible microstructures observed in real materials a variety of numerical algorithms are required.

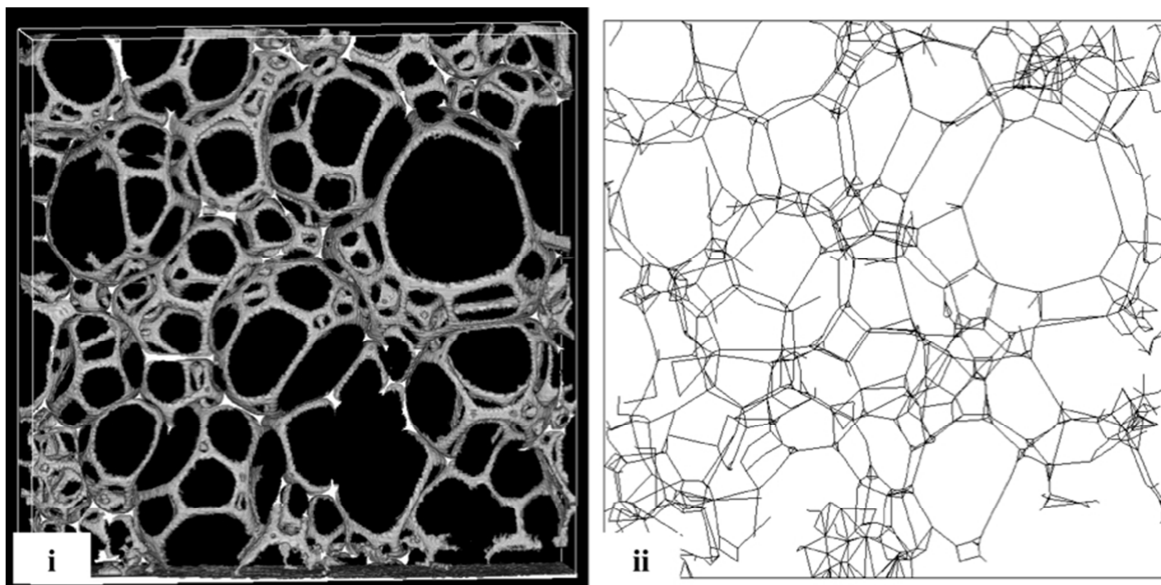


Figure 1-6: (a) Poly Urethane foam X-ray micro-tomography image (b) An equivalent beam-based model of real structure [Elliot et al. 2002].

In the case of aerogels with pore diameters measured at the nano-scale, non-destructive imaging techniques such as X-ray microCT lack sufficient resolution to

capture images with high geometrical details. Other techniques such as Focused Ion Beam (FIB) [Yao, 2007] may therefore be considered (see Section 2.2).

1.5 Objectives

The investigation will focus on the development of novel software capable of numerically generating realistic microstructures for porous materials that are meshed and ready for import directly into commercial finite element codes. RVEs created by the code will have PBCs automatically imposed, ensuring compatibility with subsequent numerical homogenisation methods. Porous materials can have a wide range of microstructures, for example, fractal or cellular, open- or closed-cell, mono- or poly-disperse, isotropic or anisotropic; the structure is usually determined by the manufacture, synthesis or growth process (see Section 1.1). For this reason, a variety of numerical algorithms are required to generate the wide range of possible microstructures. The software will generate microstructures based on structural finite elements (e.g. beam and shell) subsequently allowing relatively fast mechanical analysis. In order to create RVEs capable of undergoing large deformations self-contact within the RVE will be implemented. An important theme throughout the investigation is to relate the mechanical response of the RVEs generated by the various algorithms to their internal morphology and also to analyse the accuracy of the internal morphologies in relation to real materials.

1.6 Thesis overview

The remainder of this thesis is structured as follows. Chapter 2 begins with a literature review of numerical techniques that have been used previously by others to generate RVEs for porous materials employing a 2-d simplification of the internal microstructure. Novel modelling approaches are described that are adaptations of existing methods. In Chapter 3, 2-d RVEs are generated using one of the novel algorithms described in Chapter 2. The response of the RVE when subjected to large compressive strains is examined. Self-contact is implemented using a shell-based modelling technique. Contact strain and onset strain of densification are used to investigate RVE size-dependence. The aim of Chapter 4 is to investigate the anisotropy of 2-d beam-based RVEs generated using the techniques described in Chapter 2. The RVE response when subjected to uniaxial compressive strains in different directions is examined. Compression is applied in

directions perpendicular, transverse and off-axis to the RVE orientation. In Chapter 5, 2-d beam-based RVEs generated using numerical-methods introduced in Chapter 2 are characterised in terms of their internal morphology by performing a direct study of their geometrical parameters such as the distributions of cellular orientation and cell area. The aim is to investigate the relationship between microstructure morphology and mechanical response. In Chapter 6 numerical-modelling techniques to generate open-cellular foam-like 3-d microstructures are reviewed. Advantages and drawbacks of these techniques are discussed based on geometrical data automatically extracted from the numerically generated RVEs and subsequently compared against real foams morphologies described in the literature. Finally, Chapter 7 describes recommendations for future work.

Chapter 2 . Two dimensional modelling of porous microstructures

2.1 Two dimensional modelling of foams

Numerical generation of realistic foam microstructures is a challenging goal. A usual first step in this process is to simplify the problem by first investigating the behaviour of 2-d microstructures with the ultimate aim of extending the analysis to more realistic and more relevant 3-d microstructures. This approach has been adopted in this investigation.

2.1.1 Generation of two-dimensional beam-based Representative Volume Element (RVE)

A recognised method of generating foam-like microstructures is through Voronoi tessellation [Voronoi, 1908]. With regard to foam microstructure generation, there are two main approaches to using the Voronoi technique for space decomposition, namely classical and Laguerre-Voronoi which will be addressed in section 2.1.3. Under the first approach, each individual Voronoi cell is constructed based on the distance between its generator point and the neighbouring points. The Voronoi cell generator point is usually referred as a 'site', 'seed' or 'nuclei' in most of the literature [Aurenhammer, 1991; Zhu and Windle, 2002, Zhu et al. 2006]. The general process of generating a cellular structure from this approach is as follows: (i) identify neighbouring seeds around a given target seed, (ii) connect each neighbouring seed to the target seed using straight connecting lines, (iii) draw perpendicular lines across the connecting lines such that the connecting lines are bisected at their mid-points (iv) a Voronoi cell is generated by connecting the intersection points between the perpendicular bisector lines (see Figure 2-1).

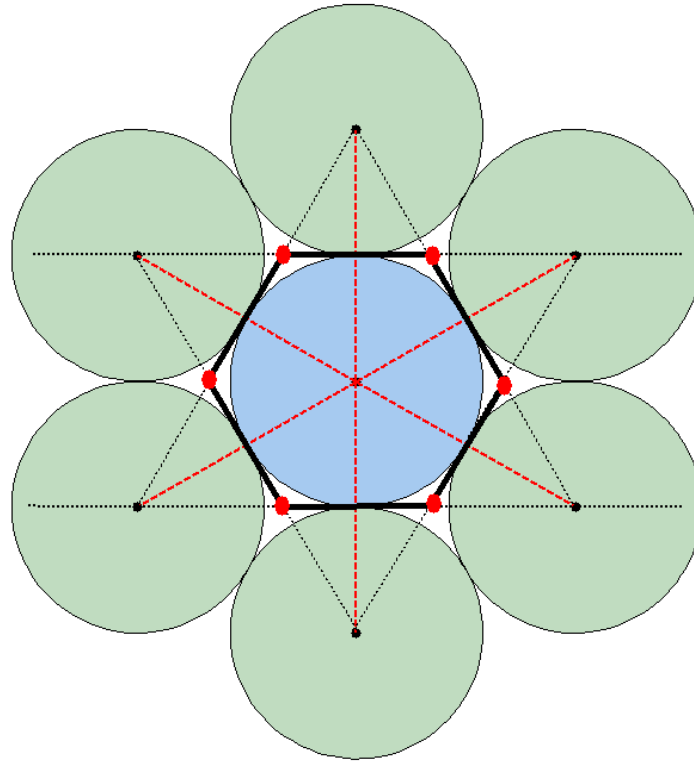


Figure 2-1: Illustrative example of Voronoi tiling using the first approach. Red points indicate intersection between perpendicular lines. The Voronoi cell is constructed by connecting these points. If the target and neighbouring seeds lie at the centre of hexagonally packed circles of equal diameter, the final Voronoi tessellation will be hexagonal.

Due to the simplicity of using the Voronoi method, numerous researchers have applied the approach to model foam microstructures [Silva et al. 1997^{a, b}; Van Der Burg et al. 1997; Shulmeister et al. 1998]. Since by definition, foams possess random microstructures, mechanisms to generate randomised seed distributions are required. To do this both Silva et al. 1997^{a, b} and Grenstedt and Tanaka, 1998 started with a regular and equally spaced seed distribution in a square matrix arrangement. An irregular Voronoi structure was then produced by adding spatial perturbations to the initial seed positions. This was achieved as follows; based on the initial body centred cube seed distribution (BCC), a perturbation was added to these initial seed coordinates in order to achieve a non-uniform seeding. The perturbation was controlled by setting an amplitude value and multiplying this by randomly selected stochastic variables generated using a uniform distribution. The weakness of this approach is based on the perturbation of the tetrakaidecahedron

seed generator; selecting high values of the perturbation amplitude results in an irregular structure that has a very different microstructural cellular morphology to actual closed or open-cell foams.

2.1.2 Two-dimensional beam-based RVE generation for mono-disperse cellular structure

Zhu et al. 2001 later proposed a novel method to quantify the degree of irregularity of 2-d Voronoi tessellation. The method allows for the generation of both regular geometries, such as a honeycomb microstructures, or highly irregular geometries with highly scattered rib lengths and cellular orientations. The result is the so-called ‘Poisson’s Voronoi’ microstructure [Tanemura, 2003]. The method works as follows: based on a honeycomb geometry a constant distance, d_0 , is calculated between each adjacent seed:

$$d_0 = \left(\frac{2A_0}{n\sqrt{3}} \right)^{0.5} \quad \text{Equation 2-1}$$

where A_0 is the area of a square region that includes all seeds and n is the number of seeds. To generate a honeycomb structure using a Voronoi tessellation, the minimum distance between each adjacent seed should not be less than d_0 . Zhu introduced a parameter, α_z , to control the degree of irregularity of the Voronoi structure based on d_0 :

$$\alpha_z = \frac{\delta}{d_0} \quad \text{Equation 2-2}$$

where δ is the minimum allowable distance between two adjacent seed points. Based on Eq. 2-2 $\alpha_z=1$ results in a perfectly regular honeycomb microstructure. As α_z tends to zero the distance between adjacent seeds becomes more variable and the resultant microstructure becomes more irregular (but not necessarily more realistic). Example microstructures have been generated in this investigation, see Figure 2-2, by implementing the algorithm described in Zhu et al. [2001].

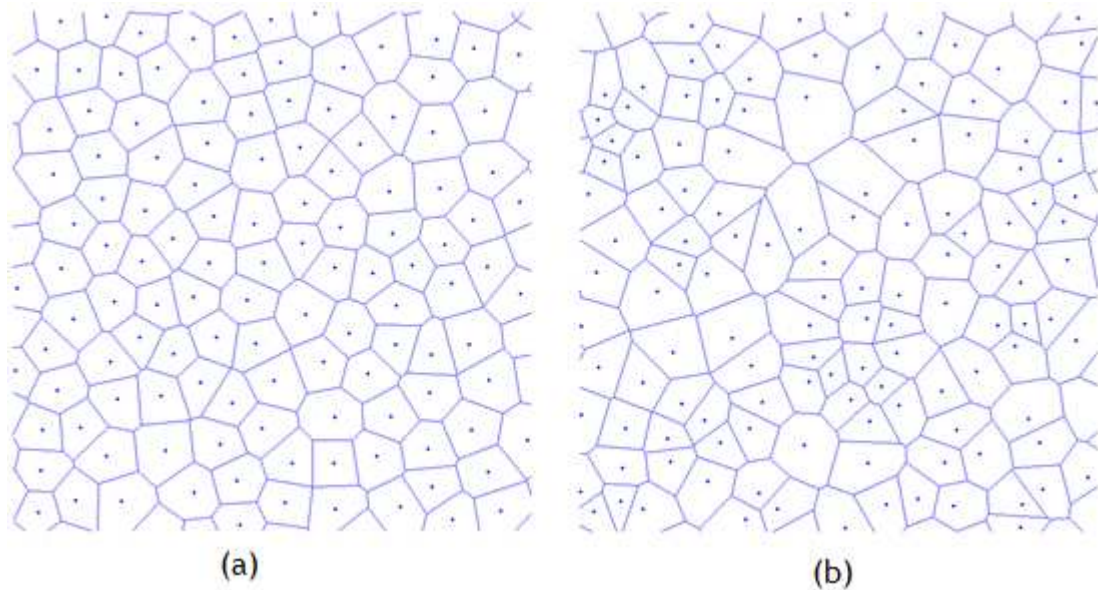


Figure 2-2: Voronoi samples with 200 cells, generated using the algorithm described in Zhu et al. 2001. (a) $\alpha_Z = 0.75$, (b) $\alpha_Z = 0.45$.

Zhu's method has several advantages over the previous approach described in Section 2.1.1. The technique is simple to apply and is quite fast and convenient for generating samples with different structural irregularities. It is also relatively simple to extend the same procedure in generating 3-d foam-like models (see Chapter 6). But perhaps its most fascinating characteristic is its power to generate different microstructures but with the same degree of irregularity, characterised by a single parameter, α_Z . However, the method does have its limitations which have been noted after implementing the method in this investigation, in a Matlab™ code. The first limitation was noted when generating seeds for $\alpha_Z > 0.8$, here the process becomes time consuming as the number of seeds per unit area increases. As mentioned before, the more regular 2-d structure will approach hexagonal network (i.e. regular honeycomb). Mathematically, it is not possible to fit fully periodic hexagonal structure into perfectly square shape RVE and due to this the simulation time will increase to generate seeds for more regular microstructure. To resolve this problem in this investigation, the method of Zhu has been modified by employing a technique introduced by Li et al. 2006 where applying Voronoi tessellation over equally spaced seeds in BCC lattice (Body Centred Cube) will result in generation of tetrakaidecahedron or Kelvin cells. Seeds are initially placed in BCC lattice and then perturbation are added based on the height of a

regular tetrakaidecahedron and amplitude which almost works as α in the Zhu method in order to controls the degree of irregularity. In this novel hybrid method seeds are initially equally spaced in a regular seeding arrangement corresponding to that of a perfectly regular honeycomb pattern. Next, a set of normally-distributed pseudo-random values are generated within a range with limits $\pm \Delta$ where Δ is calculated using

$$\Delta = \frac{\alpha \times \delta_0}{100}, \alpha \in (0,50) \quad \text{Equation 2-3}$$

And where

$$\delta_0 = \sqrt{\frac{2A_0}{N\sqrt{3}}} \quad \text{Equation 2-4}$$

Here δ_0 is the minimum distance between neighbouring seeds of a regular honeycomb cellular pattern in a closed area, A_0 , N is the number of cells and the parameter, α , controls the degree of irregularity within the RVE. Here, δ_0 is exactly the same as d_0 calculated in Eq. 2-1. These random values are then added to the initial regularly arranged honeycomb seed positions (see Figure 2-3).

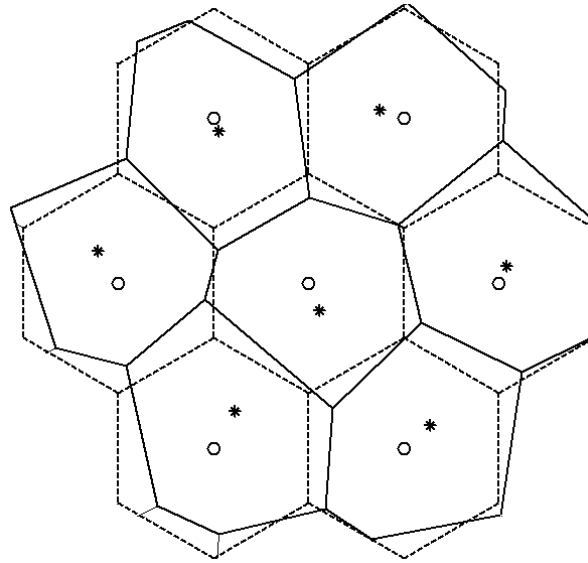


Figure 2-3: Generation of random cellular structure using a Voronoi tessellation method. The broken lines indicate a honeycomb pattern generated from regularly-spaced seeds (white circles). By adding perturbations to the honeycomb seeds, an alternative seeding (black stars) is used to generate a randomized structure.

So far, different approaches for generating randomised Voronoi cells have been discussed. However, in order to create a RVE with PBC suitable for subsequent use in the FEM, further work is required. To do this a unit square is first populated with a regular arrangement of seed positions (the precursor seeding for a honeycomb pattern). Eq. 2-3 is then used to perturb these initial seed positions to produce a unit square containing an irregular distribution of seeds. This ‘perturbed’ unit square seeding is copied nine times to create a larger square containing 3×3 identical perturbed unit square seedings. Applying a Voronoi tessellation algorithm to the resulting 3×3 structure produces a fully periodic cellular pattern within the central square, with pairs of counterpart nodes automatically generated on opposing boundaries (see Figure 2-4).

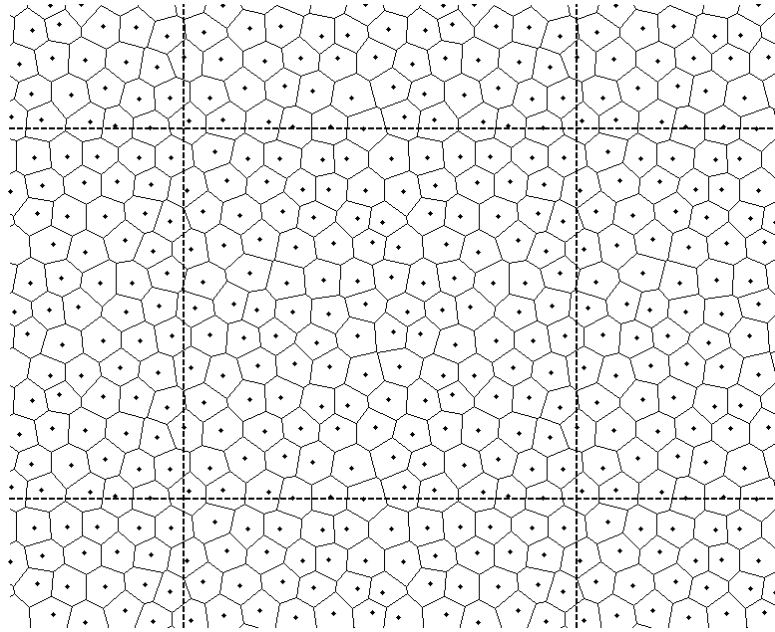


Figure 2-4: An example of a fully periodic structure (the central square).

2.1.3 Two-dimensional beam-based RVE generation for poly-disperse cellular structures

The second limitation within both Zhu’s original method and the modified version of this algorithm proposed in this research, is regarding their ability to model poly-disperse microstructures. In general all seed-based modelling techniques lead to Gaussian cell-size distributions (see Chapter 5) that may not be appropriate for some foams [Fazekas et al.2002; Gervois et al. 2002; Kanaun and Tkachenko, 2006]. The main reason for this weakness is explained as follows: in the case where there is a mixture of cells with significantly different sizes, use of the Voronoi method as described above, i.e. using bisector lines to generate the cells, results in an over-estimation of the number of Voronoi cells of small size and an under-estimation of the number of cells of large size.

To overcome this issue, instead of constructing Voronoi cells based on their seed point coordinates using the methods described in Section 2.1.1-2.1.2 each individual cell can instead be represented using a ‘hard-disk’ with a specified size and coordinate, see Figure 2.5. (Note, the method of seeding the microstructure

using hard-disks will be described later in current section). Now, cell-partitioning can be based on the location of the contact points between the hard-disks rather than the mid-way bi-sector points between seed positions. The difference in the resulting microstructure is demonstrated in Figure 2.5. This alternative method is referred to as ‘Laguerre-Voronoi Tessellation’. Here the bisectors are derived from the distance between touching point of the two disks rather than from the distance between the centres (see Figure 2-5).

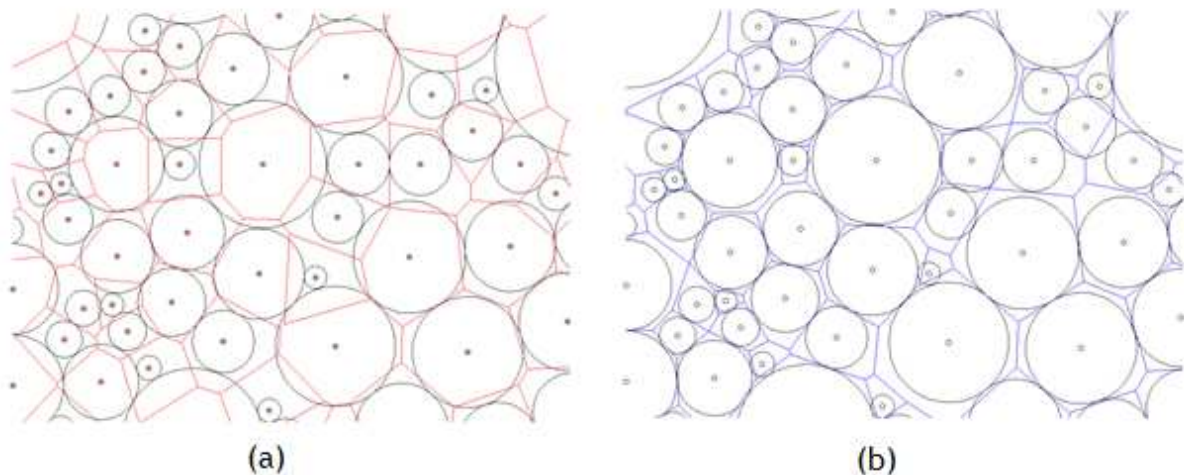


Figure 2-5: (a) Voronoi Tessellation generated from seed positions produced by an arrangement of hard-disks. (b) Laguerre Voronoi Tessellation generated using the same arrangement of hard-disks. Note the latter results in a much more poly-disperse microstructure.

In general, the method of Zhu is suitable for the generation of 2 and 3-d periodic RVEs with different degrees of irregularity, for cells with low or even a moderate degrees of size poly-dispersity (see Chapter 3 for further discussion of this point). However, for cases of significant cell size dispersion, the Laguerre-Voronoi method is more effective. Before applying the Laguerre-Voronoi tessellation method, a mechanism is required to arrange the hard-disks shown in Figure 2.5, with the maximum possible packing density.

Generally, there are two main methods that are frequently used for generating hard-disk packing: (i) Random Sequential Adsorption (RSA) [Cooper, 1988] and classical hard-disk Molecular Dynamics (MD). In the RSA method, hard-disks are

randomly generated with different sizes and coordinates. The discs are then sequentially and irreversibly placed in the RVE unless they overlap. The advantages of using RSA are its simplicity and relatively small computational resource requirement, an advantage that becomes more apparent for poly-disperse cell size distributions. Different techniques are reported in the literature for applying the RSA method, most techniques are suitable for single mode and bimodal cell size generation [Harder and Silbert, 1980; Adamczyk et al. 1997; Brilliantov et al. 1998; Rouault and Assouline, 1998; Gray et al. 2001; Richard et al. 2001; Wu et al. 2003; Gan et al. 2010;]. To generate a poly-disperse polycrystalline microstructure, Fan et al. (2004) applied a modified version of a collective rearrangement algorithm initially developed by He and Ekere (1998). In other attempt, Farr and Groot (2009) developed a new method for packing 3-d poly-disperse spheres based on a one-dimensional mapping. Although all these approaches are applicable to 2 and 3-d cases, as mentioned before, they are best suited to single or bimodal cell size distributions, a higher degree of poly-dispersity tends to be more complicated and time consuming and requires alternative algorithms.

After studying most of the mentioned RSA techniques, the Drop and Roll method [Vischer and Bolsterli, 1972; Okubo and Odagaki, 2004] was judged by the author, to a better algorithm for packing 2-d hard-disks with different degrees of poly-dispersity, two important advantages of the Drop and Roll method, compared to other packing methods, are (i) increased contact between neighbouring disks, which results in higher packing density, (ii) simplicity and (iii) a more efficient computational algorithm [Gibson, 2007]. The classical 2-d Drop and Roll method involves a fixed container with two parallel hard walls and one horizontal hard floor. A disk is first generated with a random diameter size and x-coordinate which must lie within the container area and near the top of the container. The disk is then 'dropped' towards the floor of the container until an equilibrium state is reached. In general, there are three states of equilibrium that each dropped disk must fulfil to prevent further motion, namely (i) the disk hits the hard ground (see Figure 2-6a), (ii) the disk's centre of gravity lies between the centres of gravity of at least two adjacent disks that have previously been dropped and achieved

equilibrium, see Figure 2-6b) and (iii) the centre of gravity of a dropped disk lies between that of an adjacent disk, already in equilibrium, and one of the hard walls (see Figure 2-6c).

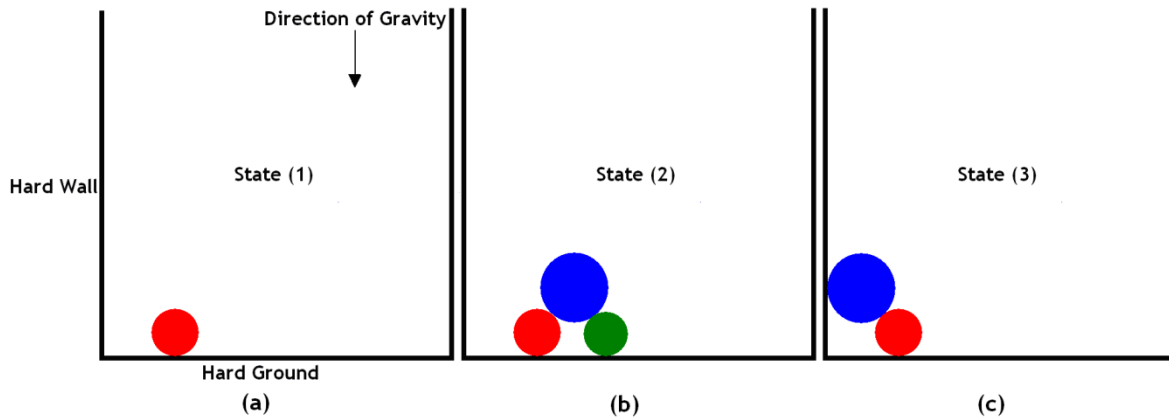


Figure 2-6: Three states of equilibrium which any disk requires fulfilling during the Drop and rolling method. (a) hitting the hard ground (b) setting between two hard disks in the way the its centre of gravity placed between the centres of two adjacent hard disk (c) its centre of gravity placed between one adjacent disk and hard wall.

If the dropped disk hits any other previously dropped disks during its fall towards the hard ground, it will roll about the centre of these disks and will continue to move until fulfilling the equilibrium conditions (ii) or (iii), as described above (see Figure 2-7). The calculation is based on the position of the falling disc's centre of gravity with reference to adjacent disks, hard walls and hard ground.

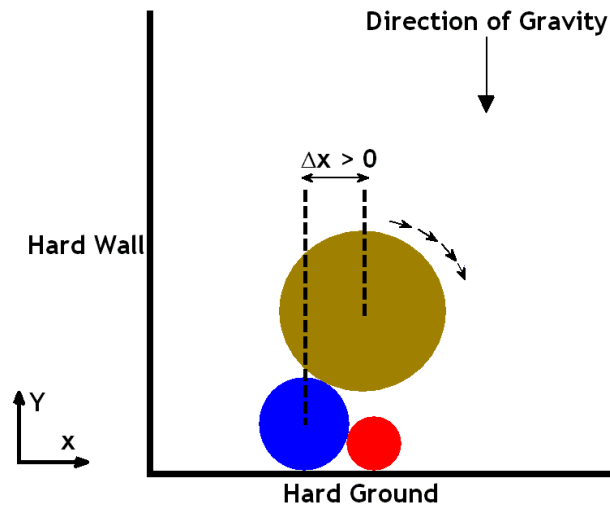


Figure 2-7: An illustrative example of the rolling disk in the Drop and Roll method. Since the target disk has a positive centre of gravity with regards of centre of adjacent disk, it rolls clock-wise.

The Drop and Roll algorithm was implemented as part of this investigation and then enhanced to make it suitable for the generation of RVEs with PBCs. By using the Drop and Roll method it is possible to construct an RVE which is periodic about the left and right hand walls of the RVE using the following procedure: (i) consider a central container C (see Figure 2-8) to be the target area for the final RVE, (ii) consider containers C_L and C_R with exactly the same size and with common walls at the left and right hand sides of container C , (iii) in each step, generate a hard disk in C and create identical disks with the same axial coordinates as in the corresponding containers, C_L and C_R (iv) the hard disk in the left and right containers must roll and propagate in the same manner as in the central container (v) the hard disks are allowed to roll freely across the side walls until reaching an equilibrium position, thus the side walls can be described as soft walls, whereas the ground is a hard wall.

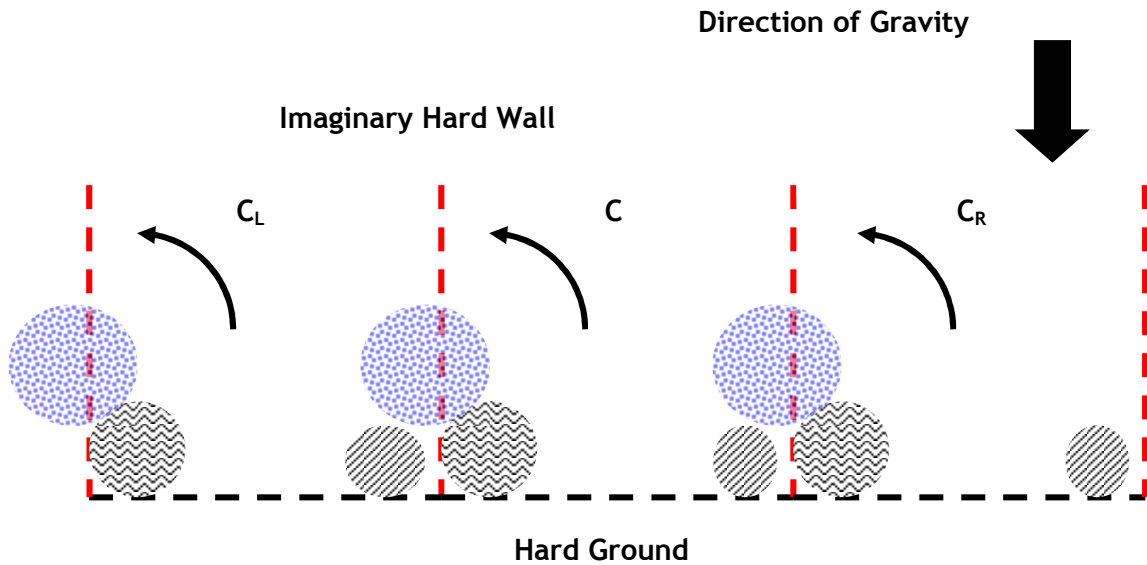


Figure 2-8: Example of generating a 2-d periodic pattern about hard walls, using the Drop and Roll method. Black discs lie on the ground, whereas the rolling disk (blue) will pass through the hard wall.

However, since some of the disks lie on the straight hard ground the 2-d RVE is not periodic across its top and bottom boundaries. To tackle this problem, rather than dropping constantly from the top direction and using a bottom hard ground wall, it was decided to drop disks from four orthogonal directions by changing both the direction of gravity and the position of the hard ground. Also, in order to avoid generation of an RVE with hard disks lying along a straight line above the ground wall, step (i) was re-defined; in this new implementation the dropped hard disks were permitted to penetrate the hard ground up to their central points, i.e. the hard ground is now better described as a semi-hard ground (see Figure 2-9).

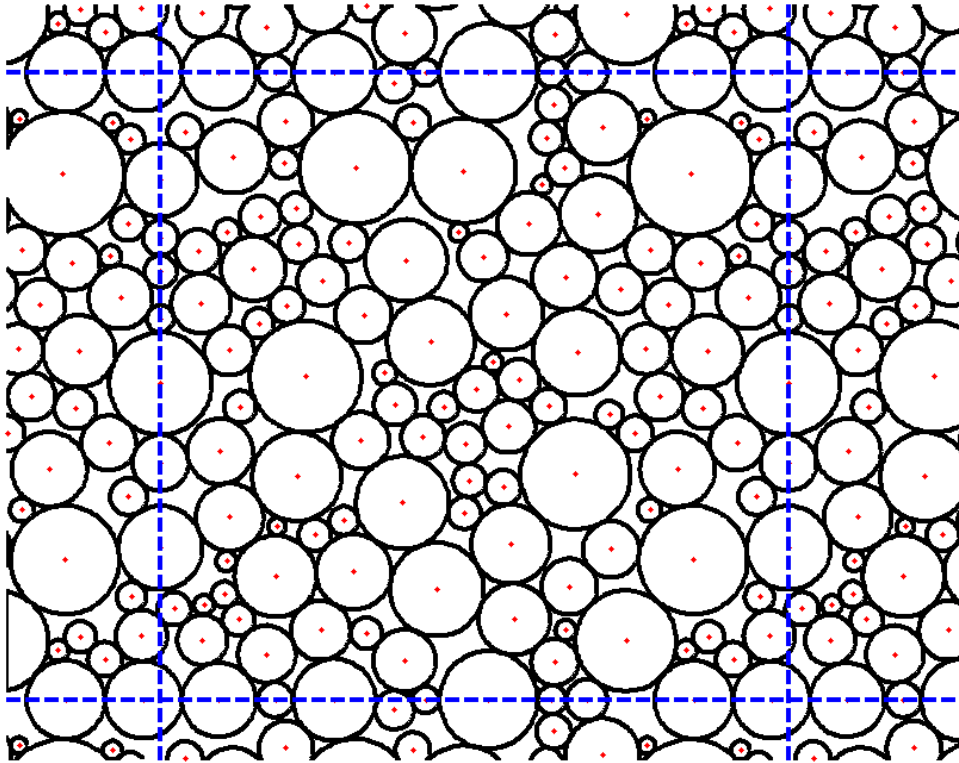


Figure 2-9: Example of periodic RVE of poly-disperse disks generated by modified Drop and Roll method (Total occupied area of square RVE by hard-disk = 80%).

It will be shown in Sections 4.2.3, 5.3.2 that RVEs generated from seed-based Voronoi techniques, such as that employed in the Zhu method, tend to generate microstructures with inherently anisotropic organisation and mechanical properties. This is particularly true for cases with a lower degree of irregularity when the cell morphology approaches a honeycomb (see Chapter 3 for further discussion). It will be shown in the next chapter that the Drop and Roll method is better suited to producing perfectly isotropic RVEs. The Drop and Roll method is therefore found to be a very efficient technique to produce isotropic RVEs with different degrees of poly-dispersity. However, its disadvantage is in (i) its relatively large computational resource requirement resulting in very time-consuming simulations, (ii) it is sometimes impossible to generate mono-sized cells within the RVE using this method and (iii) it is difficult to extend the method to the 3-d case (see Chapter 6 for further discussion of this point)

2.1.4 Mono-disperse foam-like RVE generation by employing the Lloyd's relaxation algorithm

In order to generate realistic morphologies closely resembling real mono-disperse foam microstructures, in a reasonable computational time, the Centroidal Voronoi Tessellation (CVT) method has been found to be a convenient approach. The technique can be used to construct both 2-d and 3-d periodic RVEs with a highly mono-disperse cellular size distribution. This technique is a special type of classical Voronoi method which decomposes Euclidian space into even, but not necessary equal, sub-sections [Burkardt et al. 2002]. Liu et al. 2009 considered the Lloyd's algorithm [Lloyd, 1982] to be the best technique for computing a CVT. This algorithm can be described as an iterative 'relaxation process' where a classical Voronoi cell is generated in each iteration. Each corresponding seed will then be updated using the position of the Voronoi cell's centre of mass (see Figure 2-10).

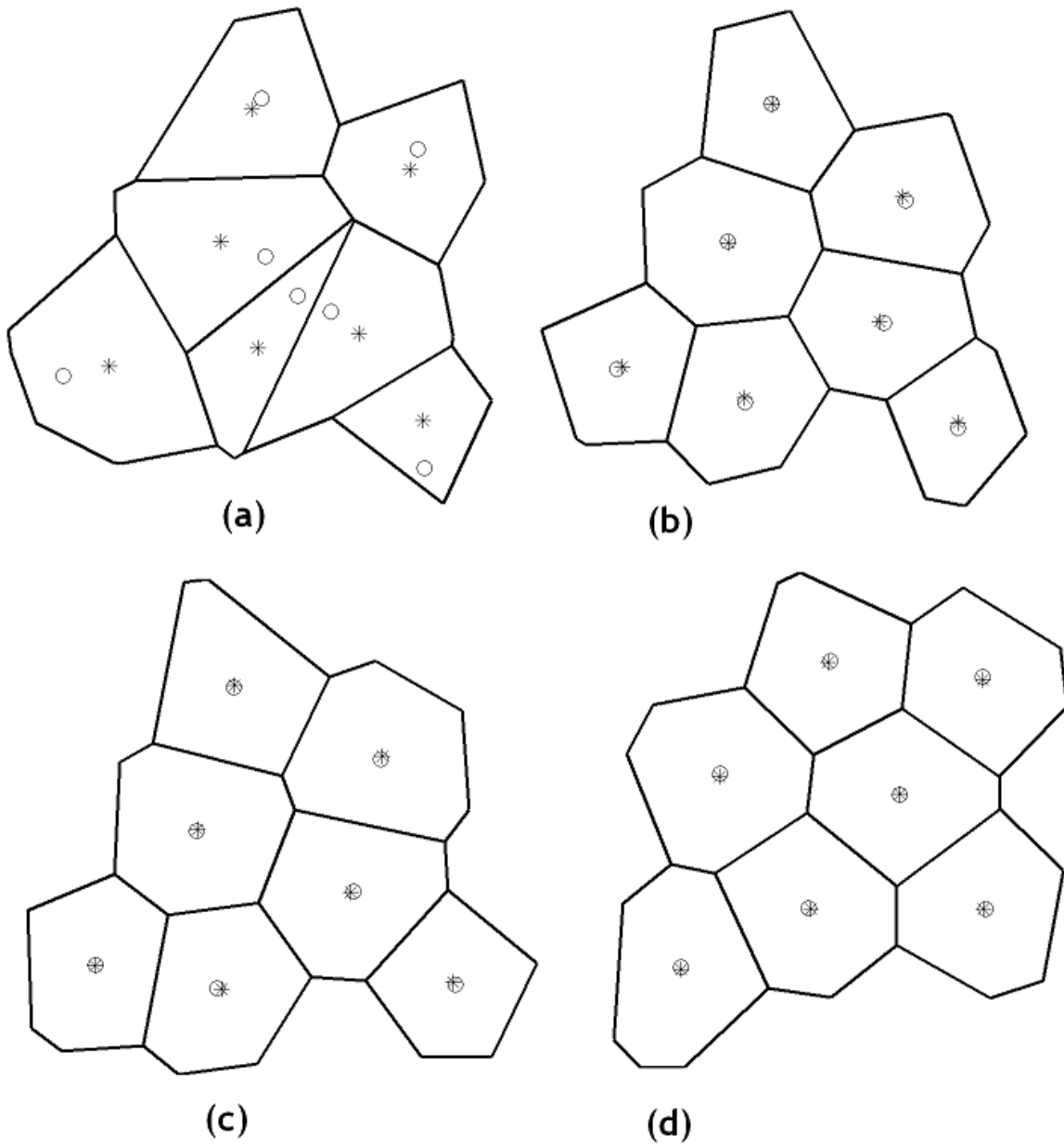


Figure 2-10: Illustrative example of Lloyd's algorithm. At each iteration (a, b, c, d) a centre of mass for each Voronoi cell is calculated (black stars) and replaced by seed (circles).

The iteration process is terminated by setting a given tolerance between the computed centre of mass and the Voronoi seed. By first generating a set of random seeds in a specified plane or space, the final microstructure will eventually appear to be similar to Voronoi models generated using algorithms similar to those described in Section 2.1.2 when using a low degree of irregularity but here the RVE has isotropic properties (as demonstrated in Chapters 3 and 5). The technique can

therefore be employed to generate periodic foam-like RVEs with almost perfect mono-disperse cell-size distribution (see Figure 2-11).

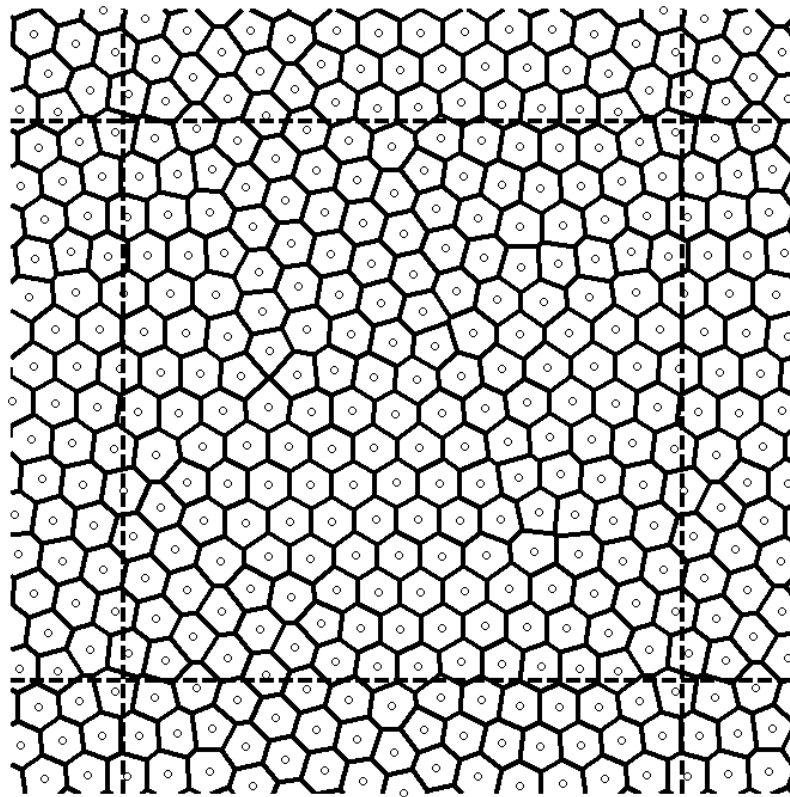


Figure 2-11: Example of a fully periodic RVE (the central square), generated using the Lloyd's relaxation algorithm

2.2 Two-dimensional modelling of aerogels

In order to create a generic periodic RVE mesh-generator for all porous materials, some attention has been paid to materials other than gas-expanded foams, namely aerogels. This part of the investigation demonstrates the idea that alternative numerical algorithms must be considered if significantly different microstructures are to be modelled.

2.2.1 Introduction

For the purposes of modelling the microstructure of a given material it is important to understand the general process of material production. A three dimensional aerogel network is generated by continuous colloidal interaction between primary and secondary particles during the sol-gel process where, primary particles aggregate to form larger blocks of secondary particles. The secondary

particles then connect to each other and form a pearl-necklace type structure separated by mesopores (see Figure 2-12).

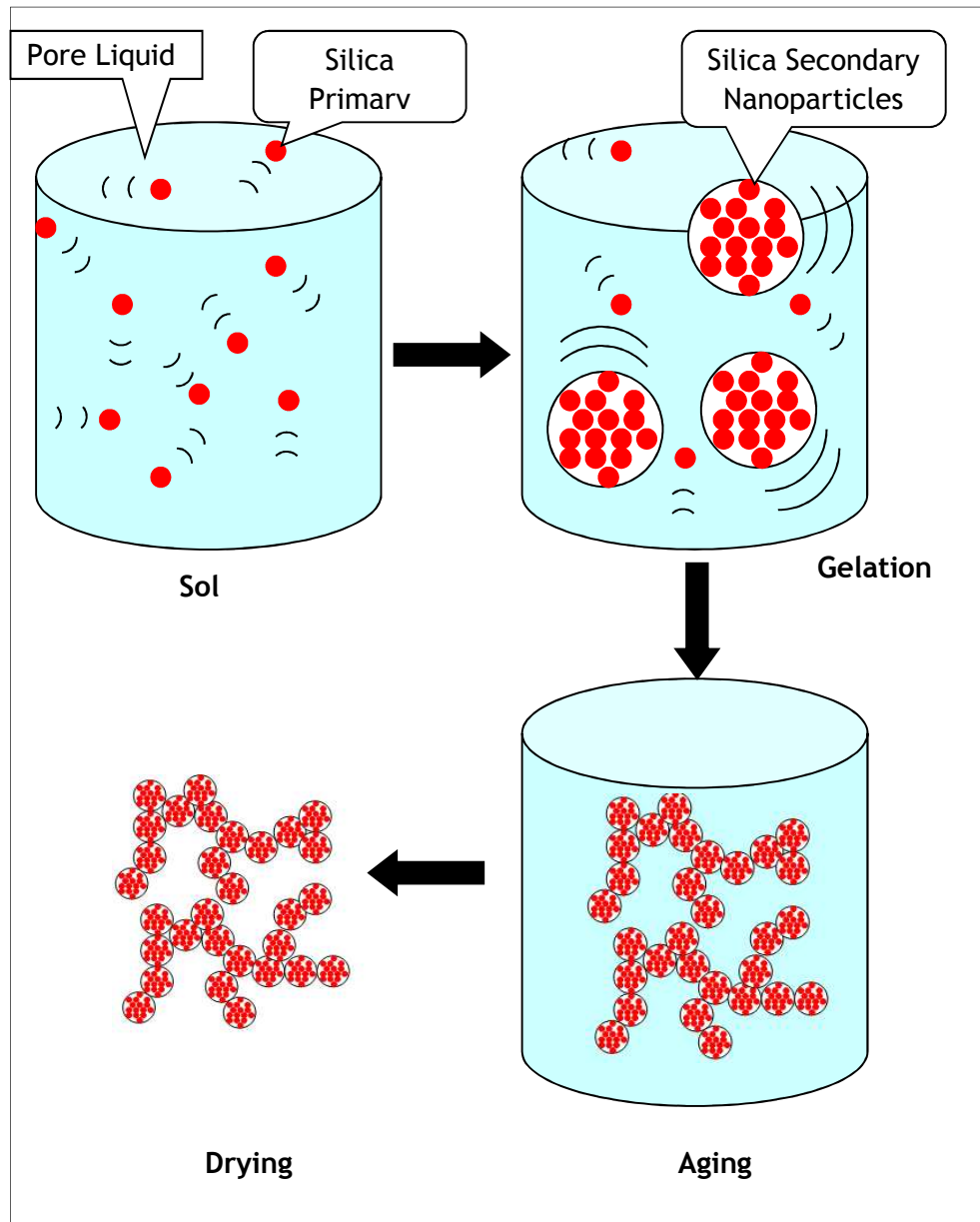


Figure 2-12: Physical representation of aerogel synthesis [Husing and Schubert, 1998].

2.2.2 Two-dimensional particle-based RVE generation methods

For a given type of precursor material e.g. silica, the microstructural geometry of aerogels tends to be similar. In chapter 3 it will be shown that, since aerogels are

porous, some of their mechanical properties, such as stiffness, can be estimated reasonably well using a simple power law relationship between stiffness and relative density. However, a more intimate understanding of the relationship between nanostructure and macroscopic properties requires detailed modelling of the underlying aerogel network morphology. As with regular gas-expanded foams, a multi-scale modelling approach can be used to predict mechanical properties using FEM. Imaging aerogels is possible by using several techniques such as Scanning Electron Microscope (SEM), Transmission Electron Microscopy (TEM) or Small Angle Neutron Scattering (SANS) [Pajnok et al. 1996; Despetis et al. 2012; Merzbacher et al. 1998]. Due to the micro and nano-scale porosities of aerogels, all these imaging techniques are required to be performed in order to study the real structure of aerogels across both the nano and micro scales [Ma et al. 2000].

Molecular Dynamic (MD) is one of the techniques employed in the past to generate a silica aerogel fractal network. The method requires large computational power with knowledge about the material chemical evolution and molecular interactions [Nakano et al. 1993; Pohl et al. 1995; Bhattacharya and Kieffer, 2005]. The colloidal movement of nanoparticles can be explained by Fick's law of diffusion [Callister, 2003]:

$$\frac{\partial \varphi_c}{\partial t} = D_c \frac{\partial^2 \varphi_c}{\partial x^2} \quad \text{Equation 2-5}$$

where φ_c is the concentration of diffusing particles, D_c is the diffusion coefficient, x is position and t is the time. Based on this diffusion law, Witten and Sander (1981, 1983) proposed a method known as Diffusion Limited Aggregation (DLA) where particles, based on a diffusive protocol, undergo continuous Brownian motion. In this algorithm, collision with any immobile particle causes the diffusing particle to stop moving. The algorithm results in a complex random dendritic structure (see Figure 2-13).

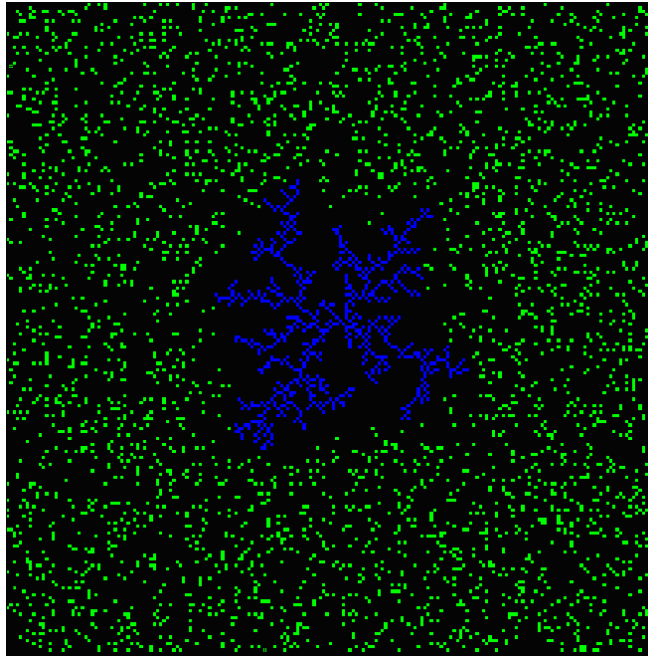


Figure 2-13: Example of 2-d fractal generated by DLA algorithm [Leto, 2007].

Using the DLA as their inspiration Meakin (1983) developed an algorithm to generate fractal structures. The algorithm predicts a microstructure comprised of several connected clusters, the final network geometry is superficially very similar to those seen in silica aerogels. In most of the literature this technique has been referred to Diffusion Limited Cluster Aggregation (DLCA) or Diffusion Limited Cluster-Cluster Aggregation (DLCCA) method [Rahmani et al. 1996]. In this modified technique, clusters as well as single particles undergo Brownian motion (diffusion) based on a diffusive protocol. As with the DLA they also stick together on contact producing larger clusters. The process continues until a final single cluster, comprised of all the initially distinct particles, is created (see Figure 2-14).

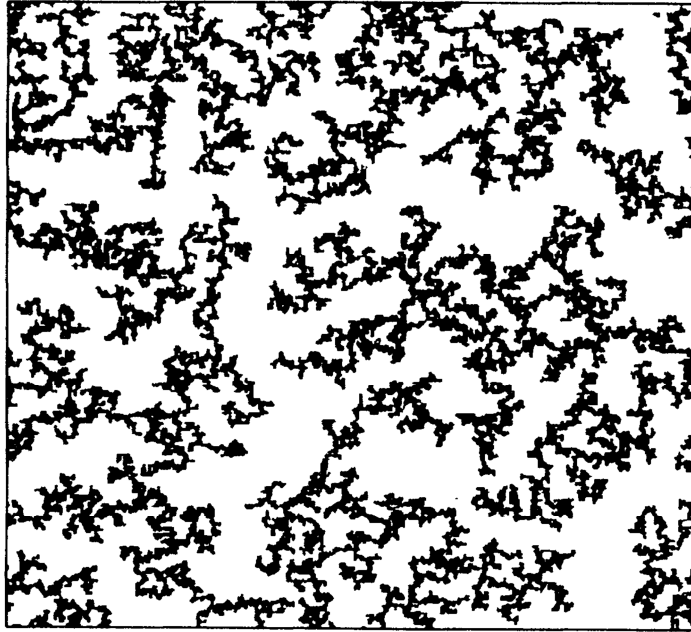


Figure 2-14: 2-d periodic Fractal structure generated by DLCA method consisting of 25000 particles [Meakin, 1983].

Generally, there are two approaches to implementing a DLCA algorithm, each involving a lattice with area, A_L , and a particle lattice density, $\rho_p = N_p/A_L$ where N_p is the number of non-overlapping particles in the lattice [Meakin and Wasserman, 1984]. These are the on-lattice and off-lattice methods. The main difference between the two algorithms is that under the first approach, each particle is represented by a square ‘pixel’ inside a lattice grid and can only perform random-walk motion whereas in the second approach, particles are represented by small disks (in 2-d) and are free to perform fully Brownian motion in any direction. Meakin (1999) found that both modelling methods have the same fractal dimensionality, equal to a universal value, but the lattice model is computationally more efficient. To define a diffusive protocol, Meakin (1983; 1999), proposed a diffusion coefficient as follows:

$$D(S) \approx S^{\gamma_F}$$

Equation 2-6

where, D , is a diffusive coefficient, S , is the mass of a given cluster and, γ_F , is the diffusion coefficient exponent. By comparing results of several simulations Meakin (1983) provided a simple way to evaluate γ_F for the 2-d case, i.e.

$$\gamma_F = -\frac{1}{2-d}, d \approx 1.4 - 1.5 \quad \text{Equation 2-7}$$

where, d , is the fractal dimensionality. Although there is some debate about the right approach to defining a diffusive protocol, particularly in regard to limiting the effect of size scale [Kolb and Jullien, 1984; Emmerling and Fricke, 1997; Gimel et al. 1999] DLCA has generally been shown to be a good method of modelling many inorganic aerogels such as silica. Nevertheless, a few exceptions to this have been noted [Roberts, 1996].

2.2.3 Generation of 2-d periodic aerogel model by DLCA

A DLCA algorithm has been implemented in this investigation using MATLAB™ software and employing Meakin's (1999) procedure (see Figure 2-15). In the pre-modelling stage based on the final targeted structure, operator must specify a lattice size, fractal density (number of particle per unit lattice), diffusion coefficient and allowable cluster/particle displacement values. From fractal density value and the lattice size, N number of non-overlapped particles are generated and labelled. During each iteration, particles (or clusters) are randomly selected and assigned to lateral and/or vertical displacement. If two particles (or cluster) collide with each other they will aggregate as a new cluster with different label. The whole process will continue in several iteration loop until one cluster to be achieved. 2-d aerogel-like microstructures have been generated where each particle is represented by a unit square cell in a lattice matrix.

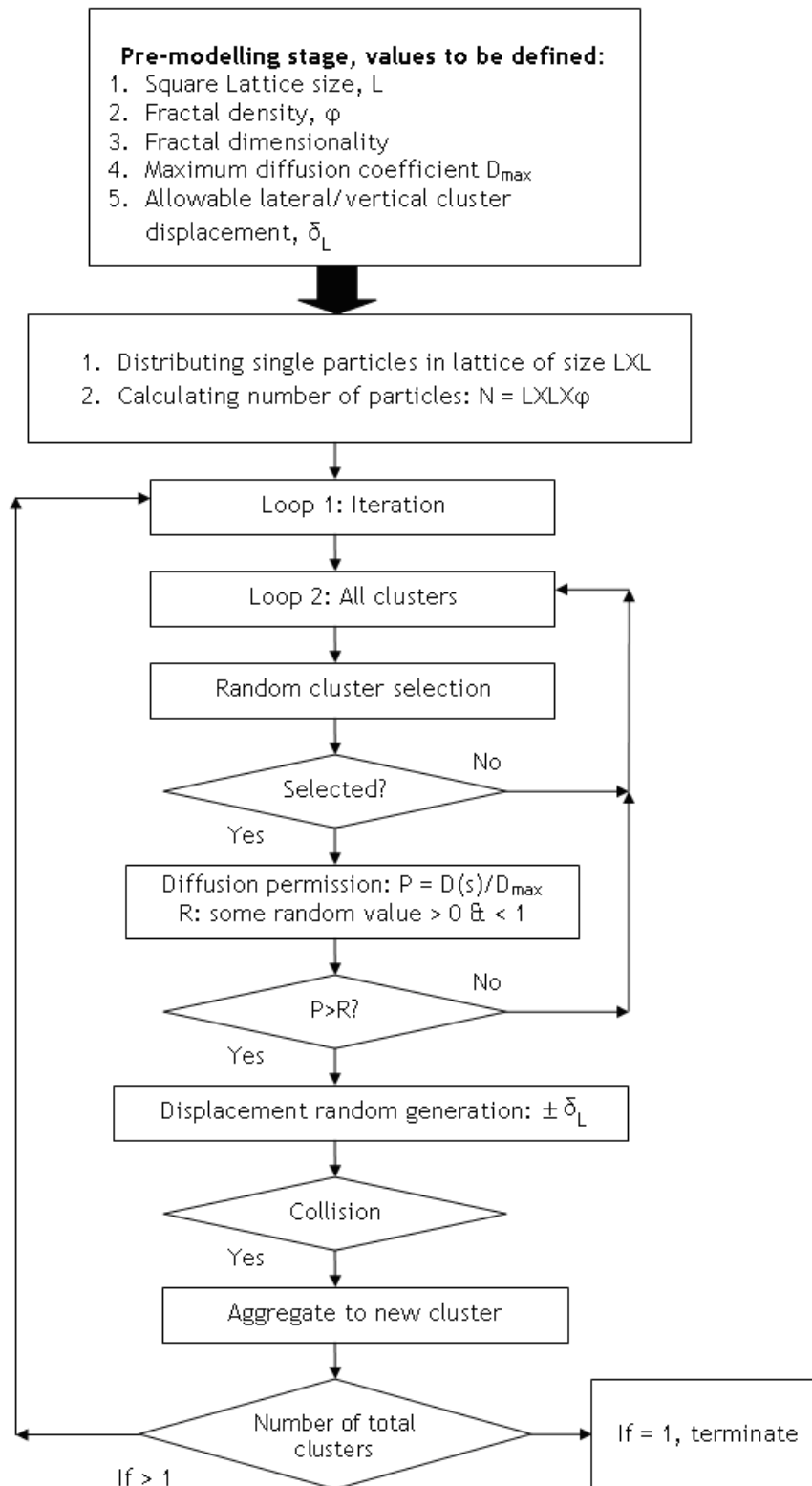


Figure 2-15: DLCA procedure based on 2-d lattice based modelling.

In the DLCA method implemented here, the algorithm has been adapted to ensure geometrical periodicity. This is achieved by transforming single particles or clusters to the counterpart boundary if the particle or cluster diffuses through the lattice boundaries.

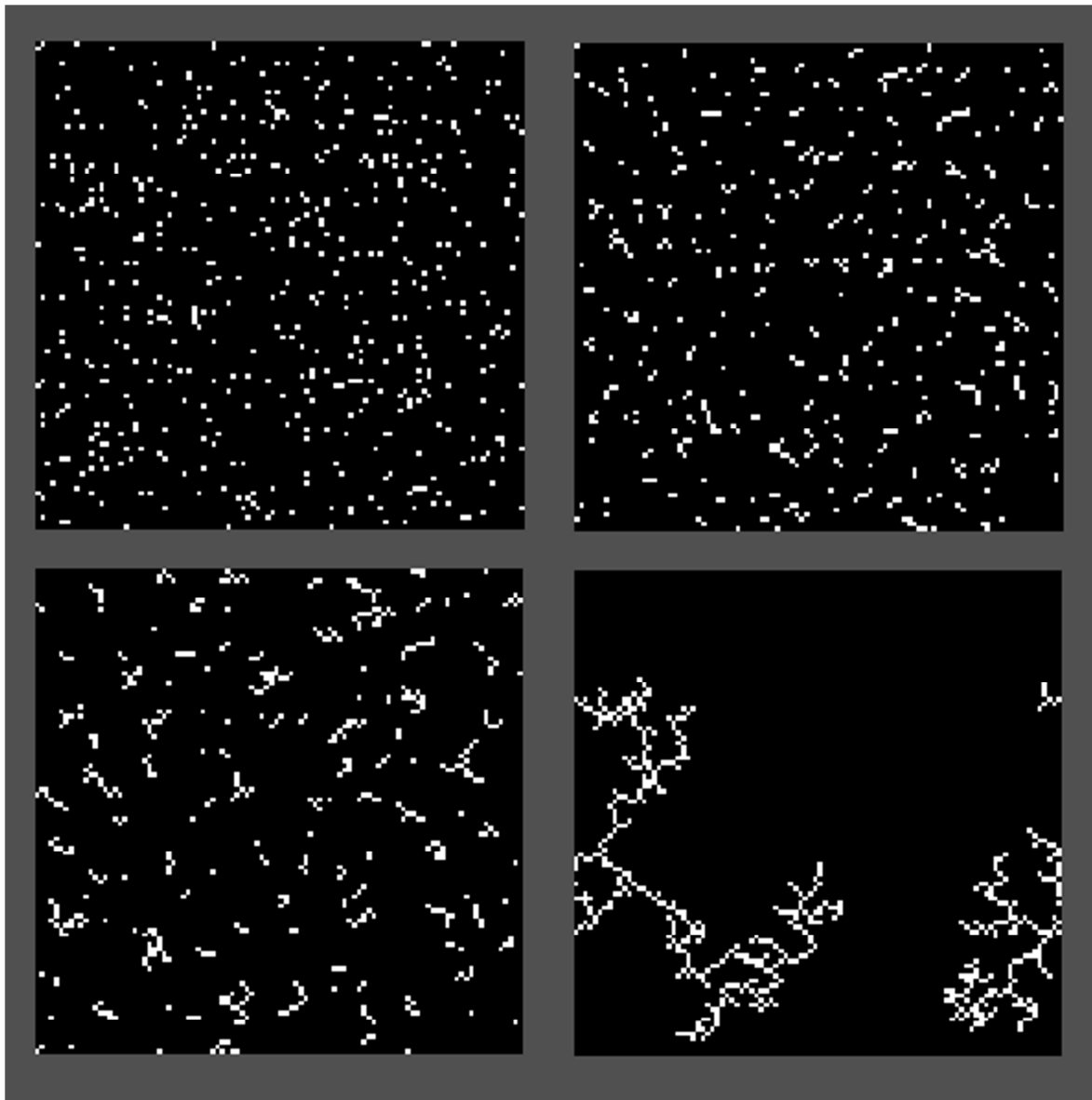


Figure 2-16: Four different stages of aggregation process. Lattice size, $L = 100$, Packing density, $\varphi=0.05$, number of particles, $N = 450$, $\delta_L=1$ and $\gamma_F = -0.5$. (top left) total number of clusters = 451 (top right) total number of clusters = 225 (bottom left) total number of clusters = 13 (bottom right) total number of clusters = 1.

2.2.4 Converting lattice-based RVE to beam-based

Classical DLCA needs to be further modified to provide a more realistic structure. This is due to the presence of ‘dangling bonds’ [Emmerling and Fricke, 1997; Ma et al. 2000] which add an artificial mass to the cluster without having a contribution on overall stiffness and strength of material. For the purpose of the current work, due to the over-simplification already introduced by considering only a 2-d microstructure, treatment of dangling-bonds is omitted. Since the final DLCA structure is similar to an assembly of randomly sized connected rods, and also (particularly for small values of the ϕ), most of the rod-like elements are of just one particle thickness, it is convenient to idealise the final microstructure as a beam-based network. Converting such as a lattice-based structure to a slender beam-based structure has been performed in only a few previous works. In such cases the beam geometry was added as a straight line connecting the centres of two adjacent particles [Ma et al. 2000; 2002]. It can be seen in Figure 2-16 that the microstructure generated from DLCA cannot lead to acceptable results when using a multi-scale RVE modelling approach due to the internal discontinuous geometry of cluster. However, for the purpose of the current section, the equivalent 2-d beam-based RVE of DLCA-generated microstructure models are generated using the same procedure as that used in modelling foam (see Figure 2-17).

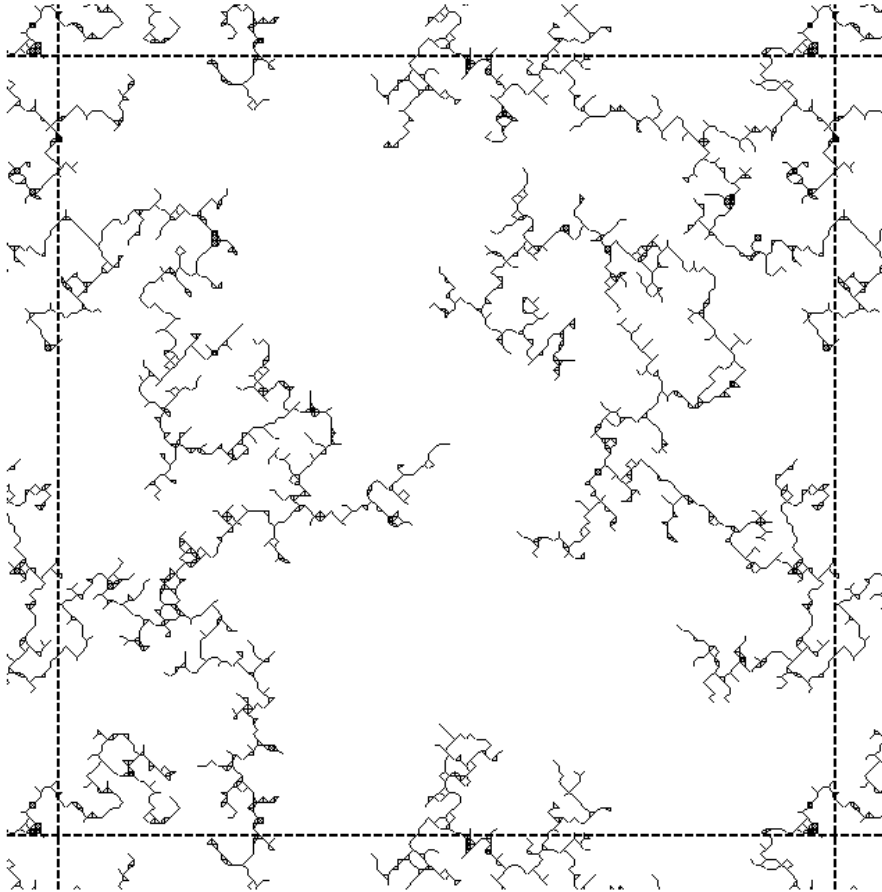


Figure 2-17: An example of a fully periodic structure (the central square) generated using the DLCA method. Beams are generated by considering straight lines between the centres of two adjacent particles.

2.3 Conclusions of Chapter 2

Use of several different algorithms to generate two dimensional idealisations of open-cell networks has been considered, and also, by using the concepts of a RVE and a PBC, several modelling methodologies have been proposed to generate beam-based structures of foams and aerogels. These models are formatted so that they can be employed easily by general purpose FE software, such as Abaqus, in order to investigate the mechanical response of these materials at the micro-scale. Advantages and limitations associated with each modelling technique were briefly mentioned in this Chapter. In the next Chapters, it will be shown that the accuracy of results produced when using a specific modelling technique, strongly depend on the type of mechanical response that is required from FE simulation. For example

the prediction of microstructure stiffness at very small compressive strain (less than 1%) is almost insensitive to RVE size and cellular morphology, however, for further compressive strain analysis more modelling and simulation complexity is required.

Chapter 3 . Mechanical Evaluation of Two-dimensional RVEs

3.1 Introduction

To investigate the mechanical response of the microstructure in plateau region, particularly for irregular and poly-disperse geometries, it is vital to include self-contact within the microstructure. Several good attempts to include self-contact in previous studies have been reported in order to simulate the impact response of foam while including the effect of densification [Zheng et al. 2005; Li et al. 2007; Borovinsek and Ren, 2008; Song et al. 2010]. These simulations were conducted without application of a PBC, a necessary omission due to the inertial response induced during high rate impacts. Thus, these studies were effectively simulations of simple macro-scale structures incorporating detail at the micro-scale. To the best of the authors' knowledge, there have been no investigations reported in the literature that consider the large-strain compressive behaviour of either a two or three-dimensional beam-based RVE that incorporates both self-contact and a periodic boundary condition. Here, a method of simultaneously including both of these features in two-dimensional RVEs, using a commercial FE code is demonstrated. Depending on the application, various material properties can be of interest when designing products incorporating foams, including stiffness, yield stress, Poisson's ratio, length and form of the plateau region and onset strain of densification [Li et al 2006^b]. In addition, during the course of this investigation an additional material parameter has been identified; the contact strain. The latter has been found to be a very useful parameter in enhancing computational efficiency through guiding simulation strategy and through predicting the onset strain of densification using relatively small RVEs (see Section 3.2.4). Due to the gradually changing form of a typical foam's stress - strain curve, exact determination of these parameters can be difficult and so, in current chapter, brief descriptions of these properties and the methods used to determine their values is presented. Properties are considered in the following order: (i) the form

of the plateau stress and (ii) the onset strain of densification and the contact strain. Prior to discussing these results, Sections 3.2.2 and 3.2.3 address some of the computational issues that have to be addressed in conducting this investigation. In order to facilitate generic comparison of results with those produced elsewhere (e.g. Zhu et al. 2002) a dimensionless ‘reduced stress’ is used throughout this investigation, (see Eq. 3-1) [Zhu et al. 2006] which allows comparison of stress results between RVEs of differing relative density and with different element modulus.

$$\bar{\sigma} = \frac{\sigma}{E_S \left(\frac{\rho^*}{\rho_S} \right)^3} \quad \text{Equation 3-1}$$

here E_S and ρ_S are the Young’s modulus and density of solid material and ρ^* is the foam density. The behaviour of cellular structures examined in this investigation is highly non-linear. The reduced stress-strain curves rarely show an initial perfectly linear response at small-strains, due to the gradual yet early onset of bending and buckling of beams within the microstructure. Defining equivalent representative quantities for the plateau region of the stress-strain curves is not straight forward and so only a qualitative comparison of the form of the reduced stress-strain curve is performed. The onset strain of densification is the point towards the end of the plateau region, at which the gradient of the stress-strain curve shows a sudden increase. It is a particularly important quantity when considering the behaviour of foams under large compressive strains such as in impact, packaging and cushioning applications. Following Li et al 2006^b, the onset strain of densification can be identified consistently and objectively using the location of the maximum of the ‘efficiency function’, η :

$$\eta(\varepsilon) = \frac{1}{\sigma(\varepsilon) \varepsilon_y} \int_{\varepsilon_y}^{\varepsilon} \sigma(\varepsilon) d\varepsilon \quad \text{Equation 3-2}$$

where, σ , is stress, ε is strain and ε_y is the yield strain of the material (taken here at 10% strain). The contact strain introduced here, is very similar to the onset strain of densification though the use of computational modelling allows a more precise definition; i.e. the strain at which self-contact within the microstructure results in an increase of 5 per cent in the stress-strain response of the RVE,

immediately prior to the permanent divergence of the two curves as the strain increases, as compared to an identical RVE deforming without self-contact. It also differs to the onset strain of densification in the method by which it is determined. By conducting simulations both with and without contact, its location becomes apparent when directly comparing the subsequent reduced stress - strain curves; the two curves follow similar paths until a certain strain, after which the curves diverge (see Figure 3-1).

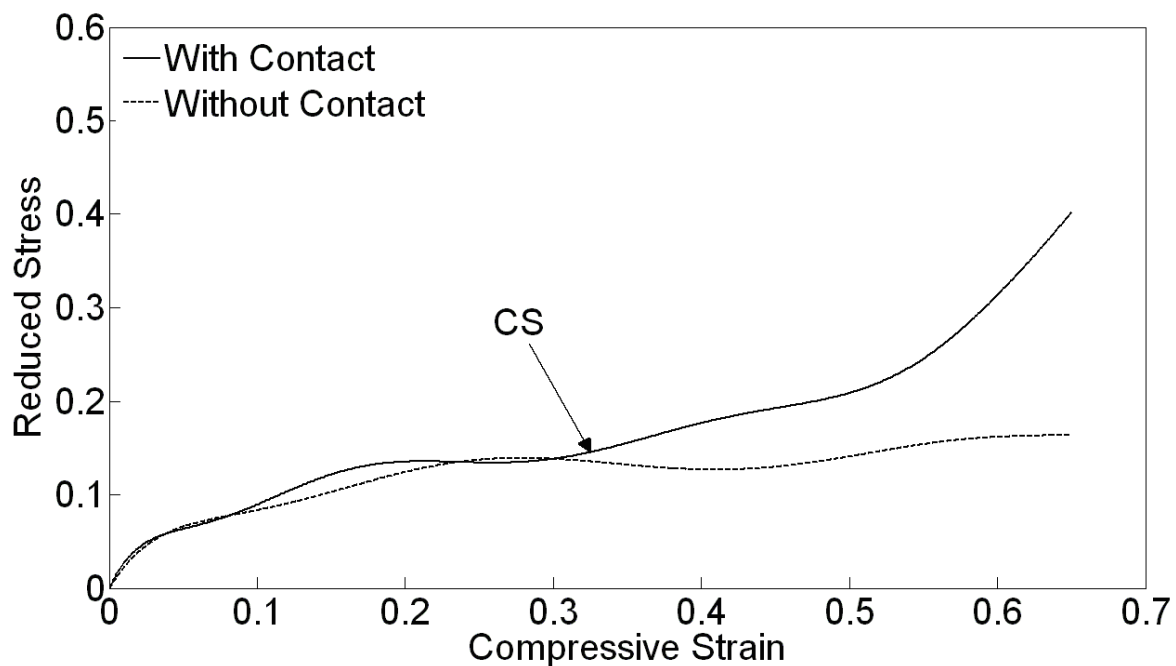


Figure 3-1: Example of determination of contact strain (for RVE generated by modified Zhu method with high degree of irregularity, i.e. $\alpha=50$).

Experience suggests that in most cases self-contact within the RVE microstructure usually starts after about 20% (minimum) compressive strain, though only begins to significantly affect the form of the reduced stress-strain curve at higher strains, i.e. at and after the contact strain. To investigate the effect of structural inhomogeneity, the modified method of Zhu and the Drop and Roll algorithms are employed in generating RVEs for use in mechanical simulations in the current chapter, here considering only uniaxial compression in the direction perpendicular to the top surface of the square RVE.

3.2 Mono-disperse microstructure created using the modified Zhu algorithm

3.2.1 RVE design

To study the effect of the degree of irregularity four different values of α have been employed in generating RVEs ($\alpha = 0, 10, 20, 50$). Examples are shown in Figure 3-2 where each image shows RVEs containing 150 cells; the smallest RVE size used in this investigation. The relative density of each RVE is kept constant however the total element length tends to increase with an increasing degree of irregularity.

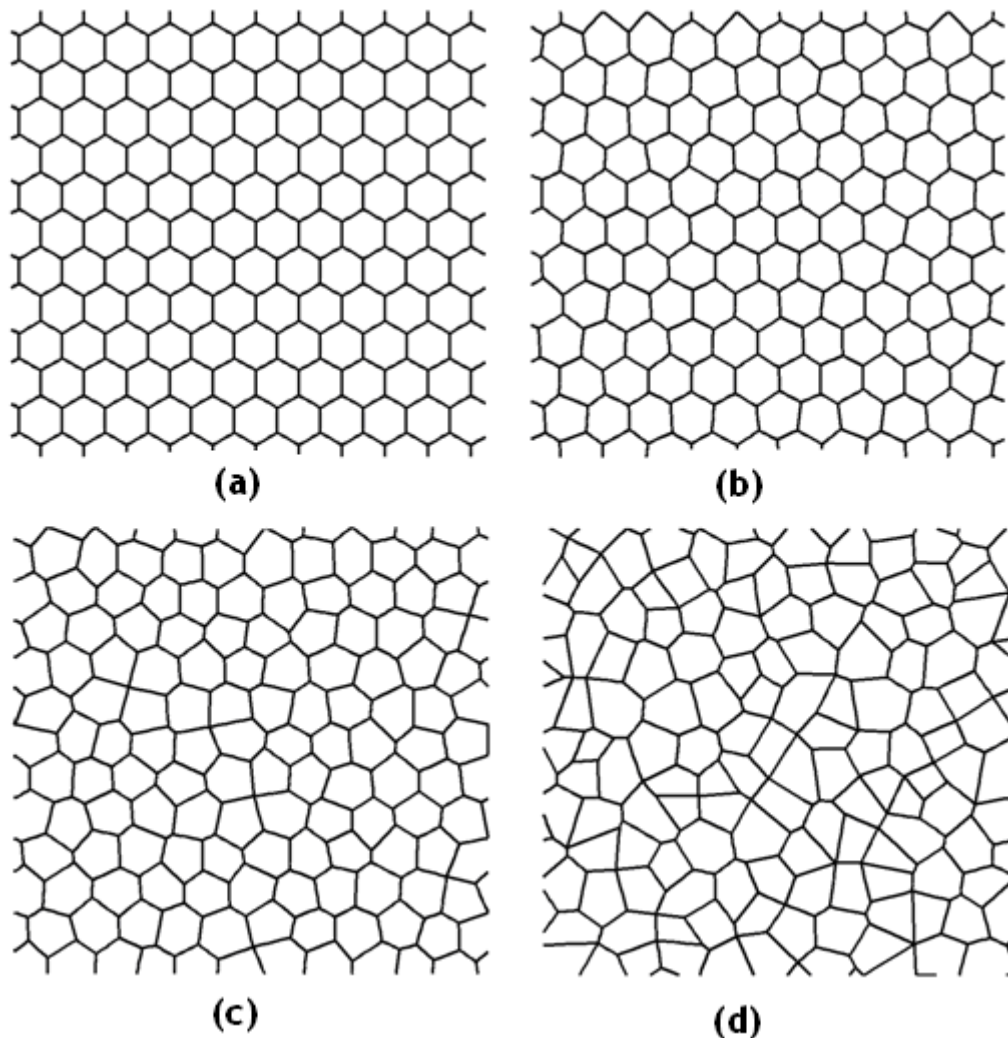


Figure 3-2: Single size RVE (about 150 cells) with different degree of irregularities with same size and material specifications. (a) $\alpha=0$, (b) $\alpha=10$, (c) $\alpha=20$, (d) $\alpha=50$.

Consequently, Eq. 3-3 implies that the average thickness of the elements tends to decrease with increasing values of α . Since only low-density open cell foams are

considered in the current investigation ($\rho^*/\rho_s=0.05$), use of beam structures of constant cross-section is a reasonable approximation. Each rib of each cell has been initially modelled using five equal length Timoshenko beam elements with a constant square cross-section of side-length, t_c . The latter is calculated using Eq. 3-3 which relates t_c to the relative density, ρ^*/ρ_s , and total length of the elements within the RVE [Zhu et al. 2001^a]:

$$t_c = \frac{(\rho^*/\rho_s)A}{\sum_{k=1}^{n_e} l'_k} \quad \text{Equation 3-3}$$

where n_e is the number of elements, A is the area of the RVE, l' is the length of each individual element and k is the number of elements within RVE. For all cases, the material model is linear elastic with a Young's modulus, E_s of 10^9 Pa, material density, ρ_s of 2000 kgm^{-3} and Poisson's ratio = 0.33 consequently it should be noted that all conclusions from this work are restricted to linear elastic behaviour. More realistic material behaviour will be included in future work in order to determine if behaviours such as plastic yielding or strain hardening significantly affect the generic findings of this work. All element cross-section properties are assigned prior to the analyses and remain constant during deformation. In the versions of Abaqus used in this investigation (up to and including version 6.12), contact detection between shell elements has been found to be significantly more reliable (less penetration) than contact detection between beam elements. Consequently, for larger strain simulations involving self-contact between the beam structures within the RVE, beam elements have been replaced by equivalent shell element-based beam structures. The technique is fully explained in the Section 3.2.3.

3.2.2 Boundary condition on periodic 2-d RVE

As briefly noted in Section 1.3, in order to apply a PBC on any two or three dimensional RVE, the structure must be fully periodic, meaning that a node on one boundary must have a counterpart at the same horizontal (on sides) or vertical (on top/bottom) position along the opposite boundary (see Figure 1-5), where the superscripts L, R, T and B indicate the left, right, top and bottom boundaries, respectively. A two dimensional PBC requires that: (1) The motion of counterpart

nodes on each pair of RVE boundaries are constrained to each other and (2) Stress continuity across boundaries is preserved. For example, considering the first condition and referring to nodes along the side boundaries of the RVE shown in Figure 1-5(b),

$$U_i^R = U_i^L + U_i^{d_i} \quad i = 1,2 \quad \text{Equation 3-4}$$

$$U_i^R = U_i^L, U_i^B \quad i = 1,2 \quad \text{Equation 3-5}$$

where U is the nodal displacement in the i^{th} direction, the subscript, i , represents the degree of freedom with $i = 1,2$ indicating displacements in the X and Y directions and $i = 3$ indicating rotation perpendicular to the X-Y plane. In order to implement the PBC, the 'EQUATION' keyword option available in Abaqus™ has been employed. Two dummy nodes are generated, indicated in Eq. 3-4 by the superscript, d_i . The second condition implies the traction vector acting on opposing boundaries of the RVE is equal and opposite at all counterpart points. Using two side nodes as an example,

$$\sigma^R \cdot n^R(r^R) = -\sigma^L \cdot n^L(r^L) \quad \text{Equation 3-6}$$

Where the unit vectors $n^R(r^R)$ and $n^L(r^L)$ are normal to the right and left boundaries at the location of the nodes. The motion of the dummy node controlling the relative displacement of the horizontal edges of the RVE is prescribed according to the imposed compression strain (and the size of the RVE) while the motion of the dummy node controlling the displacement of the vertical edges of the RVE is determined by the FE code in order to maintain stress equilibrium across the vertical boundaries. Stress continuity at the boundaries when imposing a PBC is discussed in detail by Smit et al. (1998).

3.2.3 Equivalent shell-based RVEs

Three dimensional general purpose linear shell elements with reduced integration (type S4R element in Abaqus) have been used. As with the Timoshenko beam elements, (B21), transverse stiffness is considered and the behaviour of these elements converges to shear flexible theory for thick shells and to classical theory for thin shells (Abaqus User Manual v6.9). By appropriate adjustment of their structural and material parameters, the axial and flexural mechanical response of

beam and shell elements can be made equivalent. In this investigation, the thickness of beam and shell elements is equal while the width of the shell elements in the Z direction is 10 times the thickness, see Figure 3-3.

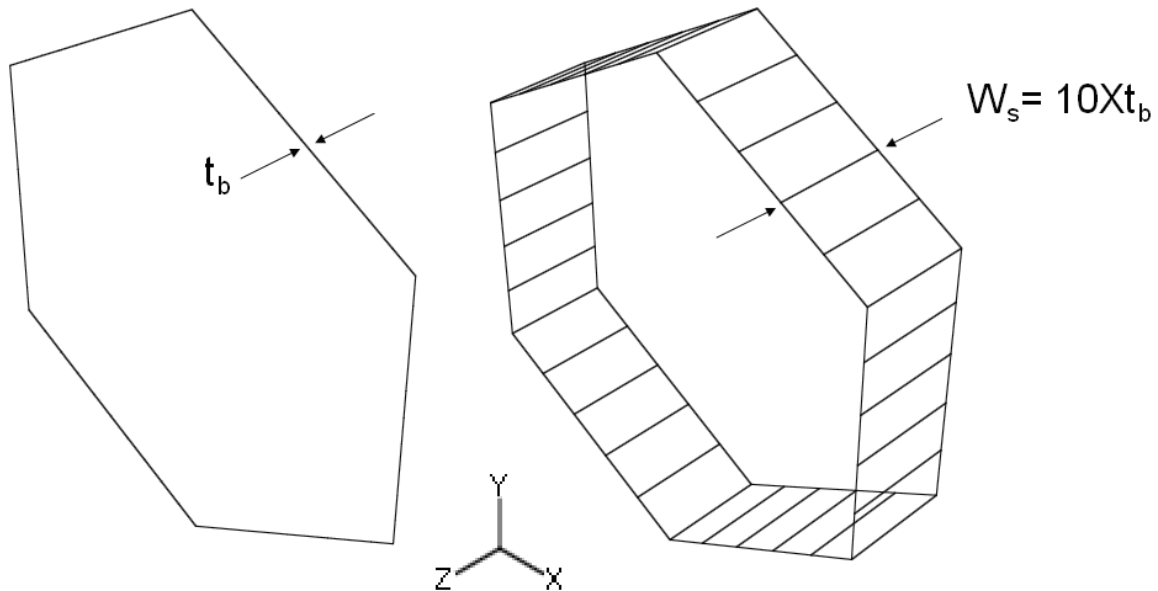


Figure 3-3: Schematic representation of four noded 3-d shell-based RVE based on 2-d beam-based RVE where the shell width is 10 times than beam and shell thickness.

Decreasing this factor results in faster simulation times but increases the risk of numerical convergence problems. Note that for reasons of computational efficiency this investigation aims to use structural elements throughout. Equivalent shell elements are therefore calibrated against beam elements rather than against a continuum element model of a beam in order to maintain the same underlying assumptions in the models and to therefore facilitate direct comparison of shell-element and beam-element based RVEs. Eq. 3-7 and 3-8 are the main structural equations for the bending modulus of rectangular cross-section beam and shell elements for slender beams and thin shells.

$$q_{beam} = EI \frac{\partial^4 w}{\partial x^4}, \quad D'_{beam} = EI \quad \text{Equation 3-7}$$

$$q_{shell} = \frac{Eh_s^3}{12(1-\nu^2)} \nabla^4 w, \quad D'_{shell} = \frac{Eh_s^3}{12(1-\nu^2)} \quad \text{Equation 3-8}$$

where q is the applied load, h_s is the shell thickness, w is the deflection (of the beam/shell), ν is the Poisson's ratio, I is the second moment of inertia of the beam, E is the Young's modulus and D' represents the flexural rigidity of beam/shell. The Poisson's ratio of the material, which is present in the shell formulation, see Eq. 3-7, is absent from the beam formulation [Saada, 1974] and so the shell's material Poisson's ratio must be set to 0 to produce an equivalent response as the beam elements. In addition, a structural element's 'effective section' Poisson's ratio controls the element's thickness behaviour as a result of axial or in-plane strains. As mentioned previously, the beam's cross-sectional area is constant, implying a default effective section Poisson's ratio of 0. In contrast, for shell elements, unless specified otherwise the element's effective section is predicted using Eq. 3-9 and can be chosen between 0 and 0.5. (Abaqus User Manual)

$$\frac{t_h}{t'_h} = \left(\frac{A_h}{A'_h} \right)^{\frac{\nu_s}{1-\nu_s}} \quad \text{Equation 3-9}$$

where, ν_s is the effective section Poisson's ratio, t_h , is the shell thickness and A_h , is the shell sectional area, the superscript indicates the original value of t and A . In order to produce a constant cross-sectional area, as with the beam elements, ν_s is chosen as 0. All nodal displacements are constrained to lie within the X-Y plane and nodal rotations are constrained about the Z axis only. By normalising the shell RVE force response by the shell width elongation factor (i.e. by dividing by 10), exactly the same mechanical response as an equivalent beam-based RVE (B21) is obtained.

3.2.4 Size and computational resource considerations

Size effects have been explored using RVEs containing 150, 600, 1350 and 2400 cells which can be conveniently referred to as the sizes 1x150, 4x150, 9x150 and 16x150 (see Figure 3-4).

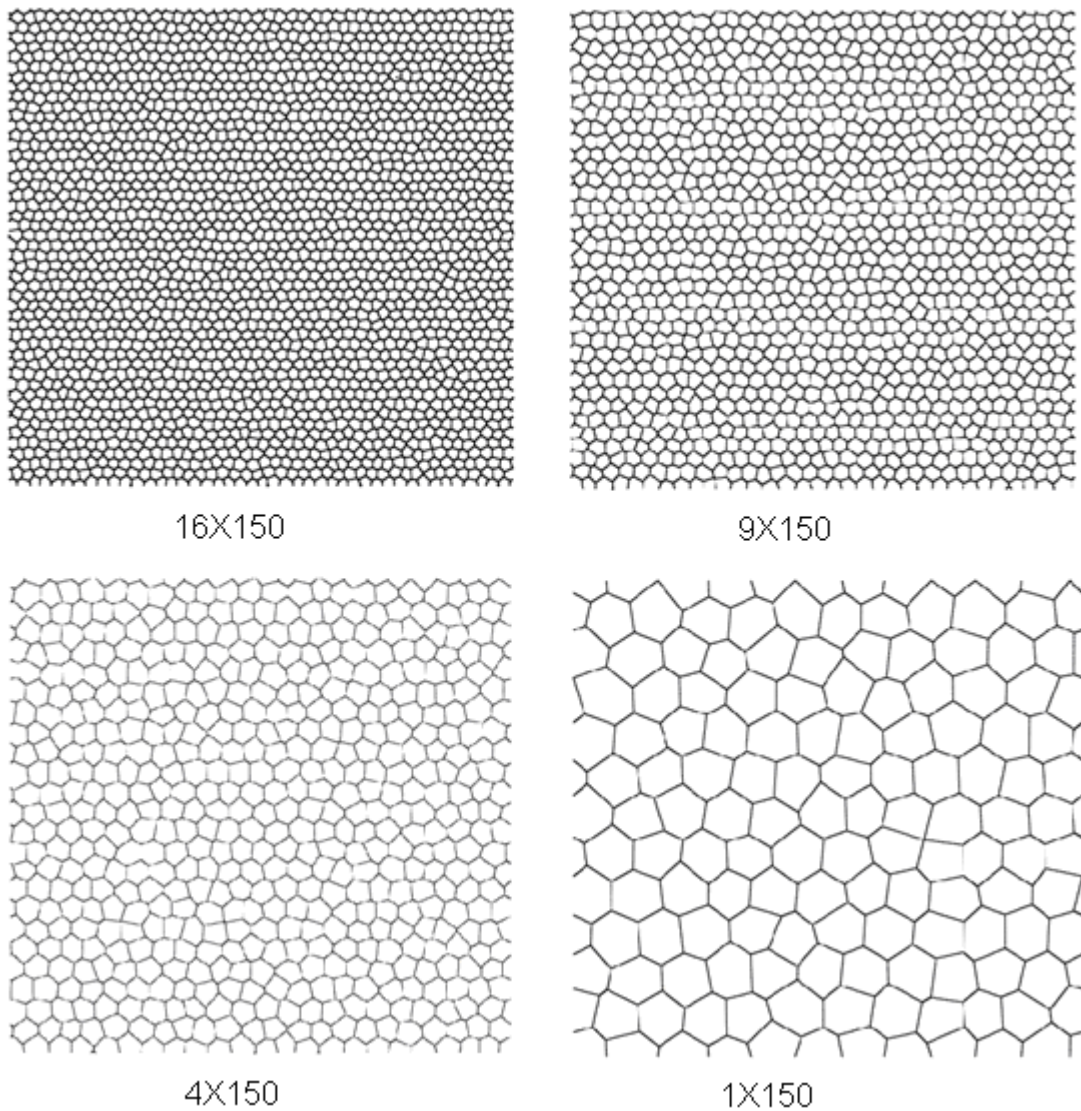


Figure 3-4: RVE 1X150, 4X150, 9X150 and 16X150 with 150, 600, 1350 and 2400 cells respectively.

Practical limitations on computational resource mean that statistical investigations into the effect of RVE size on property predictions for all α values, and the effect of α value on property predictions for all RVE sizes would be prohibitively time consuming. To illustrate, Figure 3-5 shows the computation time versus RVE size for the explicit shell-based simulations including contact (simulations conducted using a 64 bit Windows with intel(R)Xeon(R) CPU @ 2.66GHz and 12GB RAM).

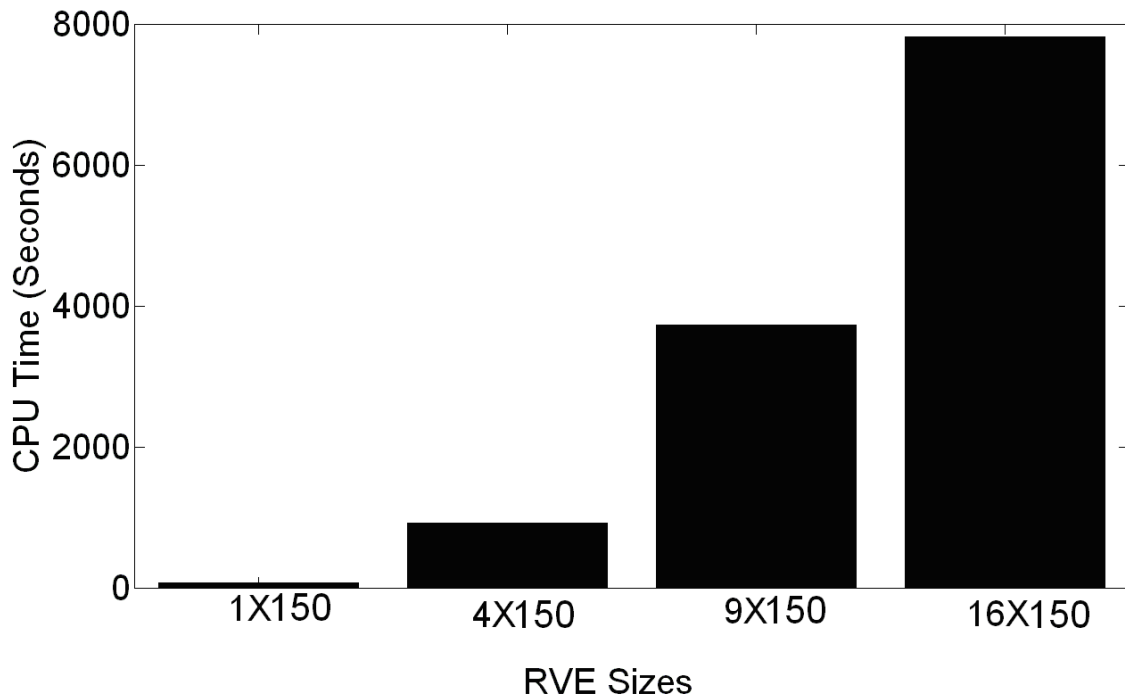


Figure 3-5: The average simulation cost of each RVE size per 5% compression.

A 16x150 cell simulation requires about 80 times longer than a 1x150 cell simulation and can take more than 35 hours to reach 80% compression - see Figure 3-5. To overcome this computational limitation it has been assumed that conclusions regarding the size effect on a given property produced using a degree of irregularity with $\alpha = 20$, can be applied to RVEs with $\alpha = 0, 10$ and 50 , see Figure 3-4. Given that the degree of irregularity, $\alpha = 20$, sits approximately midway between 0 and 50 this assumption is considered to be a reasonable compromise. This degree of irregularity is considered the most realistic representation of a two-dimensional slice of open-cellular polymer foam considered in this investigation (following preliminary visual comparison with actual micrographs of polymer foam cross sections). The strategy of extrapolating these conclusions on size effect to RVE behaviour generated using other α values means that simulations exploring the effect of changing α value can be performed with the smallest sized RVE (to reduce computational requirements) and the likely effect on predicted properties due to using this smallest RVE size can then be estimated.

3.2.5 Large strain response results

The plateau region begins at the end of linear-elastic regime and continues until the onset strain of densification. The reason behind the yielding of the foam and the form of the plateau region is generally attributed to bending, buckling or torsion (for 3-d deformation) within the foam microstructure [Banhart and Baumeister, 1998; Elliott et al. 2002; Jang et al. 2010] (or some combination of all three mechanisms). As explained in section 3-1, the onset strain of densification is determined here using Eq. 3-2. By definition, both the onset strain of densification and contact strain can only be predicted if self-contact within the RVE is modelled. It will be shown that the onset strain of densification always occurs at higher strains than the contact strain. In order to predict the onset strain of densification and contact strain the dynamic explicit method using shell-based RVEs with contact detection enabled has been employed.

Examining first the form of the plateau stress, Figure 3-6 shows how the shape of the reduced stress - strain curve changes with RVE size.

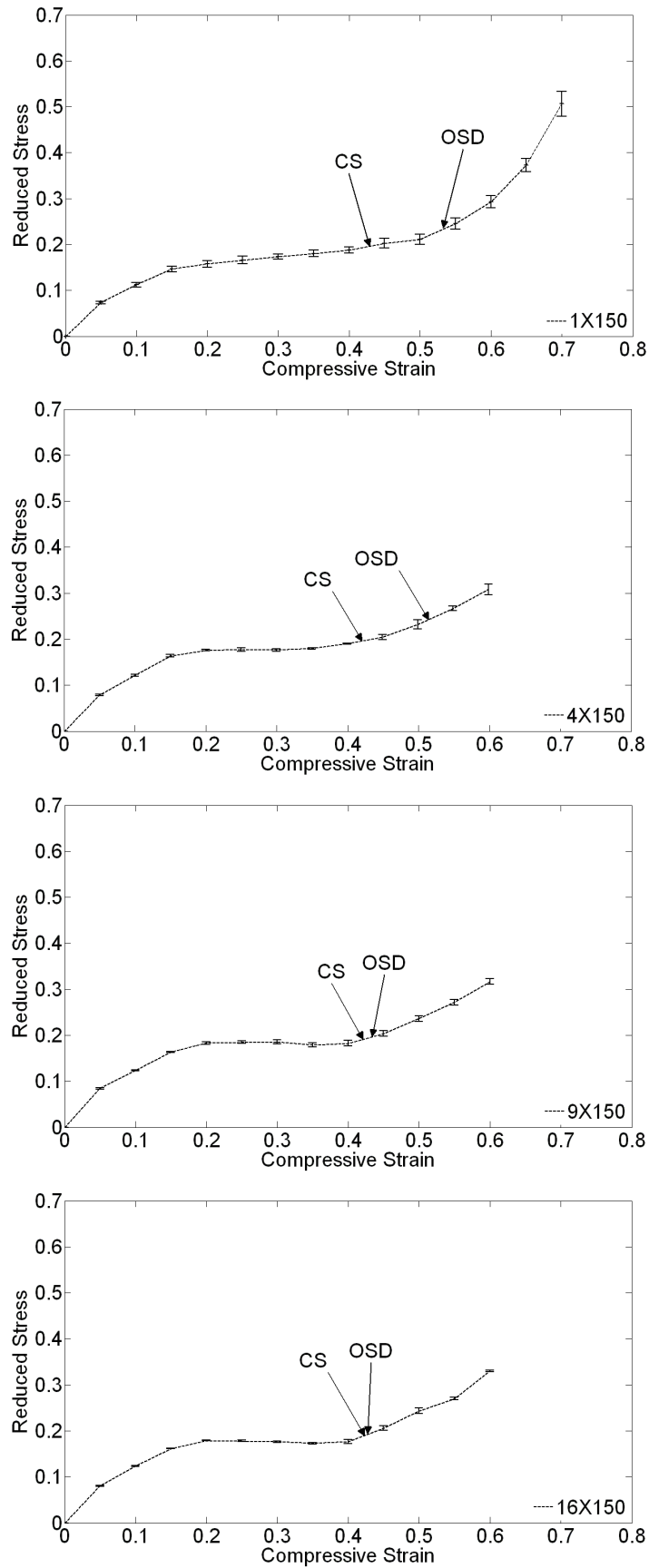


Figure 3-6: Averaged stress-strain curves for RVE with different size and $\alpha=20$. The form of plateau stress region is sensitive to the size of RVE. Densification strain

(OSD) and contact strain (CS) are indicated in the figure. Error bars indicate 1 standard deviation of 10 simulations.

The plateau becomes flatter for larger RVEs with a slightly negative gradient developing between 20 to 35% strain. This is due to an increase in stress at around 20% strain along with a small decrease in stress between 30 to 40% strain with increasing RVE size. These conclusions suggest a small RVE can be expected to provide only an approximate estimate for the magnitude of the plateau stress and the form of the plateau may be less flat and lack the slightly negative gradient seen in larger RVEs. Examining the effect of changing the degree of irregularity, Figure 3-7 shows that the form of the plateau region of the reduced stress-strain curve becomes less horizontal and more inclined as α increases, i.e. the foam behaves gradually less like an ideal energy absorbing material as the degree of irregularity increases.

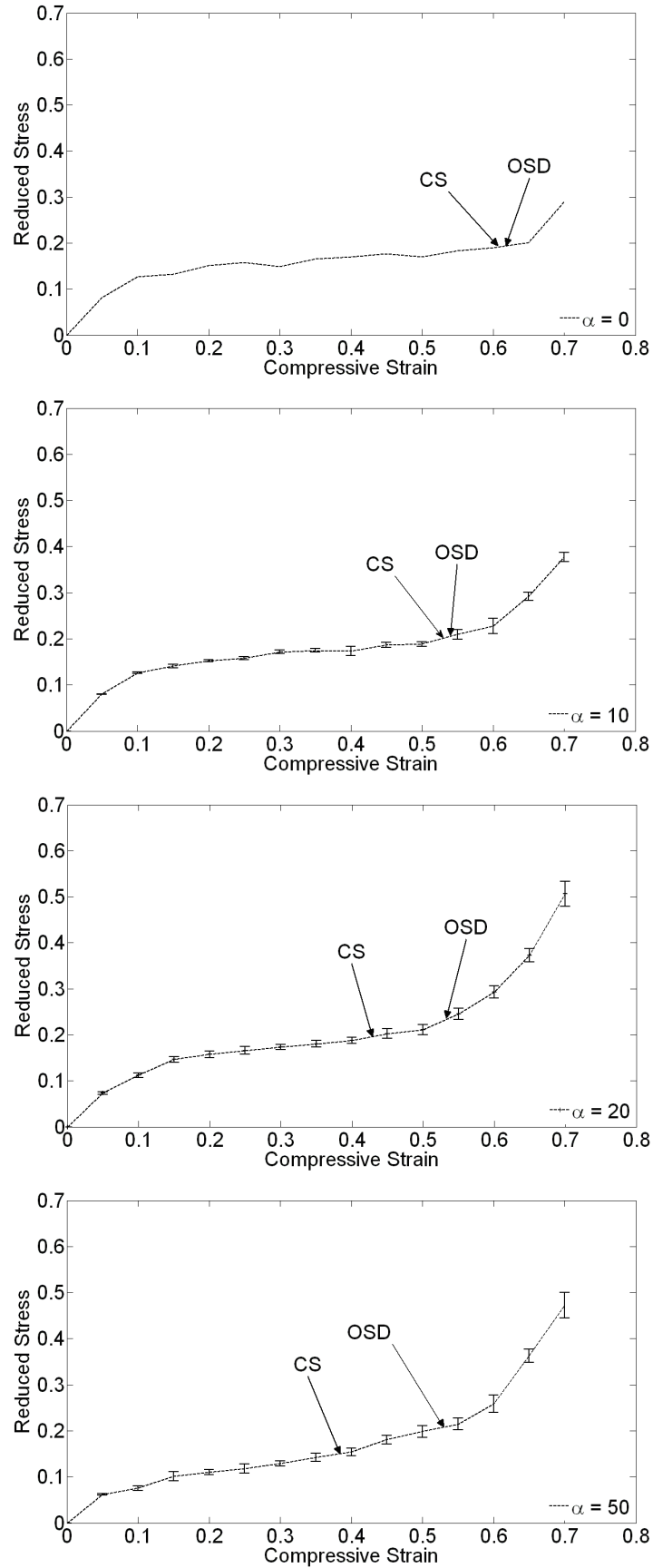


Figure 3-7: Averaged stress-strain curves for 1X150 RVE with increasing α .

The small RVE size probably serves to exaggerate the size of this positive gradient but the general trend in behaviour remains clear; an increase in the degree of irregularity increases the size of the positive slope in the plateau region. Zhu et al. 2006 made a similar comparison of the reduced stress-strain curves of two-dimensional beam-based RVEs with four different degree of irregularity (including honeycomb and Poisson Voronoi). Their results suggested that as irregularity increases, the level of the whole of the plateau stress decreases. In their investigation the RVE was constructed from about 60 cells and self-contact within the microstructure was not considered.

Examining now the onset strain of densification and contact strain, these are marked on the reduced stress - strain curves as 'OSD' and 'CS' in both Figures 3-6 and 3-7 and are also plotted as a function of RVE size in Figure 3-8 and as a function of degree of irregularity in Figure 3-9.

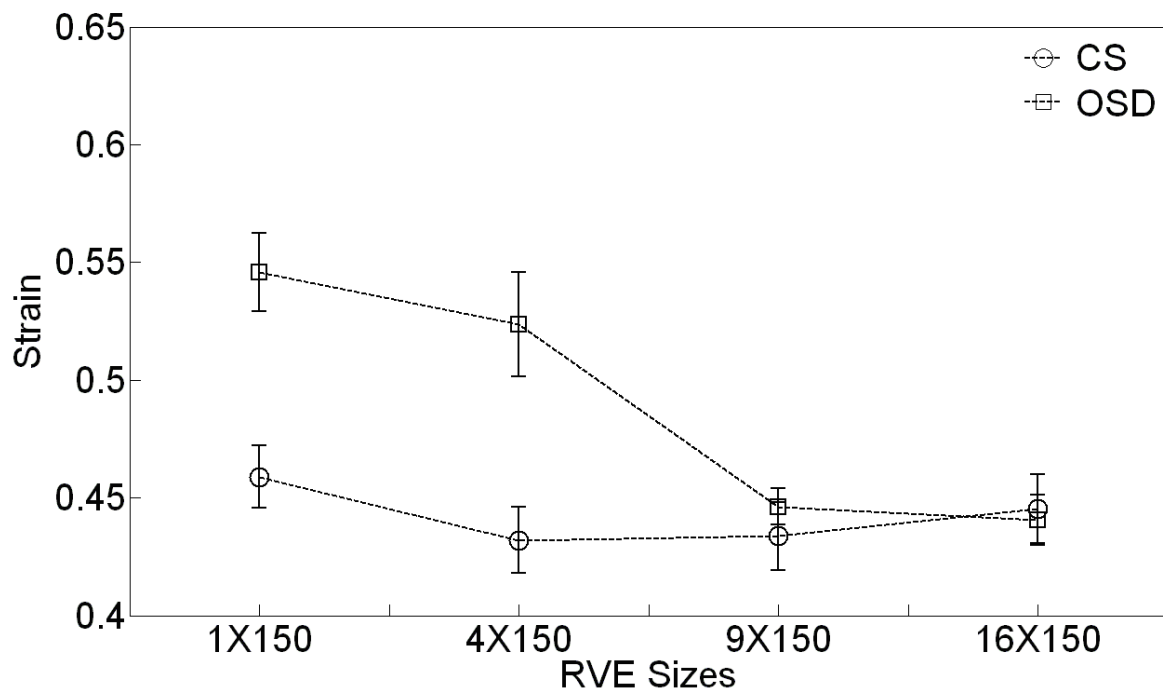


Figure 3-8: Onset strain of densification and contact strains for RVEs with different size but the same degree of irregularity ($\alpha=20$).

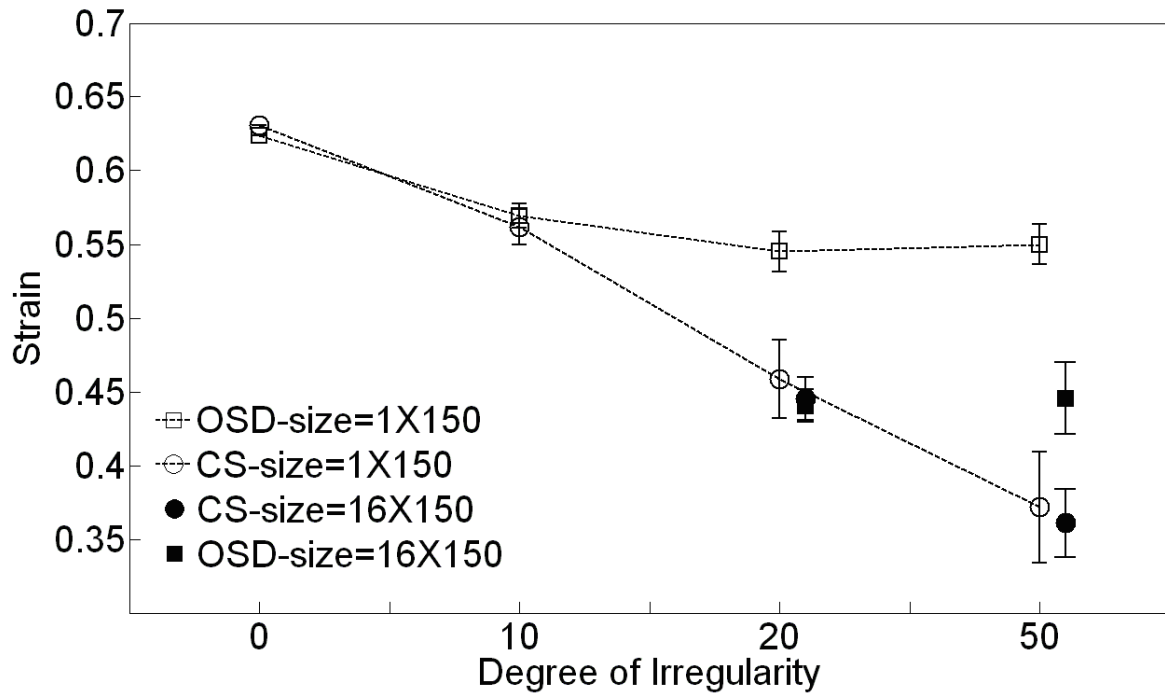


Figure 3-9: Onset strain of densification and contact strain for RVEs with varying α . Open points correspond to RVE of size 1X150 cells, closed points correspond to RVE of size 16X150 cells. (The closed points are offset slightly to $\alpha=22$ and 52 for clarity, though they still correspond to $\alpha=20$ and 50).

Figures 3-6 and 3-7 show that for a given degree of irregularity ($\alpha = 20$) the onset strain of densification decreases with increasing RVE size and converges towards the contact strain which remains almost constant with RVE size. This suggests that the onset strain of densification is more sensitive to the RVE size than the contact strain, an observation that prompts two interesting possibilities (i) *the contact strain of a small RVE could be used to predict the onset strain of densification in larger RVEs* (ii) *the difference between the contact strain and onset strain of densification could be used to quantify the influence of RVE size; a large difference would suggest the RVE is too small and can be improved by increasing its size*. If point (i) were to prove correct, this would allow dramatic savings in computational resource when aiming to correctly predict the foam's onset strain of densification. For example, referring to section 3.2.3, the smallest RVE simulations (1X150 cells) require only about 1/80th of the time of the largest RVE simulations (16x150 cells). In order to find the contact strain in the quickest time, simulations using small RVEs must be conducted, both with and without contact. Simulations

without contact are relatively fast and increase the overall computation time by around only 20 per cent. In addition to requiring longer simulation time, around 50 per cent of the largest RVE simulations (this figure depends on the degree of irregularity of the RVE) produce errors before reaching large compressive strains (due to excessively distorted elements) and have to be discarded. This discard rate effectively increases the overall computational time for the large RVEs to about 130 times that of the small RVE simulations. Thus, the time saving involved in using the contact strain of small RVEs to estimate the onset strain of densification for the large RVEs is around two orders of magnitude.

Now considering the effects of the degree of irregularity, Figures 3-7 and 3-9 show how the onset strain of densification remains almost constant as α increases while the contact strain significantly decreases. Results of Figure 3-8 and the open points in Figure 3-9 are all conducted using the smallest RVE size of 1x150 cells and are therefore likely to be adversely influenced by size effects that have been shown to strongly affect both the form of the plateau region and the onset strain of densification.

A final set of 10 simulations was conducted using RVEs with the maximum degree of irregularity ($\alpha = 50$) and using the largest RVE size. The resulting average reduced stress-strain curve is shown in Figure 3-10 and the corresponding onset strain of densification and contact strain found using this curve are plotted as filled points in Figure 3-9.

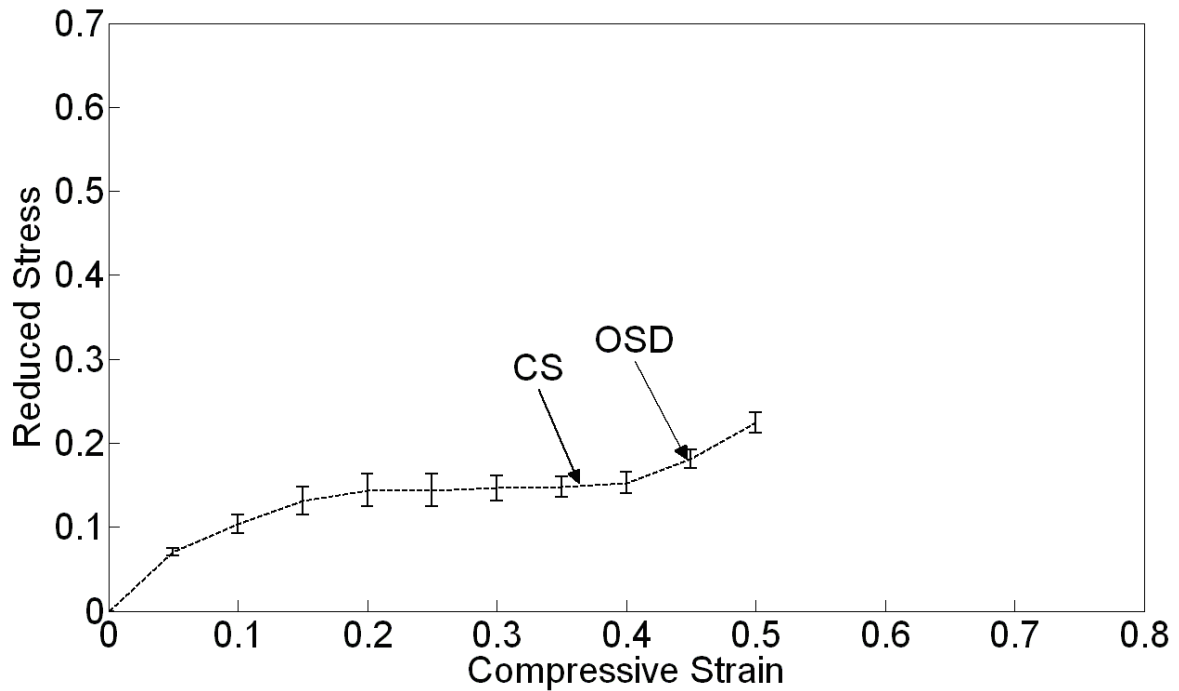


Figure 3-10: Averaged stress-strain curve for the largest RVE when $\alpha=50$.

This final set of simulations (using $\alpha = 50$) is designed to see if the same trends in terms of size effect that were found using $\alpha = 20$, also occur when using $\alpha = 50$. The results plotted in Figure 3-9 and 3-10 show once again that (a) the low strain zone of the plateau region is increased in value, creating a lower stress-strain gradient along the length of the plateau region (b) the contact strain remains stationary when the RVE size is increased from 1x150 to 16x150 cells and (c) the onset strain of densification decreases, effectively moving towards the contact strain. In this case using $\alpha = 50$, the decrease is not sufficiently large for the two strain measures to closely coincide even when using the largest RVE, though the result does suggest that the contact strain, which is again almost RVE size independent, is indeed an excellent indicator for the onset strain of densification, as suggested in point (i) above. Indeed according to point (ii) above, the result also suggests that the largest RVE (16x150 cells) should be increased further still if the adverse influence of size effects is to be fully eliminated. These final results add weight to the hypothesis that the contact strain of a small RVE can be used to predict the onset strain of densification in larger RVEs.

3.3 Poly-disperse RVE microstructure generated using the Drop and Roll method

As discussed in Chapter 2, the modified Zhu method provides a reasonably good 2-d foam-like microstructure for fairly cellular mono-disperse geometries. However, for higher degree of irregularities, the resultant structure will approach fully random Voronoi geometry (i.e. Poisson's Voronoi) which is not a good representation of the real microstructure of typical foams. As with the enhanced method of Zhu, when using the Drop and Roll method there is a control mechanism to define the geometrical degree of irregularity of the resulting RVE. The approach used here was originally suggested by Kraynik et al. (2004). This involves selecting the disk size (radius) distribution for use in generating the RVE, using a log-normal function, i.e.

$$\mu = \log \left(\frac{m^2}{\sqrt{\gamma + m^2}} \right) \quad \text{Equation 3-10}$$

$$\sigma_{sd} = \sqrt{\log \left(\frac{\gamma}{m^2 + 1} \right)} \quad \text{Equation 3-11}$$

$$r = \exp(\mu + z' \cdot \sigma_{sd}) \quad \text{Equation 3-12}$$

where m is the disk mean radius, γ is the variance of the disk radii and μ and σ_{sd} are the mean and standard deviation required to generate random data following a lognormal distribution and z' is random generated variable. γ is the main parameter controlling the degree of poly-dispersity since it defines the range of disk sizes and plays a similar role to α in the method proposed by Zhu. The 'lognrnd.m' function is available in MatlabTM (see Eq. 3-12) and directly calculates random values based on a log-normal frequency distribution function. In Eq. 3-11 and 3-12, by using mean and variance inputs (m and γ), mean and standard deviations (μ and σ_{sd}) are calculated and used in Eq. 3-12. In order to avoid generation of very large or very small disks, a limit is set within a specified interval by choosing r_{min} and r_{max} as the minimum and maximum disk radii. The

criteria to choose a smallest and largest disk sizes limits depends to the operator knowledge of the final target structure. To generate a dense packing of circular hard disks, a square with size 80X80 is considered. The following parameter values are used in Eq. 3-10-12.

$$r_{min} = 0.5$$

$$r_{max} = 5.0$$

$$m = 2.5$$

$$\gamma = 0.05, 0.1, 0.15, 0.20$$

Increasing γ results in a higher poly-dispersity of the hard disc diameters.

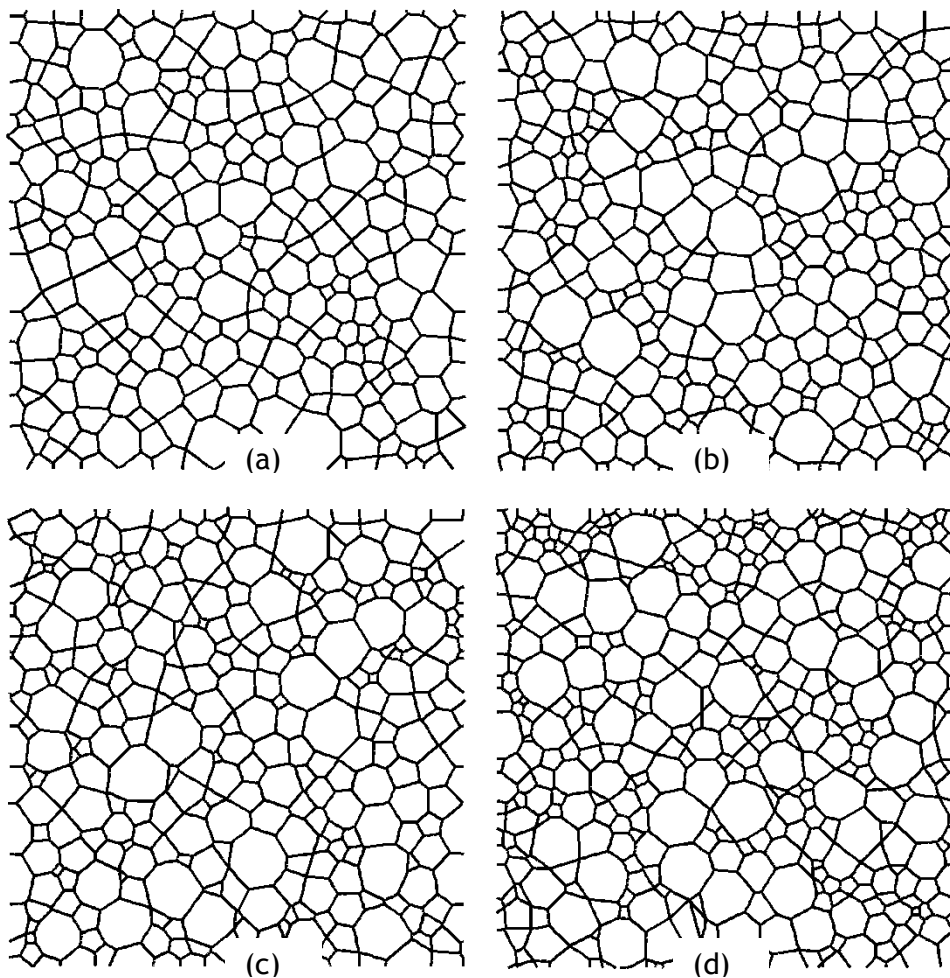


Figure 3-11: RVEs with 4 different degree of poly-dispersity: (a) $\gamma=0.05$, (b) $\gamma=0.10$, (c) $\gamma=0.15$, (d) $\gamma=0.20$. The final beam-based structures are obtained by

solving the Apollonius problem [Wolfram Mathematica®] for packed hard circular disks and then by applying a Laguerre-Voronoi tessellation.

As in the previous section, all the structures are generated based on relative densities equal to 0.05 and then converted to shell elements.

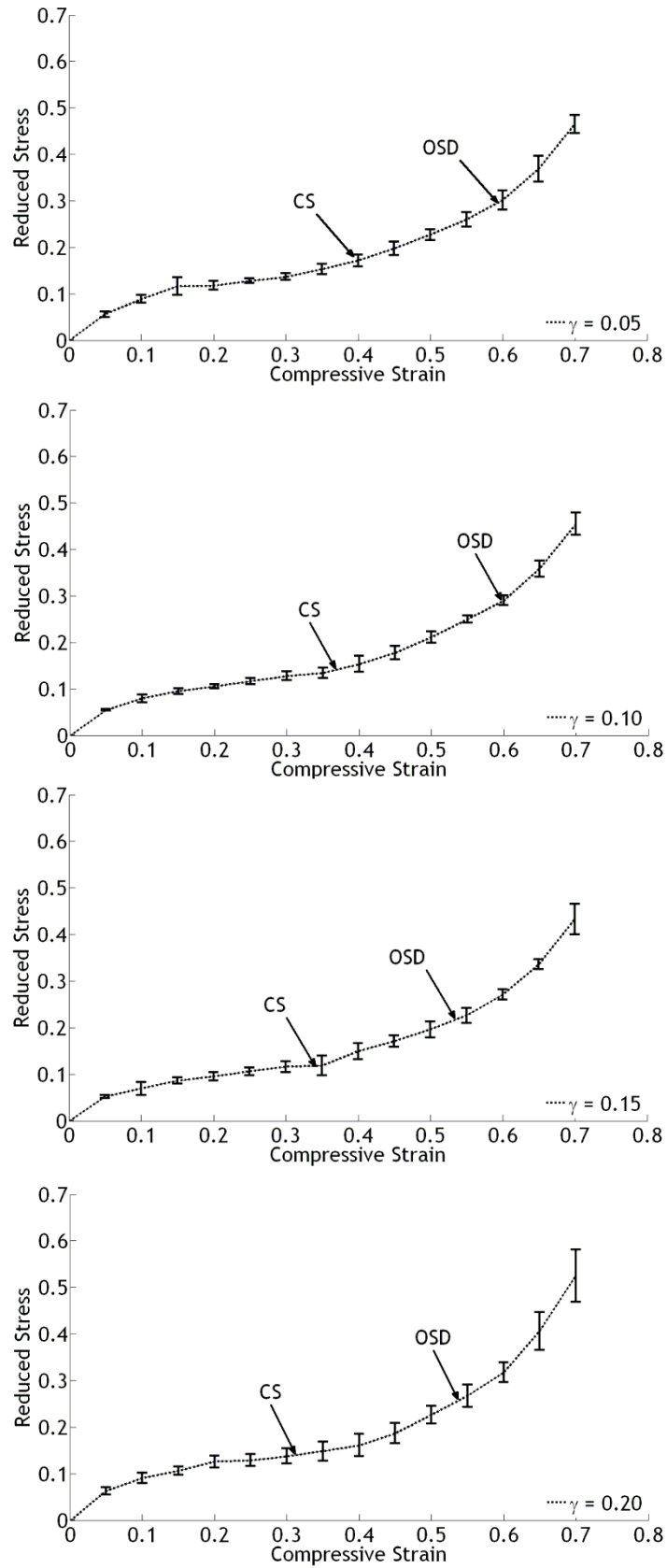


Figure 3-12: Averaged stress-strain curves for RVE with increasing γ .

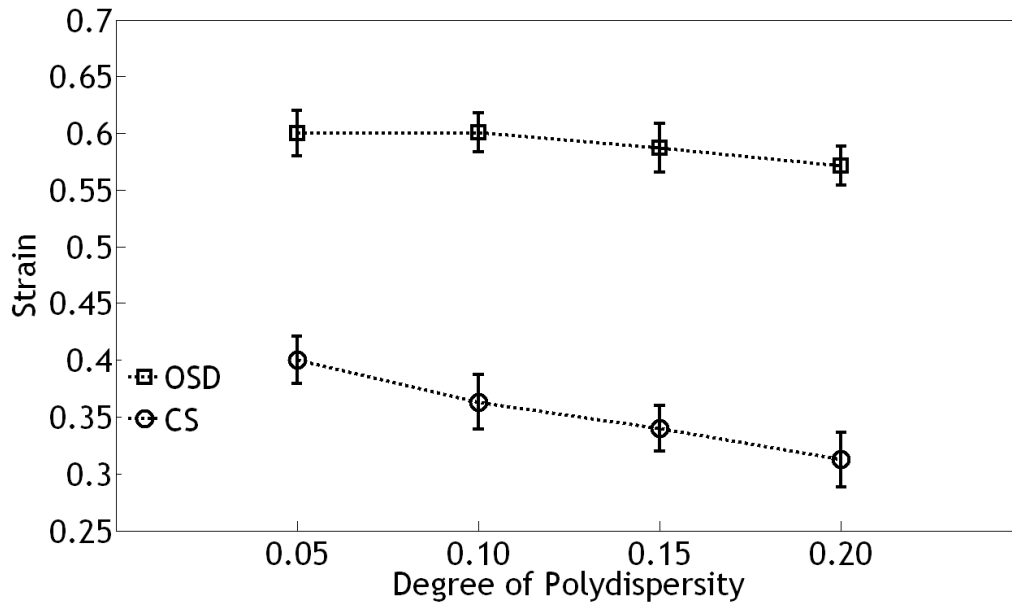


Figure 3-13: Onset strain of densification and contact strain for RVEs with varying γ .

By comparing Figures 3-7 and 3-12 and also 3-9 and 3-13 it can be seen that as the degree of irregularity increases, the contact strain (CS) shifts to lower strains. Therefore, the self-contact within the microstructure causes an earlier increase in the gradient of the stress-strain curve in the plateau region. This is unlike the microstructures generated by the modified method of Zhu with a small degree of irregularity where CS is close to OSD and will decrease for higher degree of irregularity, here the form of the plateau region was also found to be relatively insensitive to compressive strain. The same scenario is also true for RVEs generated using Lloyd's algorithm where contact strain (CS) is almost appears at 0.5 compressive strain which is mainly due to the small scatter of cellular morphology (see Figure 3-14).

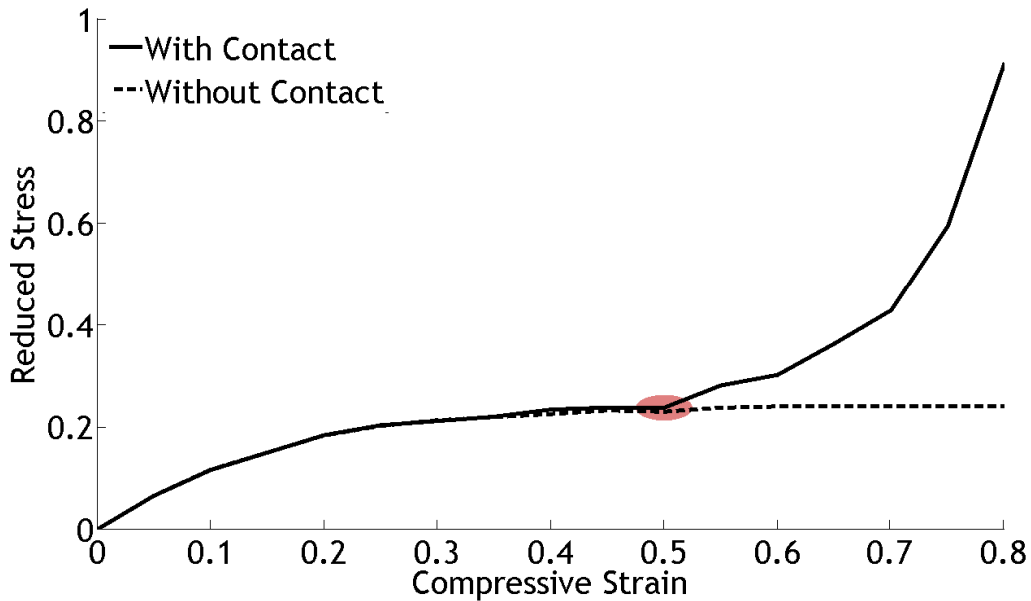


Figure 3-14: Contact effect on RVE generated by Lloyd’s algorithm. The contact strain (CS) is highlighted by red transparent circle where two curves starts to deviate from each other. Both curves are obtained as an average value of 5 simulations over statistically different RVEs.

3.4 Conclusions of Chapter 3

Two-dimensional beam-based RVEs with different size and degree of irregularity have been generated using both the Voronoi and the Laguerre-Voronoi tessellation methods. The inclusion of self-contact within the microstructure in the simulations has permitted the mechanical response of the RVEs to be investigated to very high compression strains, often greater than 80 per cent. To the best of the authors’ knowledge, this is the first time that the analysis of important mechanical properties of structural foams, such as plateau shape and the onset strain of densification, have been investigated using a periodic RVE constructed using structural elements. Use of the latter means that simulation time is dramatically reduced compared to equivalent FE investigations using 3-d continuum elements to model the microstructure. Nevertheless, these large strain properties, which so far have been investigated using only linear elastic material behaviour, are shown to be sensitive to RVE size and ideally require large RVEs of at least 16x150 cells in order to eliminate size effects. This currently leads to long computation times (greater than 35 hours for 1 simulation using the current computer specification - see section 3.2.3), which can be prohibitively costly when running multiple

simulations in order to determine average stress-strain curves and stochastic variability between results. With this issue in mind, an important finding in this investigation is the discovery that the contact strain in a small RVE appears to be an excellent indicator of the onset strain of densification in a large RVE. This finding reduces computational requirements by a factor of around 100 times for these 2-d simulations. If this discovery holds true for 3-d simulations, then the savings in computation time are expected to be considerably greater still, a question that may form the subject of a future study.

The other important achievement from studying the contact effect is a better understanding of deformation mechanisms occurring in the plateau strain region which is of great concern for porous material characterisation because it can be used as a guidance to optimise the design criteria for component including porous structure (e.g. cyclist helmets). Geometrical inhomogeneity (e.g. cellular polydispersity, geometrical irregularity) has a significant impact on mechanical behaviour of the RVEs after the initiation of Contact Strain (CS) where self-contact increasingly contributes towards the total stress in the RVE. As a result, the stress-strain slope is found to increase at earlier strains with increasing polydispersity.

Chapter 4 . Orientation Dependent Compressive Response of Two-Dimensional Representative Volume Elements

4.1 Introduction

The first step in modelling isotropic random foams should be to create isotropic RVEs. Such RVEs should have no ‘preferential’ direction, both from a mechanical and a morphological point of view [Hill, 1963; Guedes and Kikuchi, 1990; Kruyt and Rothenburg, 2004]. With this in mind, it is clear that microstructure generation algorithms designed to model isotropic random foams should ideally be free from any inherent directional bias (any intended anisotropy can easily be added to the initially isotropic RVE by the user using an affine elongation of an isotropic random microstructure). In Chapter 2 several microstructure generation algorithms were discussed and the importance of the initial seeding on the resulting RVE microstructure was emphasised. In the literature, isotropy of apparently randomly micro-structured RVEs is generally assumed to be true a priori, despite a lack of rigorous testing [Zhu et al. 2001^a; Kraynik et al. 2003]. In this chapter, the validity of this assumption is analysed. It will be shown that some microstructure generation algorithms create more mechanically isotropic RVEs than others.

One of the most computationally efficient methods to be reviewed in Chapter 2 was that proposed by Zhu [Zhu et al. 2001^b] and an enhanced version of this algorithm (see Section 2.1.2) was implemented and employed in Chapter 3 to understand the effects of self-contact on the compressive response of the RVE under large strains. The benefit of this particular algorithm lies in its power to control the geometrical irregularity of RVE for multi-scale statistical application as

well as simplicity and its ease of implementation. As described in Sections 2.1.2 and 3.2.1 the technique begins with a regular seeding that, without further modification, produces a hexagonal honeycomb structure. Random foam microstructures are generated, by perturbing the initial seeding position in a stochastic manner away from the initially regularly spaced configuration. Clearly, if the perturbation is small then the RVE behaves as a slightly perturbed honeycomb structure, if the perturbation is sufficiently large then all trace of the initial honeycomb structure will eventually be erased, prompting two questions that are important to the enhanced Zhu method of generating isotropic randomly micro-structured RVEs: (i) “just how isotropic is the in-plane response of a honeycomb microstructure?” and (ii) “what perturbation size (or degree of irregularity) is required to completely erase all trace of the initial honeycomb microstructure?”. In answer to (i), it will be shown that the response of a honeycomb structure is isotropic only under very small strain compression and becomes progressively more anisotropic with increasing strain. In answer to (ii) it will also be shown that an isotropic RVE can be created using the enhanced method of Zhu, though only for extremely irregular microstructures that are so distorted that their realism, when compared to real foam microstructures, is debateable. Consequently, a novel method of converting these highly irregular unrealistic / isotropic RVE microstructures into more useful realistic / isotropic random microstructures has been developed and is demonstrated later in this chapter. The method employs the Lloyd’s relaxation algorithm (see Section 2.1.4), application of which is shown to produce a realistic / isotropic random RVE with a mono-disperse cell size distribution. In Chapter 5 it will be shown that the form of the resulting RVE microstructure morphology compares well with many, typical gas-expanded polymeric foams (see Section 1.1.2). However, due to the mono-disperse microstructure, the method is not particularly well-suited to the generation of poly-disperse microstructures typically observed in many metallic foams (see Section 1.1.2). To create such morphological microstructures the enhanced drop and roll technique is better suited, as will be shown in Chapter 5. In that chapter the mechanical isotropy of poly-disperse RVEs created using the enhanced drop and roll method is examined for varying levels of poly-dispersity.

The remainder of this chapter is structured as follows. Section 4.2 is a review of the relevant literature. In Section 4.3 methods of applying compression in vertical, horizontal and also arbitrary directions, while still maintaining a PBC, are discussed. In Section 4.4 an investigation into the directional response of a honeycomb structure is presented. Analytical solutions proposed previously in the literature are examined before comparing these predictions against those from a honeycomb structured RVE with PBC applied. In Section 4.5, the effect of increasing the degree of irregularity on mechanical isotropy of RVEs produced using the enhanced Zhu method (employed previously in Chapter 3) is examined. An investigation into the mechanical isotropy of RVEs generated using the Lloyds relaxation algorithm is presented in Section 4.6. In Section 4.7 the isotropy of RVEs generated using the enhanced drop and roll method is investigated. Finally, in Section 4.8 a 2-d mechanical evolution of aerogel specific RVE and its challenges are discussed.

4.2 Literature review

4.2.1 Directional response of honeycomb structures

Hexagonal structures, commonly known as honeycomb, are often used as a first step towards the study of randomly structured 2-d foams [Gibson and Ashby, 1997]. Also, as described in Section 4.1, the honeycomb structure is effectively the unperturbed foam structure created using the enhanced Zhu method. For these reasons, this first section focuses on the mechanical response of honeycomb structures. The regular nature of a honeycomb structure means that it is accessible to theoretical analysis by considering a repeat unit cell. Section 4.2.2 reviews previous work in this direction while Section 4.2.3 looks at the response of a honeycomb RVE created using the enhanced Zhu method, numerical and analytical predictions are compared.

4.2.2 Analytical predictions of honeycomb response

According to Gibson and Ashby (1997), under *uni-axial* loading, the in-plane linear-elastic stiffness of the hexagonal cell in both the transverse and perpendicular directions can be calculated using Eq. 4-1 and 4-2 respectively:

$$\frac{E_1^*}{E_s} = \left(\frac{t_b}{l}\right)^3 \left(\frac{\cos \theta}{\left(\frac{h}{l} + \sin \theta\right) \sin^2 \theta} \right) \quad \text{Equation 4-1}$$

$$\frac{E_2^*}{E_s} = \left(\frac{t_b}{l}\right)^3 \left(\frac{\frac{h}{l} + \sin \theta}{\cos^3 \theta} \right) \quad \text{Equation 4-2}$$

where E_s is the linear-elastic Young's modulus of the constituent material, t_b is the beam thickness, h and l are the side lengths of the cell and θ is the beam angle (see Figure 4-1). The Poisson's ratios (v_{12}^* and v_{21}^*) in both the perpendicular and transverse directions (X_1 and X_2) are also calculated using the honeycomb geometry to be

$$v_{21}^* = -\frac{\varepsilon_2}{\varepsilon_1} = \frac{\cos^2 \theta}{(h/l + \sin \theta) \sin \theta} \quad \text{Equation 4-3}$$

$$v_{12}^* = \frac{1}{v_{21}^*} \quad \text{Equation 4-4}$$

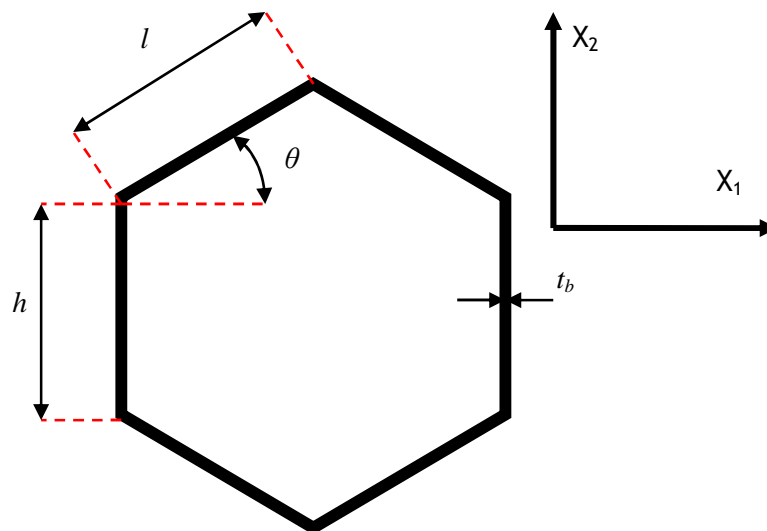


Figure 4-1: Hexagonal unit cell.

For regular honeycomb, where $h=l$ and $\theta=30$ degree, both Eq. 4-1 and 4-2 are further simplified to

$$E_1^* = E_2^* = 2.3E_s \left(\frac{t_b}{l} \right)^3 \quad \text{Equation 4-5}$$

The above relationship is a power-law function where the term t_b/l can be written in terms of the relative density ρ^*/ρ_s , as

$$\frac{\rho^*}{\rho_s} = \frac{2}{\sqrt{3}} \left(\frac{t_b}{l} \right) \quad \text{Equation 4-6}$$

thus

$$\frac{E_1^*}{E_s} = \frac{E_2^*}{E_s} = 1.5 \left(\frac{\rho^*}{\rho_s} \right)^3 \quad \text{Equation 4-7}$$

The non-linear elastic collapse stress in the X_2 direction $(\sigma_{el}^*)_2$ is calculated using Euler's buckling principle [Timoshenko and Gere, 1961] to find,

$$\frac{(\sigma_{el}^*)_2}{E_s} = \frac{n_r^2 \pi^2}{24} \frac{t_b^3}{lh^2} \frac{1}{\cos \theta} \quad \text{Equation 4-8}$$

In Eq. 4-8, n_r represents the rotational stiffness at nodal connections which varies for different loading and constraint scenarios [Gibson et al. 1981]. Eq. 4-1 to 4-8 were established for honeycomb with low relative density ($t_b/l < 1/4$) where beam bending is the major mode of deformation. Silva et al. 1995 improved these equations by also considering axial and shear deformations in order to study cases with relative densities up to 0.3:

$$\frac{E_1^*}{E_s} = \left(\frac{t_b}{l}\right)^3 \frac{\cos \theta}{(h/l + \sin \theta) \sin^2 \theta} \left[\frac{1}{1 + (2.4 + 1.5v_s + \cot^2 \theta) \left(t_b/l\right)^2} \right] \quad \text{Equation 4-9}$$

$$v_s = 0.3, \theta = 30^\circ, h = l \Rightarrow \frac{E_1^*}{E_s} = \frac{1.5 \left(\frac{\rho^*}{\rho_s}\right)^3}{1 + 4.3827 \left(\frac{\rho^*}{\rho_s}\right)^2} \quad \text{Equation 4-10}$$

$$\frac{E_2^*}{E_s} = \left(\frac{t_b}{l}\right)^3 \frac{(h/l + \sin \theta)}{\cos^3 \theta} \left[\frac{1}{1 + \left(2.4 + 1.5v_s + \tan^2 \theta + \frac{2(h/l)}{\cos^2 \theta}\right) \left(t_b/l\right)^2} \right] \quad \text{Equation 4-11}$$

$$v_s = 0.3, \theta = 30^\circ, h = l \Rightarrow \frac{E_2^*}{E_s} = \frac{1.5 \left(\frac{\rho^*}{\rho_s}\right)^3}{1 + 4.3827 \left(\frac{\rho^*}{\rho_s}\right)^2} \quad \text{Equation 4-12}$$

$$v_{12}^* = \frac{\cos^2 \theta}{(h/l + \sin \theta) \sin \theta} \left[\frac{1 + [1.4 + 1.5v_s] \left(t_b/l\right)^2}{1 + [2.4 + 1.5v_s + \cot^2 \theta] \left(t_b/l\right)^2} \right] \quad \text{Equation 4-13}$$

$$v_s = 0.3, \theta = 30^\circ, h = l \Rightarrow v_{12}^* = \frac{1 + 1.3875 \left(\frac{\rho^*}{\rho_s}\right)^2}{1 + 4.3875 \left(\frac{\rho^*}{\rho_s}\right)^2} \quad \text{Equation 4-14}$$

These equations provide analytical small-strain predictions with which to compare numerical results later in this investigation (see Section 4.4).

4.2.3 Modelling of two-dimensional random foam microstructures using a numerical RVE approach

A major limitation when using a single cell modelling approach is the inability to capture the random microstructural complexity of real foams. To overcome this limitation Zhu et al. (2001) investigated the important elastic properties of foam-

like beam-based microstructures using a 2-d Voronoi modelling technique (see Chapter 2.1.3) by applying uniaxial compression on a RVE with a periodic boundary condition. The most important results of Zhu's work are summarised in Table 4-1.

Table 4-1: Effect of cellular irregularity on 2-d foam-like microstructure elastic behaviour [Zhu et al. 2001].

		Young's Modulus	Shear Modulus	Bulk Modulus	Poisson's Ratio
Cellular Irregularity	Increase	Increase	Increase	Decrease	NA
	Decrease	Decrease	Decrease	Increase	NA
Relative Density	Increase	Decrease	NA	NA	Decrease
	Decrease	Increase	NA	NA	Increase

For low relative density and for microstructures with a reasonably low degree of irregularity, the results of Zhu et al. (2001) are in agreement with Gibson and Ashby's (1997) power-law function (Eq. 4-5). For the perfect honeycomb case with increasing relative density, Zhu's results expressed in the form of reduced Young's modulus:

$$\bar{E}_f = \frac{E_f}{E_s \left(\frac{\rho^*}{\rho_s} \right)^3} \quad \text{Equation 4-15}$$

where the final results are very close to the power-law function of Silva et al. 1995. However, as previously stated (see Chapter 2.1.1), using a classical Voronoi modelling approach (see Section 2.1.3) does not necessarily provide a realistic 2-d foam-like microstructure, particularly for cases with a high degree of irregularity. Attempting to improve the realism of the microstructure, Fazekas et al. (2002) used the Laguerre-Voronoi method (see Section 2.1.3) to generate 2-d beam-based microstructures with a range of geometrical poly-dispersities and small relative densities (<0.05). Some of the findings of Fazekas et al. (2002) were very similar to those of Zhu et al. (2001). Both the Young's modulus and the bulk modulus were found to obey Gibson and Ashby's, power-law function for low relative densities

(see Eq. 4-5), irrespective of the microstructural morphology. Another important goal of the study by Fazekas et al. (2002) was in determining the effect of the cellular area fraction on the Young's modulus and yield stress. In the case of a low relative density, Fazekas' results suggested that increasing cellular area polydispersity produced a higher Young's modulus and a lower yield stress.

The main limitation of the work of both Zhu et al. (2001) and Fazekas et al. (2002) was the restriction of the investigations to strains below the yield strain. Further, the work of Fazekas, only considered bimodal microstructures and consequently the final results were not representative of generally poly-disperse media. Zhu et al. (2006) extended the previous work of Zhu et al. (2001) to examine the behaviour of 2-d beam-based Voronoi microstructures up to much greater engineering strains of 0.6. In this attempt, microstructures with a low relative density, (ρ^*/ρ_s), consisting of uniform elastic beams were employed. An important result of this study was the prediction of the mode of cellular deformation after yielding and before densification, i.e. within the plateau region. Zhu et al. (2006) concluded that since stress monotonically increases with compressive strain, regardless of the degree of geometrical irregularity, the microstructure would not collapse before densification. For slender beams with linear elastic material, the compressive stress-strain relationship can therefore be explained by elastic beam bending in the linear region and by elastic buckling in the plateau region, by considering the mode of cellular deformation which results from beam's orientation with respect to load direction. Due to the absence of self-contact modelling beyond the plateau region and into the densification stage was not undertaken. Papka and Kyriakides (1994) studied the in-plane compression of metallic honeycomb by applying loads in vertical direction, where whole load-deformation response was characterised by three distinct regimes: (i) a stiff linear elastic response (ii) plastic buckling due to interaction between geometric and material non-linearity where stress in general stays approximately constant for increasing strain and (iii) full collapse of cells with a sharp increase of stress.

The remainder of this chapter investigates the deformation of 2-d periodic RVEs under uni-axial compression within the linear regime. The investigation make use of the modelling techniques explained in Chapter 2 and also a novel approach to obtaining the RVE uni-axial compressive response in an arbitrary direction with respect to the orientation of the square RVE (see Section 4.5-4.7).

4.3 Beam-based RVE Preparation for FE analysis

4.3.1 Application of PBC on RVE for Compression in an Arbitrary Direction

The method of applying a PBC on an RVE when vertically compressing an initially square RVE (i.e. in a direction perpendicular to the top surface of the RVE) was described in Section 3.2.2. In the current section a method of extending this procedure to compression of a rectangular RVE in any arbitrary direction is described. A full theoretical description of the method is provided in Appendix A2, here the numerical implementation of the technique in AbaqusTM is discussed.

$$U_1^{d_1} = U_1^{d_3} \cos^2 \theta_0 + U_2^{d_3} \sin^2 \theta_0 \quad \text{Equation 4-16}$$

$$U_2^{d_1} = U_1^{d_3} \sin \theta_0 \cos \theta_0 - U_2^{d_3} \sin \theta_0 \cos \theta_0 \quad \text{Equation 4-17}$$

$$U_1^{d_2} = U_1^{d_3} \sin \theta_0 \cos \theta_0 - U_2^{d_3} \sin \theta_0 \cos \theta_0 \quad \text{Equation 4-18}$$

$$U_2^{d_2} = U_1^{d_3} \sin^2 \theta_0 + U_2^{d_3} \cos^2 \theta_0 \quad \text{Equation 4-19}$$

In Eq. 4.16 to 4.19, the superscripts d_1 , d_2 and d_3 represents dummy nodes 1, 2, and 3. U_i represents displacement in the i th direction and θ_0 denotes to direction of the applied load.

4.4 Mechanical Response of Periodic Honeycomb Structure when Compressed in Arbitrary Directions

The main purpose of the current section is to investigate the mechanical response of a honeycomb structure under in-plane uniaxial compression in arbitrary directions. The two main reasons for doing this are: (i) to study the in-plane mechanical response of a hexagonal microstructure with respect to applied loading direction and (ii) to generalise the study to a 2-d foam-like structure with

geometrical irregularity. The reasons behind beginning with an investigation of a honeycomb structure, rather than a random RVE, is due to its importance to the enhanced Zhu method of generating a random RVE and also the availability of analytical predictions with which to compare the numerical results. The six-fold geometrical symmetry of the honeycomb structure, as shown in Figure 4-2, provides a method of validating the technique of applying strains in arbitrary directions.

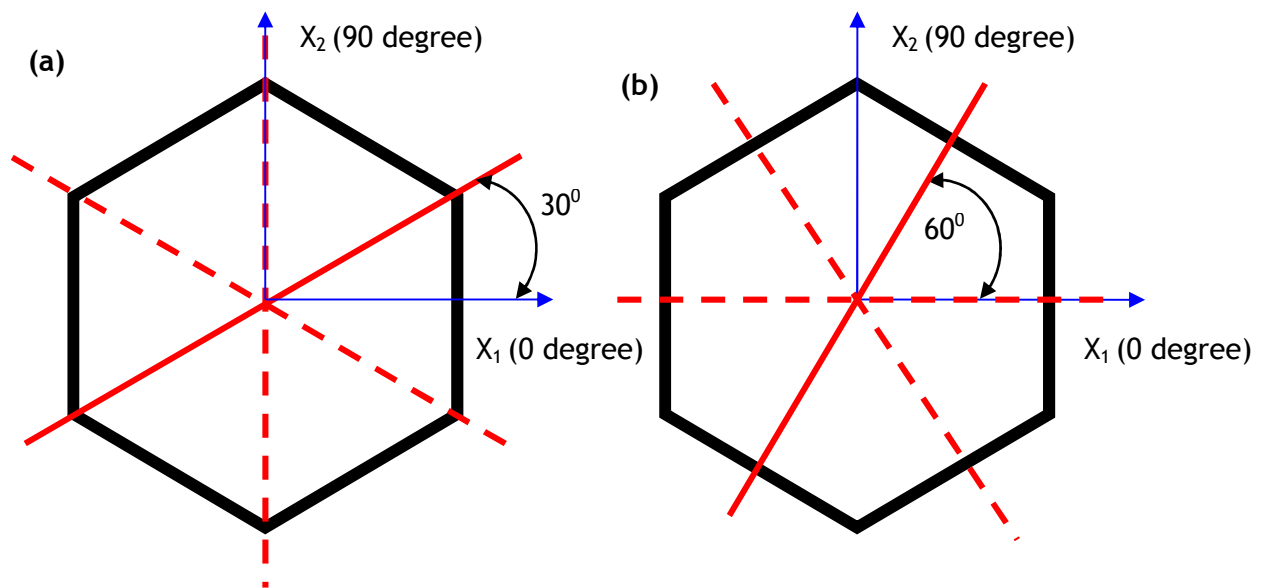


Figure 4-2: Six axes about hexagonal six nodes where spaced by 60° from each other. (a) Solid axis spaced 30° from principle axis X_1 . (b) Solid axis spaced 60° from principle axis X_1 .

Based on the symmetrical nature of the honeycomb cell, it is clear that uni-axial compression in a vertical direction (i.e. $\theta_0 = 90^\circ$) should produce exactly the same mechanical response as compression along the direction with $\theta_0 = 30^\circ$. The same is also true for compression in the directions with $\theta_0 = 0^\circ$ and $\theta_0 = 60^\circ$. Therefore, from this hypothesis, it is possible to directly check whether the approach of applying uniaxial strains in arbitrary directions (i.e. Eq. 4.16 to 4.19) is correct or not.

4.4.1 Finite element model for honeycomb structure

In this section, the FE model of the RVE microstructure is described. Since only low-density open cell foams are considered in the current investigation (ρ^*/ρ_s

=0.041), the use of beam structures of constant cross-section is thought to be a reasonable approximation. This approximation is affirmed to some degree by previous studies, for example, when modelling aluminium open cell foam using a small 3-d RVE and solid elements, the effect of variations of rib cross-sectional shape and area, as a function of length along the rib, was found to be of diminishing importance with decreasing foam relative density [Gong et al. 2005; Jang et al. 2008]. For small strain simulations with no self-contact within the structure (less than 20% compressive strain for very irregular microstructures) each rib of each cell has been modelled using five equal length 2D Timoshenko quadratic beam elements (B21 type element in AbaqusTM) with a constant square cross-section of side-length, t_b . For all cases in this chapter, the constituent material model is linear elastic with a Young's modulus, E_s , of 1GPa and a Poisson's ratio = 0.33. Consequently all conclusions from this work are restricted to linear elastic behaviour for the constituent material. The Timoshenko beam element formulation is capable of including the effects of transverse shear stiffness for thick section beams (recommended for cross section diameters up to $1/8^{\text{th}}$ of the structures axial length) and converges on the slender element result (zero-transverse shear stiffness) for elements where the cross-section diameter is less than about $1/15^{\text{th}}$ of the beam's axial length (Abaqus User Manual v6.9). The error in the structural element approximation progressively increases as the thickness/length ratio increases and inevitably leads to some error at higher relative densities. The foam density in this investigation is close to the upper limit of what can be feasibly considered using structural elements for 2-d RVEs, without causing excessively large errors due to the high rib thickness/length ratios. For a perfectly regular honeycomb structure a relative density of 0.05 in Eq. 3.3 leads to ratios of about $1/7$. For random RVEs this ratio varies from rib to rib due to changing rib lengths and the use of a constant rib thickness throughout the RVE. The average value of the ratio falls to about $1/25$ for the most irregular case, though here a small proportion of the ribs have significantly higher ratios than $1/8$. All element cross-section properties are assigned prior to the analyses and remain constant during deformation. Since the current investigation is considered as both a time- and inertia-independent analysis, the Abaqus 'Static General' with geometrical non-linearities included in the solution algorithm has been employed

for all FE simulations in this chapter. This provides an accurate response with less simulation time compared to a dynamic implicit or an explicit FE analysis.

4.4.2 Method of determining mechanical response of honeycomb RVE in different loading directions

Eq. 4-10, 4-12 and 4-14 suggest that for an elastic honeycomb of low relative density the Young's modulus and the Poisson's ratio should be identical when uniaxially compressed in both the vertical and horizontal directions. Here the mechanical response is investigated when compressed at angles $\theta_0 = 0^\circ, 15^\circ, 30^\circ, 45^\circ, 60^\circ$ and 90° to strains up to 10 percent compression. From Eq. 4-16 to 4-19, it is straight-forward to obtain strain and stress values for the vertical and horizontal directions, since the loading direction is perpendicular to the RVE surface boundary. In these two cases an overall force applied to the dummy node can be directly used to compute a compressive stress because from Eq. 4-17 and 4-18 for either $\theta_0 = 0^\circ$ or 90° , the third dummy node, d_3 , deformation is identical to d_1 or d_2 displacements. However, for compression at angles other than 0° and 90° , a three-step process is required to determine the strain-stress data.

Step1: Calculating dimensions of imaginary RVE. Consider the case where the RVE is compressed at 60° from the X2 axis. The undeformed RVE can be assumed to be part of a larger imaginary RVE (see Figure 4-3). For a RVE structure with initial height, $H0$ and width $W0$ the imaginary RVE width and height are calculated as

$$LW0 = H0 \cos \theta_0 + W0 \cos(\pi/2 - \theta_0), \quad \theta_0 = \text{Loading angle} \quad \text{Equation 4-20}$$

$$LH0 = H0 \sin \theta_0 + W0 \sin(\pi/2 - \theta_0) \quad \text{Equation 4-21}$$

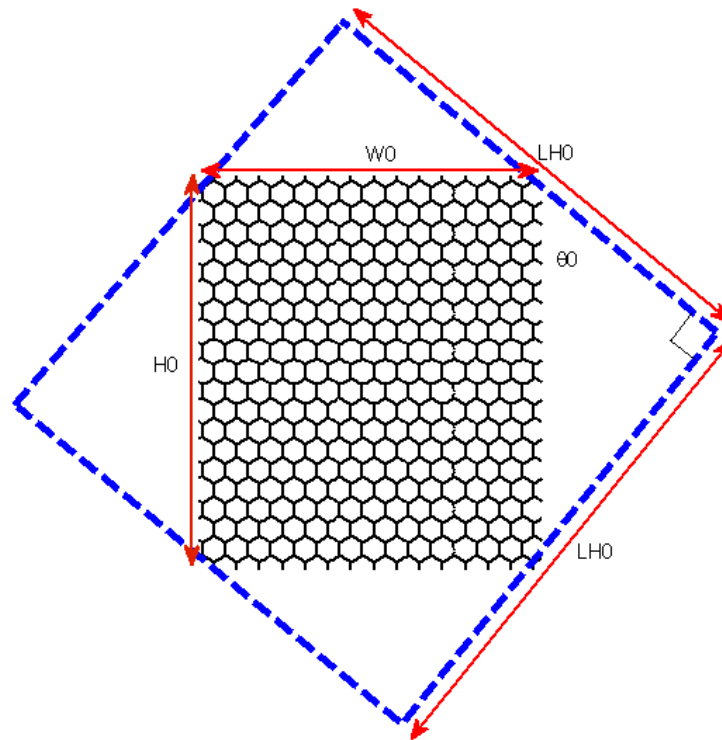


Figure 4-3: The RVE in the undeformed state. A larger imaginary RVE (blue broken lines) is constructed with boundaries perpendicular and parallel to the applied loading direction, here $\theta_0=60^\circ$.

Step 2: Correction of compressive strain. The same argument can be used to determine the size of the imaginary RVE during compression. Depending on the loading angle, the imaginary RVE will be compressed on one side and stretched on the other (see Figure 4-4). Ideally, the compression direction should remain perpendicular to the upper and lower boundaries of the imaginary RVE. However, in practice the PBC does not strictly impose this constraint and the boundaries of the RVE do not necessarily remain in a perfect rectangle during compression. From experience, a small drifting angle, θ_d , between the axis of the upper and lower faces of the RVE can occur. This angle varies from one RVE orientation to the next and is usually less than 1 degree. However, this drift angle can have some effect on the final stress-strain curve calculation. To define a physical meaning of drifting angle, for example, considering an RVE compressed at 60° , θ_0 and θ_2 are expected to be identical, as demonstrated in Figure 4-4:

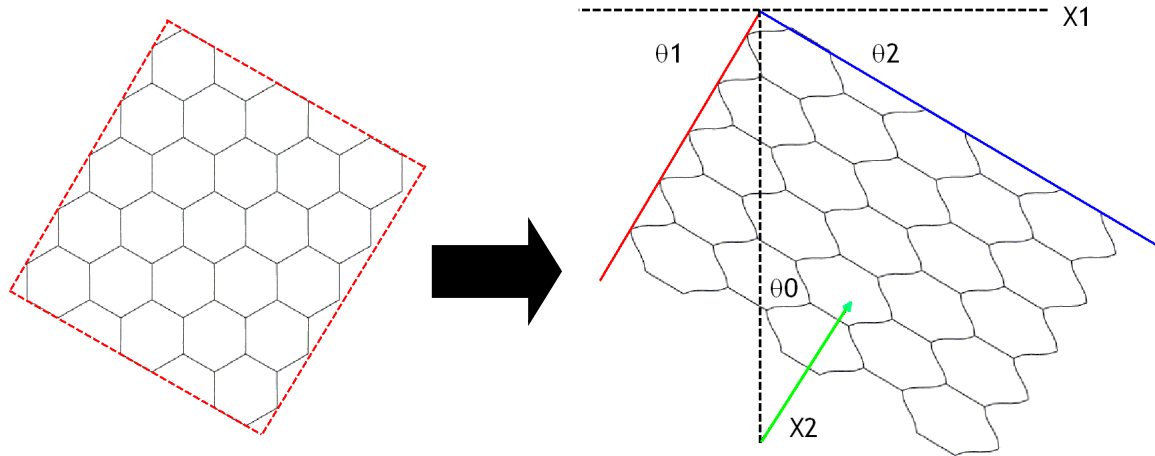


Figure 4-4: A loading vector is expected to be perpendicular to the line parallel with RVE surface but during a simulation the surface which bears compression (blue solid line) performs some slight drifting.

From Figure 4-4 a compression vector (the green solid arrow) is expected to be perpendicular to the top boundary of the box (the blue solid line). But in practice, θ_2 is slightly smaller to θ_0 by an amount, θ_d , the drifting angle. Therefore, the compressive strain is calculated as

$$\alpha' = \theta_0 + \theta_d - \theta_1 \quad \text{Equation 4-22}$$

$$\beta = \theta_0 + \theta_d + \theta_2 \quad \text{Equation 4-23}$$

$$LH = (H \sin \alpha') + (W \cos \beta) \quad \text{Equation 4-24}$$

$$\varepsilon = \frac{(LH_0 - LH)}{LH_0} \quad \text{Equation 4-25}$$

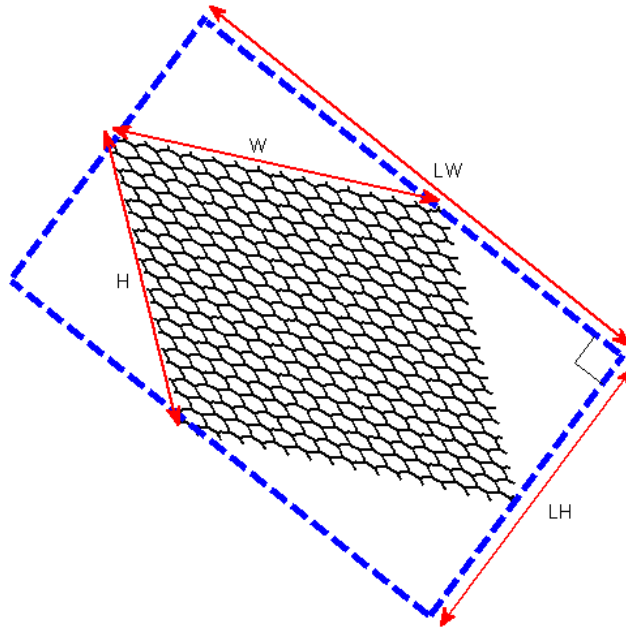


Figure 4-5: Deformed compressed honeycomb in 60° loading direction.

Step 3: Calculation of stress versus strain curve. For pure incompressible material with elastic deformation which is the subject of current research, it is possible to calculate the load by differentiating the strain energy, W_{el} , of the RVE versus displacement (see Figure 4-6).

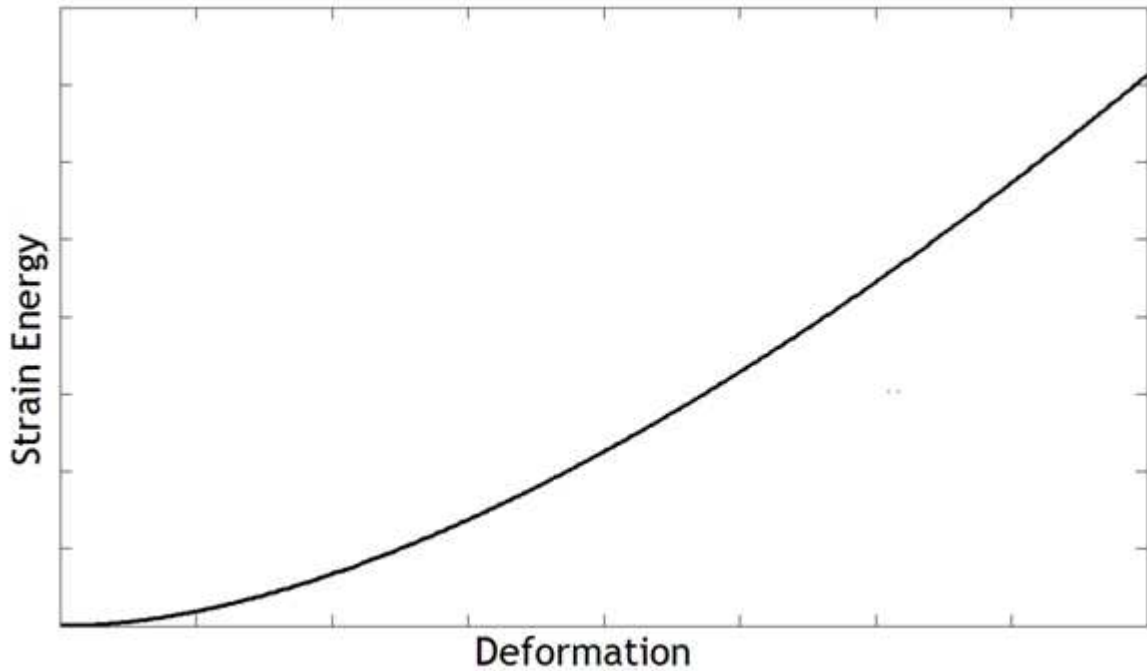


Figure 4-6: Example curve of elastic strain energy. By differentiating the strain energy, W_{el} , curve with respect to the vertical boundary deformation, u_{el} , it is possible to compute the force, F , applied on the imaginary RVE as a function of the compressive strain.

After obtaining the strain energy-deformation curve from the FE simulation, it is then possible to relate the overall force and strain energy as follows:

$$W_{el}(u_{el}) = \int_0^{u_{el}} F(u_{el}) du_{el} \quad \text{Equation 4-1}$$

$$F(u_{el}) = \frac{dW_{el}(u_{el})}{du_{el}} \quad \text{Equation 4-2}$$

Assuming that the honeycomb RVE undergoes homogenous deformation throughout, it can be argued that an imaginary RVE should also deform in a similar manner. Consequently the strain energy of the imaginary RVE should be proportionately greater than that of the actual RVE by an amount equivalent to the ratio of the areas of the imaginary and actual RVEs. The resultant force of the imaginary RVE can therefore be computed as

$$F(u_{el}) = \frac{A}{A'} \frac{d(W_{el}(u_{el}))}{du_{el}} \quad \text{Equation 4-28}$$

where deformation, $u_{el} = LH0 \times \varepsilon$, the undeformed honeycomb RVE area, $A' = LH0 \times LW0$ and the deformed imaginary RVE area, $A = LH \times LW$

Due to the 2-d nature of problem and since beam elements of square cross sectional geometry are used, the stress is calculated by simply dividing the force for the imaginary RVE by the length of the top of the imaginary RVE multiplied by the beam thickness

$$\sigma = \frac{F}{LW \times t_b} \quad \text{Equation 4-29}$$

4.4.3 Mechanical response of honeycomb RVE in arbitrary loading direction for compressive strain less than 10%

From the symmetry of the honeycomb unit cell it is expected that the mechanical response in the $\theta_0 = 30^\circ$ and $\theta_0 = 90^\circ$ directions should be identical, likewise for the $\theta_0 = 0^\circ$ and $\theta_0 = 60^\circ$ directions. The stress versus strain curves are computed at various directions, as shown in Figure 4.7.

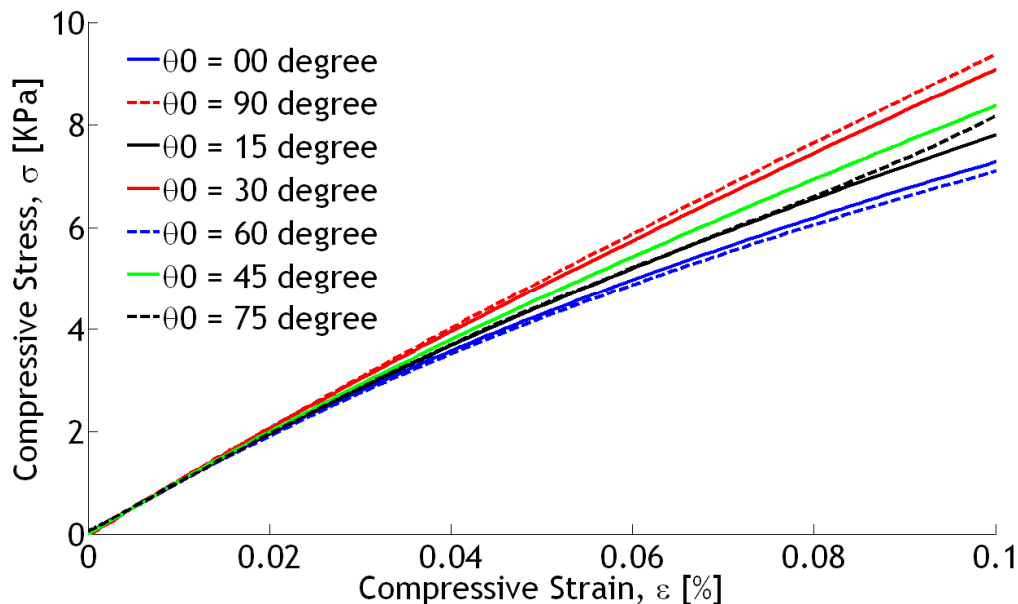


Figure 4-7: Stress-strain relationship for honeycomb RVE comprised of 325 unit cells when uniaxially compressed in several different directions.

Examination of Figure 4-7 reveals that for an increasing compressive strain, the stress-strain curves unexpectedly start to deviate from each other. This deviation is negligible for strains less than about 10%. But depending on the direction of compression, the divergence increases at different rates with increasing strain. For example, compression at $\theta_0=0^\circ$ and $\theta_0=60^\circ$ produce almost identical deformation of the microstructure within the RVEs and hence very similar stress-strain curves (see Figures 4-7 and 4-8).

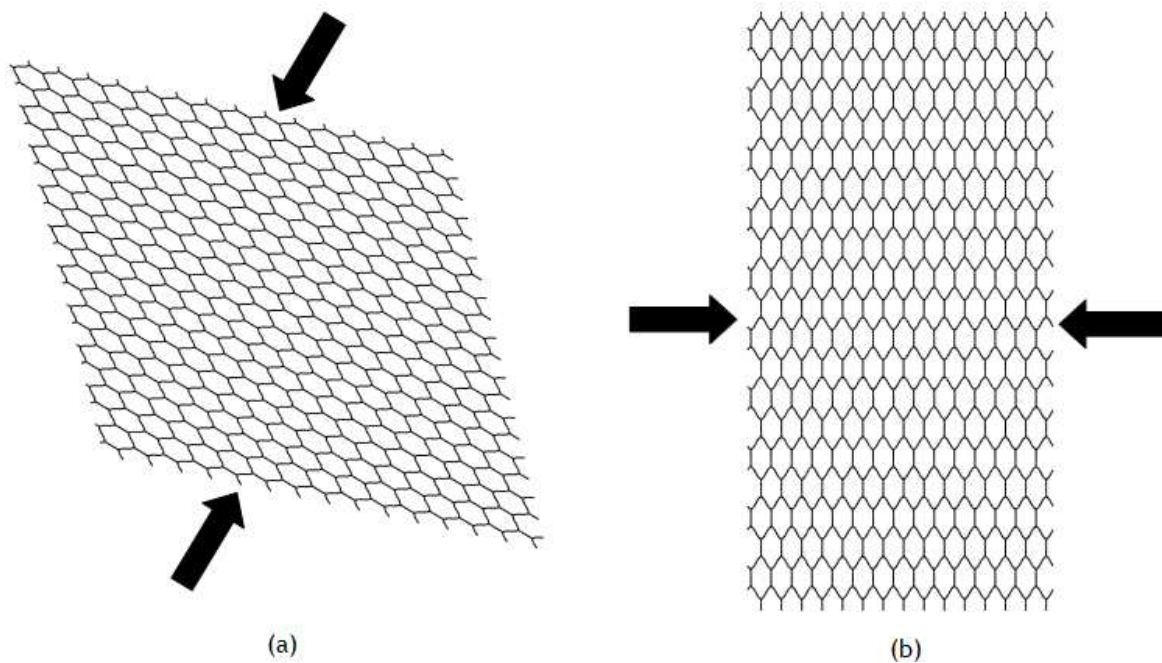


Figure 4-8: Deformed honeycomb RVE at compressive strain = 0.30 for loading directions (a) 60° and (b) 0° , respectively.

However, the same is not true for applied loads at $\theta_0=30^\circ$ and $\theta_0=90^\circ$. In this case at 15% compressive strain the two deformed microstructures are noticeably different (see Figure 4-9):

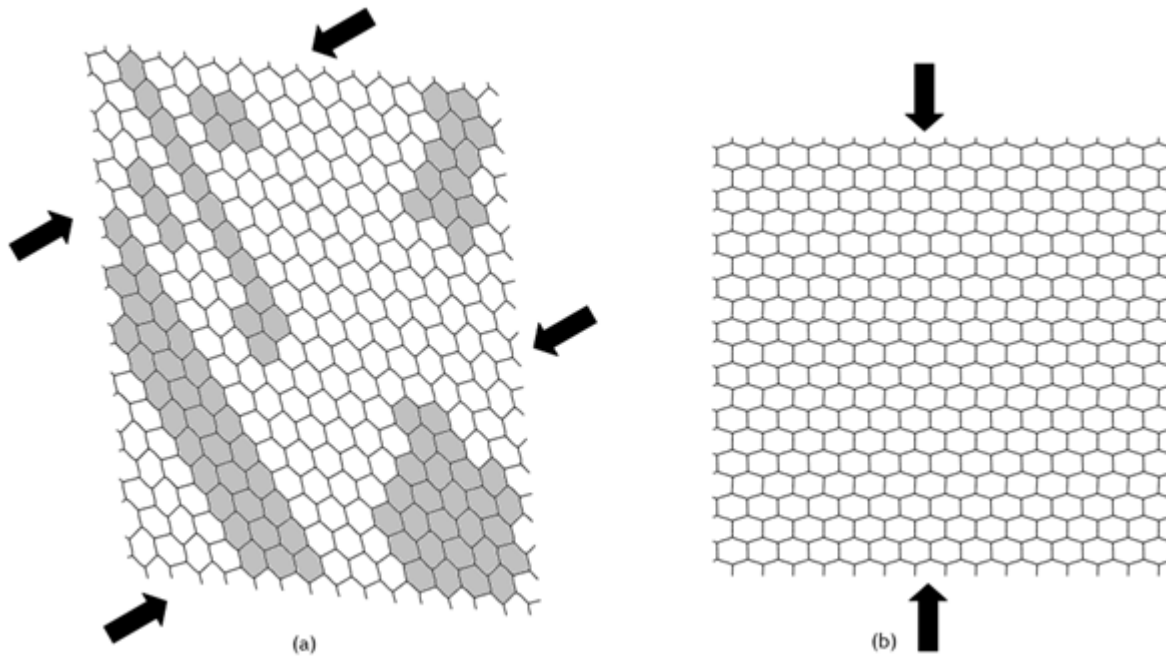


Figure 4-9: Deformed honeycomb RVE at compressive strain = 0.15 for loading directions (a) 30° and (b) 90° , respectively. For clarity, grey cells indicate regions with localised buckling.

It is generally understood that a PBC does not produce an accurate average response of RVE for a large compressive strain, particularly when non-linear deformation mechanism such as buckling become dominant [Gong and Kyriakides, 2005; Li et al. 2006]. When load is applied in a vertical direction; the stress-strain relationship is almost linear at about 10% compression. There is debate in the literature regarding the dominant deformation mechanism in this region, i.e. whether it is beam-bending [Elliot et al. 2003] or buckling [Mills, 2006] (see Figure 4.8). The source of this inconsistency is due to the shape of deformed beams and also the critical load calculation on each individual beam, which is different for various structural properties (e.g. relative density) and the type of boundary condition. However, for larger compressive strains, the stress-strain relationship starts to become non-linear due to the initiation of buckling within the microstructure. The periodic geometry of the RVE's boundaries and also the identical nodal positions on these boundaries mean that when the RVE is compressed in the $\theta_0=90^\circ$ direction, cells located at counterpart boundaries deform in exactly in a same way, even in the case of buckling (see Figure 4-9a and b), therefore the RVE region on boundaries always deform in a homogenous way. For

the $\theta_0=30^\circ$ case however, since the load direction is not perpendicular to the top and bottom surfaces (i.e. the RVE boundaries), this time, both the top and right boundaries on one side, and the bottom and left boundaries, on the other side, compress towards each other where in the case of $\theta_0=90^\circ$, only the top and bottom surfaces are compressed toward each other, and the left and right surfaces are not directly involve in compressive deformation. For compressive strains over 10%, the buckling mechanism results in different buckling patterns in the microstructure. Unlike the $\theta_0=0^\circ$ and 90° cases, different loading direction result in scatter buckling patterns where some of them are highlighted by using grey colour in Figure 4-9. Looking at the $\theta_0=30^\circ$ and 60° cases, the beam buckling mechanism is more significant when the load is applied at 30° compared to the case with compression applied at 60° . Even at large compressive strains (e.g. 30%) cells are mostly deformed in similar pattern compared to $\theta_0=30^\circ$ case. Therefore in general, applying large compressive deformation using PBC does not provide a true mechanical response in multi-directional loading. However, in the vicinity of the linear regime (typically less than 10% compressive strain) due to negligible presence of beam-buckling, the RVE's boundaries still deform periodically and therefore the final response is still valid.

The elastic properties of beam-based honeycomb with low relative density compressed in different directions can be compared. Using steps 1 to 3, as described in Section 4.4.2, the secant modulus of the stress-strain curves can be calculated. The results are given in Table 4-2.

Table 4-2: Secant Modulus (SM) calculated for different loading directions

Loading Direction	SM at $\varepsilon=0.005$ [Pa]	SM at $\varepsilon=0.01$ [Pa]	SM at $\varepsilon=0.05$ [Pa]	SM at $\varepsilon=0.1$ [Pa]
0°	1.050×10^5	1.021×10^5	0.860×10^5	0.723×10^5
15°	1.050×10^5	1.021×10^5	0.893×10^5	0.780×10^5

30°	1.050 x10 ⁵	1.042 x10 ⁵	0.973 x10 ⁵	0.900 x10 ⁵
45°	1.050 x10 ⁵	1.028 x10 ⁵	0.930 x10 ⁵	0.830 x10 ⁵
60°	1.050 x10 ⁵	1.021 x10 ⁵	0.860 x10 ⁵	0.710 x10 ⁵
75°	1.050 x10 ⁵	11.021 x10 ⁵	0.893 x10 ⁵	0.815 x10 ⁵
90°	1.050 x10 ⁵	1.053 x10 ⁵	0.993 x10 ⁵	0.930 x10 ⁵

Using a relative density of 0.041 and a Young's modulus for the solid constituent material of 1.0 GPa, Equations 4-6 and 4-7 predict a modulus of 1.063 E5 Pa which is very close to the values in Table 4-2 at $\varepsilon=0.005$.

Table 4-2 and Figure 4-9 show that at very low compressive strains, honeycomb of low relative density has an elastic modulus which is independent of the direction of compression. This result is also predicted analytically by Eq. 4-6 and 4-7. However, as the compressive strain increases, the stress values for different loading directions significantly deviate from each other. At $\varepsilon=0.1$ this difference is as much as 30%. It can therefore be said that a honeycomb structure does not produce an isotropic elastic behaviour for anything other than very small strains. The main reason for this anisotropic behaviour is due to the change in the dominant deformation mechanism in the different loading directions. This becomes more evident when analysing the deformation at even larger strains, as demonstrated in the following section.

4.4.4 Mechanical response of honeycomb RVE compressed in arbitrary loading directions for strains greater than 10%

Consider the behaviour of a honeycomb microstructure when compressed up to 30 percent strain in both the transverse and perpendicular directions ($\theta_0=0^\circ, 90^\circ$). During the first 10% compressive strain, the structural stiffness is significantly higher when compression is applied in the perpendicular direction but an abrupt yield behaviour occurs at about 10 percent strain, followed by a much more compliant compressive response (see Figure 4-10). In contrast, the structure is less stiff at low strains when compressed in the transverse direction but because no abrupt yield occurs in this direction, at compressive strains greater than around 10 percent the stiffness is higher in this direction than when the structure is compressed in the perpendicular direction (see Figure 4-10).

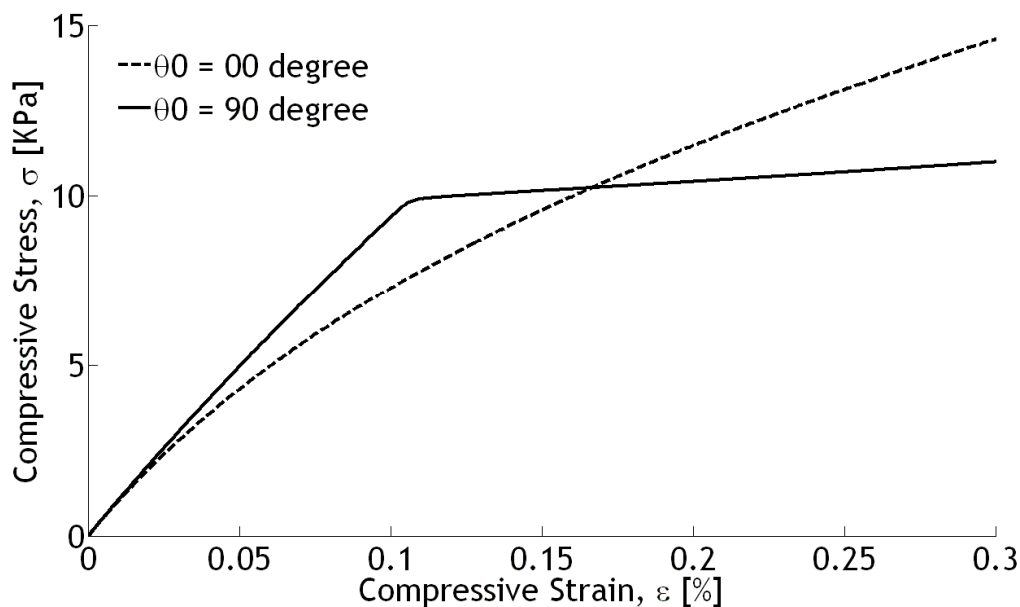


Figure 4-10: Stress versus strain curves for compression in the transverse (0 degree) and perpendicular (90 degree) directions.

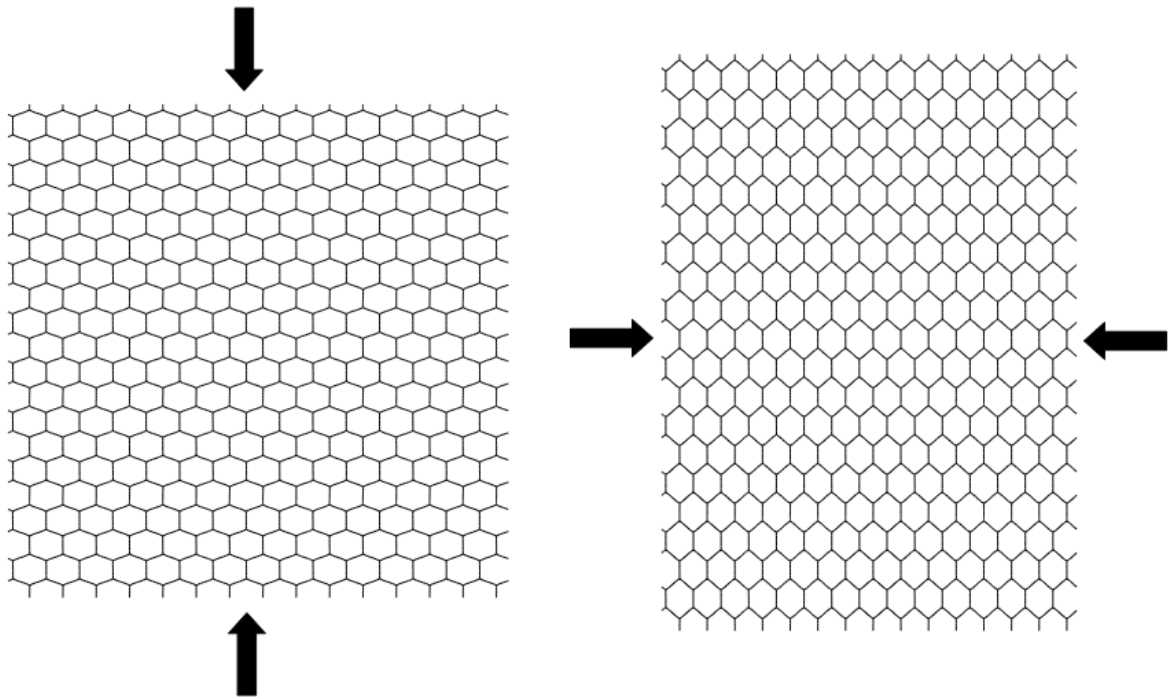


Figure 4-11: Deformed honeycomb structures at compressive strain = 0.1 with applied force at (left) perpendicular and (right) transverse direction.

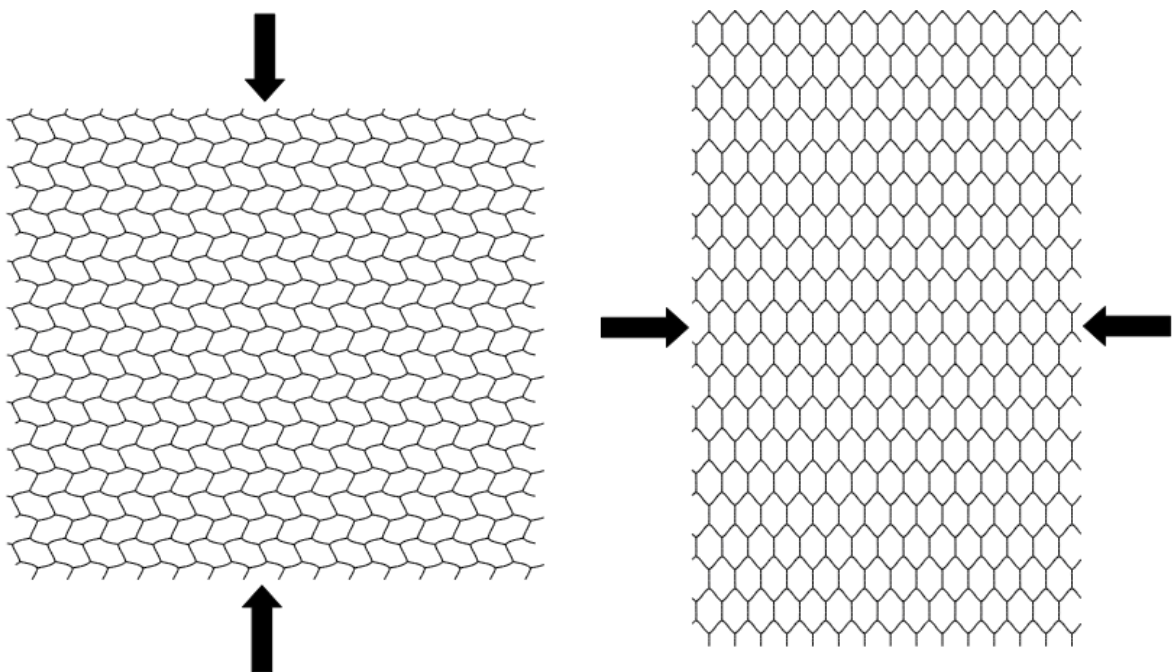


Figure 4-12: Deformed honeycomb structures at compressive strain = 0.2 with applied force at (left) perpendicular and (right) transverse direction.

Figure 4-13 shows the effect of the compressive loading direction on the Poisson's ratio (calculated as the ratio of the laterally induced to the directly applied strains) for the honeycomb structure. It should be mentioned that in real foams the Poisson's ratio is less than 0.5. However, due to the 2-d idealisation in the current investigation the Poisson's ratio is greater than 0.5 even at large compressive strains. Note that in 2-d, a Poisson's ratio of less than 1.0 corresponds to a compressible material. The geometrical anisotropy clearly also has a major effect on this property. It also should be noted that from Eq. 4-14, the Poisson's ratio of honeycomb at very small compressive strain is very close to one.

It is apparent that both the stress versus strain and Poisson's ratio versus strain curves can be correlated to cellular deformation of the structure when loaded in the perpendicular direction. For example, in the case of $\theta_0=90^\circ$, at $\varepsilon=0.1$ there is a sudden change in the gradient of the Poisson's ratio curve that occurs at exactly the same strain as the kink in the compressive stress versus strain curve.

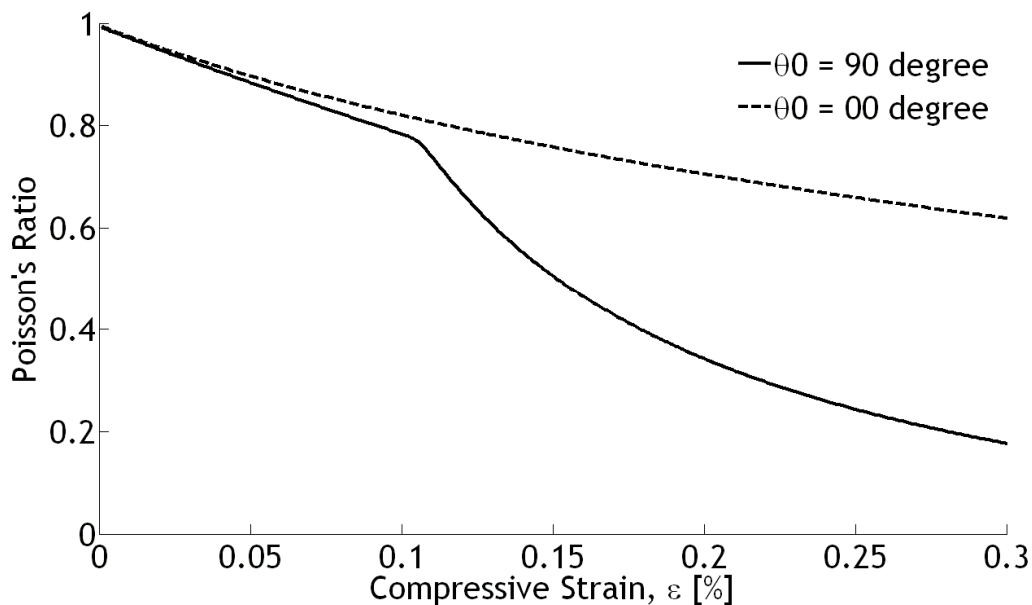


Figure 4-13: Effect of loading direction on Poisson's ratio.

The results presented in Section 4.4 clearly reveal that a honeycomb produces an increasingly anisotropic response when compressed to increasingly large compressive strains. In the next section, it will be shown that this mechanical anisotropy remains even after introducing a large degree of irregularity into the microstructure by perturbing the seed positions in order to generate a random foam microstructure.

4.5 Mechanical response of increasingly randomised RVEs generated using the enhanced method of Zhu, when compressed at 0° , 45° and 90°

In the previous section by applying a load in different directions, it was seen that for strains of less than 10%, the maximum and minimum structural stiffness of a honeycomb structure are predicted in the perpendicular and transverse directions, respectively (see Figure 4-7). In this section, microstructures generated using the enhanced method of Zhu, with progressively increasing degrees of irregularity (see Section 3.2.1) are compressed in arbitrary directions. The aim is to investigate the effect of loading direction on the RVE's mechanical response. 2-d beam-based RVEs containing about 550 cells with 6 different degrees of irregularities and a constant relative density, $\rho^*/\rho_s = 0.05$, have been generated (see for example, Figure 4-14).

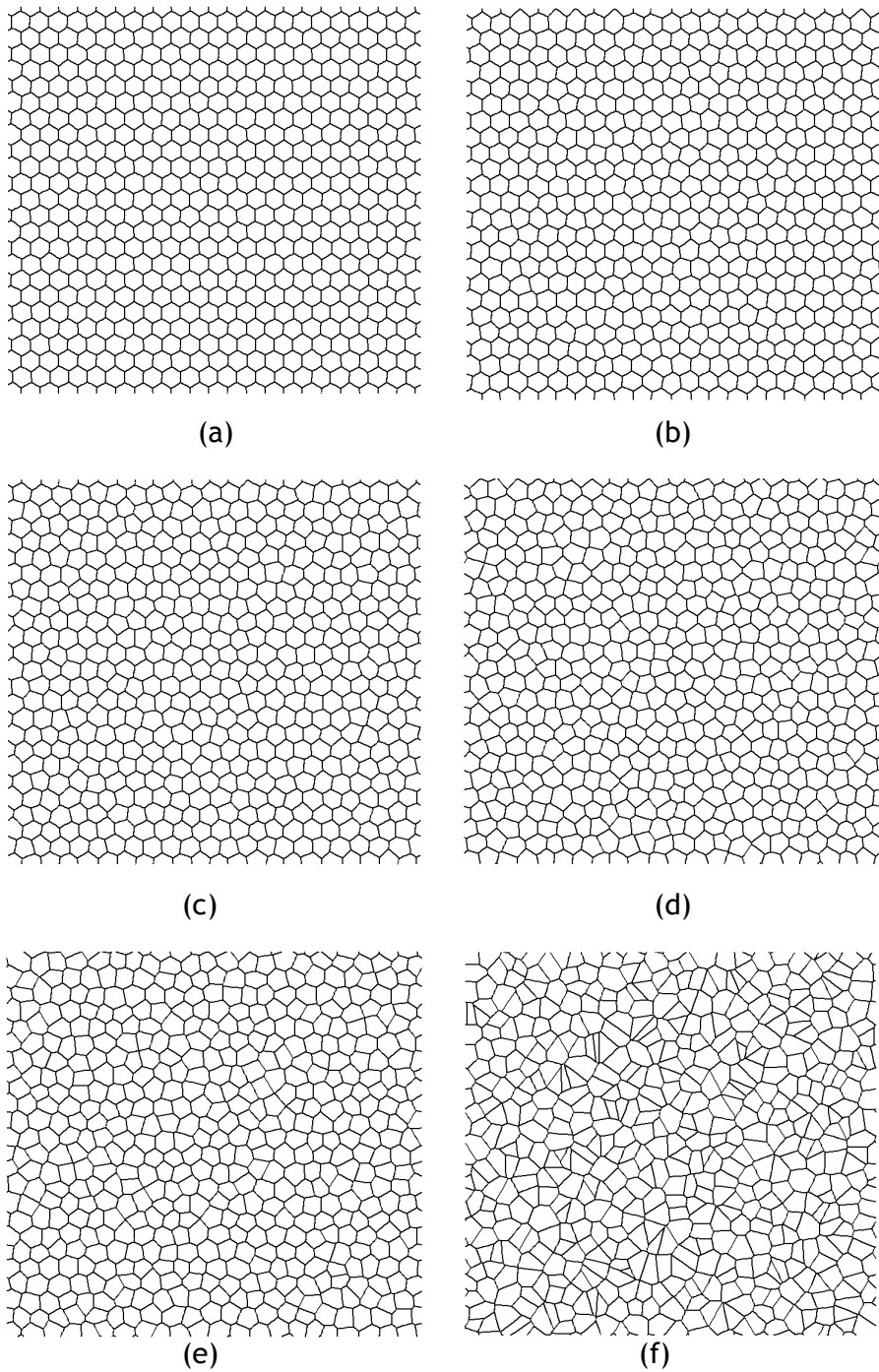


Figure 4-14: RVEs with 5 different degree of irregularity: (a) $\alpha=5$, (b) $\alpha=10$, (c) $\alpha=15$, (d) $\alpha=20$, (e) $\alpha=25$, (f) $\alpha=50$.

Over 120 RVEs have been simulated using a PBC for all cases with loading applied at $\theta_0=0^\circ$, 90° and 45° . From the previous section it was concluded that, in general, when compression is applied in directions other than $\theta_0=0^\circ$ and 90° , due to the

effect of beam-buckling, the RVE response is not accurate (see Section 4.4.3) beyond the linear regime (less than 10% strain). Therefore, for the current section the compressive strains up to 10% only are considered. The averaged stress-strain curves for each RVE case are plotted in Figures 4-15 to 4-20. Note that error bars are omitted from these figures for clarity, though the standard deviation at various levels of strain is provided in Table 4-3:

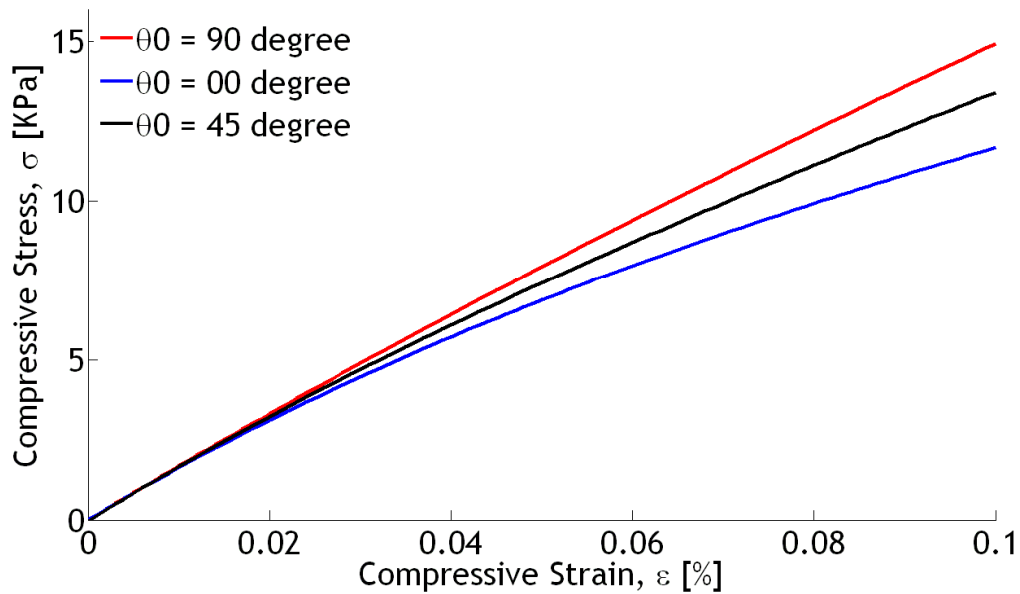


Figure 4-15: Averaged stress-strain curves for compressed RVE with degree of irregularity $\alpha=5$.

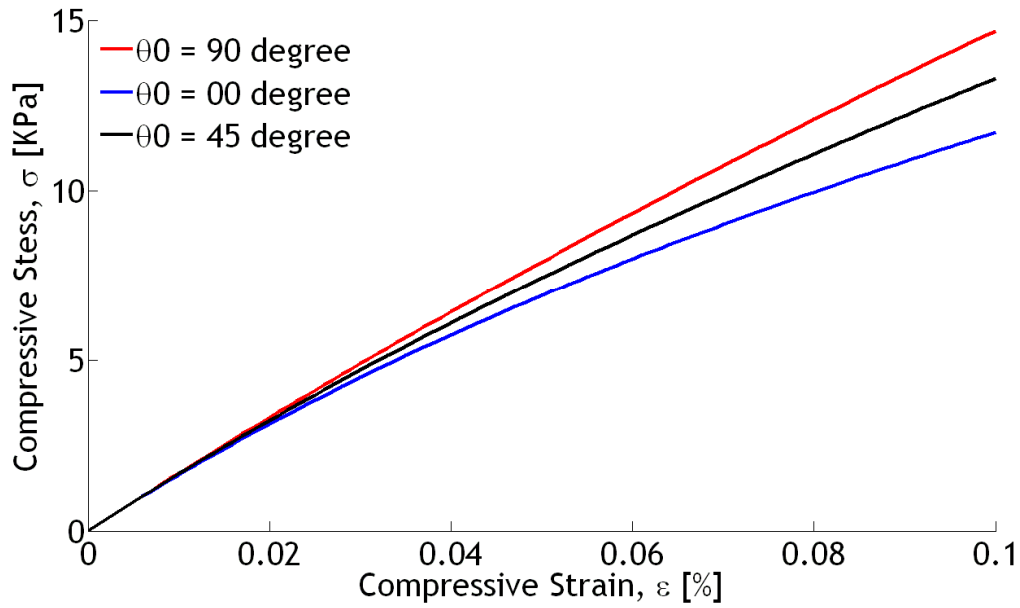


Figure 4-16: Averaged stress-strain curves for compressed RVE with degree of irregularity $\alpha=10$.

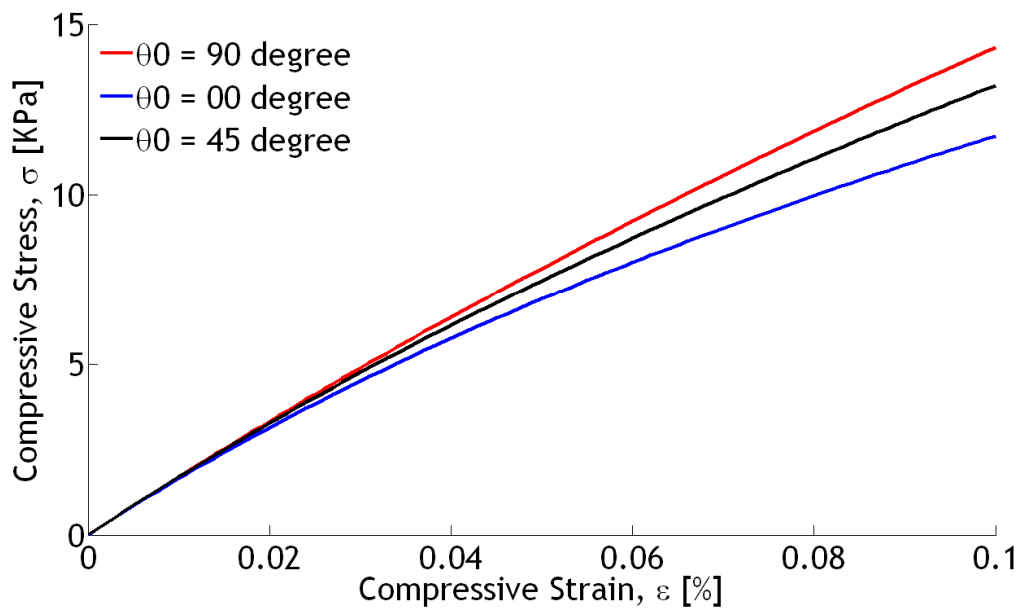


Figure 4-17: Averaged stress-strain curves for compressed RVE with degree of irregularity $\alpha=15$.

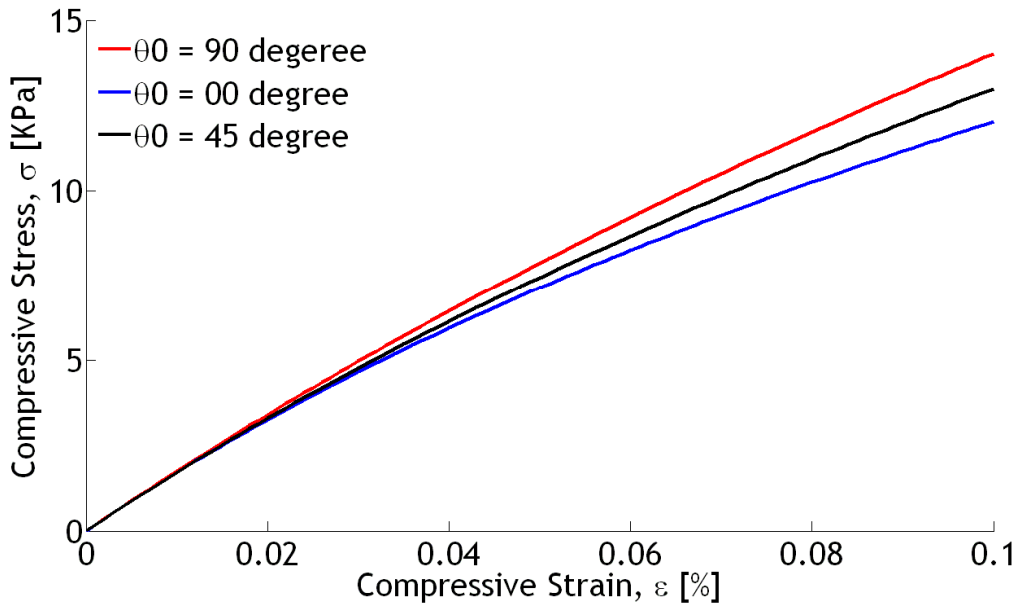


Figure 4-18: Averaged stress-strain curves for compressed RVE with degree of irregularity $\alpha=20$.

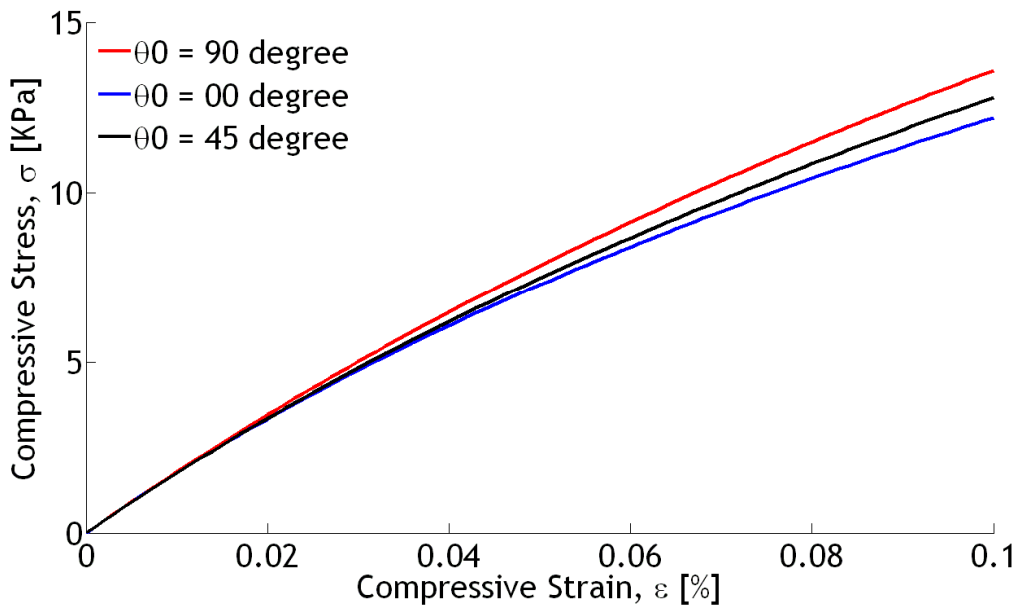


Figure 4-19: Averaged stress-strain curves for compressed RVE with degree of irregularity $\alpha=25$.

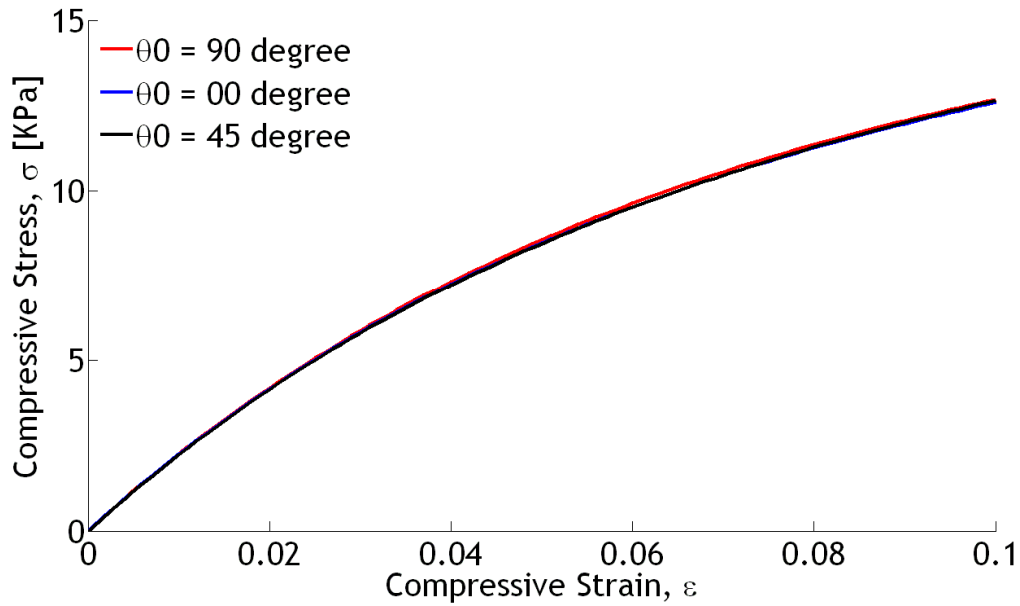


Figure 4-20: Averaged stress-strain curves for compressed RVE with degree of irregularity $\alpha=50$.

Table 4-3: Selected mean and standard deviation values for RVEs compressed in different orientations

ϵ	θ_0	σ at $\alpha=5$ [Pa]	σ at $\alpha=10$ [Pa]	σ at $\alpha=15$ [Pa]	σ at $\alpha=20$ [Pa]	σ at $\alpha=25$ [Pa]	σ at $\alpha=50$ [Pa]
0.001	90°	171±0.11	173±0.41	174±0.82	180±0.74	186±1.53	242±3.51
	0°	171±0.11	171±0.40	173±0.87	180±0.72	185±1.55	242±3.35
	45°	173±0.27	174±0.33	178±0.85	180±1.05	187±2.06	231±9.18
0.005	90°	851±0.56	856±1.98	863±4	890±3.62	915±7.49	1174±17.30
	0°	837±0.54	841±1.86	845±4.22	878±3.45	903±7.47	1170±15.39
	45°	846±0.34	851±1.83	865±4.28	877±4.96	899±11.25	1152±48.73
0.01	90°	1687±1.10	1695±3.89	1706±8	1753±14.62	1796±14.62	2260±33.95
	0°	1633±1.03	1642±3.64	1648±8.13	1711±14.27	1758±14.27	2250±28.00
	45°	1660±0.59	1673±3.65	1697±8.34	1716±9.39	1753±21.72	2227±93.78
0.05	90°	7930±5.14	7904±16.12	7832±39	7868±30.46	7847±61.27	8558±105.93

	0°	6885±3.90	6913±14.95	6927±32.21	7142±52.53	7288±52.53	8464±70.03
	45°	7424±2.11	7431±16	7468±34.03	7446±31.70	7477±81.64	8450±270.73
0.1	90°	14920±9.40	14690±18.81	14318±69	14012±62.88	13580±99.42	12676±146.25
	0°	11670±6.02	11707±24.87	11727±52.90	12023±48.98	12201±79.91	12591±116.02
	45°	13397±2.73	13292±27	13207±62.90	12987±47.18	12792±148.49	12639±285.11

Figures 4-15 to 4-20 show that the mechanical response tends to become more isotropic as the degree of irregularity increases, i.e. the stress versus strain curves produced when the RVE is loaded at 0, 45 and 90° tend to converge as the degree of irregularity increases. For example, when $\alpha=5$ the maximum difference between the mean compressive stress in the 0 and 90° loading directions at a compressive strain of 10 percent is about 22%, this value falls to about 10% for $\alpha=25$ and 1% for $\alpha=50$ (see Table 4-3). Thus the RVE with $\alpha=50$ is isotropic in its mechanical response, though this method of producing an isotropic RVE has a cost. Namely, the RVE no longer possesses a realistic microstructure, as can be seen when comparing Figure 4-14f with a cross-section of an actual polymer foam, see Figure 4-21.

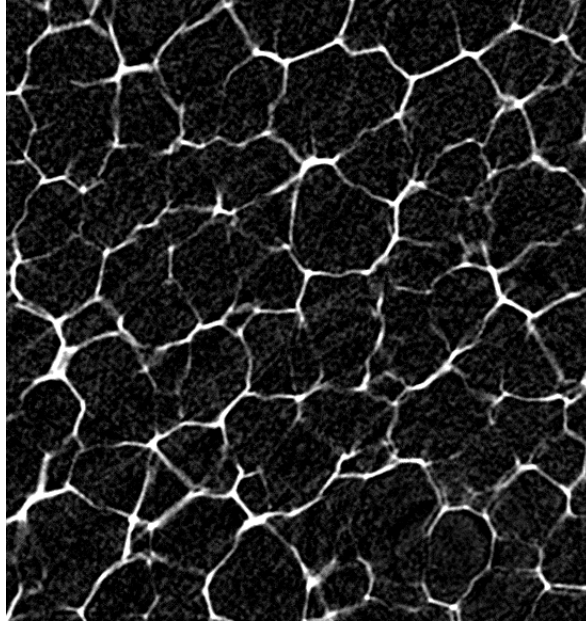


Figure 4-21: Example of 2-d slice of polymeric foam, imaged using microCT [Private communication Dr Zaoyang Guo].

4.6 Generating isotropic RVEs with realistic mono-disperse microstructures

In the previous section, a problem with the enhanced method of Zhu was revealed; isotropic RVEs can be produced using the technique but at the cost of reducing the realism of the final microstructure. So far the ‘realism’ of the microstructure has been assessed only by subjective judgement of the microstructural morphology, i.e. by visual comparison of microCT cross-sections of polymeric foam and the RVE (see Section 4.5). In Chapter 5 a novel, more rigorous method of quantifying the structural morphology of RVEs will be presented and used to verify this subjective assessment in a more objective way. For now the investigation continues and a more detailed discussion of ‘realistic’ morphologies is deferred to Chapter 5.

In this section a novel technique of generating mechanically isotropic RVEs is demonstrated. The method employs the Lloyds relaxation algorithm described in Section 2.1.4. To demonstrate the method, 20 RVEs with a PBC applied, each with over 500 cells are generated using the enhanced method of Zhu with a degree of irregularity, $\alpha = 50$. The relative density of the RVEs is 0.05 ($\rho^*/\rho_s=0.05$). The

microstructure is 'relaxed' via application of the Lloyds relaxation algorithm. An example of the effect of the algorithm on the final microstructure is demonstrated in Figure 4-22. The figure shows the microstructure before and after application of the Lloyds relaxation algorithm. The resulting RVEs are then subject to compression in the $\theta_0=0^\circ$, 45° and 90° directions. The predicted average stress versus strain curves are shown in Figure 4-23.

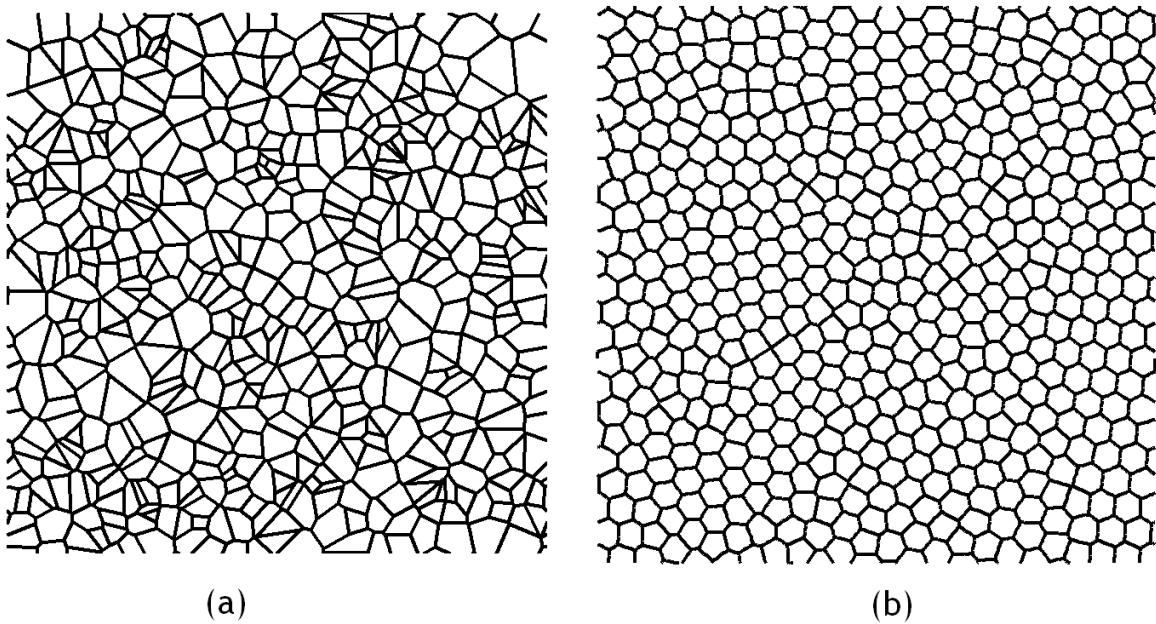


Figure 4-22: (a) microstructure before applying Lloyd's algorithm (b) microstructure after applying Lloyd's algorithm.

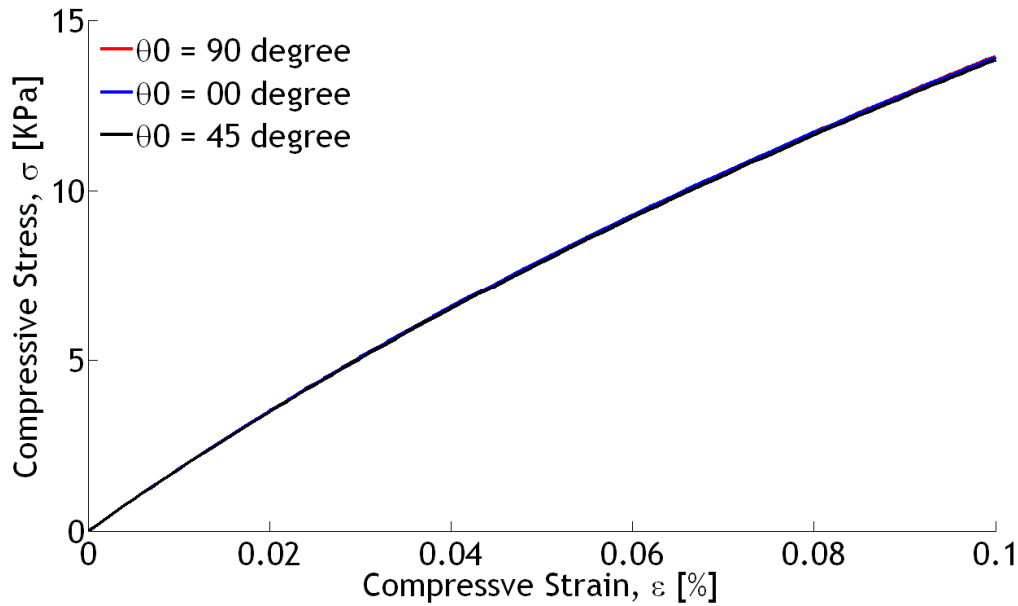


Figure 4-23: Averaged stress-strain curves for compressed RVEs in three different loading directions.

Table 4-4: Selected mean and standard deviation values for RVEs compressed in different angles

θ_0	σ at $\varepsilon = 0.001$ [Pa]	σ at $\varepsilon = 0.005$ [Pa]	σ at $\varepsilon = 0.01$ [Pa]	σ at $\varepsilon = 0.05$ [Pa]	σ at $\varepsilon = 0.1$ [Pa]
0°	188.81±3.20	929.30±15.77	1823±31.01	7963±137.54	13915±236.92
45°	190.12±2.70	924.83±12.80	1813±24.58	7913±96.64	13850±157.41
90°	187.98±3.57	925.35±17.34	1816±33.48	7946±135.85	13942±234.84

Figure 4-23 and Table 4-4 demonstrate that at a compressive strain of 0.1, the maximum difference between the averaged compressive stress versus strain curves of the RVEs for the three different loading directions is only 0.66%. The averaged Poisson's ratio of the RVEs in the transverse (0°) and perpendicular (90°) directions (see Figure 4-24) also shows that RVE generated by the Lloyd's relaxation algorithm shows no directional dependence and have almost identical curves, indicating that the deformation mechanisms in the different loading directions no longer undergo a distinct and co-ordinated change in the dominant deformation mode within the microstructure.

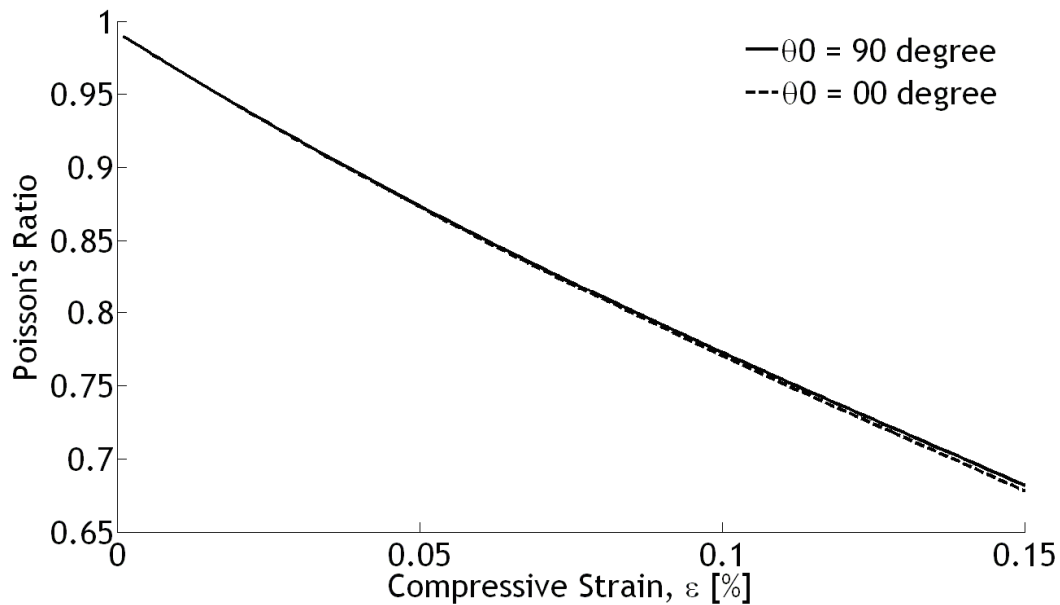


Figure 4-24: Averaged Poisson's ratio for compressed RVE in transverse and perpendicular directions. Due to 2-d modelling idealisation a Poisson's ratio is greater than 0.5.

In chapter 5 it will be shown that the structure produced by application of the Lloyds relaxation algorithm is a good morphological representation of a slice though certain polymeric foams. However, as discussed in Chapter 1, not all foams have a mono-disperse microstructural morphology. Some foams, such as polyurethane foam, can possess a very poly-disperse microstructural morphology [Elliot et al. 2002]. In Chapter 5, it will be shown that the Lloyds algorithm tends to reduce poly-dispersity and is therefore ill suited to generating poly-disperse isotropic microstructures. In this case, the Drop and Roll method, described in Section 2.1.3, would seem to be a better option. The next section examines the isotropy of RVEs generated using the Drop and Roll technique.

4.7 Mechanical response of poly-disperse structure when compressed at 0° , 45° and 90°

In this section the isotropy of RVEs generated using the Drop and Roll method (see Section 2.1.3) is investigated. To investigate the effect of microstructural poly-dispersity the same methodology as that employed in Chapter 3 (Section 3.3) is employed by considering RVEs with four different degrees of poly-dispersity ($\gamma=0.05, 0.10, 0.15, 0.20$). Due to limited computational resource the RVE size sensitivity analysis is omitted in this section. Instead reasonably large RVE structures containing over 500 cells are employed (see Figure 3-11, Chapter 3). Over 80 RVEs (20 RVEs for each degree of poly-dispersity) are simulated using a PBC for cases with $\theta_0=0^\circ, 90^\circ, 45^\circ$ and applying strains up to 10% uniaxial compression. The averaged stress-strain curves for each RVE case are shown in Figures 4-25 to 4-29.

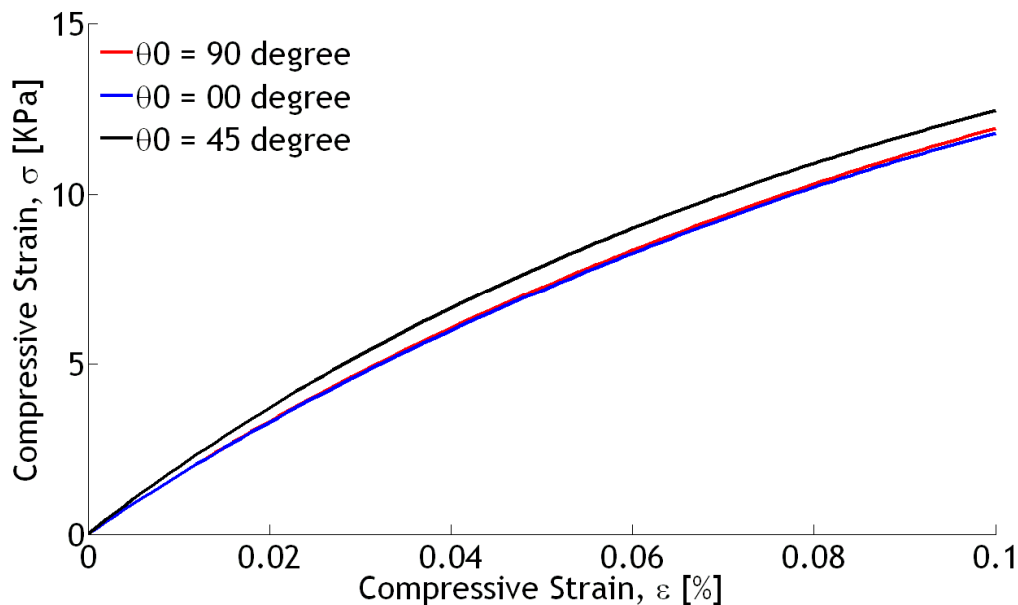


Figure 4-25: Averaged stress-strain curves for compressed RVE with degree of irregularity $\gamma=0.05$.

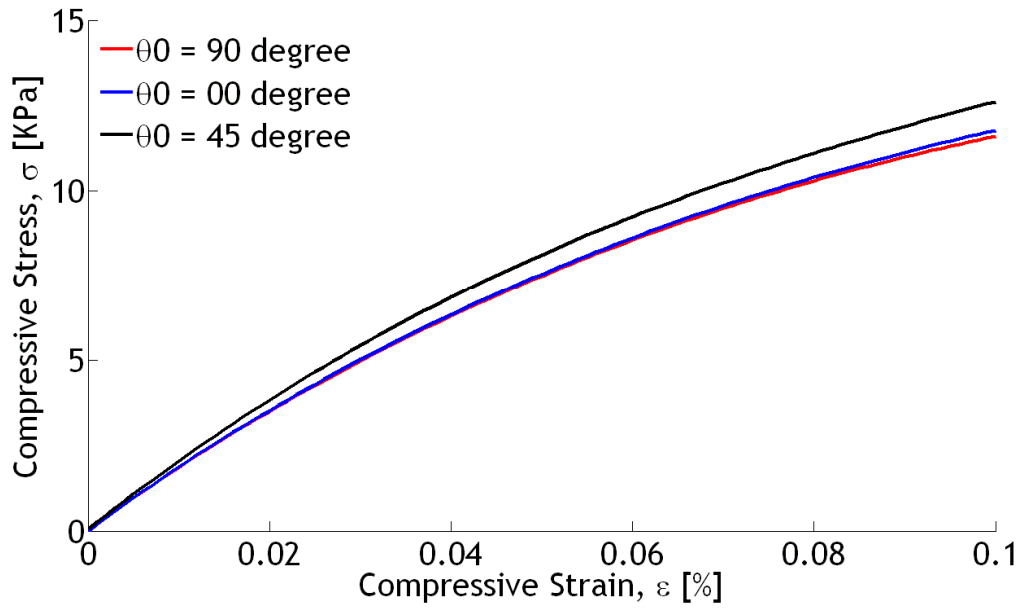


Figure 4-26: Averaged stress-strain curves for compressed RVE with degree of irregularity $\gamma=0.10$.

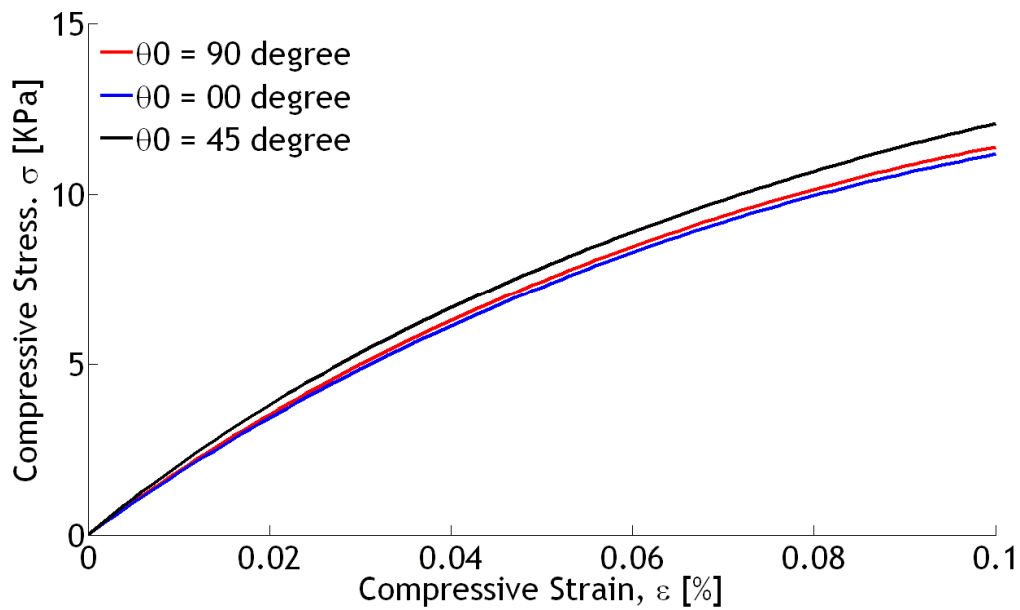


Figure 4-27: Averaged stress-strain curves for compressed RVE with degree of irregularity $\gamma=0.15$.

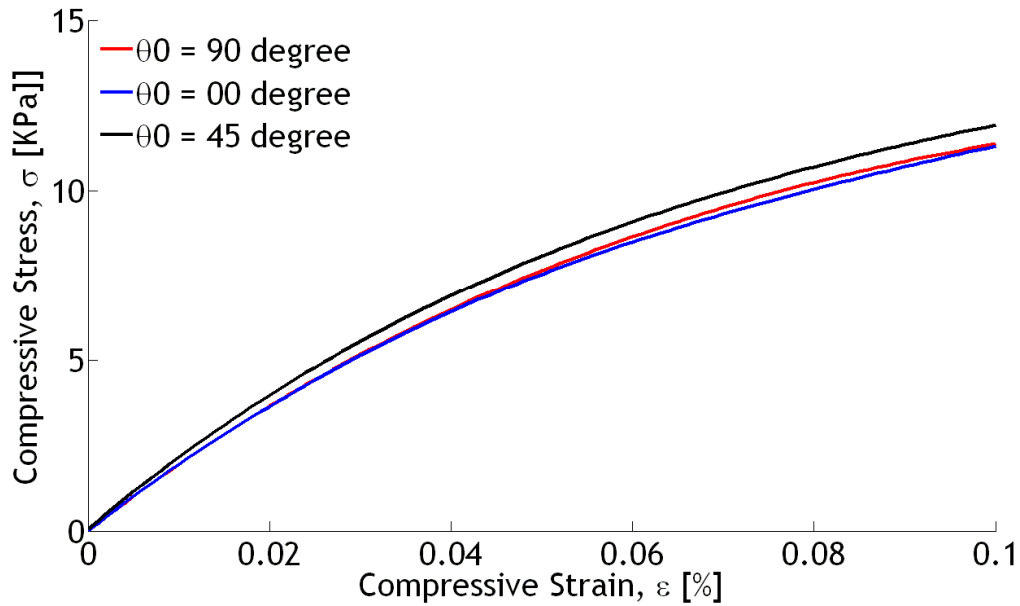


Figure 4-28: Averaged stress-strain curves for compressed RVE with degree of irregularity $\gamma=0.20$.

Table 4-5: Selected mean and standard deviation values for RVEs compressed in different angles

ε	θ_0	σ at $\gamma=0.05$ [Pa]	σ at $\gamma=0.10$ [Pa]	σ at $\gamma=0.15$ [Pa]	σ at $\gamma=0.20$ [Pa]
0.001	90°	182.60±5.54	196.33±3.45	199.13±5.10	206.95±11.91
	0°	182.26±5.28	198.18±4.00	192.42±3.88	208.03±14.44
	45°	227.27±10.44	264.64±20.66	227.16±10.70	286.38±72.13
0.005	90°	893.60±26.85	957.87±16.48	969.53±24.45	1006.30±58.04
	0°	890.83±24.88	966.42±19.84	937.68±18.76	1010.50±69.55
	45°	1027.50±38.48	1077.60±14.23	1068.40±26.09	1149.40±63.48
0.01	90°	1742.20±51.28	1858.90±31.18	2052.70±47.16	1944.70±114.07
	0°	1733.40±46.25	1873.80±39.03	1817.80±36.01	1952.50±133.27
	45°	1977.10±73.94	2047.20±38.60	2050.70±48.77	2161.90±86.85
0.05	90°	7264.20±204.85	7495.20±107.63	7446.60±185.10	7650.0±442.62

	0°	7181.00±139.95	7544.60±166.48	7280.80±126.29	7547.20±445.80
	45°	7898.70±277.22	8120.10±127.44	7849.60±162.70	8079.60±281.56
0.1	90°	11932±326.91	11600±193.40	11387±334.03	11376±547.33
	0°	11776±133.78	11771±253.13	11179±184.84	11305±398.22
	45°	12447±378.43	12610±404.53	12070±108.43	11925±359.84

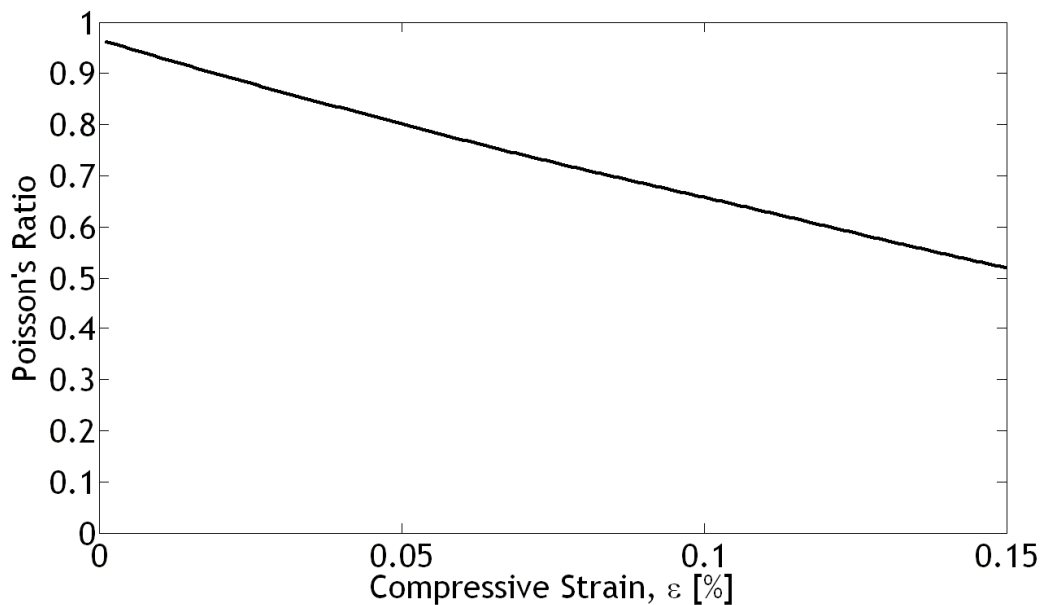


Figure 4-29: Average Poisson's ratio versus compressive strain for compression in the transverse and perpendicular directions, for the case when $\gamma=0.1$. Both curve are almost identical to each other.

Stress-strain curves in Figures 4-25 to 4-28 and the poisson's ratio - strain curve of Figure 4-29 suggest that 2-d beam-based RVEs produce an almost isotropic response in the transverse and perpendicular directions. At $\theta_0=45^\circ$, the stress values are on average about 5% larger than in the $\theta_0=0^\circ$ and 90° directions. As discussed in Chapter 2, the unmodified Drop and Roll method does not generate fully periodic patterns if the balls are all dropped in the same directions due to the influence of the flat ground surface. To overcome this problem, circular disks were randomly dropped in both the perpendicular or transverse directions (i.e. the direction of gravity was changed to up/down, left/right directions) to fulfil

periodicity requirements at the boundaries. In general, it can be said that the Drop and Roll method produces fairly isotropic RVEs in all directions. The results of Table 4-5 tend to confirm the findings of Zhu et al. (2001) and Fazekas et al. (2002), namely, as the microstructural irregularity increases, the Young's modulus also increases however, the yield stress decreases

To investigate the possible relationship between the Poisson's ratio and the mechanism of deformation, an averaged Poisson' ratio curve for case $\gamma=0.1$ is produced since it has an averaged poly-dispersity compared to other cases (see Figure 4-26). By comparing the stress-strain curve of Figure 4-26 with the deformed microstructure of several cells in the RVE, it can be concluded that unlike honeycomb (compressed at perpendicular direction) for structures with high degree of poly-dispersity, there is not a *sudden* transition between linear and plateau regimes.

4.9 Conclusions of Chapter 4

By considering the compressive response of RVEs using various modelling and evaluation techniques, it is found that microstructural irregularity has a significant effect on the averaged response of the RVE. It has been shown that the microstructure generation algorithm influences the average mechanical response and in some cases can result in un-intentional anisotropy in the resulting RVE. Methods to overcome this issue have been devised, including use of the Lloyds relaxation algorithm for mono-disperse RVEs and modification of the Drop and Roll method for poly-disperse RVEs.

Analysis of deformed cellular structures under compression shows that the dominance of beam-bending or buckling is highly dependent on the type of structure and loading direction.

Chapter 5 . Analysis of 2-d RVE microstructural morphologies

5.1 Introduction

In Chapter 1 it was explained that one of the most important characteristics of porous materials, is their ability to absorb compressive energy under almost constant stress due to the plateau region of their uniaxial compressive stress versus strain curve. Understanding the micromechanics occurring during this plateau region could potentially lead to improved macro-mechanical behaviour through optimisation of the microstructural morphology created during the foam manufacture process [Scarpa et al. 2004]. To do this effectively, a clear understanding of the influence of microstructural morphology on the macroscale response (e.g. mechanical isotropy, yield behaviour, form of the stress-strain curve, Poisson's ratio etc), is essential. To develop such an understanding, a sensitivity analysis relating microstructural morphology, micromechanics and macroscale response is required. Another important reason behind studying the micromechanics of the plateau region is to validate the microstructure generated by numerical algorithms, by comparing cellular deformation and mechanical behaviour against similar data obtained using microCT.

The remainder of this chapter is structured as follows. Section 5.2 is a review of the relevant literature foam characterisation approaches during and prior to deformation. In section 5.3, by using a passive approach, the geometrical properties of 2-d beam-based RVEs are studied by considering some important morphological parameters such as cellular orientation, area and strut length distributions. Section 5.4 uses an active approach and analyses the in-situ deformation of mono and poly-disperse 2-d beam-based RVEs under uniaxial compression. Finally, in Section 5.5 conclusions are provided.

5.2 Literature Review

Methods of conveniently quantifying the microstructural morphology are necessary. A large body of research has been undertaken previously to do this for real cellular materials. The methods can be grouped into two categories, *passive* and *active* characterisation. The term ‘passive’ implies characterisation of the foam microstructure in a rest state while the term ‘active’ implies characterisation of the foam microstructure while the foam is subject to stress and strain.

5.2.1 Passive characterisation

Historically, this was the first characterisation method to be developed. In 1982 Dawson and Shortall (1982) used optical and scanning electron microscopy to evaluate the microstructure of closed-cellular polyurethane foams, considering parameters such as individual cell elongation and face (window) shape (individual cell surface geometry). Montminy et al. (2001, 2004) later used Nuclear Magnetic Resonance and x-ray microCT with open-cell polymeric foams to evaluate the distribution of geometrical parameters such as strut length, strut intersection angles and windows area (individual cell surface area). Comparison of experimental data with predictions from existing microstructure theories for foams [Plateau, 1873; Matzke, 1946] revealed that the 3-d network of some types of polyurethane foams significantly differed (e.g. cell geometries, struts length, cell surface area, etc) from those predicted using equilibrium and aqueous based modelling approaches that are currently available in the literature [Montminy et al. 2004]. Grosse et al. (2009), recently performed a volume image analysis of ceramic sponges using MRI and x-ray microCT techniques. By measuring face and strut diameter it was found that the structure of ceramic sponges exhibit preferential microcellular orientation and therefore the cells are better fitted using ellipsoidal rather than spherical shapes. Benouali et al. (2005), studied the influence of cell shape anisotropy on the mechanical behaviour of closed-cell aluminium foams using x-ray microCT. The main parameters to be investigated included cell size distribution and cell shape anisotropy, determined using an ellipsoidal fitting algorithm. By applying compression on the same specimen in different directions it was confirmed that the anisotropic compressive response of the aluminium foam was the direct result of its initial cellular anisotropy.

5.2.2 Active characterisation

Increases in computational power have made it possible to study *in-situ* changes of the microstructural morphology during mechanical deformation. Using x-ray microCT, Elliot et al. (2002) characterised the micromechanics of an open-cell polyurethane foam under compression. Real 3D images were converted into beam-based structures. By extracting nodal displacements, the deformation mechanisms of the compressed foam was studied using the FEM, however due to the non-periodic geometry of specimen a robust comparison with existing foam mechanical theories was not established. In contrast to previous studies, which suggested buckling to be the dominant deformation mechanism under large strains [Gibson and Ashby, 1997, Mills, 2007], Elliot concluded that a cooperative severe bending and reorientation of struts was the main reason behind the structural collapse and sudden reduction of stiffness of the foam microstructure. Dillard et al. (2005), performed quantitative image analysis on an open-cell nickel foam, under both tension and compression. Parameters such as cell volume distribution, number of faces per cell, number of sides per face and strut length distribution were all measured prior to deformation. By fitting each cell with an equivalent ellipsoid at different stages of compression, it was found that struts clearly buckled in the compressive loading direction, a result that apparently contradicts the conclusion of Elliot et al. (2002). Other investigations have been conducted using numerically generated microstructures, due to the difficulties associated with image-based approaches such as absence of geometrical periodicity, very high computation and memory requirements to convert pixel- to structural-based models, the difficulty of resolving individual elements in high compressive strain modes. Hardenacke and Hohe (2009), studied the effect of microstructural disorder on foam micromechanics using 2-d beam-based RVEs generated using classical Voronoi and Laguerre methods where a strong link between cellular morphology and scatter of mechanical responses were found.

5.3 Passive Morphological Characterisation of 2-d Beam-Based RVEs

Following a similar methodology to that reported in previous investigations [Montminy et al. 2001; 2004], several codes have been developed using the MATLAB programming environment, to automatically calculate microstructural-morphology parameters from the 2-d RVEs generated using the algorithms reported

in Chapters 2 and 4. Parameters of interest include cell anisotropy and area distribution as well as strut intersection angle, number of struts per cell and strut length distributions. The cell anisotropy and area distribution are determined using ellipse-fitting methods [e.g. Dillard et al. 2005; Benouali et al. 2005]. These fitting techniques are described in detail in the following section.

5.3.1 Quantification of cellular anisotropy

Several approaches can be used to fit ellipses (or ellipsoids in 3-d) to cells within the numerically generated RVEs. These include a linear least squares method [e.g. Hart and Rudman, 1997] or a method involving calculation of the second moment of area of the entire polygonal surface [Mebatsion et al. 2006]. However, for the case of irregular closed polygons, Green's theorem has been found to be one of the most efficient approaches [Mulchrone and Choudhury, 2004, Mebatsion et al. 2006] and has therefore been adopted in this investigation. For the purpose of the current chapter, to evaluate the individual cellular geometrical properties such as orientation, aspect ratio and area, by considering each cell as a closed polygonal geometry (for 2-d case), the governing equations used in fitting an ellipse to an arbitrary polygon with n nodes are described in this section.

Consider nodal coordinates as x and y , the area of a given cell (closed polygonal surface with n number of elements) is calculated as [Mulchrone and Choudhury, 2004]:

$$A_p = \frac{1}{2} \sum_{i=1}^n (x_i y_{i+1} - x_{i+1} y_i) \quad \text{Equation 5-1}$$

By applying Green's transformation, the first moment of inertia is calculated and is equivalent to the centroid of the polygon,

$$x_c = \frac{1}{6A_p} \sum_{i=1}^n (x_i - x_{i+1}) (x_i y_{i+1} - x_{i+1} y_i) \quad \text{Equation 5-2}$$

$$y_c = \frac{1}{6A_p} \sum_{i=1}^n (y_i - y_{i+1}) (x_i y_{i+1} - x_{i+1} y_i) \quad \text{Equation 5-3}$$

The second moment of inertia is calculated as:

$$I_{xx} = \frac{\sum_{i=1}^n (y_i^2 + y_i y_{i+1} + y_{i+1}^2) (x_{i+1} y_i - x_i y_{i+1})}{12} \quad \text{Equation 5-4}$$

$$I_{yy} = \frac{\sum_{i=1}^n (x_i^2 + x_i x_{i+1} + x_{i+1}^2) (x_{i+1} y_i - x_i y_{i+1})}{12} \quad \text{Equation 5-5}$$

$$I_{xy} = \frac{\sum_{i=1}^n (2x_i y_i + x_i y_{i+1} + x_{i+1} y_i + 2x_{i+1} y_{i+1}) (x_{i+1} y_i - x_i y_{i+1})}{24} \quad \text{Equation 5-6}$$

By using the above equations, it is possible to construct a matrix for the second moments of inertia, Π :

$$I_{uu} = I_{xx} - A_p y_c^2 \quad \text{Equation 5-7}$$

$$I_{vv} = I_{yy} - A_p x_c^2 \quad \text{Equation 5-8}$$

$$I_{uv} = I_{xy} - A_p x_c y_c \quad \text{Equation 5-9}$$

$$\Pi = \begin{bmatrix} I_{uu} & -I_{uv} \\ -I_{uv} & I_{vv} \end{bmatrix} \quad \text{Equation 5-10}$$

Eq. 5-10 can be represented as an inertia ellipse. By finding the eigenvalues and eigenvectors of Eq. 5-10, we can obtain the principal orientations of the ellipse, i.e. the orientations of the semi-major and semi-minor axes. However, since the eigenvalue method could potentially produce two solutions, and therefore two different orientations, it was decided to use another approach to calculate the axes of the semi-major and semi-minor orientation. Consider an arbitrary polygon with centroid, C , and area A_p , by calculating the distance from the centroid to each node, it is possible to produce a reasonably accurate estimation of the ellipse orientation. This value can be directly compared with the eigenvalue solutions in order to choose the right orientation:

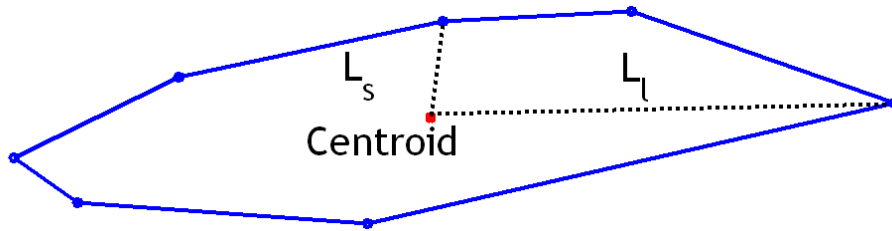


Figure 5-1: Example of the shortest (L_s) and longest (L_l) polygon nodal distances from centroid.

Figure 5.2 shows an example of how this simple fitting procedure can be used to fit ellipses to random polygonal cells, in this case generated using a Voronoi algorithm (see Section 2.8).

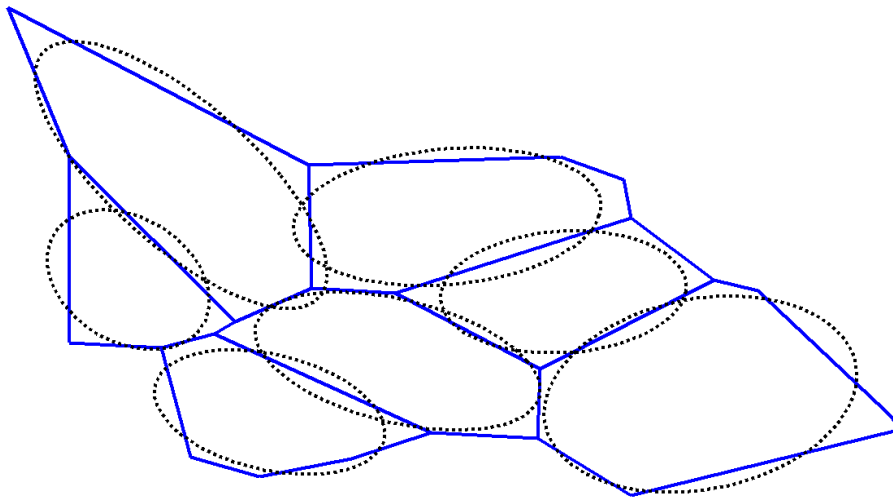


Figure 5-2: Example of ellipse fitting for a random Voronoi structure.

5.3.2 Morphological Analysis of RVEs Generated using the Enhanced Method of Zhu

Given the ultimate goal is to generate realistic RVEs, it is useful to be able to characterise the microstructural morphology as accurately as possible. To this end, various characteristic microstructural morphological parameters can be calculated, and are analysed in this and the following sections. Note that in this chapter only 2-d RVEs are considered, consequently no data on microstructural statistical

distributions from real foams are available for comparison, i.e. comparison of 2-d and 3-d data is not particularly useful and could be misleading. Nevertheless, the techniques demonstrated in this chapter are designed as a first step towards analysis of 3-d RVEs, a topic address in Chapter 6.

By using the enhanced method of Zhu, explained in Section 2.1.2, the cellular anisotropy and poly-dispersity of RVEs with five different degrees of irregularity ($\alpha = 5, 10, 15, 20$ and 25) has been investigated. For each degree of irregularity, over 50 RVEs, each containing about 550 cells, were generated and ellipses were fitted to the cells within the RVE. Example RVEs with progressively increasing irregularity are shown in Figure 5-3 together with the fitted ellipses.

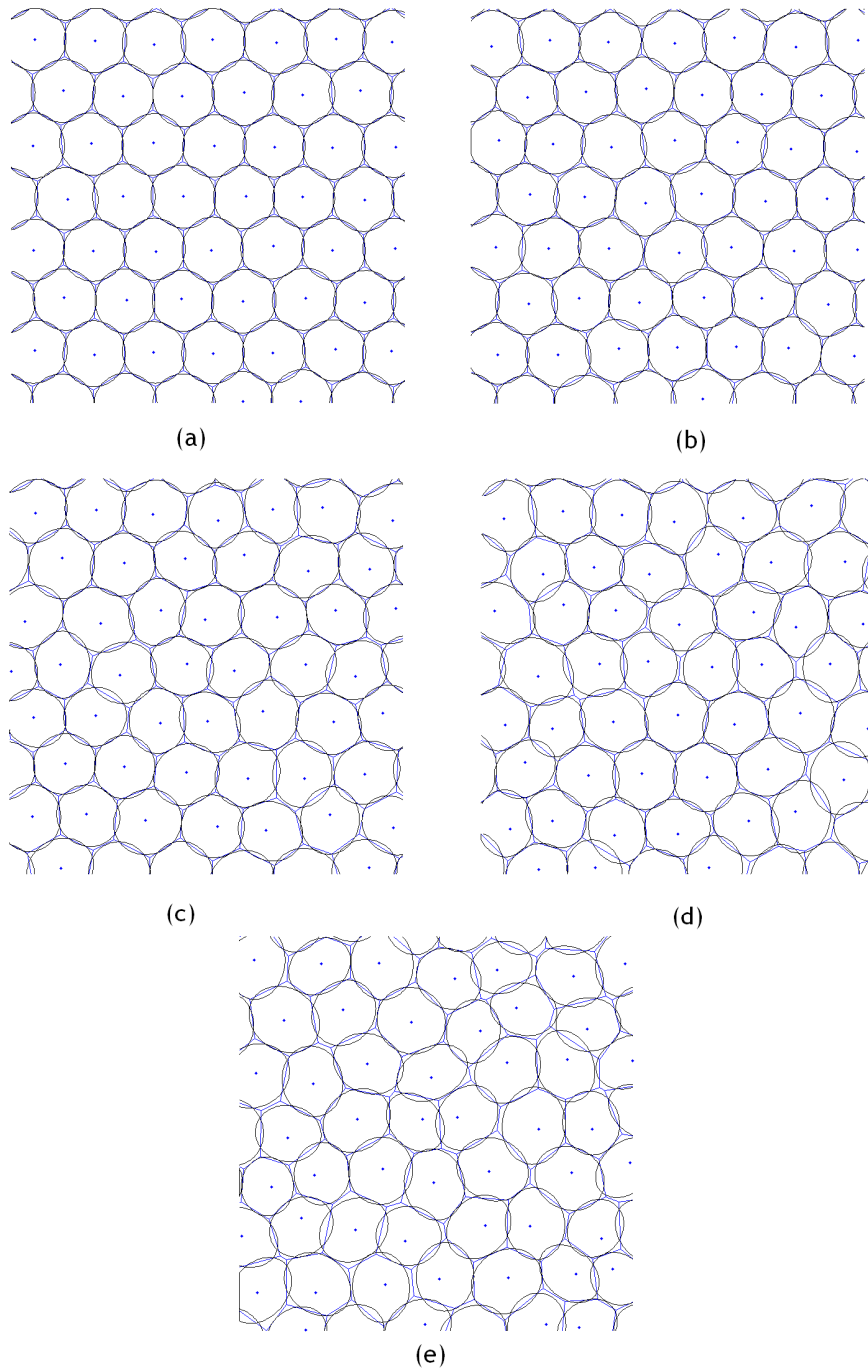


Figure 5-3: An example of RVEs with five different degrees of irregularities: (a) $\alpha=5$, (b) $\alpha=10$, (c) $\alpha=15$, (d) $\alpha=20$, (e) $\alpha=25$. By employing Green's theorem, an ellipse is fitted in each cell (black lines).

To investigate the cellular orientation and poly-dispersity in the undeformed RVEs, a convenient method of visualising the information in a concise and clear way has been devised. Since each individual cell is elongated in the direction of its semi-major axis, the orientation of this axis about the centre of polygon (or equivalent

fitted ellipse) is used to show the overall cellular orientation in a polar graph. Also, to capture the cellular area variations, the area of each individual polygon is multiplied by the sine and cosine of semi-major axis orientation (see Figure 5-4).

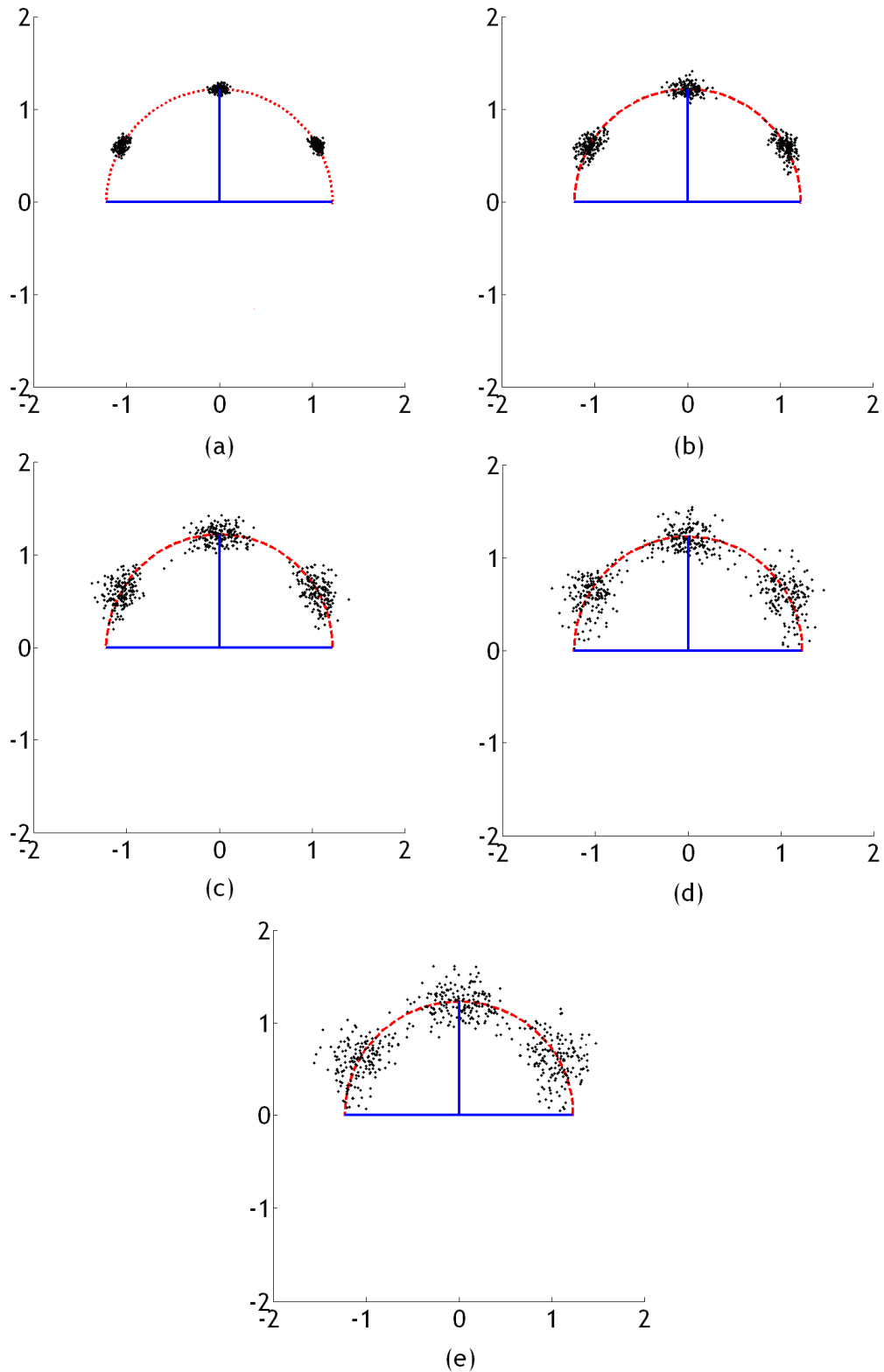


Figure 5-4: Polar representation of cellular orientation multiplied by area of each individual cell (black dots) for microstructures with different degrees of irregularity: (a) $\alpha=5$, (b) $\alpha=10$, (c) $\alpha=15$, (d) $\alpha=20$, (e) $\alpha=25$. The radius of the circle with red dots represents an average value of the data (black dots).

Figure 5-4a, shows that for RVEs with very slight irregularity ($\alpha = 5$) almost all the cells are orientated close to the angles 30° , 90° and 150° . This is to be expected as the structure is close to that of a regular honeycomb structure. The area of the cells is almost constant, i.e. mono-disperse, as indicated by the fact that the points lie close to the red circle. As the degree of irregularity increases from 5 to 25, the data becomes progressively more scattered around those angles and the points (distance from origin indicates area of the cells) shows increasing scatter away from the red circle (radius indicates the average value of cell area), indicating that the cell microstructure becomes progressively more poly-disperse as microstructural irregularity increases. The same cellular orientation and poly-dispersity information, for each degree of irregularity, can be represented using probability histograms, see Figure 5-5 and 5-6. In the following histograms, for the purpose of clarity, the data are represented in 10 'bins'. In each figure the bin width is constant but changes between figures.

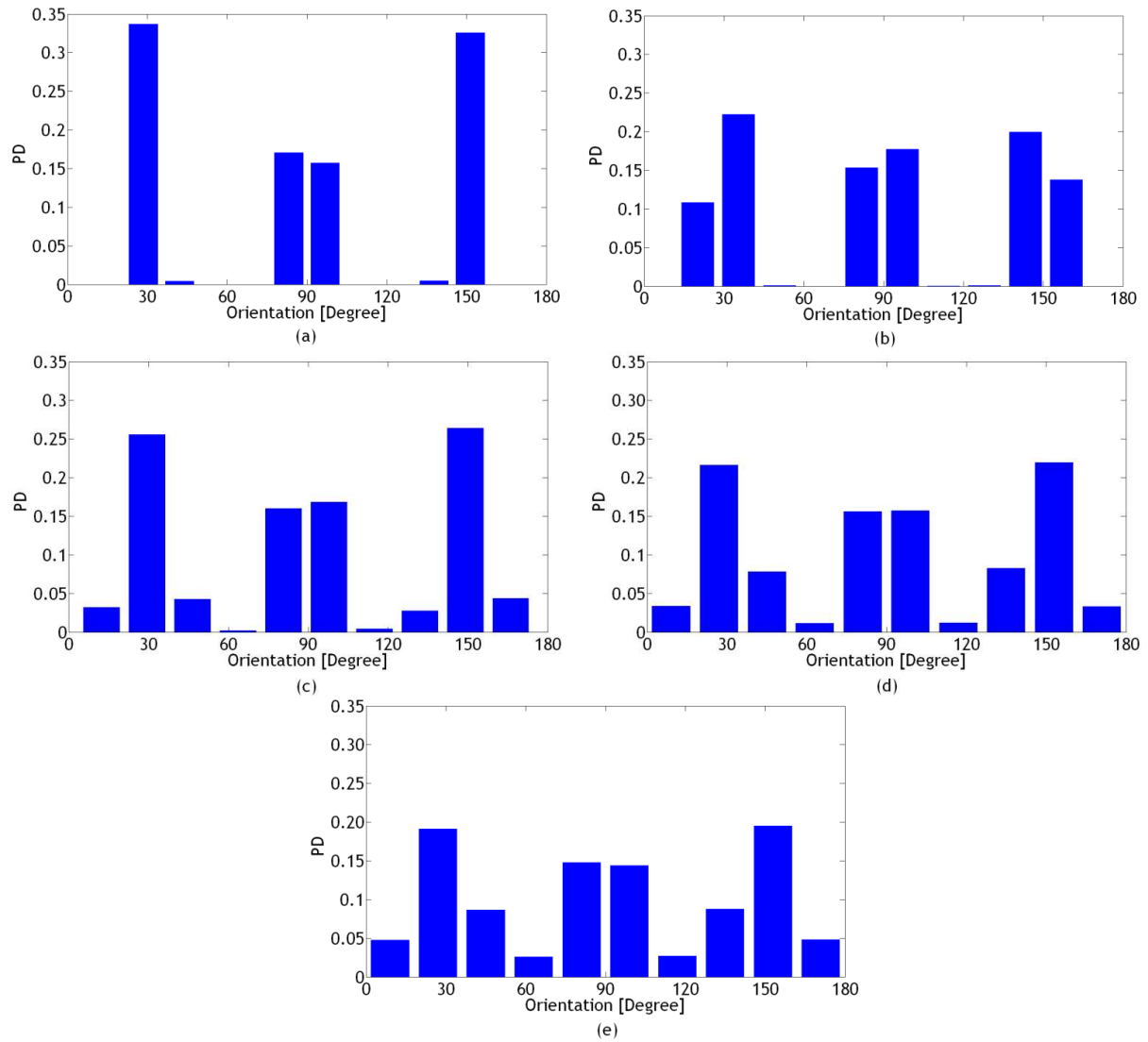


Figure 5-5: Probability distribution of cellular orientation for undeformed state of microstructure and different degrees of irregularity: (a) $\alpha=5$, (b) $\alpha=10$, (c) $\alpha=15$, (d) $\alpha=20$, (e) $\alpha=25$. Each column has almost 10 degree width.

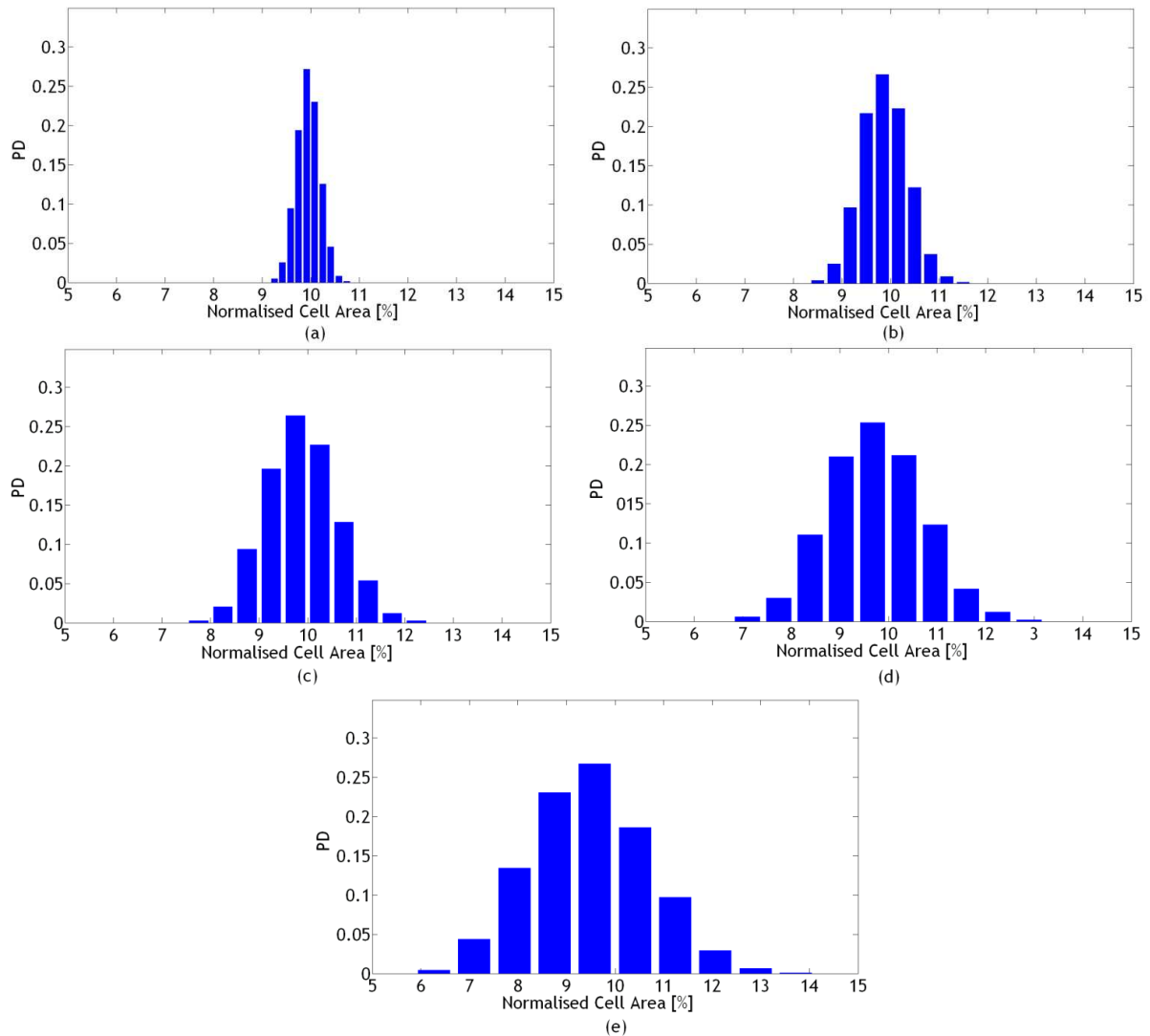


Figure 5-6: Probability distribution for cellular area obtained from procedure explained in Figure 5-8; for different degrees of irregularity: (a) $\alpha=5$, (b) $\alpha=10$, (c) $\alpha=15$, (d) $\alpha=20$, (e) $\alpha=25$.

As discussed in Chapter 4, a realistic and isotropic RVE should have no preferred directional orientation, i.e. in terms of Figures 5-4 and 5-5 there should be no concentration of the points in any particular direction. By increasing the degree of irregularity, α , the cellular orientations tend to become less concentrated in any particular direction and the RVE tends to become more isotropic. This result is in agreement with the mechanical investigation of Chapter 4 and therefore clearly demonstrates the link between cellular and mechanical anisotropy. However, a side effect of generating this isotropy in the RVE is a much more poly-disperse microstructure, see Figures 5-4 and 5-6. For the case with the lowest degree of

irregularity the RVE cells have very similar areas and the probability distribution can be fitted using a normal distribution function. When α increases the band of probability distribution of the normalised cell area increases as well. Thus, if the target morphology of the foam to be modelled is both isotropic and mono-disperse then further modification to the microstructure is required, as demonstrated in Section 4.6 and discussed further in Section 5.3.

The effect of increasing the degree of irregularity, α , on the strut intersection angle, the number of struts within each cell and the normalised strut length are all investigated, results are shown in Figures 5-7, 5-8 and 5-10. The distribution of strut intersection angles and the number of struts within each cell is shown in Figures 5-7 and 5-8, results reveal the majority of cells contain 6 struts and the internal angle is close to 120° , similar to a honeycomb hexagonal structure. As the degree of irregularity increases the distribution of intersection angles becomes much wider, with a slight skew developing towards larger angles. A few cells containing either 5 or 7 struts are also generated, i.e. in addition to the predominantly hexagonal cells a few pentagons and heptagons are generated. Closer visual inspection of several cells produced using a high degree of irregularity often reveals very short strut elements within each cell, these short strut lengths do not exist in 2-d image slices of real mono-disperse foam microstructures (see Figure 4-23).

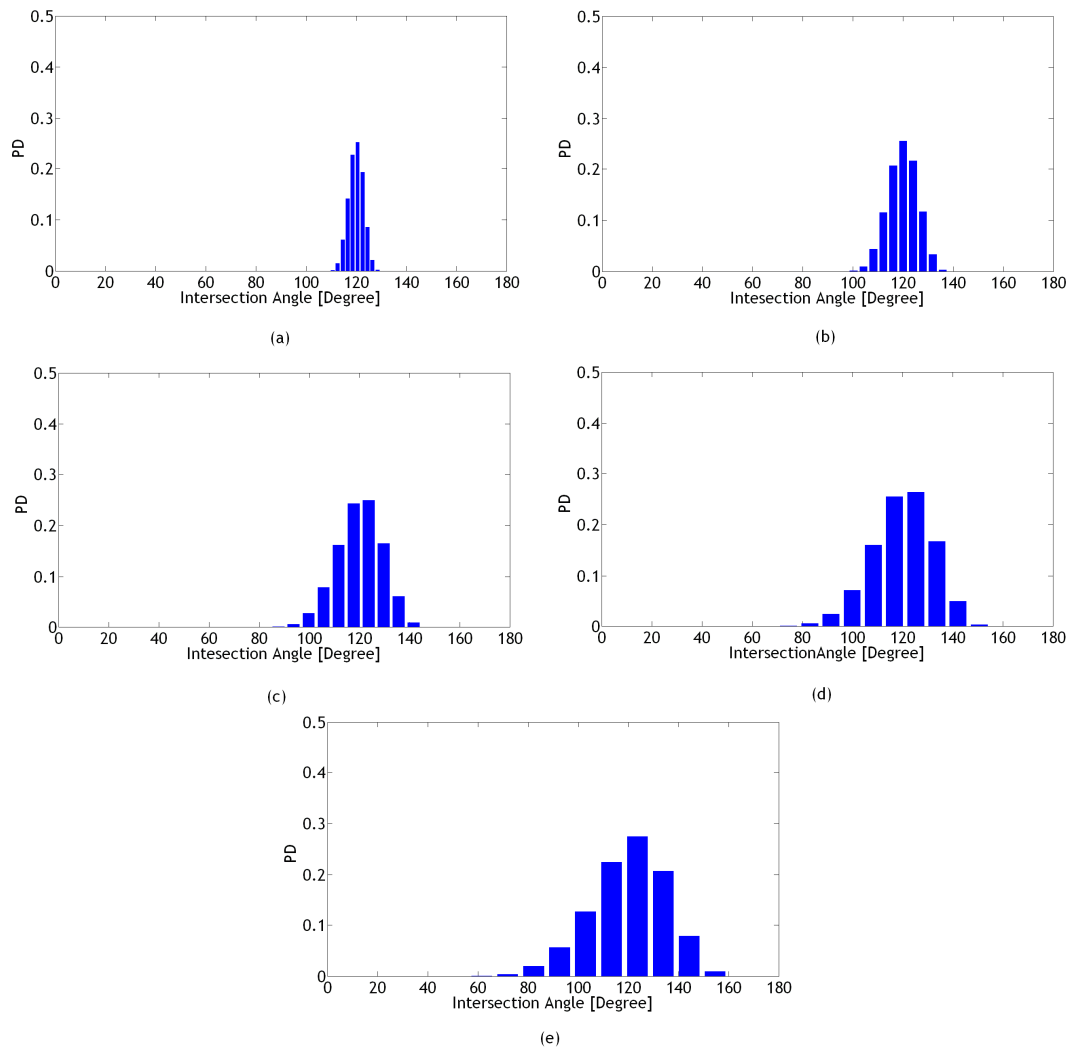


Figure 5-7: Probability distribution for strut intersection angle within each cell for undeformed microstructures using different degrees of irregularity: (a) $\alpha=5$, (b) $\alpha=10$, (c) $\alpha=15$, (d) $\alpha=20$, (e) $\alpha=25$.

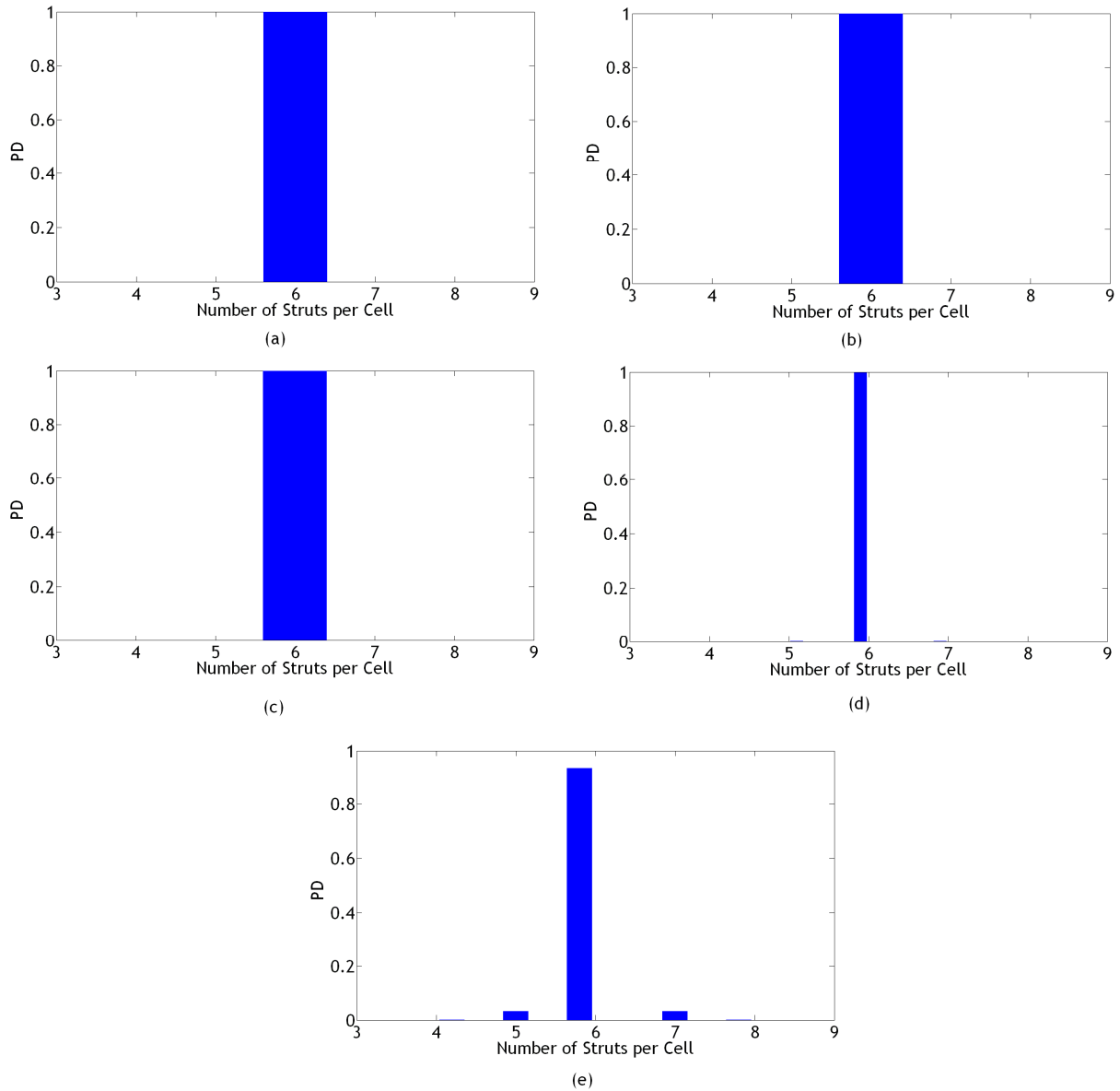


Figure 5-8: Probability distribution for number of struts within each cell for undeformed state of microstructure for different degrees of irregularity: (a) $\alpha=5$, (b) $\alpha=10$, (c) $\alpha=15$, (d) $\alpha=20$, (e) $\alpha=25$.

To understand the distribution of the strut element lengths, probability distribution histograms have been generated using the following procedure:

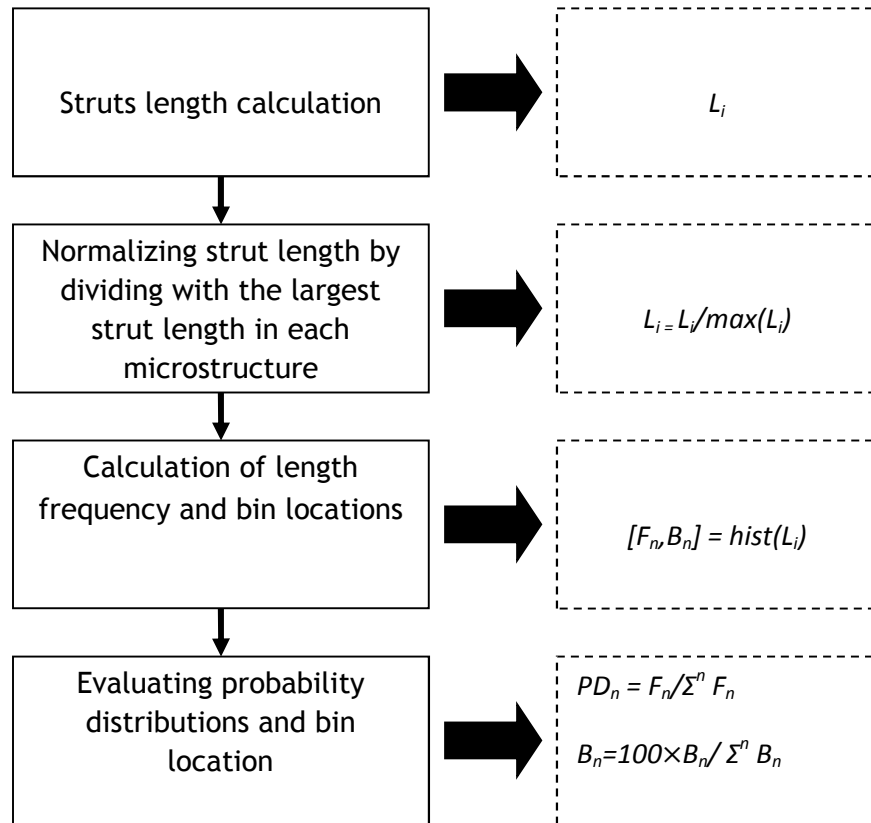


Figure 5-9: Strut length probability distribution procedure. A MATLAB function hist (histogram) is used in this procedure.

Figure 5-10 shows the probability distribution of normalised struts lengths, it can be seen that as α increases the number of very small elements also increases. Thus, when using this technique, i.e. the enhanced method of Zhu described in detail in Section 2.1.2, it can be concluded that increasing α causes the cell shape to deviate away from that of a perfect hexagon and a growing number of very short struts are generated within the microstructure. Referring to Chapter 4, idealising open-cell foam as a beam-based network, is valid for small beam thickness to length ratios ($1/8^{\text{th}}$), therefore increasing the number of small length struts will affect the mechanical response obtained from FE analysis. However, to define the geometrical irregularity of the microstructure, the average cell shape (number of struts per cell) cannot be considered as the primary consideration. For example, as it is possible to have five or six sided polygons with one or two very sharp angles (see Figure 5-2) which have very different geometries compared to regular pentagons or hexagons. Therefore, another dominant factor determining

the degree of irregularity is the strut intersection angle distribution. It should be noted that in the case of real, predominantly mono-disperse foams, the fraction of short struts is very low [Kraynik et al. 2003] (according to Plateau's law - see Section 6.2.1) due to foam relaxation processes. As a result of surface area (energy) minimisation, the majority of short struts vanish, this point will be discussed further in Chapter 6.

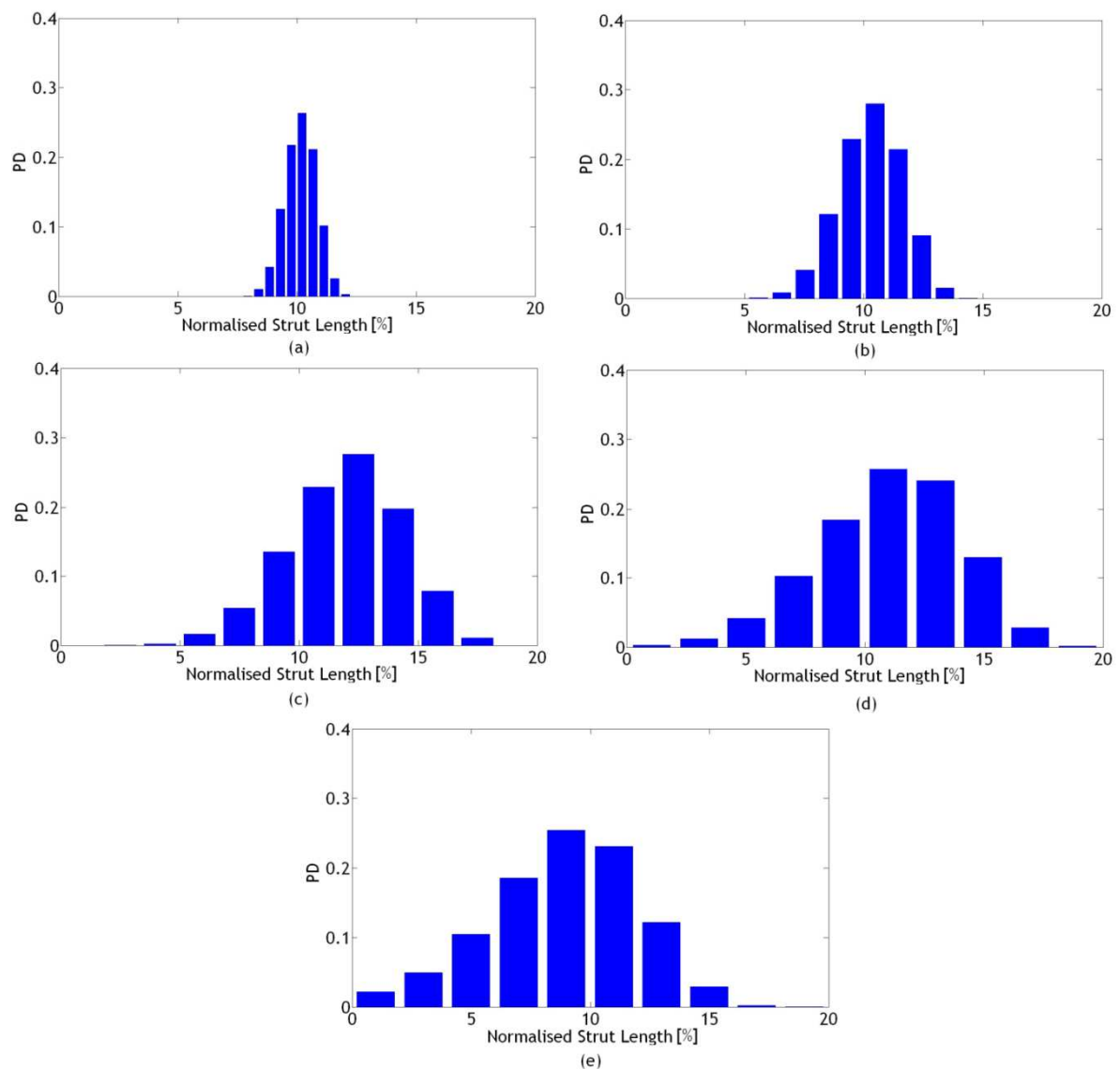


Figure 5-10: Probability distribution for strut length obtained from procedure explained in Figure 5-8; for different degrees of irregularity: (a) $\alpha=5$, (b) $\alpha=10$, (c) $\alpha=15$, (d) $\alpha=20$, (e) $\alpha=25$.

5.3.3 Morphological Analysis of RVEs Generated using a combination of the Enhanced Method of Zhu and the Lloyd's Relaxation Algorithm

In Section 4.6 it was shown how the Lloyd's relaxation algorithm can be used to alter the microstructure generated using the enhanced method of Zhu, effectively creating an RVE with a much more isotropic mechanical response. Here, over 50 RVEs, each containing 550 cells generated using the enhanced method of Zhu have been altered by employing the Lloyd's relaxation algorithm. The same analysis methods described in Section 5.3.2 and 5.3.3 are used to characterise the resulting relaxed RVE microstructural morphology. Figure 5-11 shows a relaxed RVE generated by first employing the enhanced Zhu method with a degree of irregularity of 25, followed by application of the Lloyds relaxation algorithm. Figure 5-12 shows the cellular orientation and area distribution.

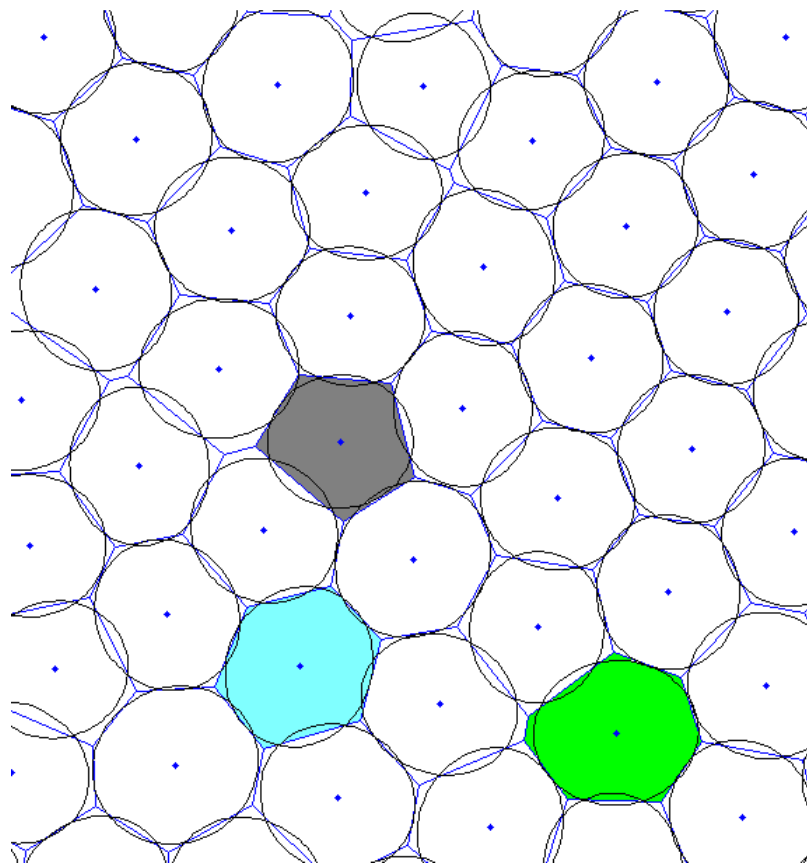


Figure 5-11: An example of structure generated by Lloyd's algorithm. By employing Green's theorem, an ellipse is fitted in each cell (black lines). Example pentagonal (grey colour), hexagonal (light blue colour) and heptagonal (light green colour) cells are highlighted in the figure.

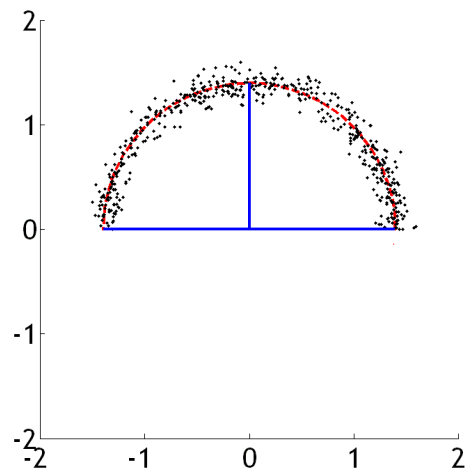


Figure 5-12: Polar representation of cellular orientation multiplied by area of each individual cell (black dots) for microstructures generated by Lloyd's relaxation. The radius of the circle with red dots represents an average value of data (black dots).

Figure 5-13 is a direct comparison of two examples of the initial and relaxed RVE microstructures.

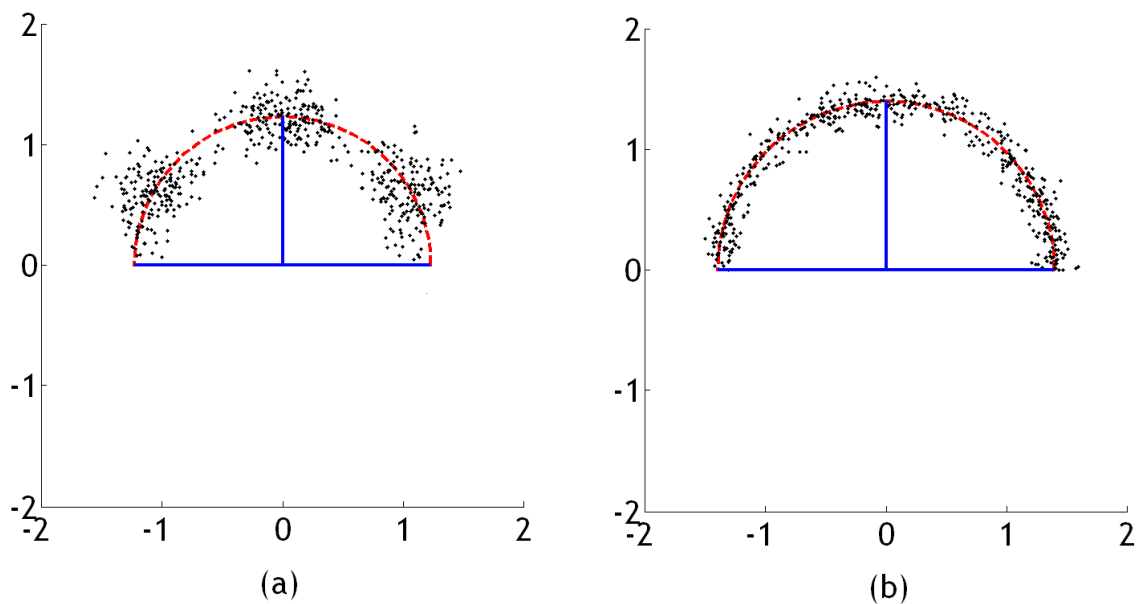


Figure 5-13: Cellular orientation of microstructure: (a) before Lloyd's relaxation (b) after Lloyd's relaxation.

Notably, it is difficult to see any obvious difference in the two RVE microstructures when comparing the RVEs by eye. However, comparison between Figures 5-4e and 5-12 clearly reveals a significant difference between the two structures before and after application of the Lloyds algorithm. Thus the latter appears to show good potential to generate Voronoi-based RVEs with cell orientations completely randomised, while keeping the cell area distribution width extremely low. As in Section 5.3.3, the same information can be represented as probability density distribution histograms, see Figures 5-14 and 5-15.

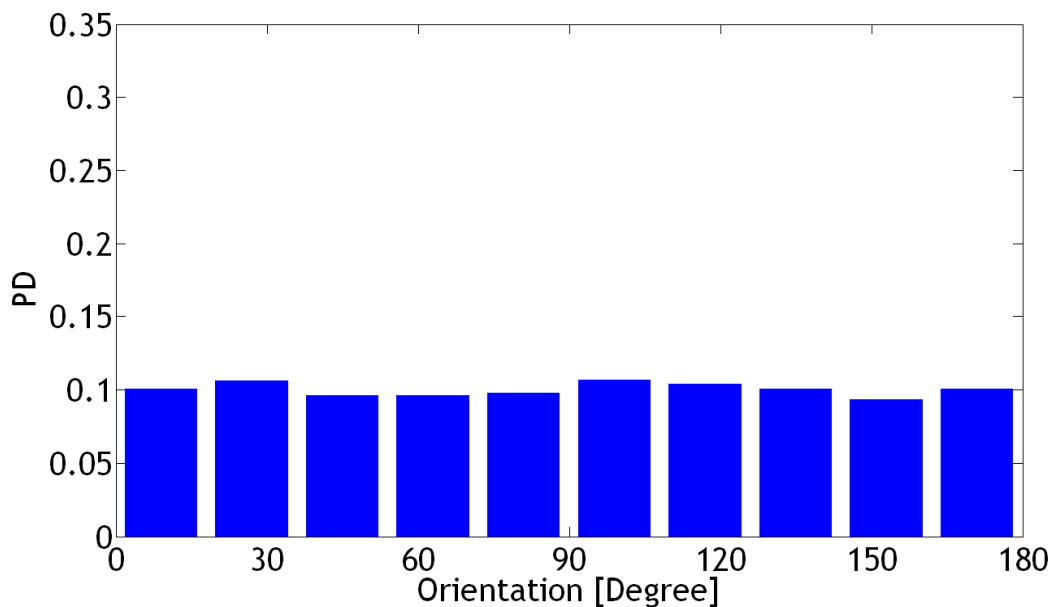


Figure 5-14: Probability distribution of cellular orientation for undeformed state of microstructure generated using Lloyd's algorithm.

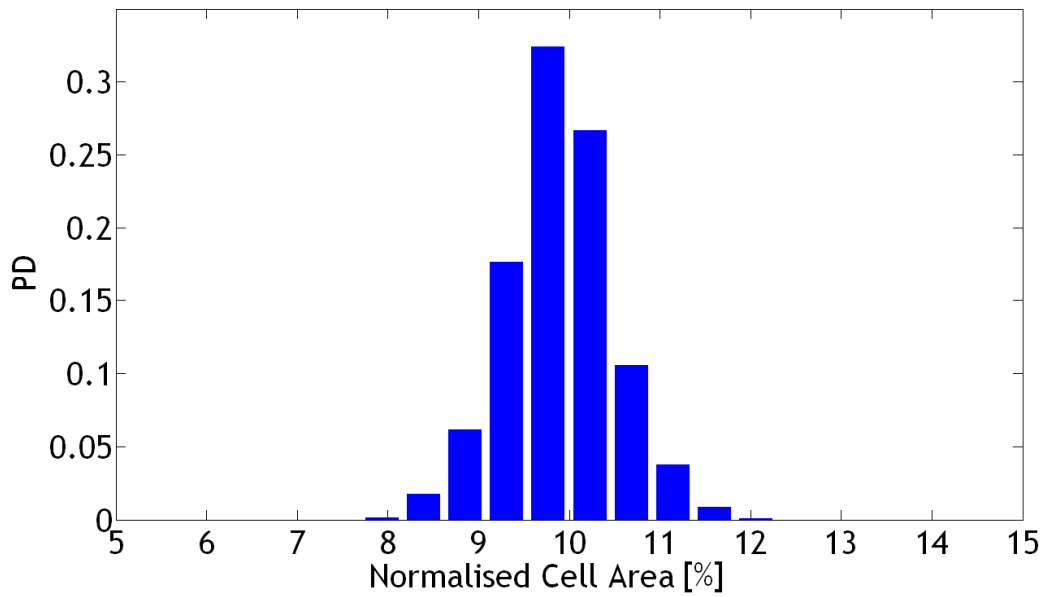


Figure 5-15: Probability distribution for cellular area obtained from procedure explained in Figure 5-9, using Lloyd's relaxation algorithm.

The probability distribution histograms of strut intersection angle and strut length distributions are also given in Figures 5-16 and 5-17. They indicate that the majority of cells have internal angles close to 120° .

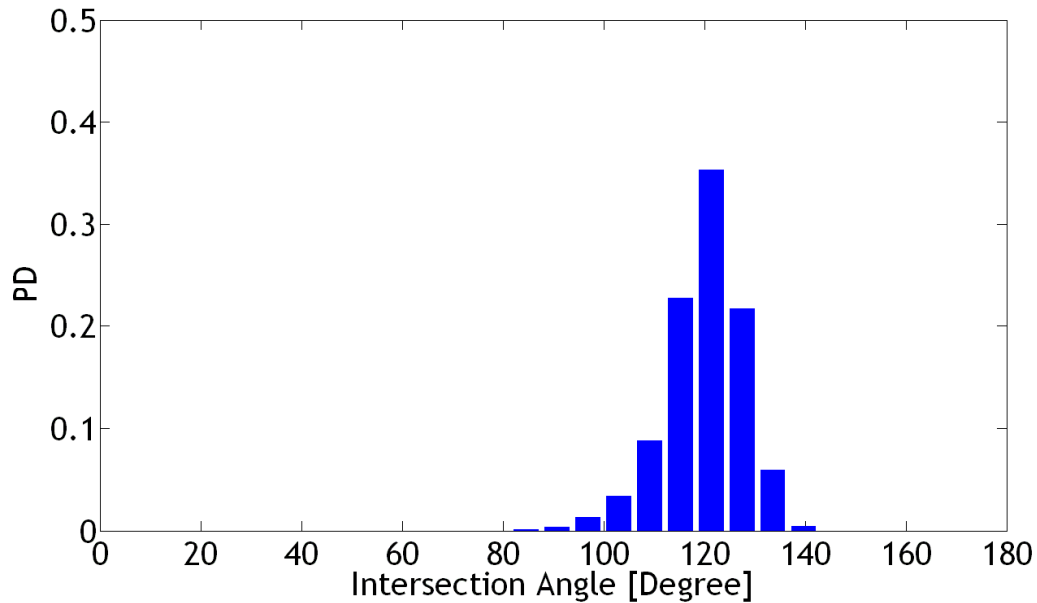


Figure 5-16: Probability distribution for struts intersection angle within each cell for undeformed state of microstructure generated using Lloyd's relaxation algorithm.

However, unlike RVEs generated using the enhanced method of Zhu alone, the number of cells that have internal angles close to 120° (two struts that make with intersection angle close to 120° inside each cell) is larger through considering PD peaks (less than 0.3 for modified Zhu method and near 0.4 for Lloyd's algorithm) at Figures 5-7 and 5-16. By comparing Figures 5-10e and 5-17, it can be seen that the Lloyd's relaxation algorithm generates RVE microstructures with less short struts, compared to the modified method of Zhu.

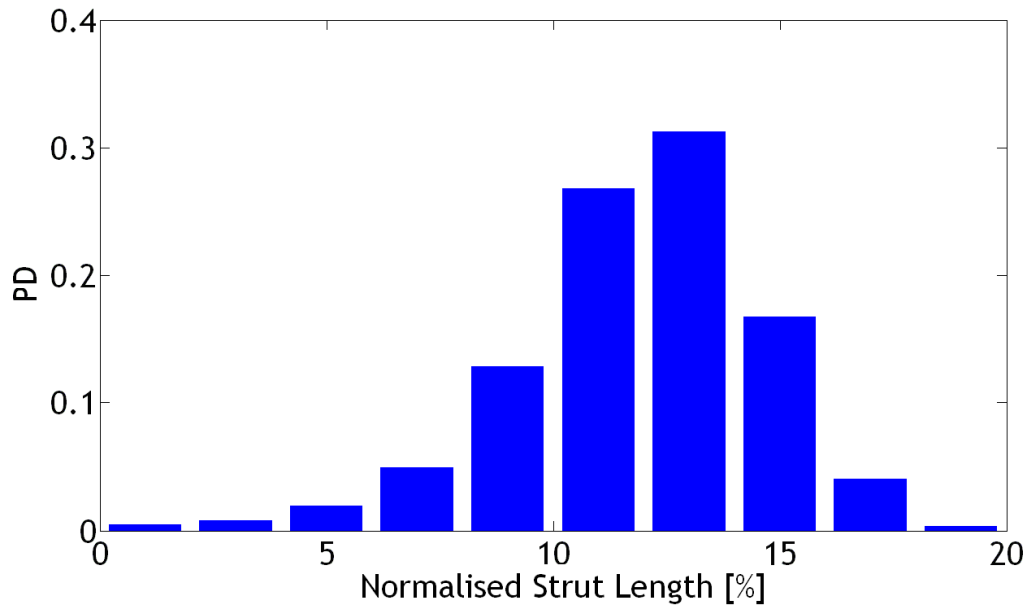


Figure 5-17: Probability distribution for struts length obtained from procedure explained in Figure 5-9, using Lloyd's relaxation algorithm.

Visual inspection of several RVEs generated using the Lloyd's relaxation algorithm, shows that a considerable numbers of pentagonal and heptagonal cells have been generated without small elements. The increased proportion of such cells is also indicated in Figure 5-18.

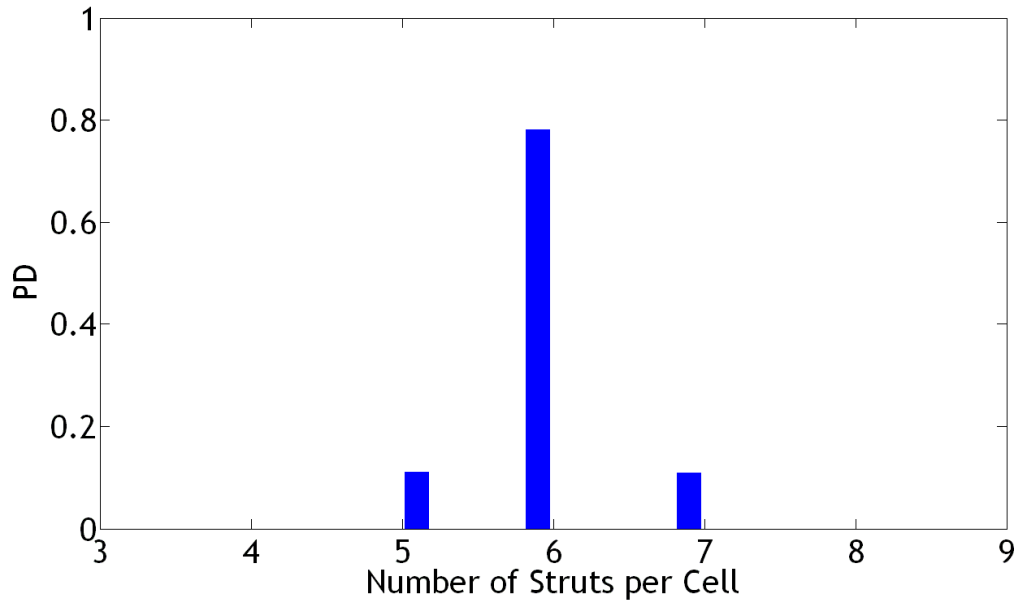


Figure 5-18: Probability distribution for number of struts within each cell for undeformed state of microstructure generated using Lloyd's algorithm.

5.3.4 Analysis of the Microstructural Morphology generated using the Drop and Roll method

In Sections 5.3.2 to 5.3.3 it was shown that morphologically mono-disperse and isotropic RVEs could be generated using a combination of the enhanced method of Zhu and the Lloyd's relaxation algorithm. In this section, similar morphological analysis methods are used to characterise the RVE microstructures created using an alternative microstructure generation algorithm; the Drop and Roll method (see Section 2.1.3). This alternative method can generate isotropic RVEs while also producing a high degree of poly-dispersity within the RVE microstructure. Using this method RVEs with four different degrees of poly-dispersity have been generated, see Figure 5-19.

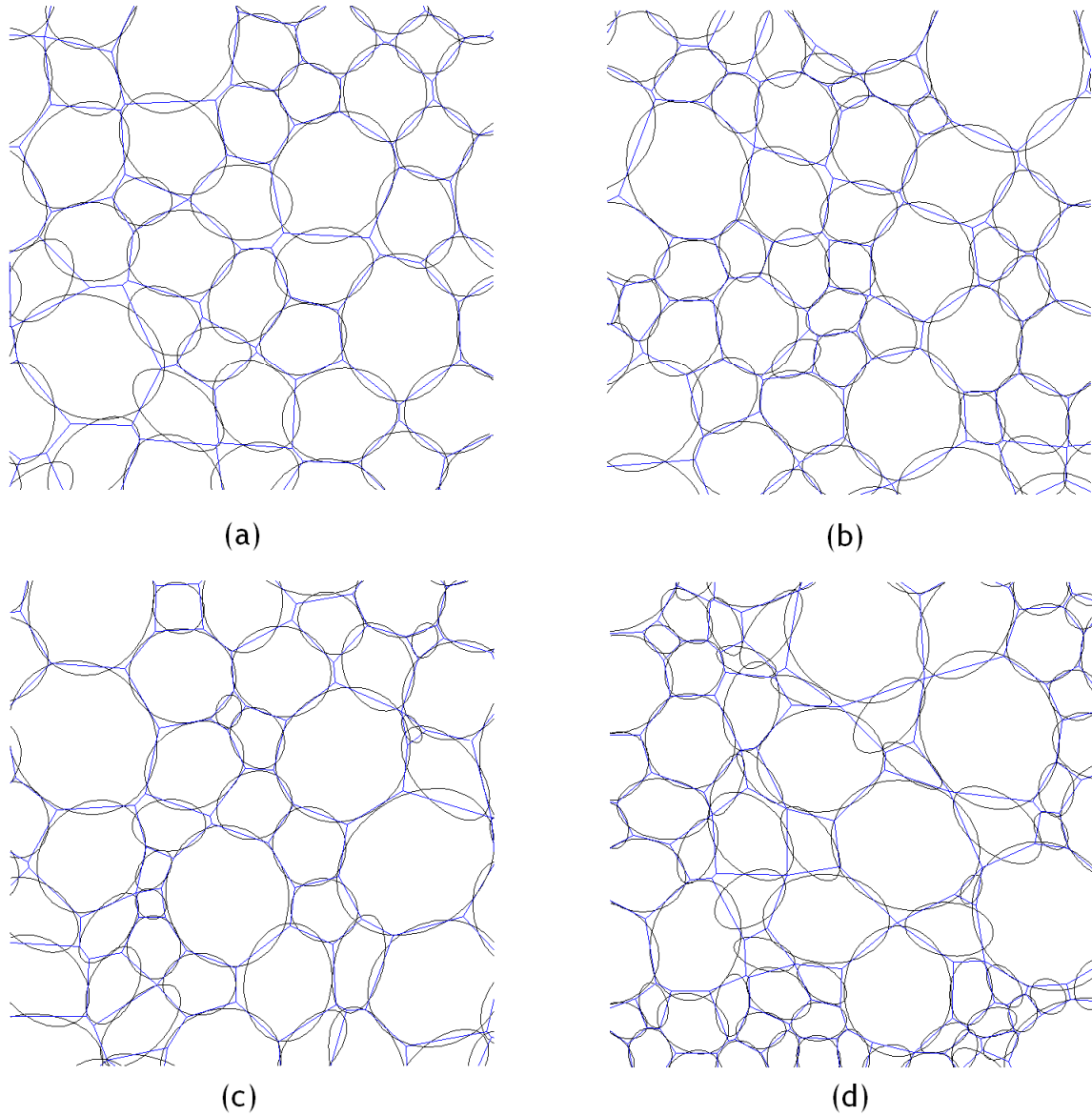


Figure 5-19: An example of RVEs with four different degrees of poly-dispersity: (a) $\gamma=0.05$, (b) $\gamma=0.10$, (c) $\gamma=0.15$, (d) $\gamma=0.20$. By employing Green's theorem, an ellipse is fitted in each cell (black lines). For each case 50 RVEs are generated, each containing 550 cells (on average).

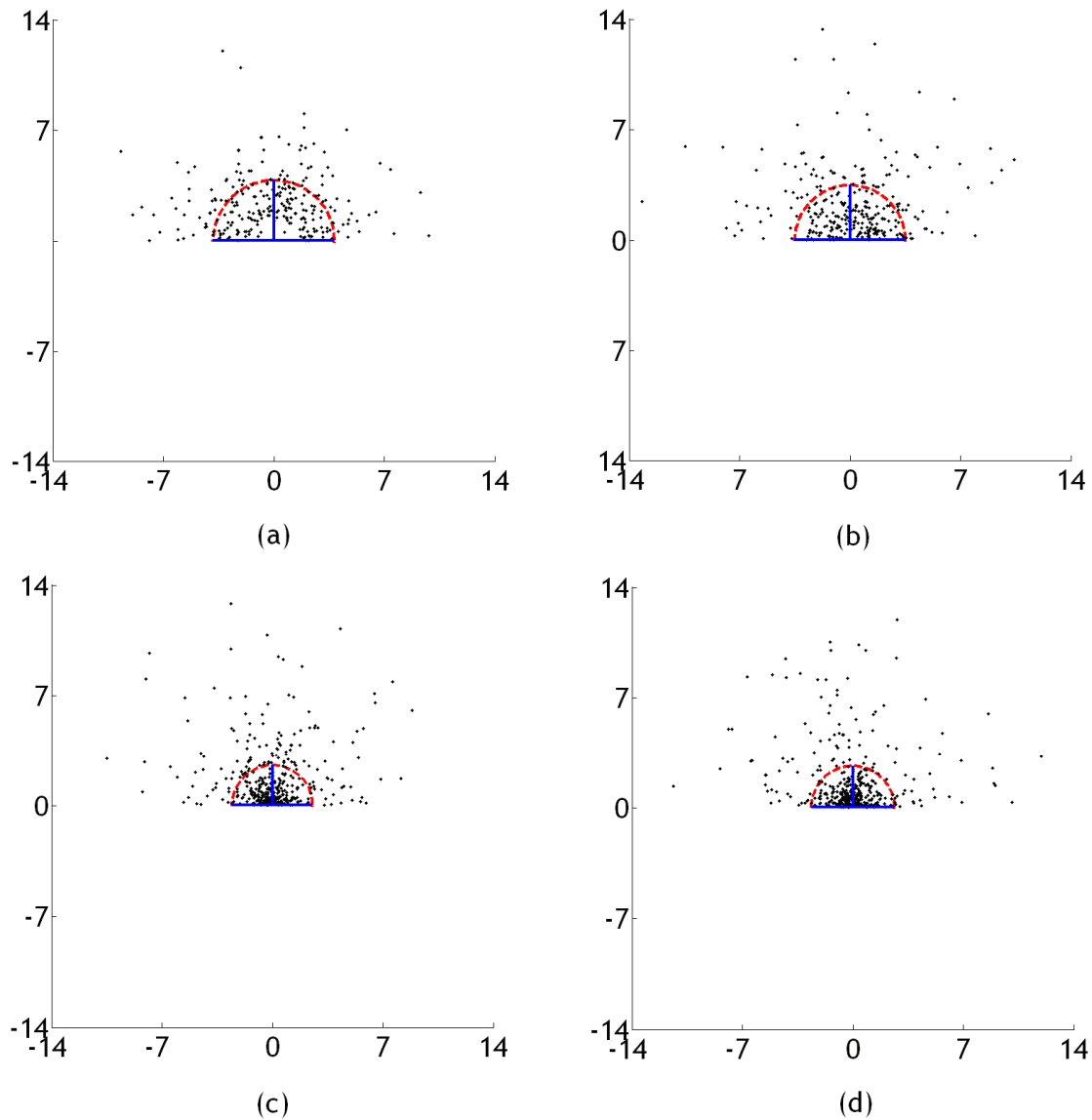


Figure 5-20: Polar representation of cellular orientation multiplied by area of each individual cell (black dots) for microstructures with different degrees of polydispersity: (a) $\gamma=0.05$, (b) $\gamma=0.10$, (c) $\gamma=0.15$, (d) $\gamma=0.20$. The radius of the circle with red dots represents an average value of data (black dots).

As discussed in Chapter 3, the most efficient way to produce a hard disk seeding for a poly-disperse foam-like microstructure is by using log-normal [Evans et al. 1993] or gamma [Cody, 1976] distributions to randomly generate hard disk radii and then use the modified Drop and Roll technique to efficiently pack the disks within a minimum area (by shooting the discs from randomised orthogonal directions). In this investigation a log-normal distribution has been applied, the resulting distribution of cell orientations and areas are shown in Figure 5-20. The

cell orientation shows no obvious preferred direction for all cases and the cell areas are highly variable, the scatter increases with increasing γ , i.e. the poly-dispersity is increases with increasing γ .

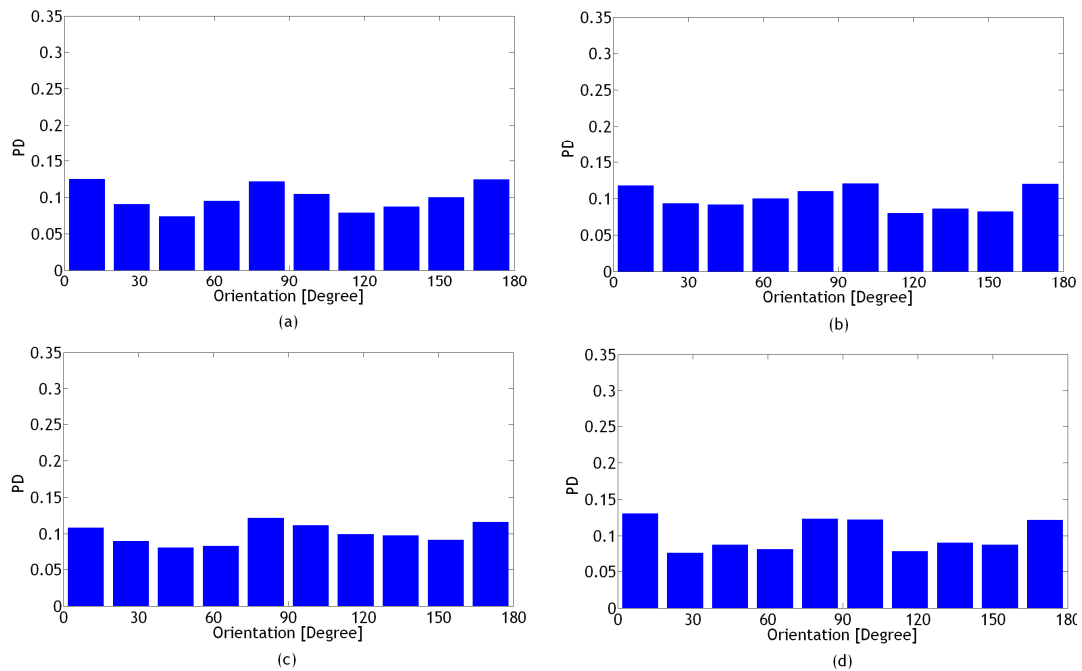


Figure 5-21: Probability distribution of cellular orientation for undeformed state of microstructure with different degrees of poly-dispersity: (a) $\gamma=5$, (b) $\gamma=10$, (c) $\gamma=15$, (d) $\gamma=20$.

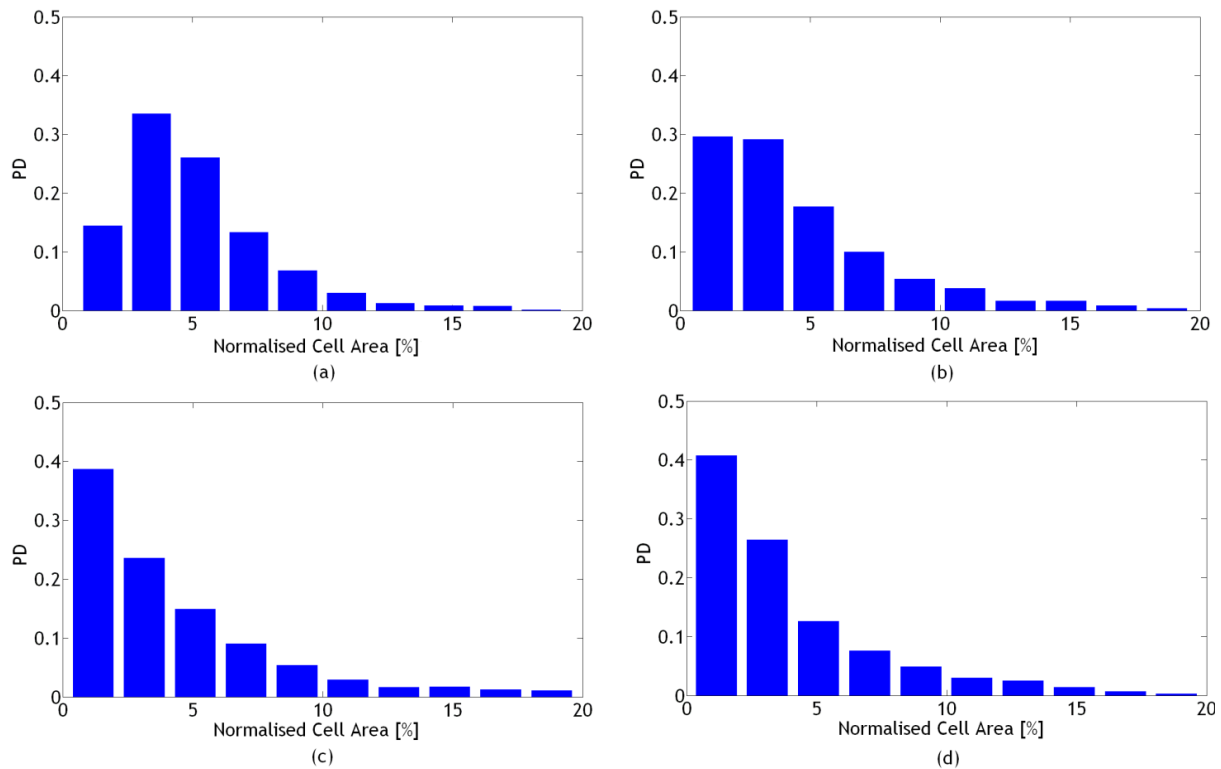


Figure 5-22: Probability distribution for cellular area obtained from procedure explained in Figure 5-9 for different degrees of poly-dispersity: (a) $\gamma=5$, (b) $\gamma=10$, (c) $\gamma=15$, (d) $\gamma=20$.

Again, the same information can be plotted in probability distribution histograms, see Figures 5-21 and 5-22. The cells are fairly randomly orientated. However, due to a limitation in generating 2-d periodic microstructures using the Drop and Roll method (as explained in Section 3.3), there is always some small boundary effect on the RVE. Since hard disks are only allowed to enter perpendicularly or transversely into the RVE box when generating the seeding, this induces a boundary effect that can be noticed in Figure 5-21. Slight peaks in the probability distribution occur at 0° , 90° and 180° i.e. perpendicular to the boundaries of the RVE. Nevertheless, as shown in Section 4.7, this boundary effect becomes less significant with an increasing number of cells within the RVE and is negligible for RVEs containing over 500 cells. In this case the mechanical behaviour was shown to be almost completely isotropic (see Figure 4.29). Figure 5-22 shows that the shape of the distribution of cell areas is very different to that shown in Figure 5-6 and can be well fitted using a log-normal distribution. This is to be expected given that the same type of function was used to generate the seeding discs using the Drop

and Roll method. As γ increases, the probability of generating smaller cells is seen to increase. This can also be seen in Figure 5-20 which shows a denser clustering of points within the red circle at higher values of γ and a shrinking of the radius of the circle.

Turning again to analysis of the strut intersection angle, strut number and strut length distributions reveals a very different morphology to the RVEs generated using either the enhanced method of Zhu and the combined Zhu/Lloyds approach. Figure 5-23 shows a relatively skewed distribution of intersection angles (compare with Figure 5-7) with a longer tail of the distribution towards smaller intersection angles. The majority of cells have hexagonal and pentagonal shapes due to the presence of 6 and 5 struts in each cell (see Figure 5-24). However, there is now a much more significant number of cells containing a different number of struts, i.e. the number of quadrilateral, pentagonal, heptagonal and octagonal cells is significant, especially for cases with higher degrees of poly-dispersity, γ . Visual inspection of several microstructures with different γ and also the probability distribution histograms of strut length (Figure 5-25) reveals a significant number of short struts within almost all types of cell, but particularly in quadrilateral cells.

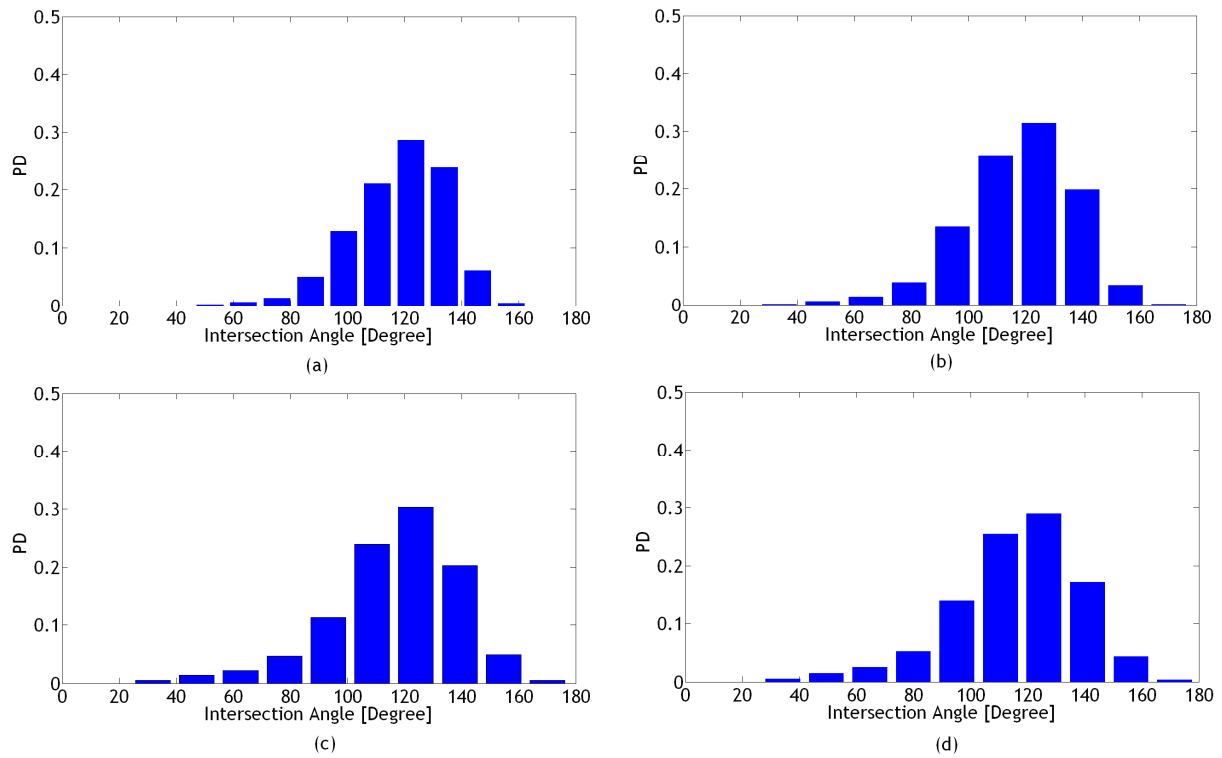


Figure 5-23: Probability distribution of struts intersection angles in undeformed state and with different degrees of poly-dispersity: (a) $\gamma=5$, (b) $\gamma=10$, (c) $\gamma=15$, (d) $\gamma=20$.

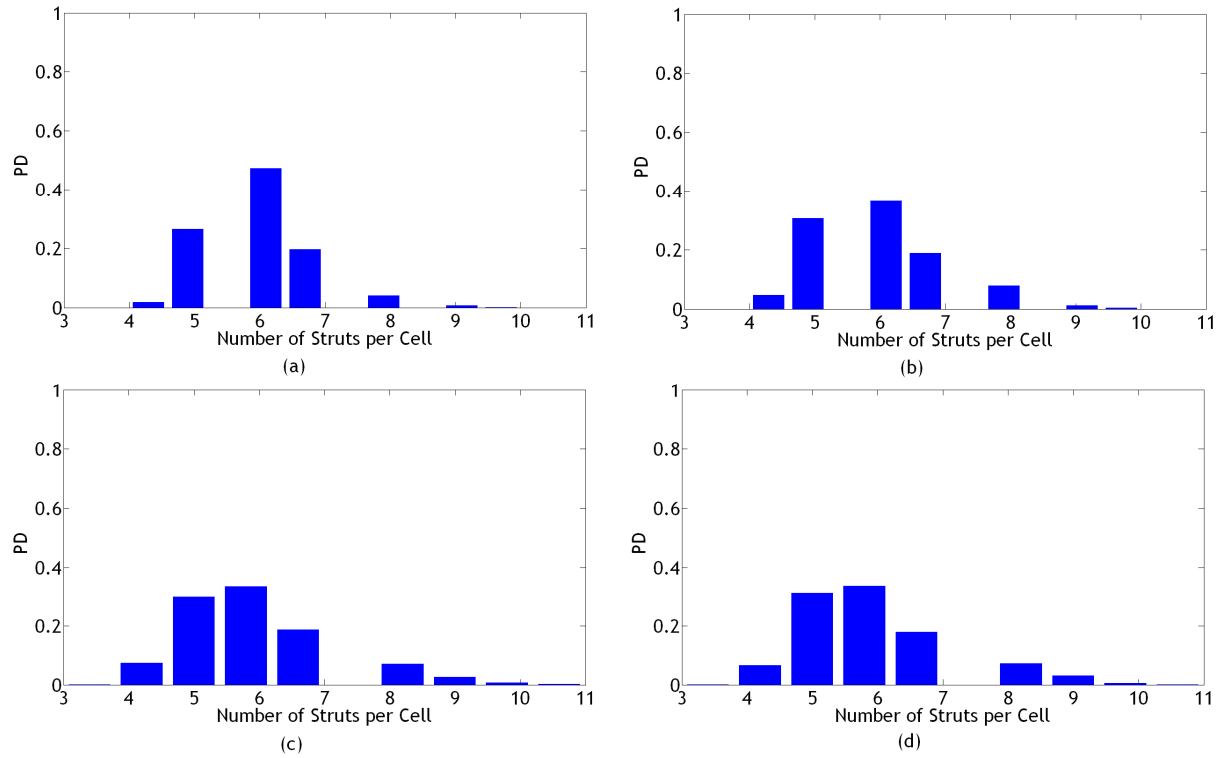


Figure 5-24: Probability distribution of number of struts within each cell in undeformed state and with different degrees of poly-dispersity: (a) $\gamma=5$, (b) $\gamma=10$, (c) $\gamma=15$, (d) $\gamma=20$.

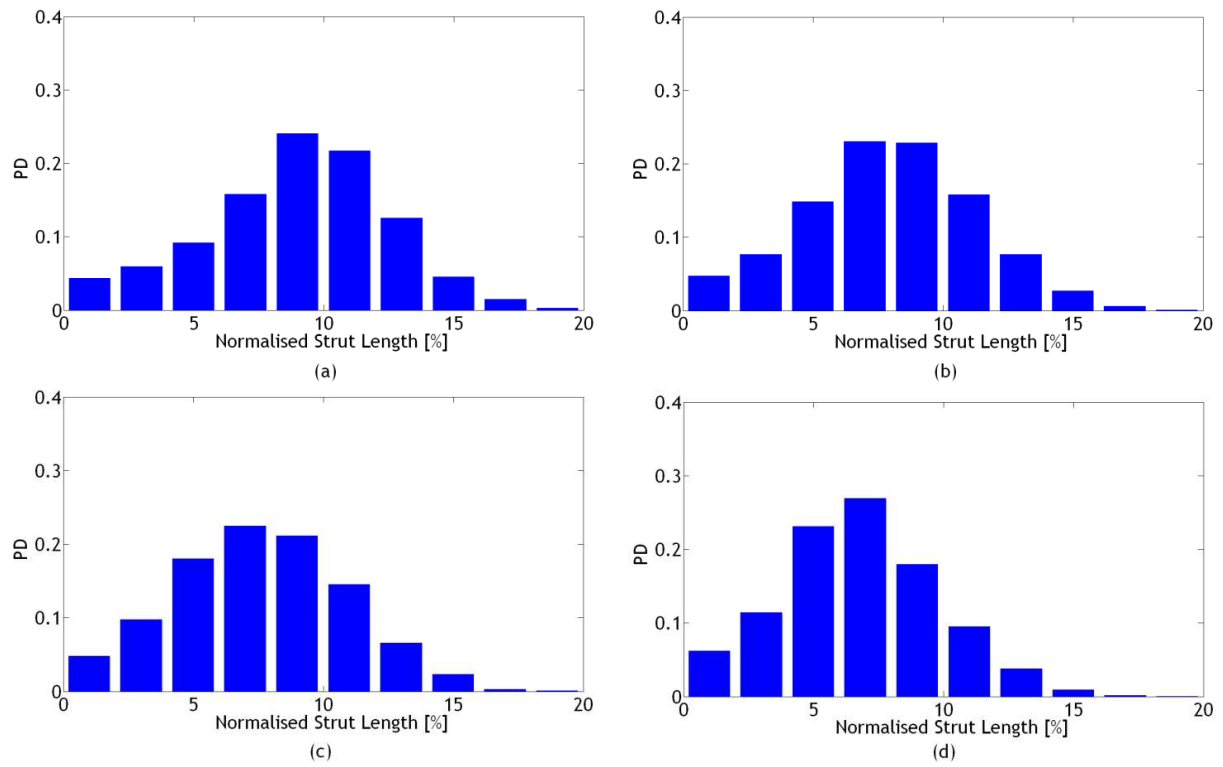


Figure 5-25: Probability distribution for struts length obtained from procedure explained in Figure 5-9 for different degrees of polydispersity: (a) $\gamma=5$, (b) $\gamma=10$, (c) $\gamma=15$, (d) $\gamma=20$.

It is also worth noting that some of the cells are of unusual and perhaps unrealistic shape, e.g. triangles or containing very sharp angles (usually less than 90°). These are due to use of the Apollonius method involved in conducting the Laguerre-Voronoi RVE generation using hard disks. Although the number of these unusual and unrealistic geometries is small, in Chapter 7 an attempt to further reduce their presence is described.

5.4 Active Morphological Characterisation of 2-d Beam-Based RVEs

In Section 5.2, 2-d beam-based microstructures of mono- and poly-disperse RVEs were characterised. Important morphological information such as distribution of cell orientation and area, strut intersection angle, strut length and the number of struts per cell were all considered. All the RVEs considered in Section 5.3 were analysed in the undeformed state. The aim of current section is to study the in-situ deformation (i.e. activated RVE geometry) of 2-d foam-like microstructural RVEs under uniaxial compression, while imposing a PBC. Based on the results of Section 5.3, RVEs generated using the Lloyd's relaxation algorithm and the Drop and Roll method have been used, i.e. isotropic mono- and poly-disperse RVE microstructures. By using morphologically and mechanically isotropic RVEs the subsequent morphological/mechanical investigation should be independent of the applied loading direction. Due to the importance of the plateau region when designing products for protective and cushioning applications, compressive strains of up to 40% have been considered, i.e. well beyond the likely elastic yield strain of the foam. It should also be noted that the contact strain (see Section 3.2.5) for mono-disperse RVEs was determined to be around 0.5 (see Figure 3-14) whereas for poly-disperse RVEs the contact strain was determined to be around 0.35 (see Figure 3-13). Therefore, it is convenient to use beam elements to analyse RVE generated using Lloyd's relaxation algorithm where in the case of polydisperse RVE due to initiation of contact, the shell-based modelling is employed.

5.4.1 Morphological Evaluation of Mono-disperse Beam-Based RVE under Compressive Loading

Over 50 beam-based RVEs, each containing more than 500 cells, have been generated using the Lloyd's relaxation algorithm. As each RVE contains over 500 cells it is assumed that there is no requirement to consider larger RVE sizes (i.e.

size effects are negligible at such large RVE size - see Chapter 3). Since the contact strain of mono-disperse RVEs is around 0.5, the effect of self-contact within the RVE should be negligible. For this reason, the Abaqus Dynamic Implicit solver has been used (self-contact is not modelled). To characterise the evolution of microstructure morphology during deformation, probability distributions of the cellular orientation and area have been computed at different stages of compression, see Figure 5-26 and 5-27. The rate of change data of cell area are obtained in a similar fashion as Figure 5-9 based on ratio of each cell area in its deformed and undeformed states.

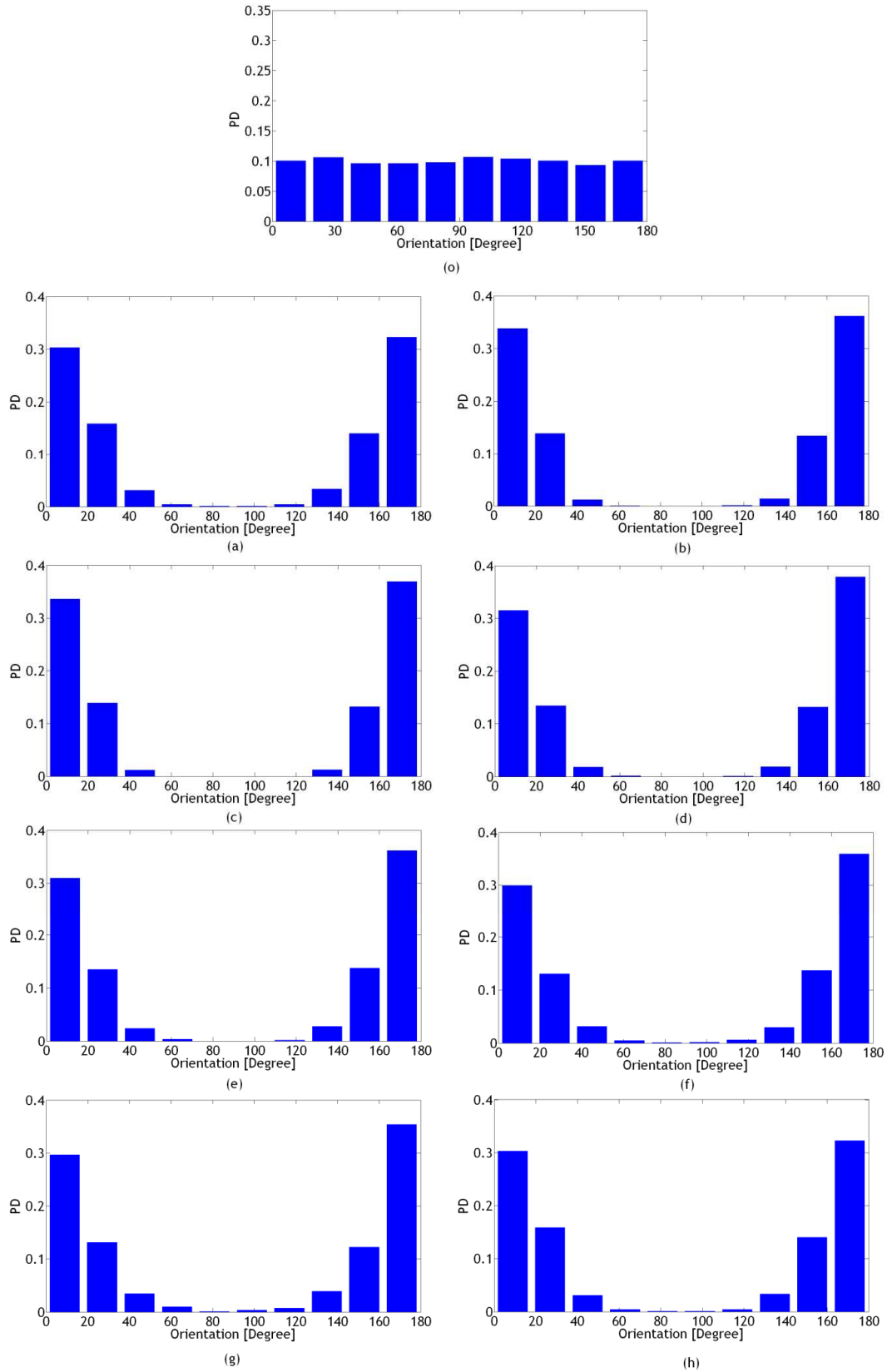


Figure 5-26: Probability distribution for cellular orientations evaluated in different compressive strains: (o) $\varepsilon=0.00$ (a) $\varepsilon=0.05$ (b) $\varepsilon=0.10$ (c) $\varepsilon=0.15$ (d) $\varepsilon=0.20$ (e) $\varepsilon=0.25$ (f) $\varepsilon=0.30$ (g) $\varepsilon=0.35$ (h) $\varepsilon=0.40$.

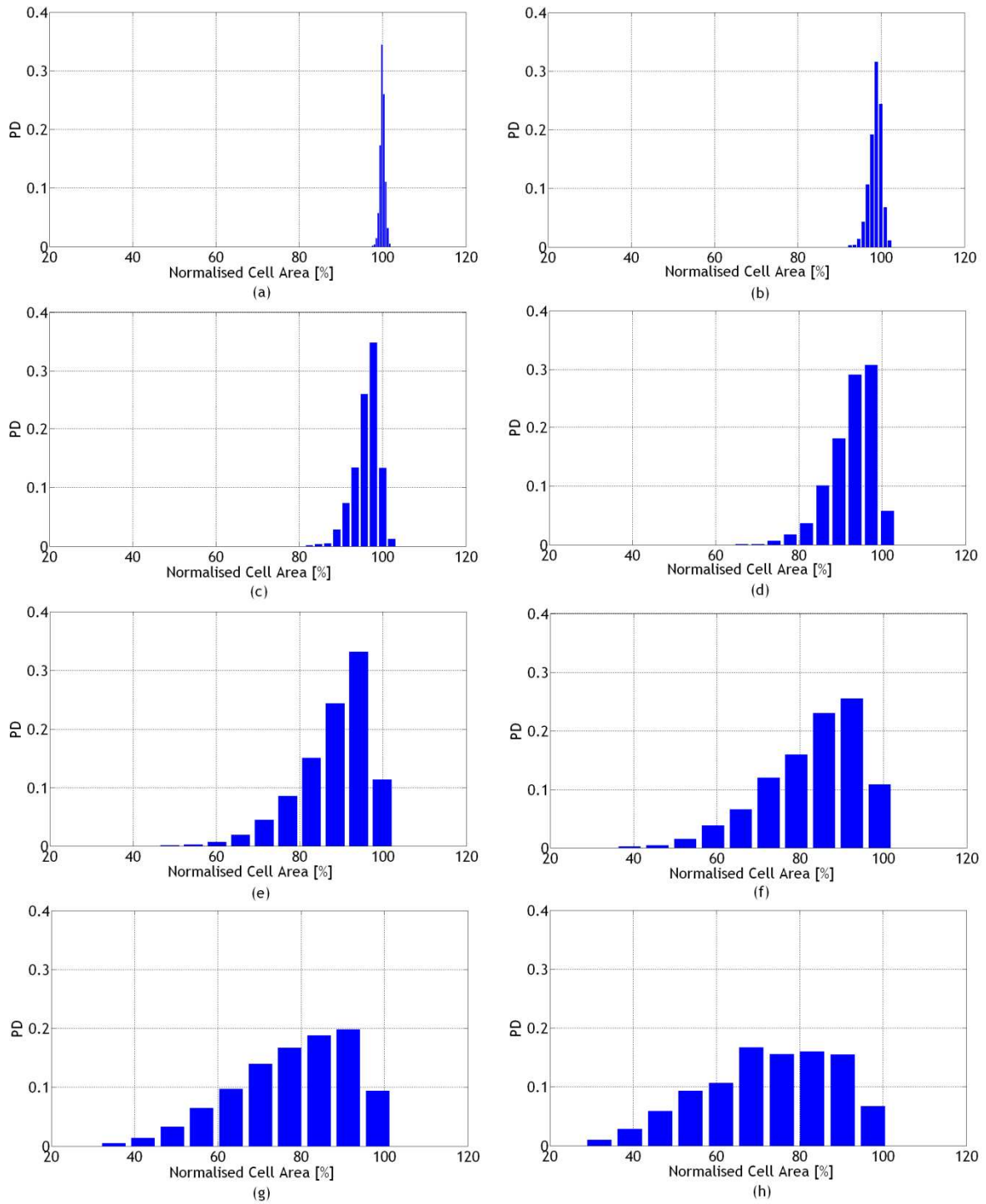


Figure 5-27: Probability distribution for cellular area evaluated in different compressive strains: (a) $\varepsilon=0.05$ (b) $\varepsilon=0.10$ (c) $\varepsilon=0.15$ (d) $\varepsilon=0.20$ (e) $\varepsilon=0.25$ (f) $\varepsilon=0.30$ (g) $\varepsilon=0.35$ (h) $\varepsilon=0.40$.

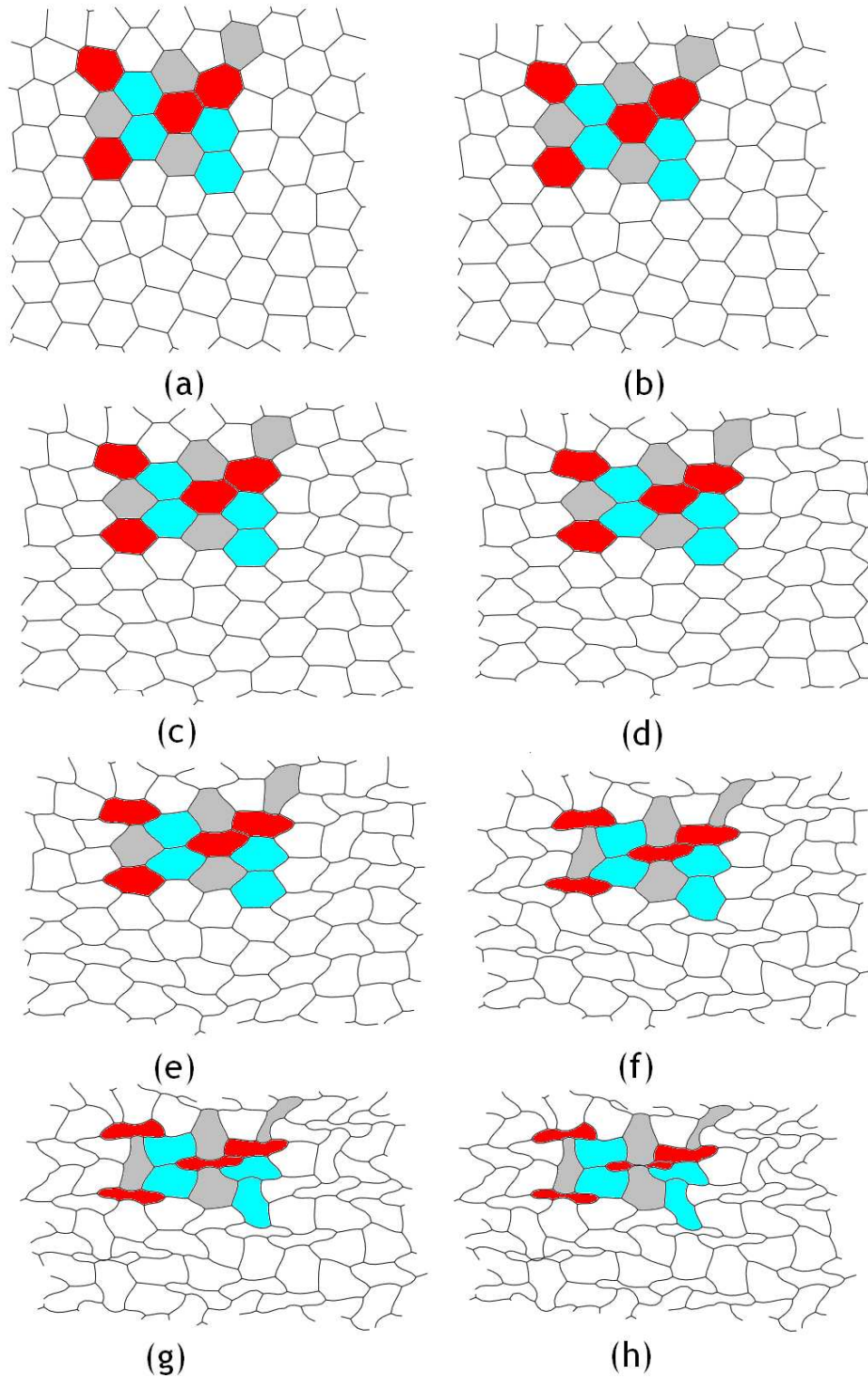


Figure 5-28: Illustrative example of visual inspection of deformed cellular structures evaluated in different compressive strains: (a) $\epsilon=0.05$ (b) $\epsilon=0.10$ (c) $\epsilon=0.15$ (d) $\epsilon=0.20$ (e) $\epsilon=0.25$ (f) $\epsilon=0.30$ (g) $\epsilon=0.35$ (h) $\epsilon=0.40$. The different texture colors are used to follow the different deformation states of selected cells during compression.

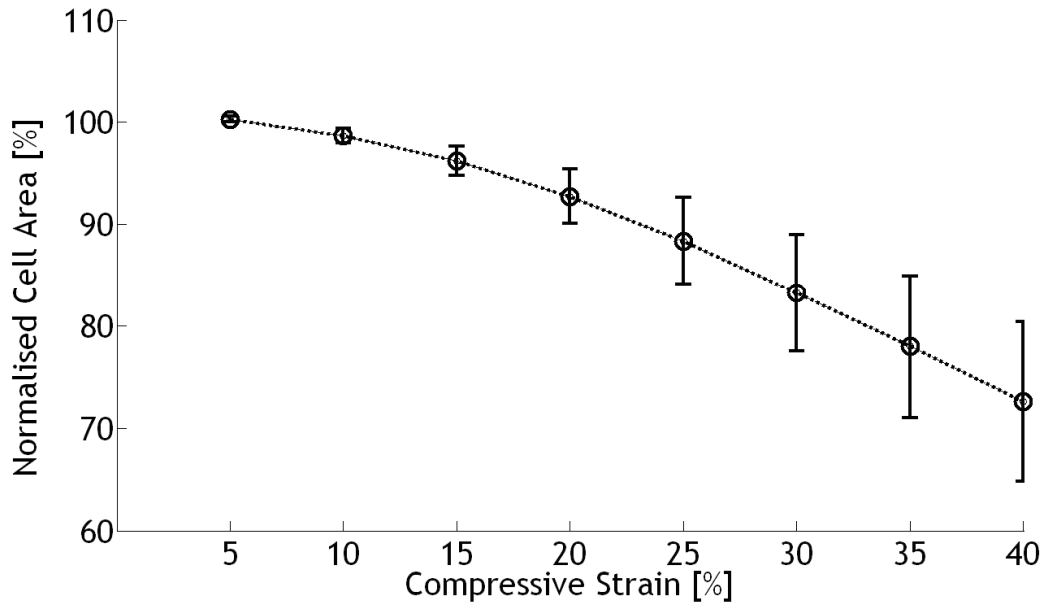


Figure 5-29: Mean normalised cellular area at different stages of compression. Error bars indicate the standard deviation of each data.

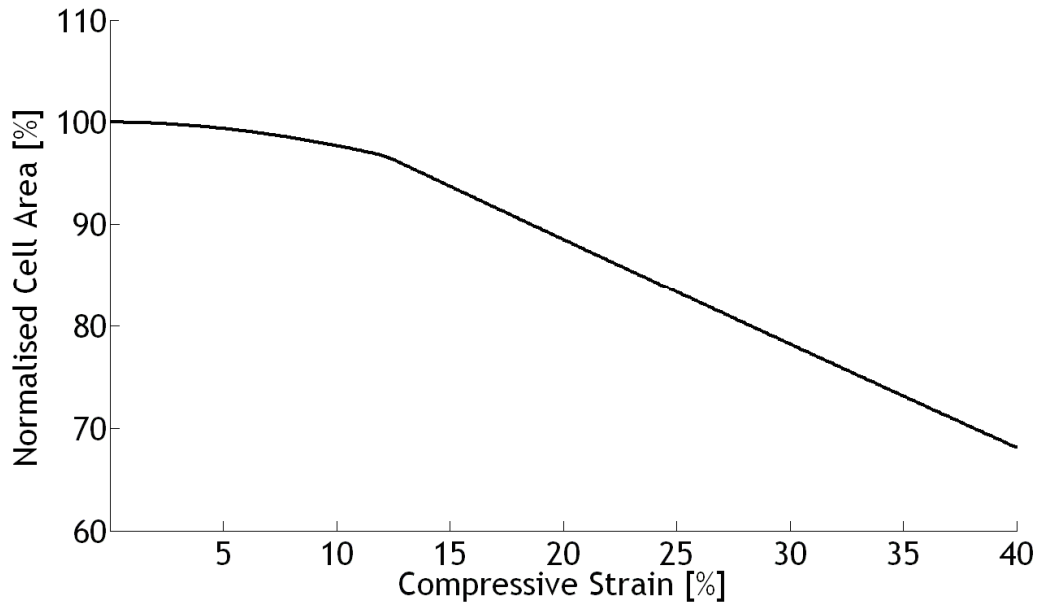


Figure 5-30: Normalised cellular area for perfect honeycomb compressed at perpendicular direction.

From Figure 5-26 it can be seen that when the load is applied on the RVE, 60% of the cells are immediately deformed such that the direction of the major-axis of the ellipses fitted to the cells are orientated in a direction transverse to the loading direction, i.e. at 0° and 180° . The shapes of the resulting probability distribution histograms shown in Figure 5-26 do not vary significantly with increasing strain, from 0.05 to 0.40. This indicates that the cells continue to deform in the same manner without any subsequent rotation of their principal directions, as might be expected.

In Figure 5-27 the change in the cellular area distribution is shown to be quite dramatic and can be understood by comparing this data with the microstructure shown in Figure 5-28. If the cells all reduced in area at the same rate then the distribution shown in Figure 5-27 would remain unchanged. However, contrary to this, the distribution is seen to rapidly spread out, indicating that some cells compress at a much faster rate than others. This is confirmed by visual analysis of Figure 5-28. To illustrate, cells marked in blue are examples of those cells that tend to resist compression whereas those marked in red tend to collapse. The grey

cells show compressive behaviour somewhere between these two extremes. Note that all the elements in the RVE have identical material stiffness (linear-elastic) and cross section.

In Section 5.3.3 it was also shown that the RVE microstructure, generated using the Lloyd's relaxation algorithm, consists of fairly constant strut length and cell shape, in this respect it is similar to a honeycomb microstructure. It is therefore interesting to compare the evolution of these two microstructures under increasing compression, see Figures 5-29 and 5-30. Comparison shows that both microstructures undergo fairly similar average cell compression rates. However, the honeycomb microstructure demonstrates a slight kink in the curve just after 10% compressive strain. Furthermore, after passing about 20% strain, the increasing scatter in the randomised Lloyd's RVE suggests that while some cells in this microstructure resist collapse, this is at the expense of other cells that undergo large buckling and compression in order to accommodate the bulk compressive strain across the RVE.

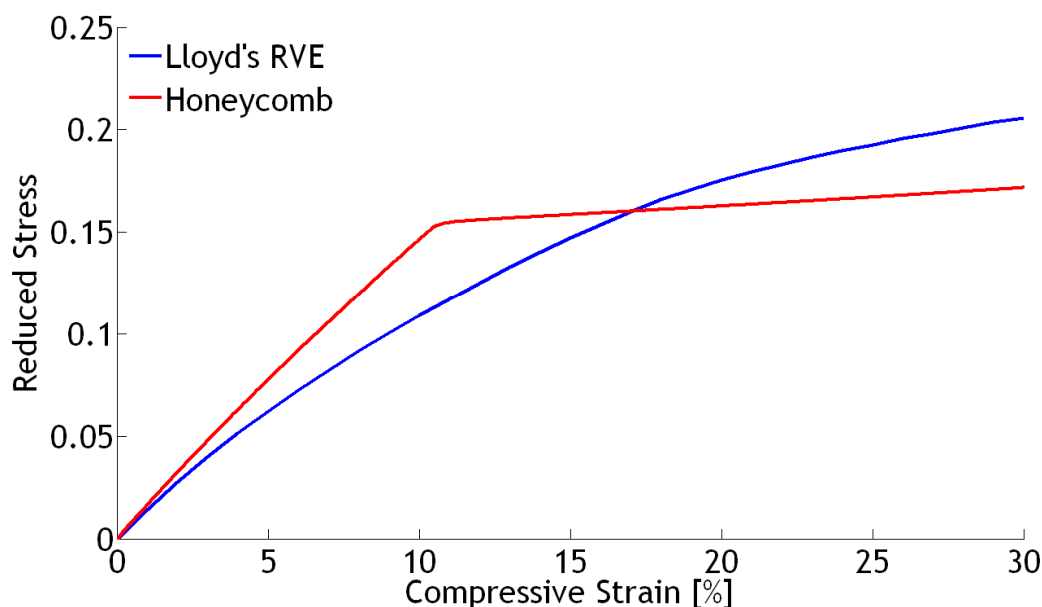


Figure 5-31: Reduced stress-strain curves for honeycomb and Lloyd's generated RVE under uniaxial compression in perpendicular direction.

Referring back to the mechanical response of the two RVEs (see Figure 5-31, repeated here from Figure 4.12 for convenience), the kink in the cellular area versus compressive strain curve of the honeycomb RVE (see Figure 5-30) is seen to occur soon after the kink in the corresponding stress-strain curve (see Figure 4.14), i.e. the cells begin to uniformly collapse at this strain.

Based on the stress-strain curves of two cases (see Figure 5-31), the Lloyd's generated RVE has more stiffness than honeycomb after about 17% compressive strain and less before 12%. Based on the work of the current study, it is believed that based on structural geometry of RVE, the combination of both beam-bending and buckling mechanisms controls the deformation and mechanical response in plateau region, where the dominancy of each mechanism depends to the cellular morphology within the RVE and also stage of compressive strain.

5.4.2 Morphological Evaluation of Poly-Disperse Shell-Based RVE under Compressive Loading

To study the evolution of cellular morphology of poly-disperse microstructures, RVEs with a degree of poly-dispersity of 0.1 have been generated. These RVEs have similar morphologies to those of higher poly-dispersity and are therefore assumed to be representative of this generic class of RVE, i.e those generated by the modified Drop and Roll method.

As discussed in Section 5.3, the contact strain for poly-disperse RVEs is around 0.35. This means that in order to achieve strains of 40%, to permit direct comparison with the results of Section 5.4.1, self-contact within the microstructure must be considered. For this reason, instead of employing a beam-based RVE, an equivalent shell-based RVE is used, using the technique described in Chapter 3.

In order to fully understand the evolution of the microstructural morphology of these poly-disperse RVEs, the evolution of cells within three distinct size

categories (small, medium and large) have been monitored where. The separate categories for small, medium and large cells correspond to 1-32.9%, 33%-65.9% and 66%-100% of initial normalised cellular area. To allow direct comparison of how the areas of these small, medium and large cells evolve with compressive strain, their areas have been normalised by dividing by the area of the largest cell in the same RVE within the same size grouping, e.g. the areas of all medium sized cells are divided by the area of the largest cell within the medium sized grouping, consequently all cell areas in all size grouping range up to 100%. The resultant cell area probability distribution histograms have been generated and compared at increasing compressive strains in Figures 5-33 to 5-40.

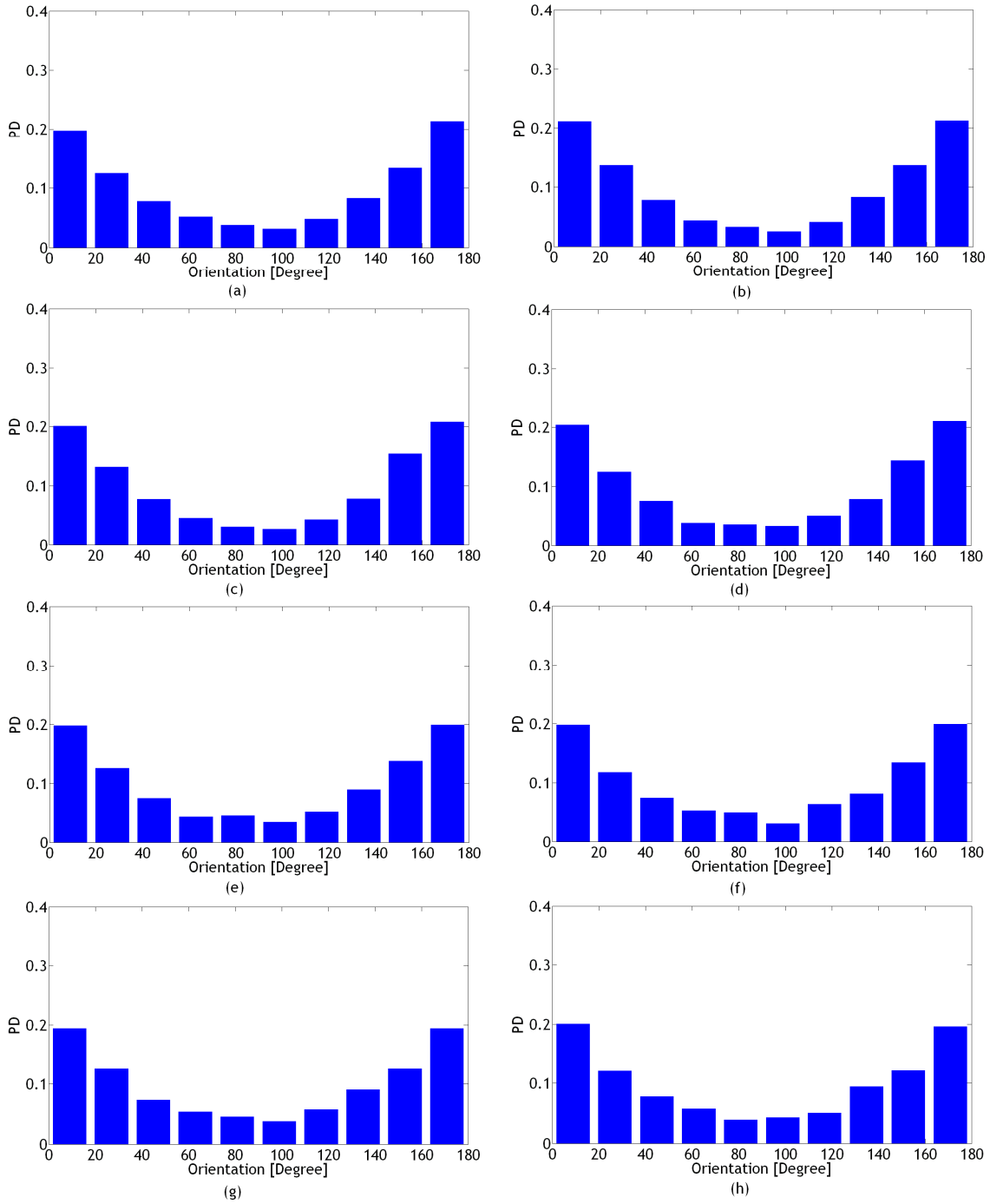


Figure 5-32: Probability distribution for cellular orientations evaluated in different compressive strains: (a) $\epsilon=0.05$ (b) $\epsilon=0.10$ (c) $\epsilon=0.15$ (d) $\epsilon=0.20$ (e) $\epsilon=0.25$ (f) $\epsilon=0.30$ (g) $\epsilon=0.35$ (h) $\epsilon=0.40$.

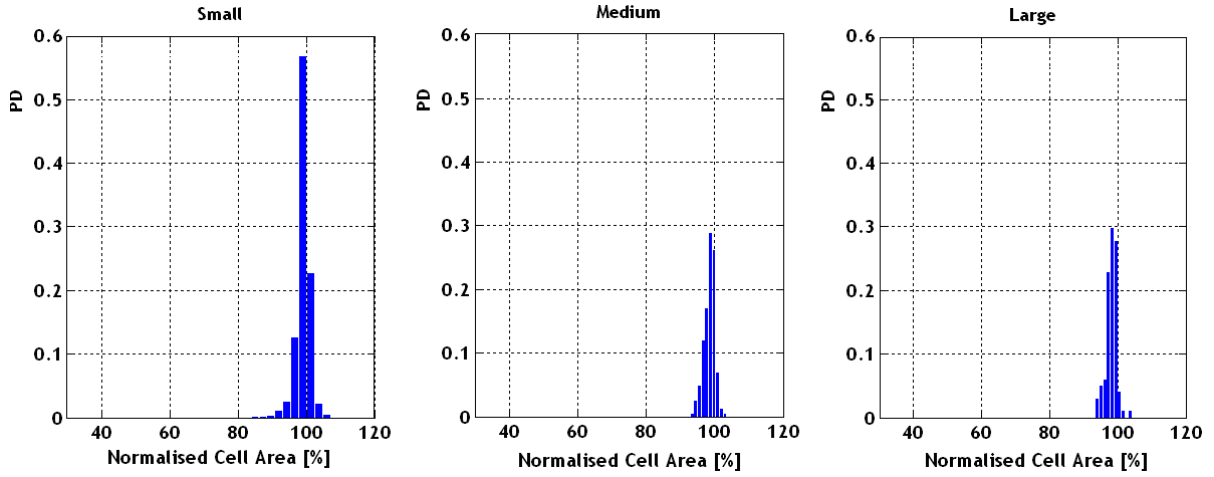


Figure 5-33: Probability distribution for normalised cellular area evaluated at 5% compressive strain.

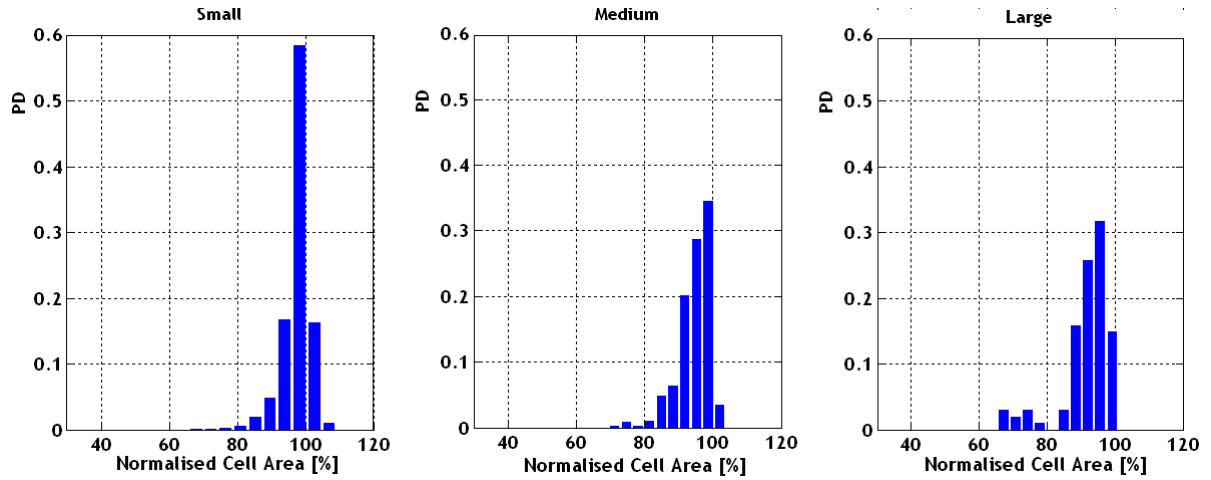


Figure 5-34: Probability distribution for normalised cellular area evaluated at 10% compressive strain.

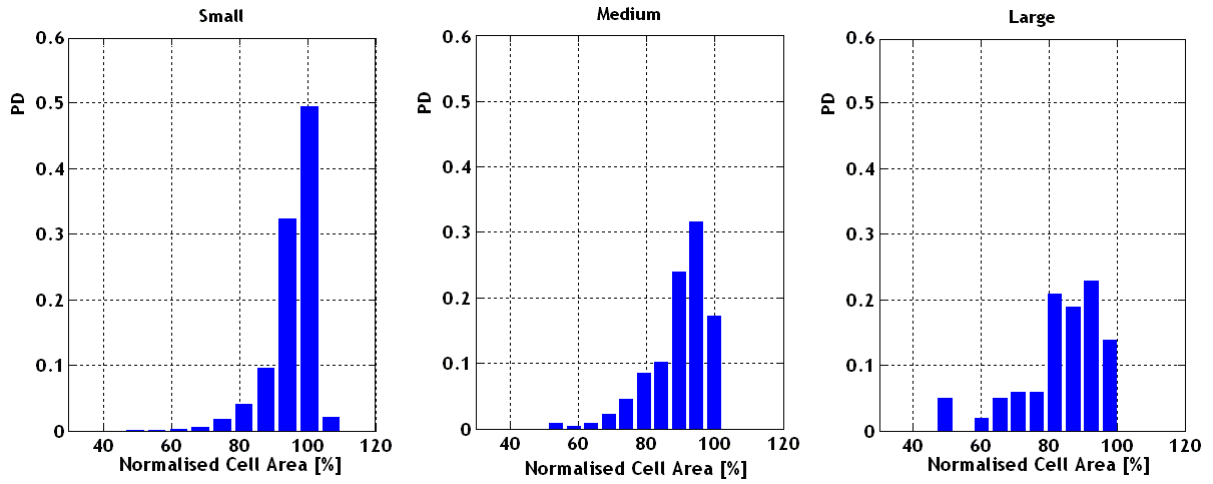


Figure 5-35: Probability distribution for normalised cellular area evaluated at 15% compressive strain.

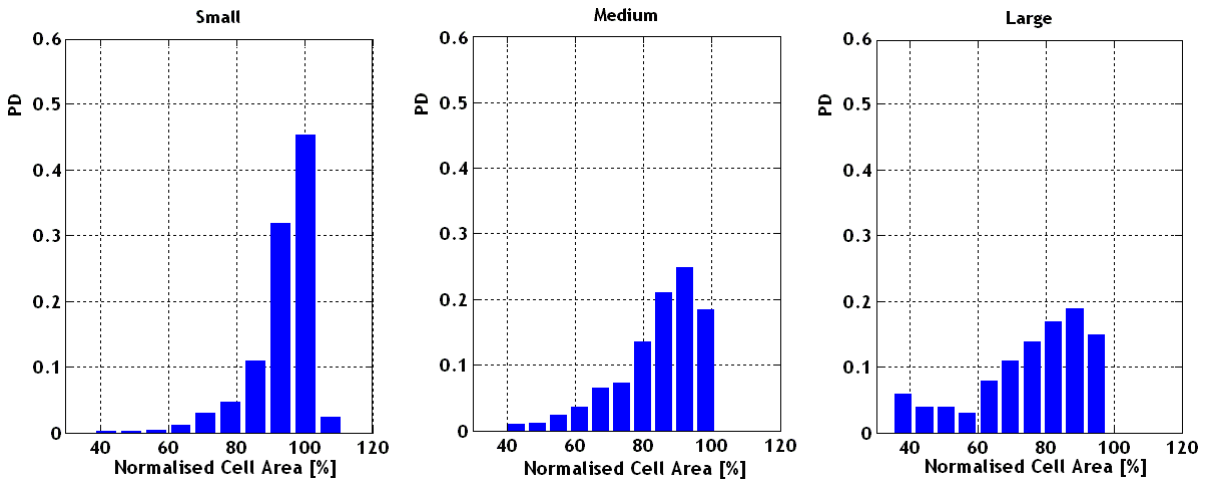


Figure 5-36: Probability distribution for normalised cellular area evaluated at 20% compressive strain.

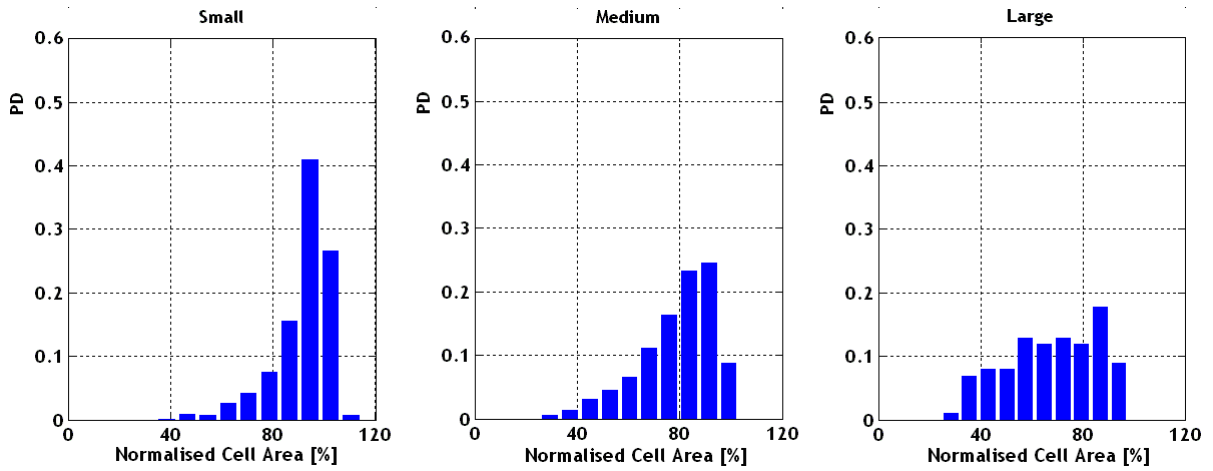


Figure 5-37: Probability distribution for normalised cellular area evaluated at 25% compressive strain.

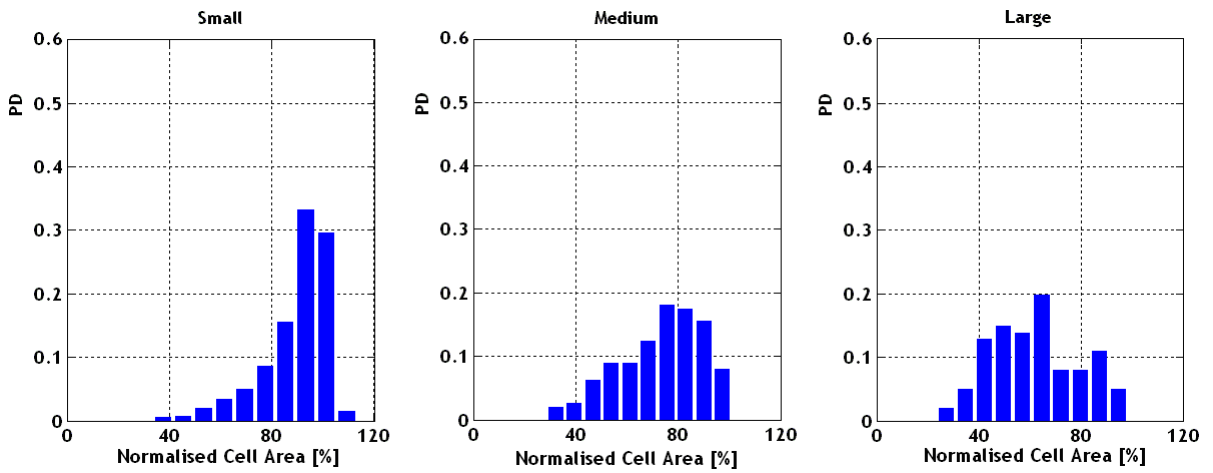


Figure 5-38: Probability distribution for normalised cellular area evaluated at 30% compressive strain.

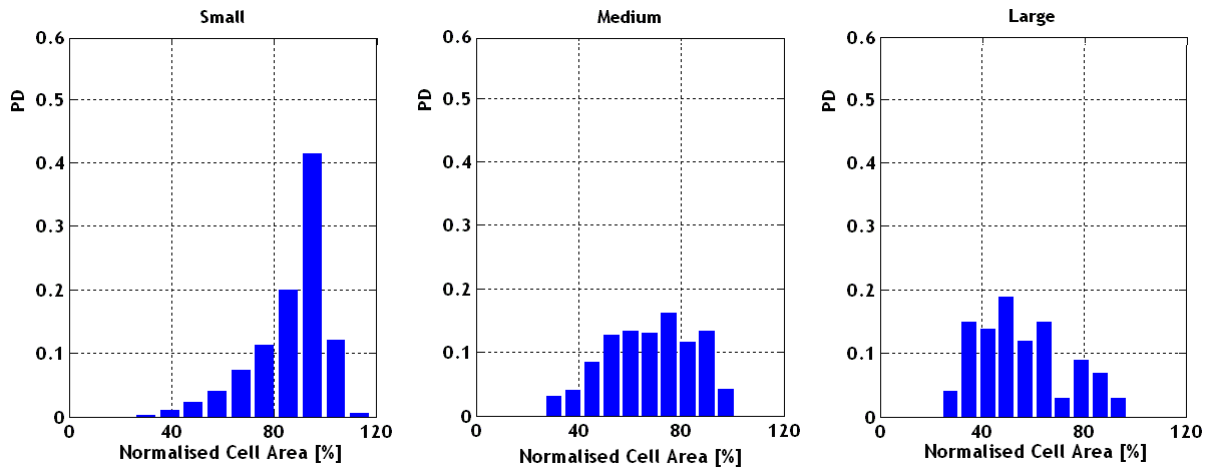


Figure 5-39: Probability distribution for normalised cellular area evaluated at 35% compressive strain.

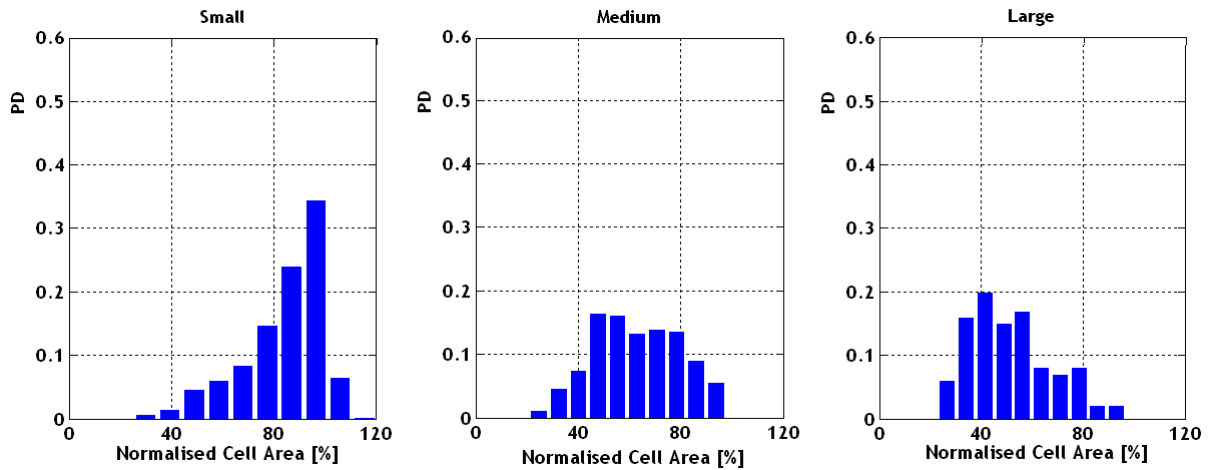


Figure 5-40: Probability distribution for normalised cellular area evaluated at 40% compressive strain.

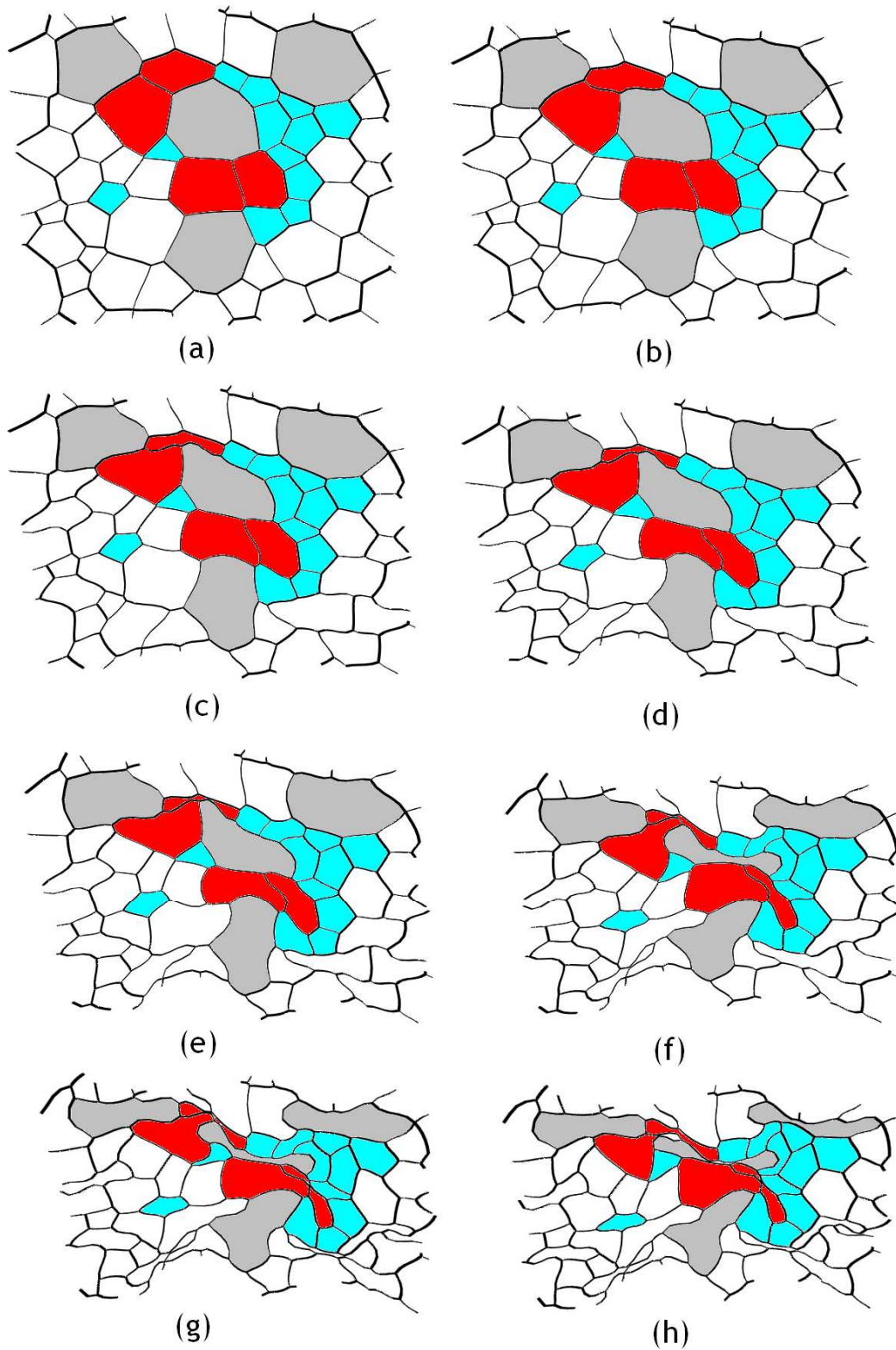


Figure 5-41: Illustrative example of visual inspection of deformed cellular structures evaluated in different compressive strains: (a) $\epsilon=0.05$ (b) $\epsilon=0.10$ (c) $\epsilon=0.15$ (d) $\epsilon=0.20$ (e) $\epsilon=0.25$ (f) $\epsilon=0.30$ (g) $\epsilon=0.35$ (h) $\epsilon=0.40$. Grey cells correspond to the large-size cells, red to the medium-sized cells and blue to small-sized cells.

Looking first at the probability distribution histograms of cellular orientation (see Figure 5-32), as with the mono-disperse RVEs of Section 5.4.1, the majority of cells are re-orientated with their longest axis aligned in the direction perpendicular to the loading direction at an early stage of compression. The distribution subsequently shows little change with increasing compressive strain, indicating that the same cells that eventually undergo collapse at large compressive strains are probably the those that are most susceptible to re-orientation at small strains. However, in comparison with the mono-disperse RVEs (see Figure 5-26), a larger proportion of the cells resist reorientation. This behaviour can be explained by analysing the cell area probability distribution histograms of Figures 5-33 to 5-40. These show that the change in cell area distribution is much smaller for the small cells than the larger cells, i.e. the small cells are much more resistant to deformation and therefore re-orientation during compression of the RVE, than the large cells. Since the majority of cells are contained in this small size grouping (see Figure 5-22) this reduces the proportion of cells susceptible to re-orientation within the RVE compared to the mono-disperse RVEs of Section 5.4.1.

Figure 5-42 shows the normalised area versus compressive strain for the three size groups. A clear difference in behaviour is observed with the smallest cells compressing by only about 15% (at 40% compressive strain), compared to the largest and mid-sized groups that each compress by about 50% and 40% respectively. The reason for the greater compressibility of the largest cells is due to the longer struts which have a much lower resistance to buckling than the shorter struts in the smaller cells [Timoshenko and Gere, 1961].

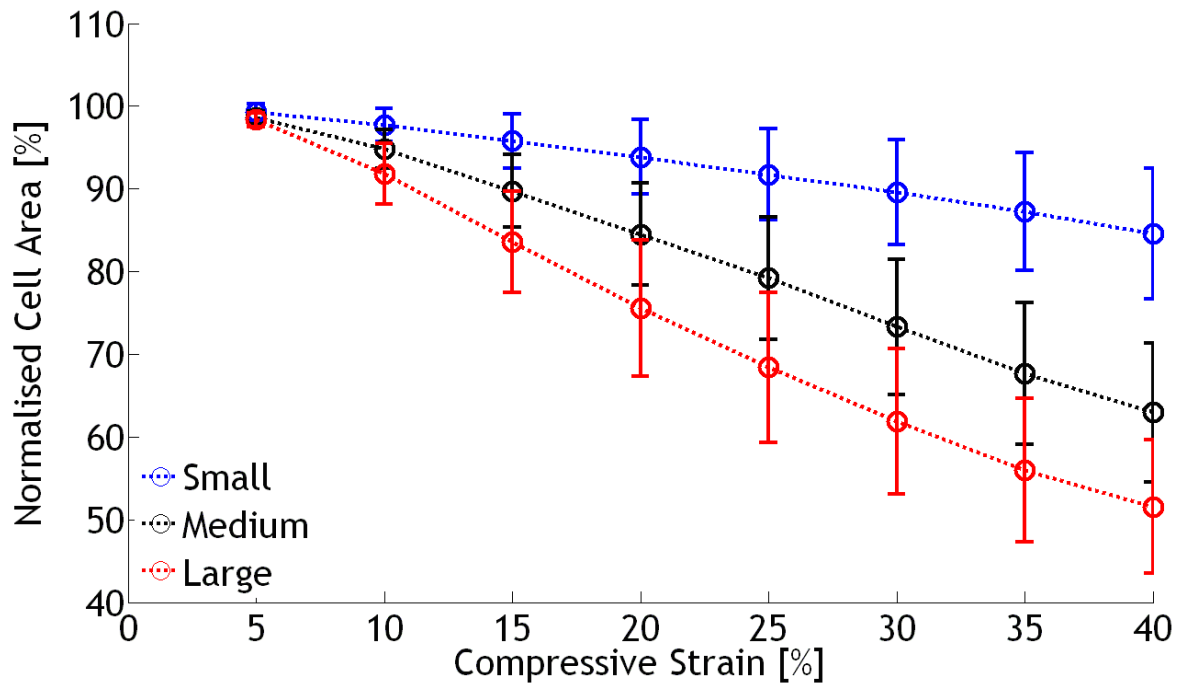


Figure 5-42: Normalised cellular area at different stages of compression for three different groups of cells.

5.5 Conclusions of Chapter 5

Statistical analysis has been performed on the undeformed microstructural morphology of RVEs generated using a variety of methods. With regards to the mono-disperse structure, it was found that using different modelling methods will result in RVEs with different geometrical features and hence mechanical response (see Chapter 3). RVEs that are produced using the enhanced method of Zhu are in general unintentionally anisotropic. On the other hand, by employing the Lloyd's relaxation algorithm it is possible to generate isotropic microstructures with all the cells randomly orientated in different directions and with the cell shapes reasonably similar to those observed using microCT in real foam (e.g. Figure 4-23). RVEs generated using the Drop and Roll method are also fairly isotropic though do show slight preferential orientations towards the perpendicular and the transverse directions.

Similar morphological characterisation methods were employed to study the changing morphology of 2-d beam-based microstructures under uniaxial compression using Isotropic RVEs generated using the Lloyd's relaxation algorithm

and Drop and Roll method. Due to importance of the plateau regime in many foam large strain engineering applications such as cushioning and impact energy absorption, the focus of this investigation was on the deformation mechanisms governing mechanical response of the foam in this region.

Chapter 6 . Characterisation and Modelling of 3-d Foam Microstructures

6.1 Introduction

As mentioned in Chapter 1 and elsewhere in subsequent chapters, 2-d modelling of porous materials such as foams, is a dramatic over-simplification of the real situation. However, it is nevertheless good practice to use 2-d modelling to develop the required microstructure generation algorithms and associated analysis methods necessary for the study of more complex 3-d microstructures. This chapter represents the beginning of an investigation focusing on the characterisation and modelling of 3-d open-cell foams. By extending the methods established previously for 2-d foams (see Chapters 2 to 5) the work begins to address the wider and more challenging topic of modelling 3-d microstructures.

The structure of the rest of this chapter is as follows, in the next section a literature review on the microstructure of real foam microstructure and relevant modelling techniques are presented. In Section 6.3 by using both mono and poly-disperse foam-like modelling techniques 3-d beam-based RVEs are generated and their morphological properties are analysed and compared to real foam data presented initially in Section 6.2. Final conclusions are given in Section 6.4.

6.2 Literature review

6.2.1 Plateau's law

By studying soap film networks, Plateau (1873) established some basic rules to explain the 3-d morphology of bubbles in an equilibrium state [Neimark and Vignes-Adler, 1995]:

- Three liquid soap plates generate an angle equal to 120^0 . This region is known as Plateau border
- Each four Plateau borders make a tetrahedral angular configuration ($\approx 109.47^0$)

Taylor (1976) proved that when unstable geometrical networks settle in an equilibrium state, the final structure tends to minimise its surface area according to Plateau's rules. However, despite the simplicity of Plateau's rules, it was set up based on observational examination for liquid bubbles geometry in equilibrium state.

6.2.2 Euler's law for convex polyhedral

In 18th century, Euler (1707-1783) proposed a simple mathematical rule to relate the number of vertices, V_n , edges, E_n , and surfaces, F_n , of 3-d convex polyhedral in the following manner [Abigail, 2011]:

$$V_n - E_n + F_n = 2 \quad \text{Equation 6-1}$$

Coxeter [Weaire and Hutzler, 1999] extended the above formula to relate the average number of polyhedral faces, $\langle f \rangle$, to the average number of edges per face, $\langle n \rangle$:

$$\langle f \rangle = 12 / (6 - \langle n \rangle) \quad \text{Equation 6-2}$$

The above relationships are based on 3-d geometries in a cellular network of polyhedral in an equilibrium state, consequently, they can be used as a *rule of thumb* to study the morphological characteristics of foam materials produced and prepared by fulfilling the stability and equilibrium criteria.

6.2.3 Characterisation of Micro-Structure of Real 3-d Foams

In 1946 Matzke [Matzke, 1946] presented the first systematic study of cellular network morphologies. By constructing a uniform soap bubble network and using dissecting microscopy, Matzke managed to measure some geometrical features of single bubble cells, such as volume and face shape. About 98% of cell faces were reported to have quadrilateral, pentagonal and hexagonal configurations.

Although, this novel work was considered to be a fundamental reference in understanding foam geometry, there are several limitations when applying the results to understand metallic and polymeric foams, namely: (i) soap bubbles were the base of this study and these can have very different morphological characteristics compared to metallic and polymeric foams (ii) as stated by Matzke, the surface force has a significant influence on the cell geometry which varies significantly between different types of foam (iii) a 3-d network of soap bubbles is usually considered to be a mono-disperse cellular structure and so is not particularly applicable for the study of poly-disperse foam.

Advances in imaging technology have made it possible to perform more accurate geometrical studies of real foam microstructures. Dawson and Shortall (1982) performed scanning electron microscopy on closed-cell polyurethane foam and concluded that a 3-d network of pentagonal dodecahedron is a suitable model for representing low-density foam. By employing nuclear magnetic resonance and x-ray microCT Montminy et al. (2001) characterised a 3-d network of polydisperse open-cell polyurethane foam and found that about 60% of faces were pentagonal, 23% were quadrilateral and 17% were hexagonal. Distribution graphs of strut length, strut intersection angle and face area were produced for statistical investigation. Later, Montminy et al. (2004) continued their investigations on a more poly-disperse polyurethane foam, extracting further important geometrical parameters. Unlike the previous investigation on aqueous foam by Matzke (1946), where almost 70% of cell faces were found to be pentagonal, in this case only about 55% of faces were found to have pentagonal configurations. Shortly afterwards, Dillard et al. (2005) used x-ray microCT to investigate the microstructure of an open-cell nickel-metal foam. In some ways the results were similar to those found by Montminy et al. (2004), i.e. about 57% of cell faces had pentagonal geometry and the rest were of quadrilateral and hexagonal shapes. The most commonly occurring cell in the investigation by Dillard was found to contain 12 faces including two quadrilateral, eight pentagonal and two hexagonal faces. However, the different material and cell volume distributions of the two foams meant that the distribution of cell shapes and the number of struts per face was

found to be significantly different. Figure 6-1 shows examples of the microstructures of the two different foams.

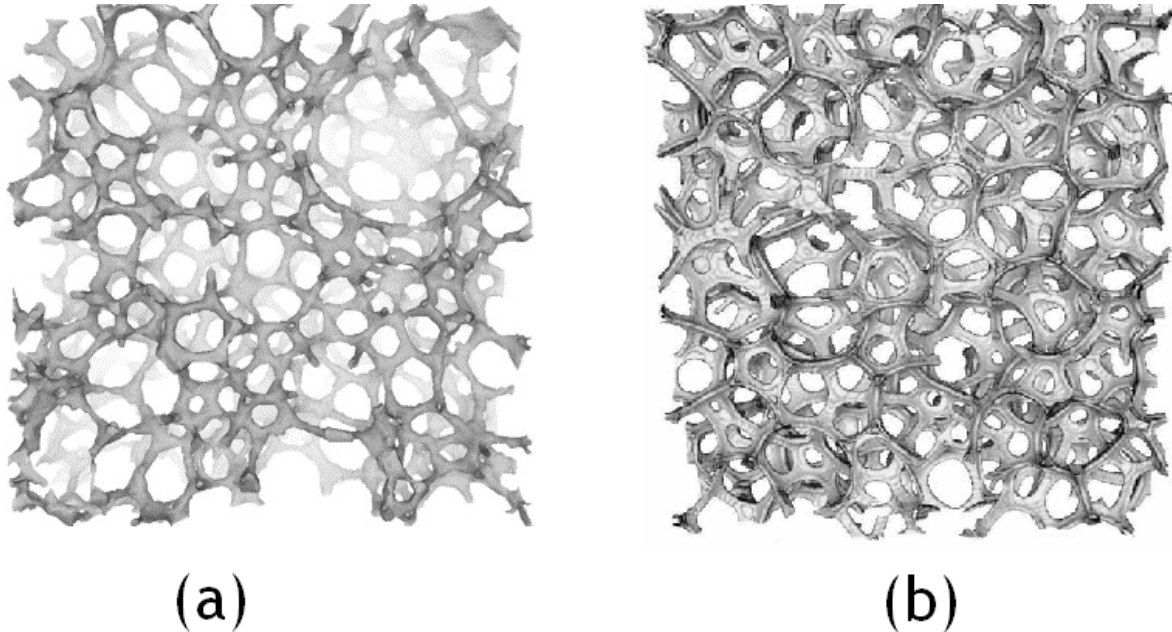


Figure 6-1: Different volume size distributions (degree of poly-dispersity) for foams investigated by (a) polyurethane foam, Montminy et al. (2004) and (b) nickel foam, Dillard et al. (2005).

6.2.4 Previous numerical-based modelling of 3-d foam microstructures

The first 3-d foam model was proposed by Lord Kelvin, [Thomson, 1887] based on surface minimisation theory. A regular truncated octahedron (8 hexagonal and 6 square faces) was proposed as the most efficient method of filling a volume of space by cells with the smallest possible surface area (see Figure 6-2). It also should be mentioned that the space filling Kelvin cell contains non-straight edges and non-planar surfaces with small curvature which is directly results from area surface minimisation boundary constrains.

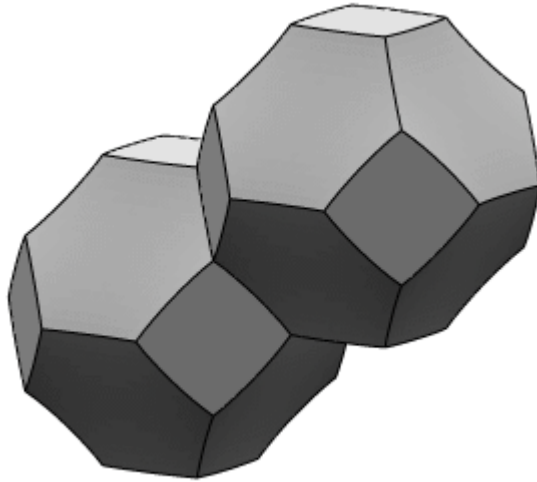


Figure 6-2: Space filling Kelvin cell [Brakke, 2009].

Later, by examining soap froth rheology [Weaire, 1992; 2008] methodologies for modelling an equivalent 2-d structure of soft condensed matter (such as foam in the early stages of its evolution) were studied. A new 3-d space-filling arrangement of cells consisting of irregular dodecahedron (5 pentagonal faces) and tetrakaidecahedron (2 hexagonal and 12 pentagonal faces) was proposed [Weaire and Phelan, 1994], see for example Figure 6-3:

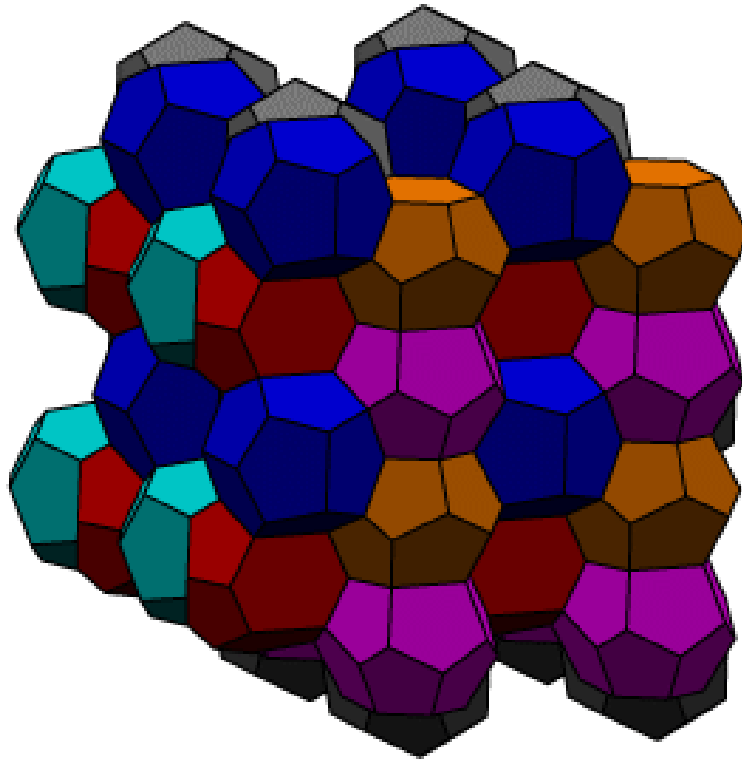


Figure 6-3:3-d space filling Weaire-Phelan partition [Brakke, 2009].

Several attempts to generate universal foam models by solving partial differential equations of pattern formation problems have been proposed [e.g. Gabbrielli, 2009]. All aim to produce modelling methodologies that suit all types of foam microstructure. However, recent studies have shown that these methodologies do not fully capture the geometrical variability of foam microstructure [Redenbach, 2009]. In the investigation presented so far in Chapters 2 to 5, variability has been found to have a significant impact on the final micro-macro response, particularly at large-strains, see Chapters 3 and 4. This suggests that capturing realistic variability may be an important step in accurately modelling the mechanical response of foam microstructures.

Zhu et al. (2000) proposed a method of generating 3-d foam microstructures, based on the Voronoi tessellation technique, using a special Voronoi seed distribution scheme. The 2-d version of Zhu's modelling technique was explained

previously in Chapter 2. In the 3-d method proposed by Zhu, the regularity of the structure is controlled by the following parameter

$$\alpha'_z = \frac{\delta'}{d'_0}, \quad \alpha'_z \in [0,1] \quad \text{Equation 6-3}$$

Where α'_z is the 'degree of irregularity' and if set to 0, the final structure will be a fully random Voronoi geometry whereas if $\alpha'_z=1$, in theory, a regular network of tetrakaidecahedron cells (i.e. Kelvin cells) should be achieved. In Eq. 6-3, d'_0 is the minimum distance between any adjacent seed (or nuclei) and is defined as

$$d'_0 = \frac{\sqrt{6}}{2} \left(\frac{V_0}{N\sqrt{2}} \right)^{1/3} \quad \text{Equation 6-4}$$

where, V_0 , is the volume of 3-d RVE and N is the number of seeds (or nuclei) inside the volume used to generate the Voronoi cells.

Later, by implementing the method proposed by Grenstedt and Tanaka (1999), Li et al. (2006^a), proposed a body centred cubic seed distribution as the initial regular arrangement (by applying the Voronoi method a regular Kelvin cell arrangement is consequently generated). By adding a perturbation (see Eq. 6-5) to this initial regular arrangement of seed positions an irregular Voronoi-based microstructure was produced

$$\begin{aligned} x_i^k &= x_i^{-k} + a' L_t \varphi_i^k \\ i &\in \{1,2,3\} \\ a' &\in [0,1] \\ \varphi_i^k &\in [-1,1] \end{aligned} \quad \text{Equation 6-5}$$

Here x_i^{-k} represents the initial body centred cubic seed distribution, L_t is the height of tetrakaidecahedron, φ_i^{-k} is a random variable generated from a uniform distribution and a' is the degree of irregularity. By comparing Eq. 6-4 and 6-3 similarities are evident, namely the use of a controlled perturbation to generate the randomised seeding. However, the power of Zhu's method is in generating N

cells, with a defined degree of irregularity, within a specified volume, V_0 . In contrast, the method proposed by Li [Li et al. 2006^a], provides no control over the final RVE volume. This becomes particularly problematic for cases with a higher degree of irregularity (i.e. when α' approaches 1), since the number of seeds randomly placed outside the cubic RVE will increase, which in turn also increase the total surface area of RVE. Nevertheless, the method proposed by Zhu has its own issues and suffers from the same problem as its 2-d counterpart (see Section 2.1.2). Namely, for cases with a high degree of regularity (i.e. when α'_z approaches 1) the method is computationally demanding (at least from this author's experience) and is therefore time consuming. For example, to fit 300 randomly-generated seeds within a specified volume the algorithm requires 200 minutes for an RVE comprised of 300 seeds (for $\alpha'_z = 0.85$), when using a PC of the following specification (64 bit Windows with intel(R)Xeon(R) CPU @ 2.66 GHz and 12 GB RAM).

Inspired by the experimental results of Matzke (1946), Kraynik et al. (2003) developed a procedure to generate random mono-disperse 3-d foam-like microstructures with similar morphologies to real mono-disperse foams. Molecular dynamics were used to create the initial seeding (see Section 6.3.2) and the Voronoi -Laguerre method (see Section 2.1.3) was then used to create a Voronoi-Laguerre based cellular network. A relaxation algorithm, 'Surface Evolver' [Brakke, 1992] was applied to further modify the microstructure. This code (currently available as an open source software [Brakke, 2009]) is designed to minimise the surface energy (and therefore the area) based on pre-defined volume and body constraints as well as initial structural morphology. The algorithm is applied while being accompanied by cyclic tension-compression loading in a so-called 'annealing process', designed to provoke further microstructural relaxation. The annealing process is continued until Plateau's laws for foam microstructural morphology [Taylor, 1976] (see Section 6.2.1) are satisfied and a minimum surface area (or minimum strut length) is achieved. Kraynik et al. (2003) made a comparative study on foam-like microstructures by using several algorithms (see Table 6-2):

Table 6-1: Short description of modelling techniques used by Kraynik et al. (2003). See Section 6.3 for definition of the acronyms used in this table.

Method	Description
RA-RCP	Sphere packing generated by random closed packing method, subjected to both Relaxation and Annealing process
RA-RSA	Sphere packing generated by random sequential adsorption method, subjected to both Relaxation and Annealing process
R-RCP	Sphere packing generated by random closed packing method, subjected to Relaxation process, only
R-RSA	Sphere packing generated by random sequential adsorption method, subjected to Relaxation process, only
V-RCP	Sphere packing generated by random closed packing method, subjected to Voronoi modelling, only
V-RSA	Sphere packing generated by random sequential adsorption method, subjected to Voronoi modelling, only

It should be noted that RA-RCP, R-RCP, RA-RSA and R-RSA microstructures are achieved by subjecting initial V-RCP and V-RSA models to relaxation and relaxation-annealing process. Both RA-RSA and RA-RCP microstructure were shown to have very similar geometrical patterns to Matzke's results, both in terms of the average number of faces per cell ($\langle f \rangle \approx 13.70$) and the average number of struts per face ($\langle n \rangle \approx 5$) (see Figure 6-4):

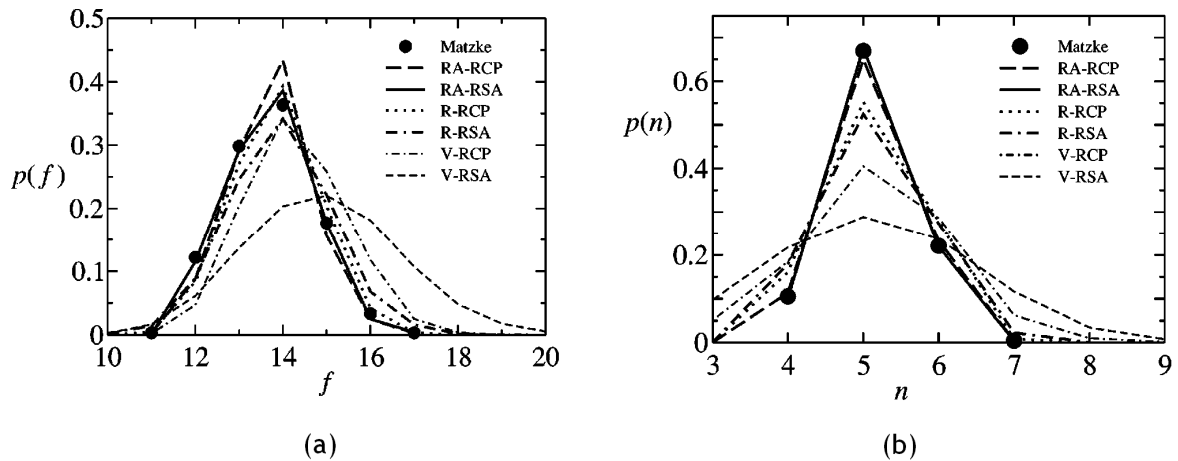


Figure 6-4: (a) distribution of cells with f faces (b) distribution of faces with n struts (from Kraynik et al. 2003).

By applying the same procedure, Kraynik et al. (2004) studied random poly-disperse 3-d microstructures. In that work, rather than using the Random Sequential Adsorption method (see Chapter 2), molecular dynamics was employed to generate a random packing of hard spheres. Next, using the Laguerre-Voronoi technique, an initial 3-d microstructure was generated for subsequent modification using Surface Evolver. The average strut length and number of faces per cell was found to decrease with increasing poly-dispersity. In yet another investigation, Kraynik (2006) advised against the use of unmodified (or un-relaxed) Voronoi-type microstructures in representing foam. The results of that paper showed such microstructures are unrepresentative of the actual geometrical features contained in real foams. In contrast, the relaxed microstructures generated using Surface Evolver were found to compare much more favourably with real mono-disperse foam microstructures (see Figure 6-4).

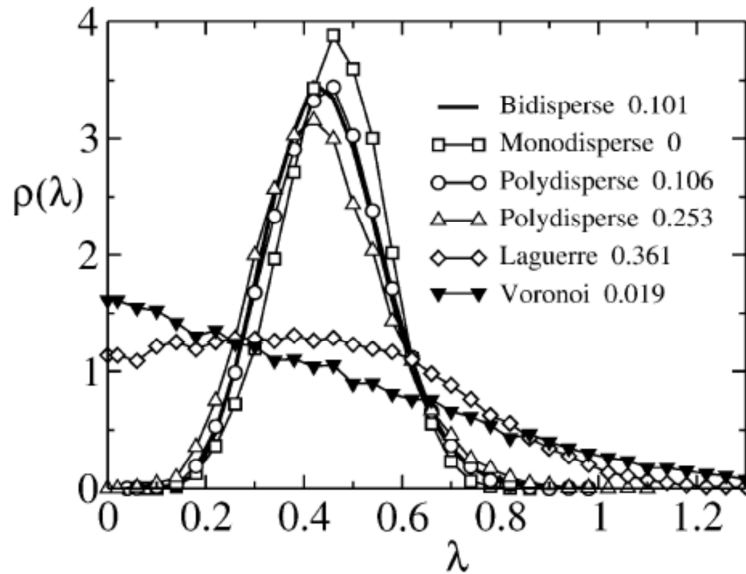


Figure 6-5: The probability distribution of the normalised strut length, λ , for different microstructures generated using various methods [Kraynik, 2006]. λ is scaled by cube root of average cell volume

6.2.5 Mechanical evaluation of numerically generated microstructures

Zhu et al. (2000) analysed 3-d beam-based Voronoi structures with a range of microstructural degrees of regularity, α'_z , (see Eq. 6-3). Slender beams with constant cross-sectional area were employed, consequently the work was applicable to foam of low relative density (<0.09). Using a PBC, small strain uniaxial compression was applied to a cubic RVE in a vertical direction. Findings were very similar to the 2-d beam-based Voronoi investigation [Zhu et al. 2001], namely, an decreasing degree of irregularity (approaching towards regular kelvin-based structure) resulted in decreasing Young's and shear moduli and decreasing bulk modulus. The Poisson's ratio was relatively insensitive to the degree of irregularity compared to the 2-d case. This insensitivity of the Poisson's ratio for the 3-d RVE microstructure was assumed to be due to the symmetric geometry of the tetrakaidecahedron-like unit cell microstructure in the perpendicular and transverse directions. In contrast, the geometry of the 2-d RVE is more akin to a honeycomb-based network, a microstructure that is known to be asymmetric in the orthogonal directions (see Section 4.4). Zhu and Windle (2002), extended the previous study to high strain compression of periodic 3-d beam-based Voronoi RVEs. Straight beam elements with circular cross section and elastic constituent

material were used within the microstructure and uni-axial compression was applied. The investigation revealed that a lower degree of irregularity (i.e. a more regular microstructure) resulted in a lower tangential modulus at low strains but a higher reduced-stress at high compression. By treating each individual cell using a spring-based model [Zhu et al. 2000], Zhu found that for an irregular structure, the main deformation mechanism under small strain was beam-bending and twisting, whereas for larger strains beam buckling was the more dominant deformation mechanism. Li et al. (2006) employed a perturbed Kelvin's cell microstructure to seed their RVE (see Eq. 6-5). Using different strut cross-sectional geometries and variable beam thicknesses, the mechanical response of 3-d beam-based RVEs under uni-axial compression were studied. For microstructures of low relative density, findings were very similar to those of Zhu et al. (2000). Namely a higher degree of irregularity resulted in an increasing Young's modulus. However, increasing the non-uniformity of strut cross-sectional areas reduced the Young's modulus.

Using x-ray microCT Jang et al. (2008) analysed the geometrical parameters of open-cell polyurethane and aluminium foams, including cell size, strut length and anisotropy ratio distributions. These parameters were then used to construct three models: (i) a regular network of Kelvin-cells, (ii) an irregular network of perturbed Kelvin cells and (iii) a random foam-like network created using Surface Evolver similar to those produced by Kraynik et al. (2003). Their final results suggested that both random and regular Kelvin-cell microstructures produce very reasonable predictions for the elastic mechanical response of polyurethane and aluminium foams. However, a key factor in achieving this success was the use of shear deformable beam elements and non-uniform strut area distributions. These parameters were found to be influential for higher relative densities. (The polyurethane foam used in the investigation had relative densities in the range 2.2-2.8%, whereas the aluminium foam had a relative density was about 8%. By considering foams with relative densities less than 0.5% the effect of strut area distribution and resultant shear effect became less important). Jang et al. (2010) extended the previous investigation on the mechanical response of numerically generated microstructures under high compressive strains, considering open-cell

aluminium foam. Again their results demonstrated that a Kelvin-cell based microstructure produced a fairly reasonable mechanical prediction compared to experimental results, equally as good as predictions produced using RVEs generated using Surface Evolver. Note however that there were some differences in the post-limit elastic response and the deformation localisation patterns within the microstructure when comparing the two methods.

These studies provide some of the best examples of work focussing on the mechanical response of 3D beam-based RVE foam microstructures. However, the main limitation with all these efforts is in ignoring the self-contact within the RVE microstructure that, in reality, must occur at large compressive strains. In Chapter 4, it was shown that, particularly for cases with high degrees of irregularity, it is very important to model self-contact since the deformation mechanism and consequently the mechanical response are strongly influenced after the RVE is compressed beyond the contact strain (see Section 3.2.5).

6.3 Morphological characterisation of 3-d beam-based RVEs

As discussed by Kraynik (2006), Voronoi-based structures are a very approximate method of modelling foam-like microstructures. The aim of the work in this section is to generate periodic mono- and poly-disperse RVEs and examine their geometrical parameters, such as cell volume distribution, number of faces per cell, number of struts per face and strut length distribution. These are then compared to experimental data measured from mono-disperse foams by Matzke (1946) and from poly-disperse foams by Montminy et al. (2004). To do this the 2-d microstructure generation algorithms described in Section 2.1.1 have been extended to the 3-d case (see Section 2.1.1) and are used to generate the results in this chapter.

6.3.1 Geometrical Study of 3-d RVEs

According to Plateau's law of surface energy minimisation for mono-disperse foams [Plateau, 1873; Kraynik et al. 2003] (see Section 6.2.1), the probability distribution graph of cell volume should obey a normal distribution with a reasonably small variance. Employing the Lloyd's relaxation algorithm (on any fully irregular Voronoi-based 3-d microstructure, see Section 2.1.2) and also using a 3-d version of the method proposed by Zhu with a range of degrees of irregularity ($\alpha'_z=0.5, 0.6, 0.7, 0.8$), 20 periodic RVEs for each case have been generated (periodic RVEs with 512 cells). The reduced cell volume distribution (normalised by RVE volume) is calculated and shown in Figure 6-6. The results show that the Lloyd's relaxation algorithm generates a very mono-disperse cell volume distribution with a small normalised standard deviation. In contrast the enhanced method of Zhu produces cell volume distributions that are normally distributed but have much larger PD curve band (i.e. higher volume variance), i.e. they are much more poly-disperse.

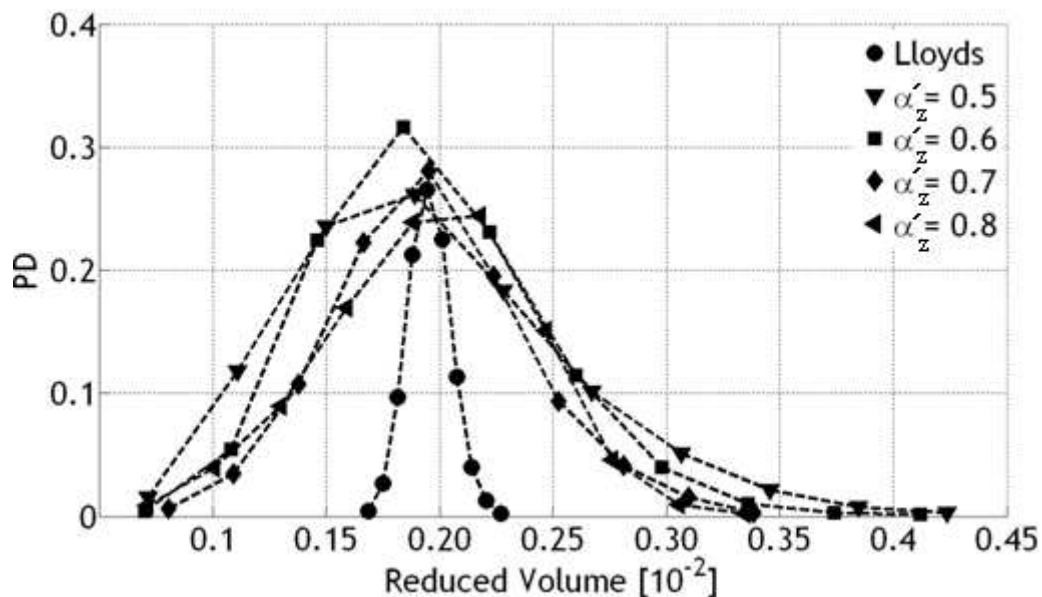


Figure 6-6: Probability distribution of cellular volumes generated by Lloyd's algorithm and Zhu method. The cell volumes are linearised by cubic RVE volume, equal to unit 1.

In order to make a further direct comparisons with the results reported by Matzke (1946), the number of struts per cell face and the number of faces per cell have also been determined, see Figures 6-7 and 6-8.

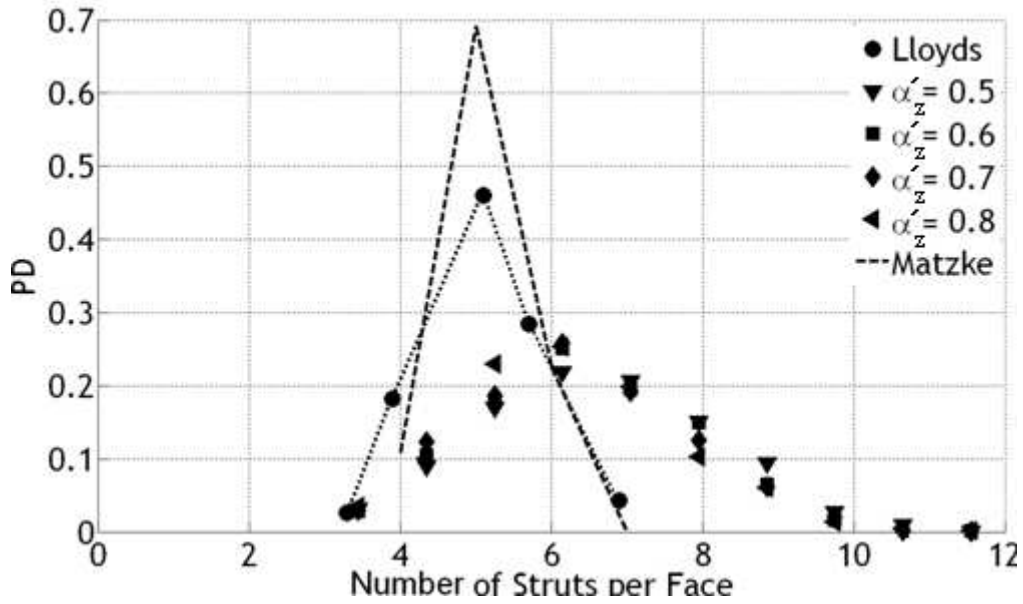


Figure 6-7: Number of struts per cellular faces for RVEs generated by the Lloyd's relaxation algorithm and modified method of Zhu. To make a direct comparison, the result measured by Matzke (1946) from a mono-disperse soap froth is also included.

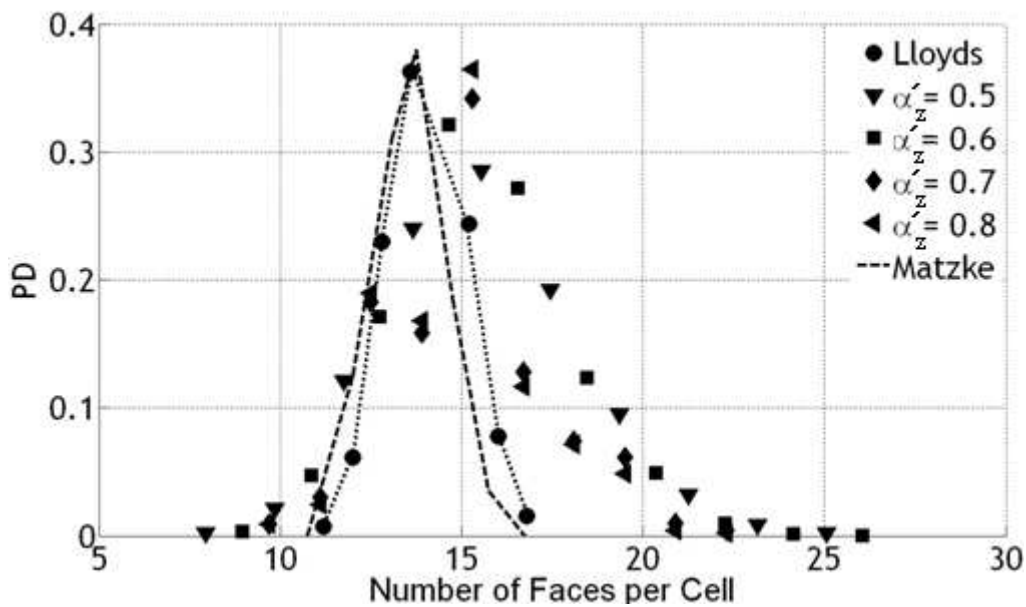


Figure 6-8: Number of faces per cell for RVEs generated by the Lloyd's relaxation algorithm and the modified method of Zhu. To make a direct comparison, the result measured by Matzke (1946) from a mono-disperse soap froth is also included.

From Figures 6-7 and 6-8 it can be seen that the 3-d version of the enhanced method of Zhu does not produce a realistic mono-disperse foam-like microstructure. In contrast, the Lloyd's relaxation algorithm, produces a much more favourable comparison with experimental data measured from a mono-disperse foam, both in terms of face shape and cell topology. RVEs generated by the Lloyd's relaxation algorithm, on average, contain about 3% triangular, 18% quadrilateral, 46% pentagonal, 28% hexagonal and 4% heptagonal faces (see Figure 6-7). About 6%, 23%, 36%, 25%, 8% and 1.5% of cells generated using the Lloyd's relaxation algorithm have 12, 13, 14, 15, 16, 17 faces, respectively (see Figure 6-8).

Since mono-disperse foams have a polygonal space-filling structure, it is possible to use Euler's formula [Mills, 2007] to check whether RVEs generated using the Lloyd's relaxation algorithm have a satisfactory space-filling geometry. The average number of struts per face is determined to be, $n_L = 5.1476$ and the average number of faces per cell, $f_L = 14.0755$. Here the subscript, L , indicates values generated using the Lloyd's relaxation algorithm. Consider Eq. 6-6 and 6-5, the resultant n_E and f_E computed using Euler's formulae are in very close agreement with their counterpart values obtained using the Lloyd's relaxation algorithm, i.e.

$$\text{for } f_L = 14.0755 \Rightarrow n_E = 6 - \frac{12}{f_L} = 5.1474 \quad \text{Equation 6-6}$$

$$\text{for } n_L = 5.1476 \Rightarrow f_E = \frac{12}{6 - n_L} = 14.0778 \quad \text{Equation 6-7}$$

In Chapters 4 and 5 it was shown that 2-d RVE microstructures with isotropic cellular orientations also have isotropic mechanical properties. It follows that the microstructural morphology of 3-d RVEs can likewise be used to anticipate their mechanical response. Using a similar procedure to that used in Chapter 5, though here fitting ellipsoids to the cells within the RVE rather than ellipses, the cellular orientation and size distribution in RVEs generated using the Lloyd's relaxation

algorithm can be obtained. In a similar fashion as with the 2-d Lloyd's angular distribution graph (see Chapter 5), here angles between 0° to 360° are considered, and then multiplied by the length of the semi-major axis of ellipsoid. All results are then normalised by the mean length of the semi-major axis of all the cells in each RVE. The resulting data are shown in Figure 6-9.

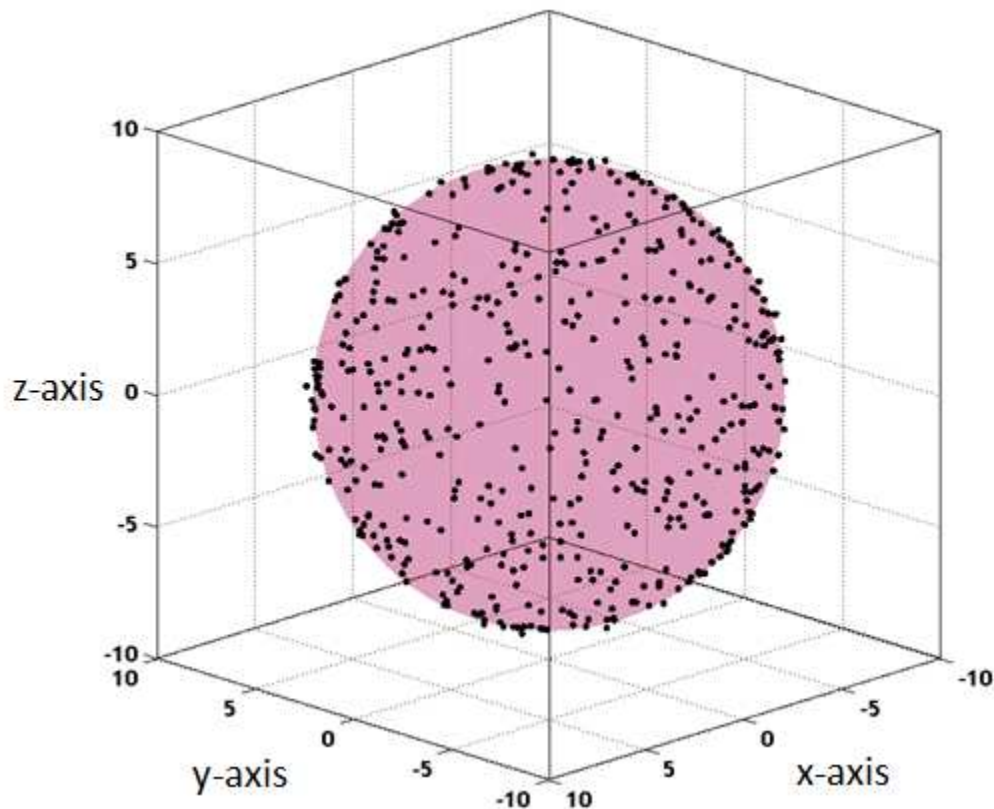


Figure 6-9: Polar representation of cellular orientation multiplied by fitted ellipsoid semi-major axis of each individual cell (black dots) for microstructures generated by Lloyd's relaxation. The radius of the pink sphere represents an average value of data (black dots).

From Figure 6-9, it is evident that, as with the 2-d counterpart, the 3-d microstructure is fairly isotropic, with cells evenly orientated across the full range of directions.

Struts length distribution within the microstructure is another key geometrical parameter and, as with the cell volume distribution, this should follow a normal distribution with a small relative standard deviation [Kraynik et al. 2003]. By using Surface Evolver and the annealing process, Kraynik et al. (2003) performed extensive studies on mono-disperse foam-like geometries finally suggesting the following criteria for a realistic strut distribution for a relaxed mono-disperse foam.

$$\lambda_{\min} \approx 0.25\langle\lambda\rangle \quad \text{Equation 6-8}$$

Here λ represents the normalised strut length and the $\langle \rangle$ bracket indicates the average value. The data are shown in Figure 6-10, all strut lengths are normalised by the cube root of the cellular volume

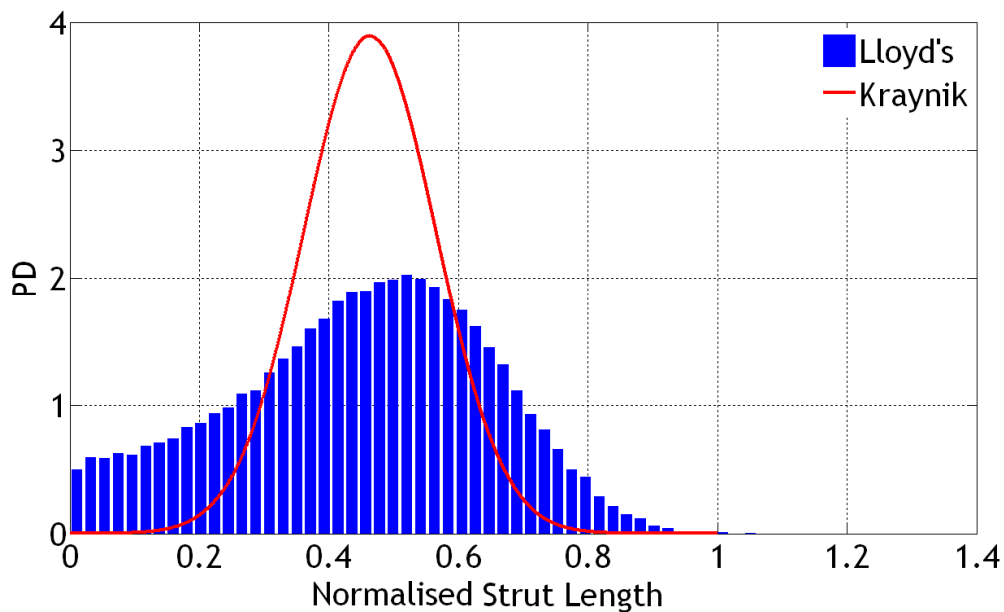


Figure 6-10: Distribution of strut lengths for RVEs generated using the Lloyd's relaxation algorithm and using the method proposed by Kraynik et al. (2003).

Comparison of the strut length probability distribution curves generated by the Lloyd's relaxation algorithm and by Kraynik using Surface Evolver for mono-disperse microstructures [Kraynik et al. 2003], indicates that about 30% of struts lie outside the 'realistic' length distribution predicted by Kraynik [Kraynik et al. 2003]. Nevertheless, the average value of strut length is reasonably close for both

cases, i.e. $\langle \lambda_K \rangle = 0.46$, from Kraynik et al. (2003) and $\langle \lambda_L \rangle = 0.53$ from the Lloyd's relaxation algorithm. The reason behind this difference is mainly due to the lower fraction of pentagonal faces generated using the Lloyd's relaxation method, i.e. about 46% of total faces compared to around 67%, measured by Matzke (1946) and predicted by Kraynik (see Figure 6-4). Also the number of quadrilateral and hexagonal faces generated by the Lloyd's relaxation algorithm is about 14% higher than that measured by Matzke (1946) and predicted by Kraynik.

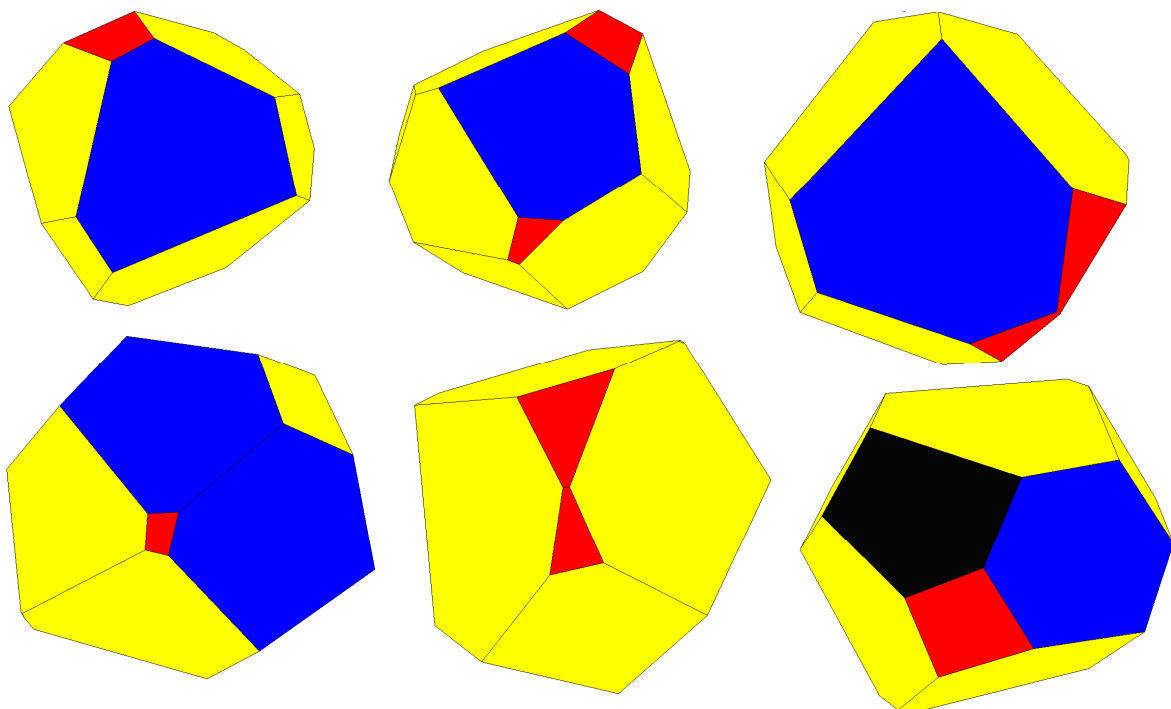


Figure 6-11: Examples of cell face geometries generated using the Lloyd's relaxation algorithm. Red, black and blue indicates quadrilateral and pentagonal, hexagonal faces, respectively.

Visual inspection of the cells generated using the Lloyd's relaxation algorithm show that a large numbers of quadrilateral faces (red faces in Figure 6-11) have small surface areas and very small strut lengths. Also, the majority of hexagonal faces (blue faces in Figure 6-11) contain small strut lengths, usually shared with quadrilateral faces. As a result of these unrealistic struts there is a lower number of pentagonal faces and a greater fraction of small struts. Nevertheless, those

quadrilateral surfaces with internal angles at around 90° and of reasonably large area, lying adjacent to pentagonal and hexagonal faces, will also have a realistic geometry (see bottom-right cell in Figure 6-11).

6.3.2 Geometrical Study of Poly-Disperse RVEs

The modified Drop and Roll method was employed in Chapters 4 and 5 to generate 2-d isotropic RVEs with poly-disperse cell-size distributions. However, the algorithm is much less computationally efficient when extended to the generation of 3-d RVEs. In the 2-d version, hard-circular disks have the option to roll only left or right following contact with another disk (see Section 2.1.3). In the 3-d version, there are an infinite numbers of planes in which hard-spheres can fall. In order to obtain an isotropic and homogenous distribution of spheres in different planes, a much greater amount of computation time is required and the algorithm is much more complex.

In Chapter 2, several algorithms to generate the packing of 3-d spheres were reviewed. In the author's opinion after comparing all those methods, classical molecular dynamics appears to be the best method to generate an isotropic and poly-disperse 3-d sphere-packing arrangement, especially because it can be viewed as an idealised foam rheological process corresponding to manufacture using gas-injection techniques [Kraynik, 1981, 1988]. The aim of current section is therefore to study the general topological features of 3-d isotropic, poly-disperse foam-like structures, generated using Molecular Dynamics (MD), rather than using a 3-d version of the Drop and Roll method, and compare these results with statistical data obtained from real materials using 3-d imaging techniques.

In 1990 Lubachevsky and Stillinger proposed a non-equilibrium MD algorithm to generate 2-d mono-disperse hard-circular disks with a periodic boundary condition. In their method, seeds or nuclei of particles are first distributed in the square lattice and in random non-overlapping locations. Next, initial velocity components (in the x and y plane) are applied to each particle, again with randomised values. In order to obtain a fairly mono-disperse packing, constant seed growth rates are used together with a small time step. Particles are allowed to move along their

individual trajectories until impact with another particle. In the case of particle impact, a classical elastic-collision protocol is used to update the new velocity and trajectory of particles. The Lubachevsky and Stillinger algorithm or ‘L-S algorithm’, has since been used by others, to generate random 3-d poly-disperse hard-sphere packings by controlling particle growth rate and the size of the time step [e.g. Kansal et al. 2002].

In the current research, a very similar algorithm to the L-S algorithm has been implemented with one main modification. In the L-S algorithm, if particles leave the square lattice, another particle of exactly the same size and velocity enters the lattice from the counterpart boundary. However, this requires the application of a very small time step and also affects the final RVE geometry at the boundaries. In the modified L-S algorithm, as with the method proposed by Zhu for periodic modelling of 3-d foam microstructures, a square cube containing initial particle seeds is considered. 26 identical cubes with the same local seed positions are repeated around its sides. Based on desired volume size distribution, all seeds are subjected to individual growth rates (usually following a log-normal or gamma function for poly-disperse volume distributions [Kraynik et al. 2006]). When the simulation starts, all the particles in the neighbouring cubes move and grow in exactly the same way as the corresponding seeds in the central cube. In so doing, any boundary effects in the final RVE are eliminated. The simulation terminates when the sphere packing fraction (total volume of spheres divided by the cubic RVE volume) exceeds a specified limit which can be defined a-priori by the operator. A flowchart of the modified L-S algorithm is shown in Figure 6-12.

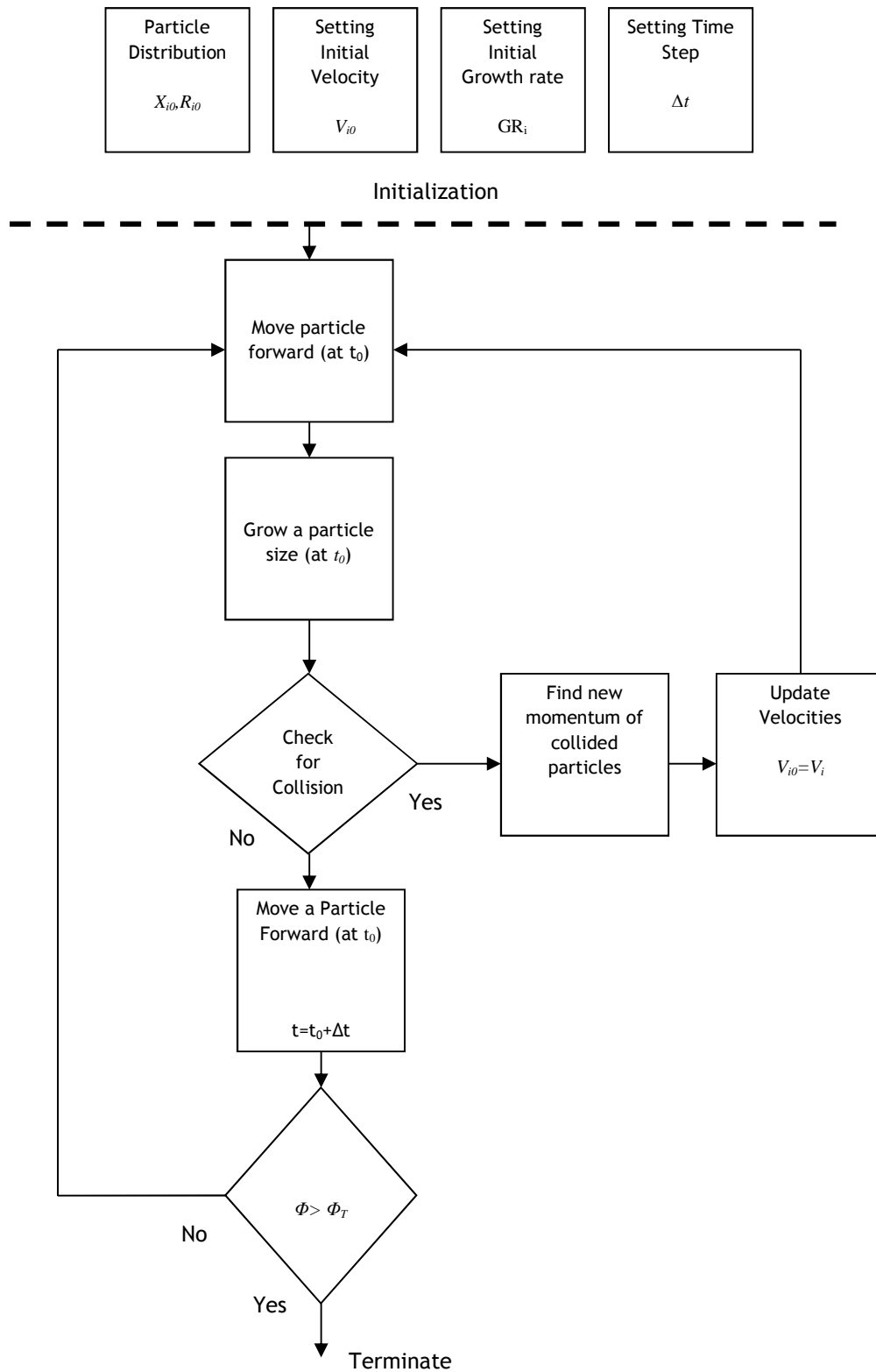


Figure 6-12: Flowchart of the modified L-S molecular dynamics algorithm, designed to generate a periodic poly-disperse random sphere-packing.

The new enhanced L-S MD algorithm proposed in this investigation does have some limitations. The first problem is due to ‘sphere escape’ from the cubic RVE container. This can frequently occur when a growing sphere continues to move in its original trajectory without colliding with other spheres. The second problem with this method is the requirement of performing several trial and error simulations in order to understand the effect of seed velocity and growth rate on the final microstructural morphology. Repeating such simulations requires a considerable amount of time and computational power. Due to these limitations only two successful simulations were achieved (out of a total of 30 simulations where each one takes about 2 hours to complete). Each simulation involved 125 particles, the initial growth rate of the particles follows a log-normal distribution which is generally considered a good method to generate foam-like poly-disperse volume arrangements [Kraynik et al. 2006].

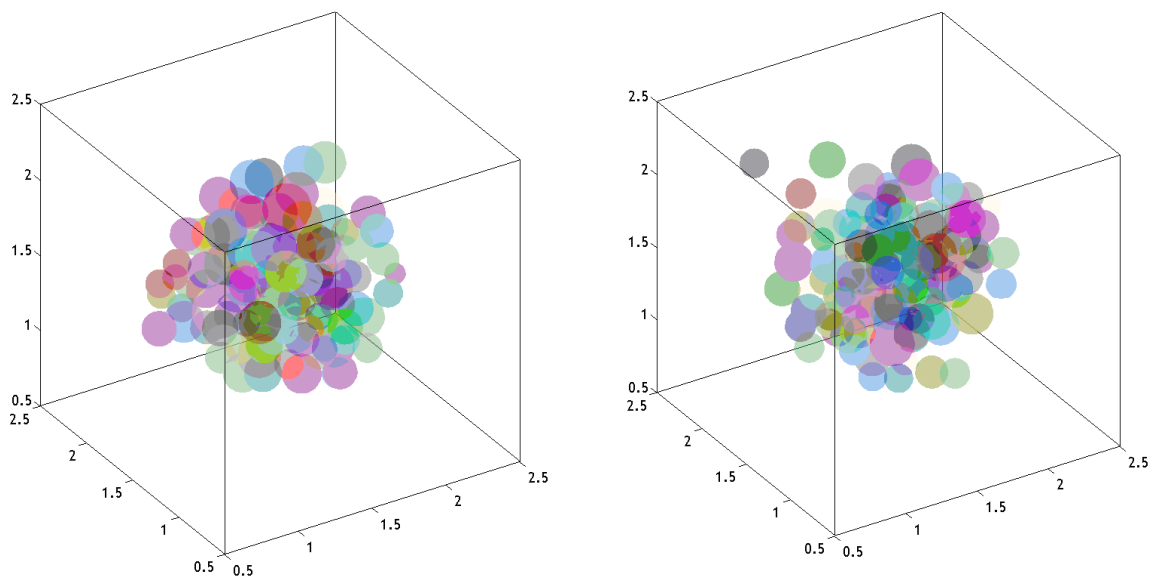


Figure 6-13: Two poly-disperse samples, containing 125 spheres, generated using the enhanced L-S algorithm. The packing density fraction before termination of the simulation was $\Phi=0.64$. The hard spheres are shown in different colours for easier for viewing.

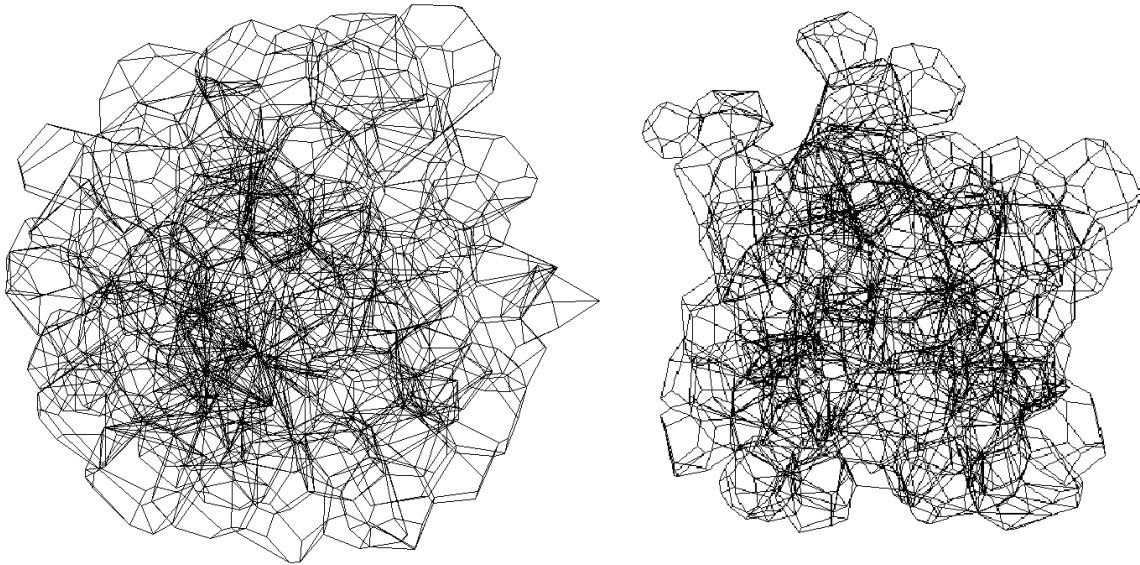


Figure 6-14: 3-d beam-based representation of spheres with poly-disperse volume generated using the 3-d Voronoi-Laguerre method.

The final cellular volume distributions of both RVE microstructures are reasonably well-described using log-normal distributions (see Figure 6-15). Unlike mono-disperse foam microstructures, poly-disperse foams are more challenging to characterise, as they tend to have a very wide range of cellular morphologies, determined by their manufacture and preparation conditions. As mentioned in Section 6.2, Montminy et al. (2004) performed detailed studies on the microstructure of open-cell polyurethane foam and measured a variety of microstructural morphological parameters including cell volume fraction distribution, number of struts per cell, face area fraction, strut length and strut intersection angle distributions. The data provide a means of evaluating the predictions of the modified L-S algorithm.

The comparison presented here begins with the cell volume distribution, (see Figure 6-15). The data show that the modified L-S algorithm is able to generate hard sphere packing with volume size poly-dispersity following a log-normal cellular volume distribution (see Figure 6-15a and b). The main parameters that control the cellular volume distribution in the modified L-S algorithm are growth rate and time step. Therefore, one of the main fundamental steps towards

generating microstructures similar to real foam materials, is to apply a parametric analysis to determine how growth rate and time step can be manipulated to generate the required hard sphere packing in order to produce microstructures with statistically similar volume distributions as real data.

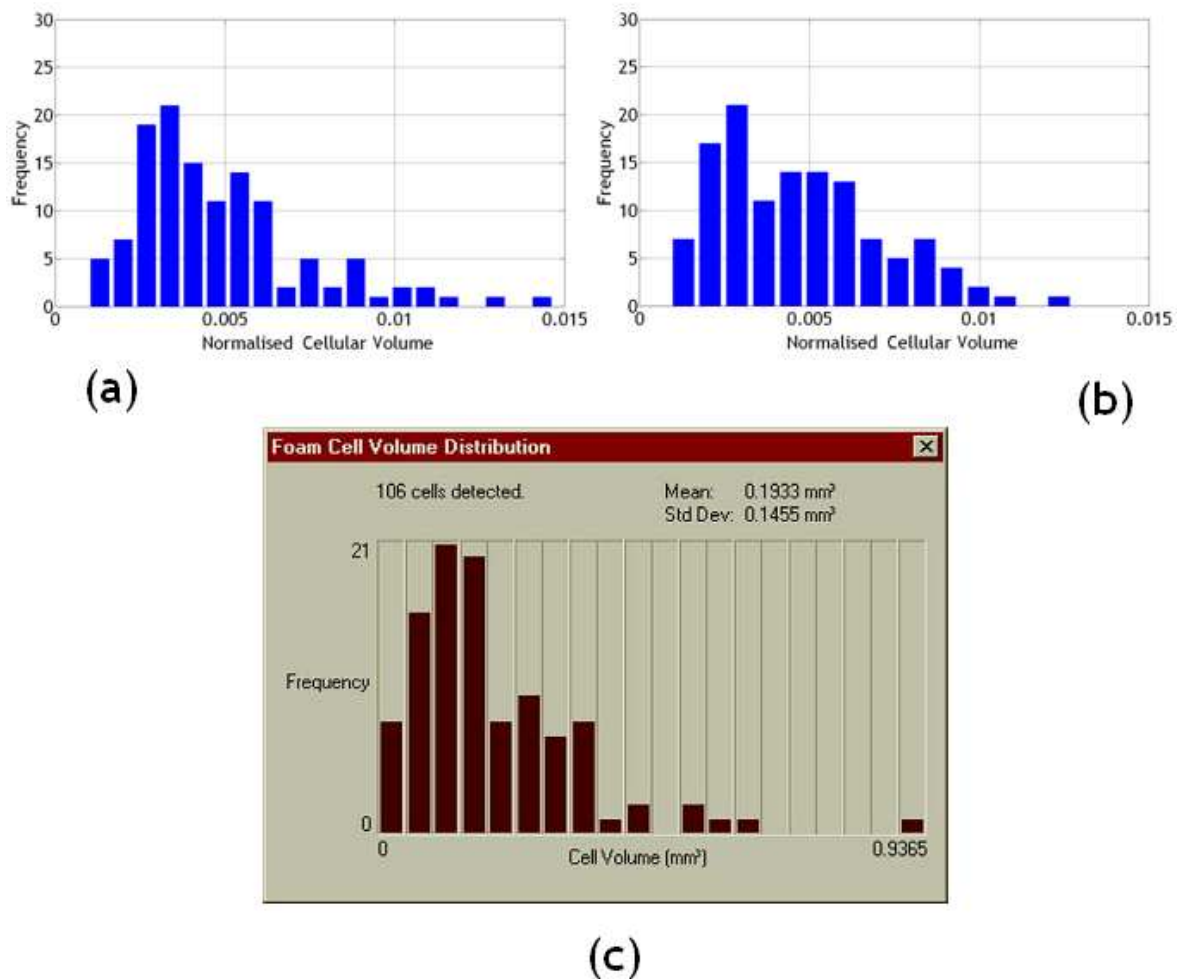


Figure 6-15: (a) and (b) Cellular volume fraction of the two poly-disperse RVEs. Cell volumes are normalised by the total volume of the RVEs. (c) Results from the investigation by Montminy et al. (2004) on an open-cell polymeric foam.

Histograms showing the face frequency versus the number of struts per cell face (also called ‘windows’ in some texts) within the two RVEs generated using the modified L-S algorithm are presented in Figure 6-16. Table 6-2 shows the frequency of the different types of polygon within the microstructure.

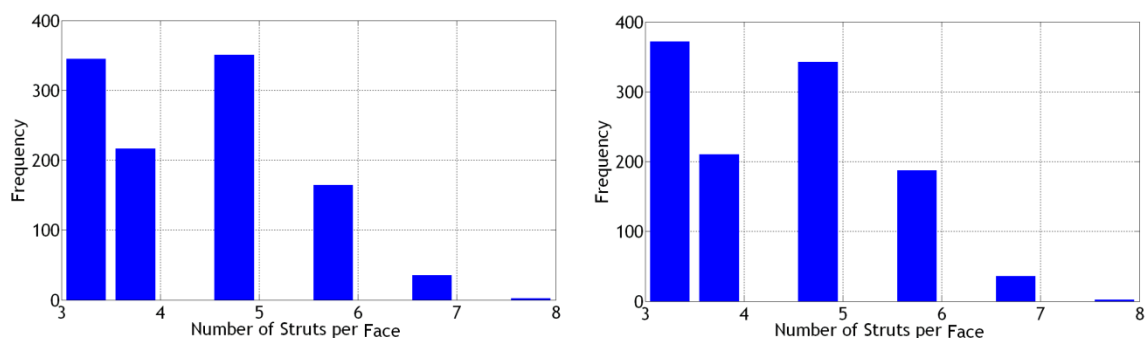


Figure 6-16: Number of struts per face for the two RVEs generated from seedings created using molecular dynamics.

Table 6-2: Comparison between the frequency of face geometry for the two RVEs, generated from seedings created using the enhanced L-S MD algorithm and experimental measurements made by Montminy et al. (2004). In the last column, the area fraction for each window (or face) shape in the numerical RVE is also generated.

Type of Window Shape	Fraction of cells (MD) [%]	Fraction of cells (Montminy et al. 2004) [%]	Area Fraction (MD) [%]
Triangular	32	1	6.50
Quadrilateral	18	24	13.20
Pentagonal	30	55	40.10
Hexagonal	16	19	31.83
Heptagonal	3	1	7.90

Referring to see Table 6-2, the results from Montminy et al. (2004) reveal pentagonal geometries contributed 55% of the overall number of measured faces, this fraction is lower at 30% in the numerical RVEs. The fraction of quadrilateral and hexagonal faces are in reasonably good agreement with the Montminy data, however, the fraction of triangular faces is significantly higher in the numerical RVEs. Again, as with the mono-disperse case, visual inspection of several cells (see Figure 6-17), shows that even though the total surface area of the triangular faces

is small (6.50%) compared to the other face geometries, due to their large number, there are many unrealistically small struts inside the RVE microstructure.

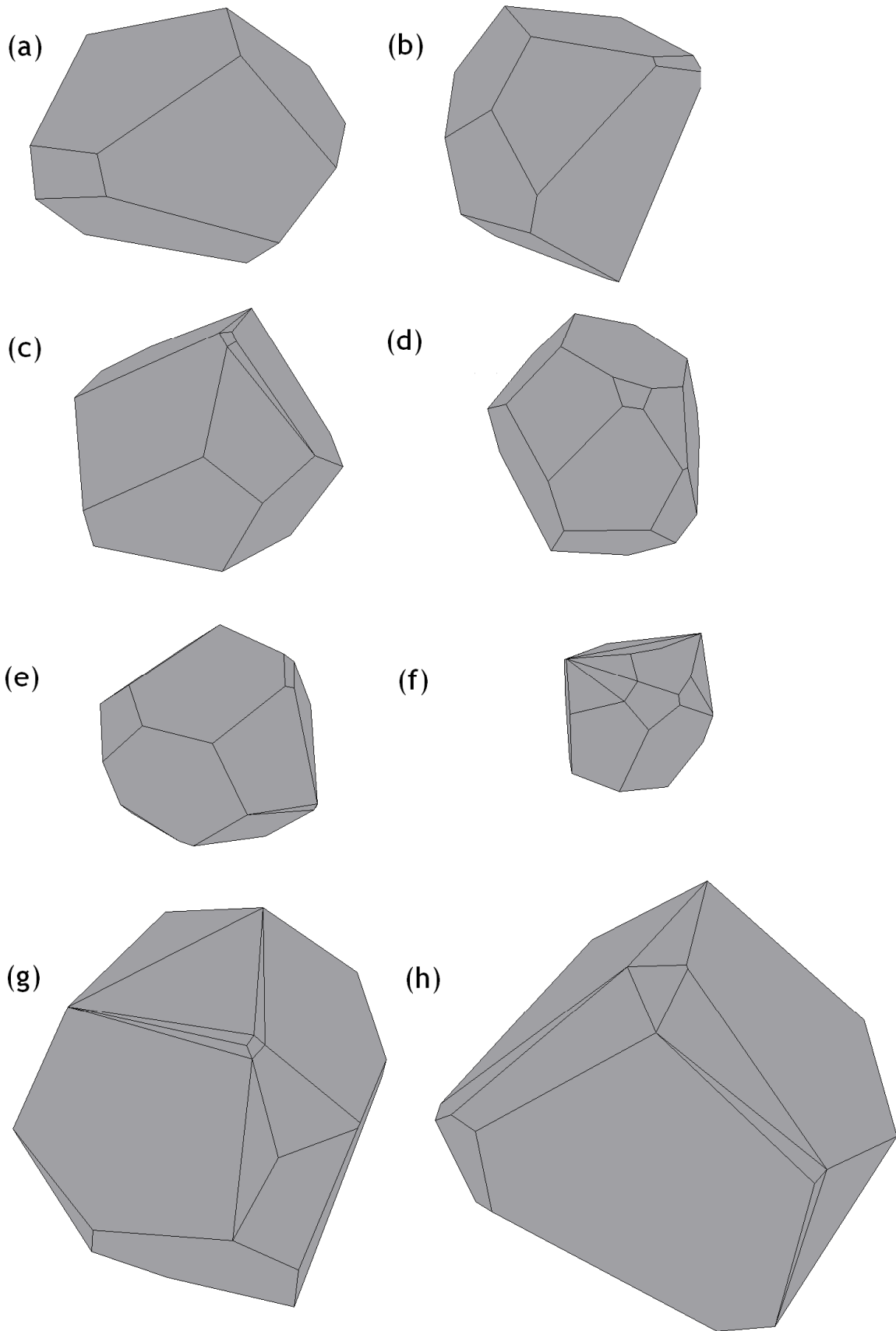


Figure 6-17: Example of poly-disperse cells with different topologies.

The average number of faces per cell for each numerical RVE is 17.82 and 18.40. These figures are significantly higher than those determined by Montminy et al. (2004), i.e. 13.01 (see Figure 6-18 and Table 6-3).

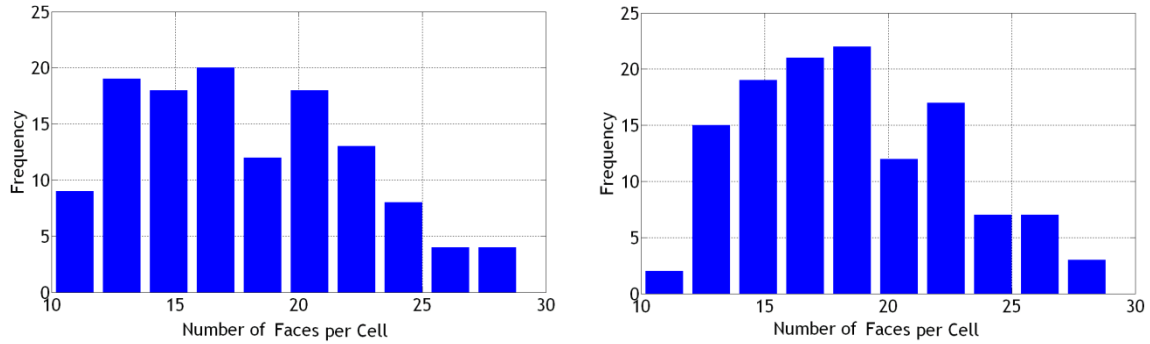


Figure 6-18: Distribution of number of faces per cell, for the two numerically generated RVEs.

Table 6-3: Comparison between the numbers of faces in the numerical RVEs and from Montminy et al. (2004).

Number of faces per cell	Frequency (MD) [%]	Frequency (Montminy et al. 2004) [%]
7	-	3
8	-	4
9	-	4
10	4	7
11	5	18
12	6	11
13	13	12
14	9	13
15	9	9
16	8	4

17	12	8
18	5	5
19	7	-
20	11	-
21	7	1
22	6	-
23	7	-
24	5	1
25	3	-
26	2	-
27	2	-
28	1	-
29	3	-

Comparing the fraction of different cellular morphologies, using Table 6-3, it is seen that the RVEs generated using MD have a large number of cells containing a very large number of faces, most of these faces tend to be triangular, which according to the data of Montminy et al. (2004) is not the case for real foam microstructures. Unlike a real poly-disperse foam where face area distribution closely follows a log-normal distribution (see Figure 6-19c), the two numerical RVEs have very different face area distributions. Figure 6-19 shows two peaks in the distribution of the numerical data. The first higher peak has a relatively narrow distribution and is associated with the triangular faces.

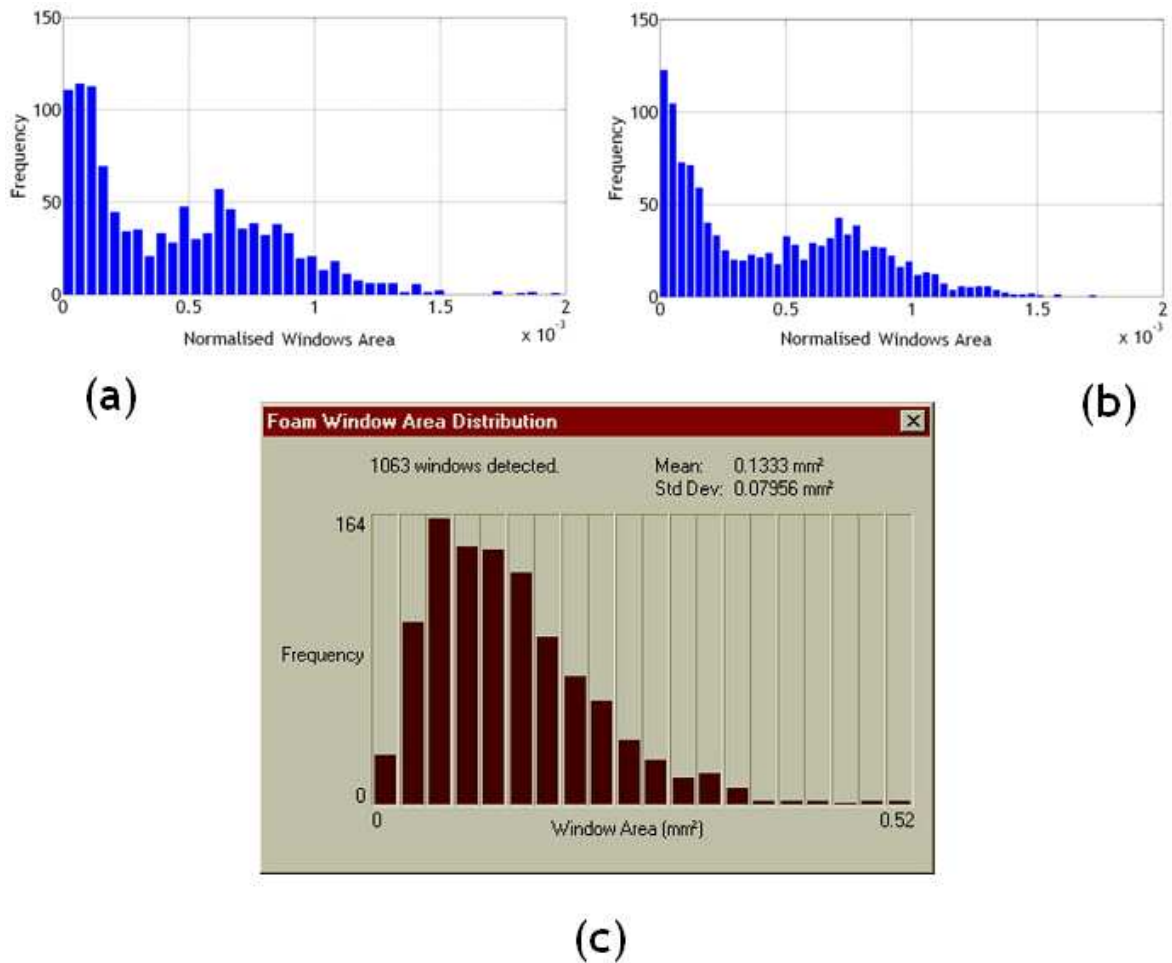
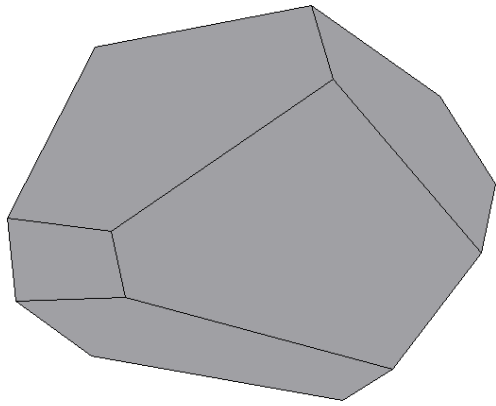
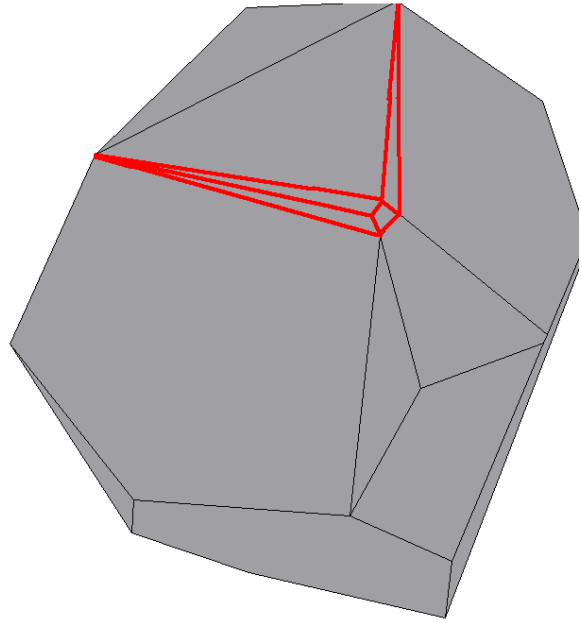


Figure 6-19: (a) and (b) Face area fraction distribution for two numerical RVEs. All areas are normalised by the total surface area within the microstructure. (c) Results from the investigation by Montminy et al. 2004 on an open-cell polymeric foam.

Both visual inspection and direct calculation of strut length for different types of face shape, reveals a strong correlation between small struts and triangular faces (e.g. see Figures 6-20a, and b). As a result, the strut length distributions in the two numerical RVEs are not in very good agreement with those of real poly-disperse foam, compare figure 6-21a, b and c.

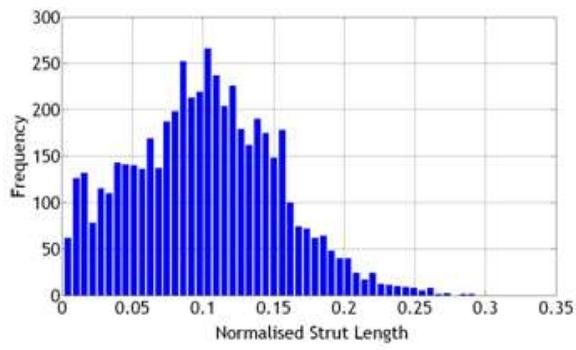


(a)

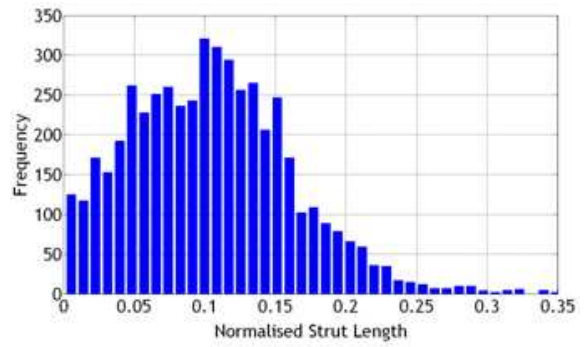


(b)

Figure 6-20: (a) Cell without triangular surfaces (b) cell with triangular surfaces. The majority of triangular surfaces have very sharp internal angles resulting in generation of very small struts (highlighted red struts).



(a)



(b)



(c)

Figure 6-21: (a) and (b) normalised strut length for two MD samples. All lengths are normalised by total microstructure volume. (c) Results from the investigation by Montminy et al. 2004 on an open-cell polymeric foam.

The mean value of the strut intersection angle measured by Montminy et al. (2004) was 106.7 ± 17.78 degrees. In comparison the values measured within the two numerical RVEs is 90.29 ± 37.48 and 90.36 ± 36.95 , respectively.

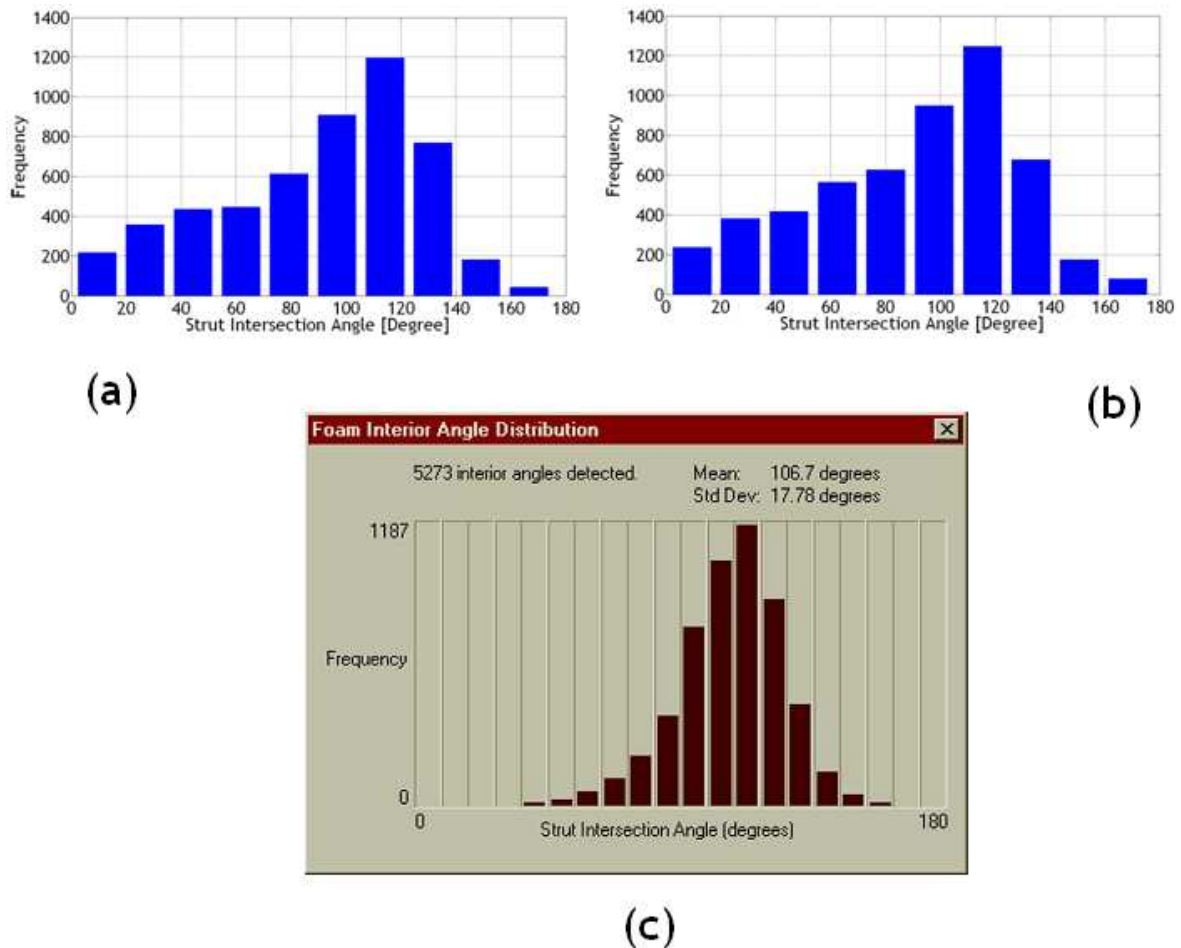


Figure 6-22: Strut intersection angular distribution for two MD samples.

In the case of real poly-disperse foam, the strut intersection angles are distributed from 45 to 160 degrees, with a modal value at about 120 degrees. The distribution bound for the numerical RVEs is much wider, from 5 to 175 degrees with modal values at just under 120 degree. The majority of the small intersection angles (less than 45°) are a direct results of the triangular faces, which contain at least one very sharp angle.

6.4 Conclusions of Chapter 6

The microstructural morphology of real foams obtained from imaging experiments, has been compared with 3-d numerically generated RVEs for foam-like materials. A 3-d version of the enhanced method of Zhu and the Lloyd's relaxation algorithm have been used to generate predominantly mono-disperse 3-d microstructures, while a new enhanced L-S MD algorithm has been used to generate poly-disperse 3-d microstructures.

RVEs generated using the enhanced 3-d method of Zhu method were found to have relatively poor morphological characteristics compared to experimental data obtained by analysing mono-disperse soap froth in the investigation by Matzke (1946) . Mono-disperse microstructures generated using the Lloyd's relaxation algorithm were found to have much better correspondence of parameters including cellular volume distribution, number of struts per face and number of faces per cell. However, due to presence of triangular surfaces (or quadrilateral surfaces with one very small strut) the numbers of pentagonal faces was found to be about 23% less than the data produced by Matzke (1946). The presence of a large number of triangular surfaces in the numerical RVE also resulted in a large fraction of small and unrealistic struts that affect the strut length distribution (see Figure 6-7).

Unlike the mono-disperse case, poly-disperse RVEs generated using the new enhanced L-S MD algorithm had very different geometrical parameters compared to data measured by Montminy et al. (2004) from a real 3-d poly-disperse foam. The main reason behind this discrepancy was due to the presence of unrealistic triangular surfaces or quadrilateral surfaces containing one very small strut. It is worth noting that in the mono-disperse case only about 10% of surfaces had poor triangular-like geometries (3% triangular+7% quadrilateral with one very small strut) whereas for the poly-disperse case this effect was about 4 times larger. One of the steps that Kraynik et al. (2003) used to modify RVEs was a relaxation

process involved the use of Surface Evolver to eliminate such triangular surfaces by applying a morphological transition method [Fortes and Ferro, 1985].

Another important factor affecting the L-S MD generated RVEs is the packing density of hard-spheres which was about 64%. Therefore, by even applying Voronoi-Laguerre method, the resultant cell volume will be significantly larger than the sphere volume that Laguerre-Voronoi cell is constructed around it.

It can be concluded that a method of eliminating triangular surfaces and improving the sphere packing density could potentially lead to much more realistic foam-like microstructural morphologies particularly for the poly-disperse case.

Chapter 7 . Conclusions and Future Work

7.1 Conclusions

Chapter 1 contained a general overview of the different types of porous materials that are considered in this research, with brief descriptions of their mechanical properties and internal morphologies. The modelling and mechanical evaluation approaches used in this investigation are also addressed.

In Chapter 2 various modelling methodologies to generate 2-d periodic RVEs for foam- and aerogel-like microstructures were reviewed. These methods were adapted in creating new algorithms, designed to be more effective in generating 2-d beam-based RVEs with periodic microstructures. A detailed description of these new algorithms was provided.

In Chapter 3, using the 2-d modelling techniques described in Chapter 2, beam-based RVEs were generated for both mono- and poly-disperse foam-like microstructures. RVEs were subjected to large compressive strains using a PBC. Internal self-contact within the RVE was modelled. The influence of this self-contact on the RVE's large-strain mechanical response was examined. The effect of geometrical irregularity on the RVE's large strain response was also investigated. Results suggested that as geometrical irregularity increases the contact strain (CS) will shift to lower strains. The comparison between contact strain (CS) and onset strain of densification (OSD) suggests that the efficiency method of determining the onset strain of densification is relatively insensitive to the degree of irregularity of the of RVE.

Chapter 4 is an investigation into the isotropy (or possible lack of isotropy) in the mechanical response of 2-d RVEs generated using the modelling techniques described in Chapter 2. The mechanical response of 2-d beam-based RVEs employing a PBC, under compressive loading in arbitrary directions was investigated. Results indicated that hexagonal honeycomb microstructures produce an anisotropic mechanical response. This is also true for RVEs generated using the enhanced method of Zhu with low to moderate degrees of irregularity. However, as α increases the mechanical response of the RVE tends to be more isotropic but at the cost of generating an increasingly unrealistic microstructure. In contrast, RVEs generated using the Lloyd's relaxation algorithms were found to be mechanically isotropic while having a realistic morphology. It should also be mentioned that the Lloyd's algorithm can effectively produce final regular and isotropic geometry when the initial microstructure configuration (before the relaxation) contains very random and irregular geometries (e.g. Poisson Voronoi). The Drop and Roll method was shown to have a good potential for generating poly-disperse microstructures with fairly isotropic mechanical response.

The intention of Chapter 5 was to: (i) establish the link between the internal morphology and the mechanical response of the RVEs and (ii) to evaluate the modelling techniques used to generate 2-d foam-like microstructures in terms of their ability to create realistic morphologies. As expected, RVEs with an isotropic cellular orientation distribution produced an isotropic mechanical response when compressed in arbitrary loading directions and RVEs with an anisotropic cellular orientation distribution produced a corresponding anisotropic mechanical response. The influence of cellular orientation distribution was found to increase at higher compressive strains, particularly in the plateau region of the stress-strain curves. It was also shown that the cell-collapse rate strongly depends on the cellular size distribution. Larger cells tended to collapse and deform faster than smaller cells. With regards to the mono-disperse case, such as RVEs generated using the Lloyd's relaxation algorithm, although the cells have almost equal sizes and morphologies, some of the cells were found to collapse and deform faster than

others, an effect possibly related to the cell's orientation with respect to the loading direction.

Chapter 6 focuses on the more challenging problem of 3-d modelling. A literature review of numerical techniques for 3-d modelling is provided together with a review of image-based investigations. Modelling and characterisation techniques employed in previous chapters are adapted to generate 3-d foam-like RVEs with periodic microstructures. The morphologies within RVEs generated using the Lloyd's relaxation algorithm were found to correspond closely with real mono-disperse foams microstructures. However, poly-disperse microstructures produced using a modified MD technique failed to generate realistic foam-like morphologies due to the presence of a large number of sharp triangular surfaces within the RVEs.

7.2 Future work

The work conducted so far in this investigation has successfully achieved many of the objectives outlined in Section 1.5. Nevertheless, multi-scale modelling of porous, randomly organised microstructures is a challenging topic and there is ample scope for future work. In this section a few ideas to further progress the research are outlined. Ideas include investigations into:

- the mechanical response of 3-d foam-like microstructures when compressed in arbitrary loading directions.
- the effect of both material and geometrical anisotropy on the mechanical response of both 2-d and 3-d RVEs, i.e. the investigation could be extended to consider anisotropy of the constituent material behaviour (due to higher elongation in a preferred direction) in addition to the geometrical anisotropy of the RVE already considered in this investigation.

- the effect of self-contact within 3-d RVEs of foam-like periodic microstructures on the mechanical response. Some preliminary steps in this direction have already been taken and are briefly described here. Due to the 3-d connectivity of beam elements in 3-d RVEs, it is not possible to use the equivalent shell-based microstructures, as with the 2-d case (see Chapter 3). To overcome this problem, two RVEs can be generated. The innovative method involves combining beam and shell elements to generate mutually constrained prism-like constructions, representing the individual ribs (struts) within the RVE, see Figure 7-1.

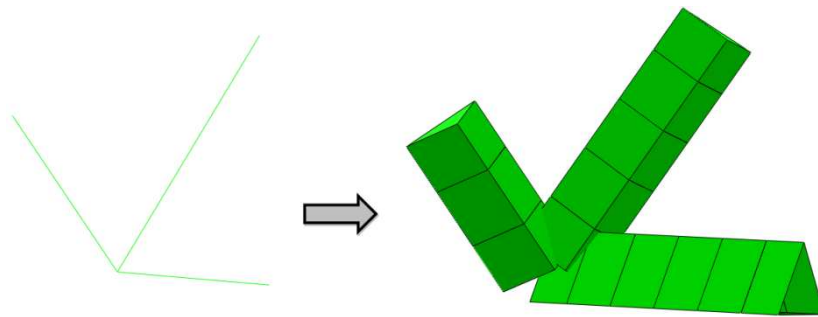


Figure 7-1: Beam to shell-based prism conversion.

The periodic beam-based RVE, see Figure 7.2a, can be compressed. To model self-contact within the RVE, a second RVE based on the shell-based prism structure is generated, with same structural configuration as that of the beam-based RVE, e.g. see Figure 7.2b. The deformation of the shell-based RVE is constrained to counterpart beam elements. The mechanical properties of the shell elements are set to be very much lower than those of the beam elements and therefore make a negligible contribution to the mechanical response of the RVE due to deformation. However the shell elements do make a significant contribution when self-contact within the RVE occurs.

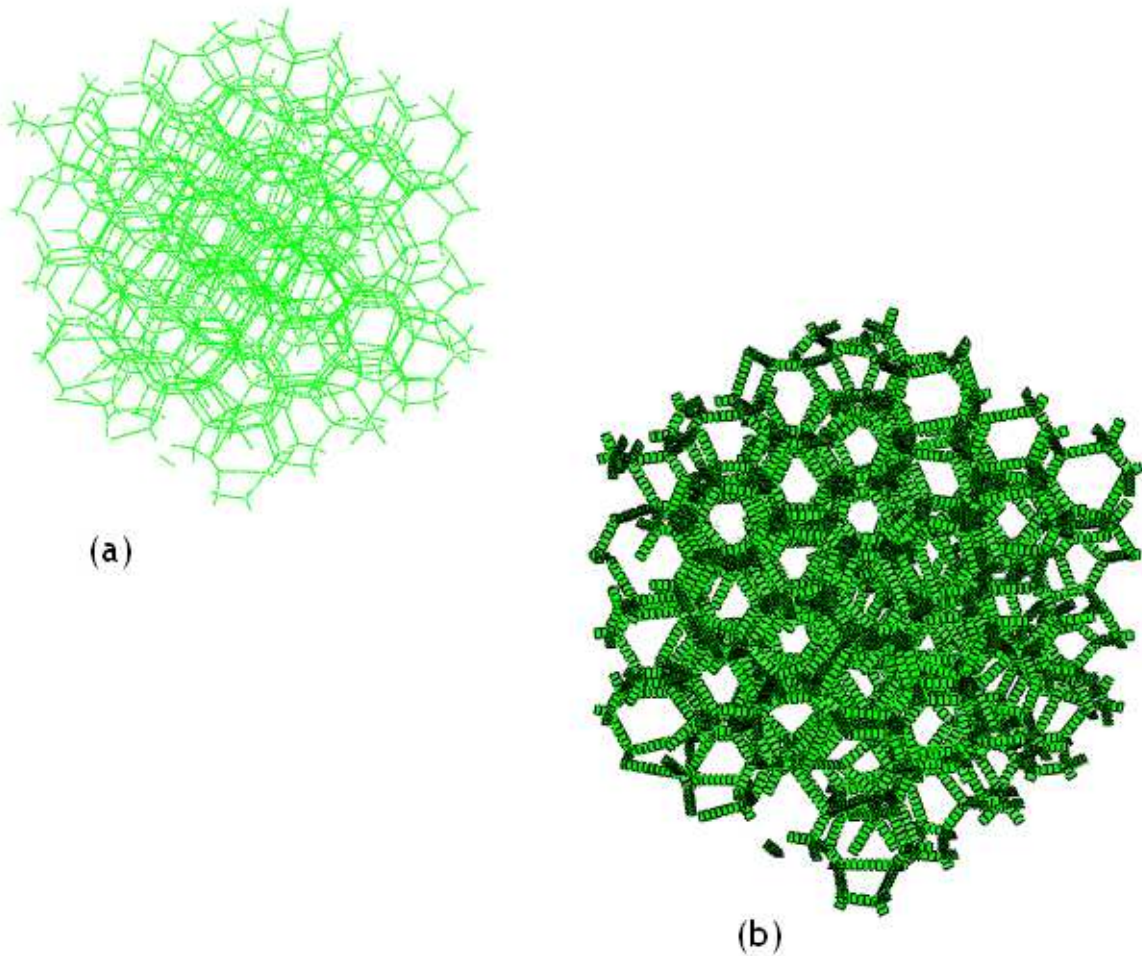


Figure 7-2: (a) 3-d periodic beam-based RVE. (b) 3-d prism shell-based RVE.

- Improvements of the morphological accuracy of 3-d RVEs. In Chapter 6 it was stated that the problem with 3D RVEs generated using a combination of MD and the Laguerre-Voronoi method was the high portion of sharp triangular surfaces within the resulting RVE. An algorithm to automatically eliminate these triangular surfaces could potentially lead to much more reasonable, morphologically-enhanced poly-disperse foam-like microstructures. One of the main steps of the Surface Evolver software [Brakke, 2009] is detection and elimination of such unrealistic surfaces. Thus, direct comparison of enhanced 3-d morphologies with those generated using both Surface Evolver and also those created from real image-based models would be an interesting next step for the research.

Appendix 1: Uni-axial compression of periodic honeycomb structure in an arbitrary direction

To apply deformation in arbitrary directions with respect to the orientation of the RVE other than in the perpendicular and transverse directions, a two dummy node set-up is not useful and an alternative method is required.

Considering uniaxial compression in the vertical direction, the deformation gradient tensor, \underline{F} , can be written as follows

$$\underline{F} = \begin{bmatrix} \lambda_1 & 0 \\ 0 & \lambda_2 \end{bmatrix} \quad \text{Equation A1-1}$$

where λ_1 and λ_2 are the principle stretch values in the X1 and X2 directions. From Eq. 3-4 $\lambda_1 = U_i^R - U_i^L = U_i^{d1}$ and $\lambda_2 = U_i^T - U_i^B = U_i^{d2}$ so the boundary condition is set in Abaqus as following:

$$\begin{aligned} U_1^{d2} &= 0 \\ U_2^{d2} &= \lambda_2, \text{ Defined by operator} \\ U_2^{d1} &= 0 \\ U_1^{d1} &= \lambda_1, \text{ To be defined through FE simulation} \end{aligned} \quad \text{Equation A1-2}$$

Now, if \underline{F} is to be calculated for uniaxial compression at an arbitrary angle, θ , then this is equivalent to rotating the reference system. So in rotated system $\underline{F}^1 = \underline{R}^1 \underline{F} \underline{R}$ where \underline{R} is a rotation matrix:

$$\underline{R} = \begin{bmatrix} \cos \theta & \sin \theta \\ -\sin \theta & \cos \theta \end{bmatrix} \quad \text{Equation A1-3}$$

$$\underline{F}^t = \begin{bmatrix} \lambda_1 \cos^2 \theta + \lambda_2 \sin^2 \theta & \sin \theta \cos \theta (\lambda_1 - \lambda_2) \\ \sin \theta \cos \theta (\lambda_1 - \lambda_2) & \lambda_1 \sin^2 \theta + \lambda_2 \cos^2 \theta \end{bmatrix} \quad \text{Equation A1-4}$$

Therefore, dummy nodes displacements (indicated as d_1 and d_2) can be re-written based on a new frame of reference that is shown in Eq. A1-4 as the following:

$$U_1^{d_1} = U_1^{d_3} \cos^2 \theta + U_2^{d_3} \sin^2 \theta \quad \text{Equation A1-5}$$

$$U_2^{d_1} = U_1^{d_3} \sin \theta \cos \theta - U_2^{d_3} \sin \theta \cos \theta \quad \text{Equation A1-6}$$

$$U_1^{d_2} = U_1^{d_3} \sin \theta \cos \theta - U_2^{d_3} \sin \theta \cos \theta \quad \text{Equation A1-7}$$

$$U_2^{d_2} = U_1^{d_3} \sin^2 \theta + U_2^{d_3} \cos^2 \theta \quad \text{Equation A1-8}$$

By setting a value of only one component of the third dummy node, d_3 , it is possible for the FE solver to obtain the other dummy nodes values for uniaxial compression in the desired direction.

References:

Abigail., K., <http://plus.maths.org/content/eulers-polyhedron-formula>, 2011

ABRAMOVITCH, H., BURGARD, M., EDERY-AZULAY, L., EVANS, K. E., HOFFMEISTER, M., MILLER, W., SCARPA, F., SMITH, C. W. & TEE, K. F. 2010. Smart tetrachiral and hexachiral honeycomb: Sensing and impact detection. *Composites Science and Technology*, 70, 1072-1079.

ADAMCZYK, Z., SIWEK, B., ZEMBALA, M. & WERONSKI, P. 1997. Influence of polydispersity on random sequential adsorption of spherical particles. *Journal of Colloid and Interface Science*, 185, 236-244.

AMIRA., Zuse Institute Berlin., FEI Visualisation Sciences Group,
<http://www.vsg3d.com/amira/overview>

ANTHOINE, A. 1995. Derivation of the Inplane Elastic Characteristics of Masonry through Homogenization Theory. *International Journal of Solids and Structures*, 32, 137-&.

Mathworld, <http://mathworld.wolfram.com/ApolloniusProblem.html>

AURENHAMMER, F. 1991. Voronoi Diagrams - a Survey of a Fundamental Geometric Data Structure. *Computing Surveys*, 23, 345-405.

AYERS, M. R. & HUNT, A. J. 2001. Observation of the aggregation behavior of silica sols using laser speckle contrast measurements. *Journal of Non-Crystalline Solids*, 290, 122-128.

BANHART, J. 2001. Manufacture, characterisation and application of cellular metals and metal foams. *Progress in Materials Science*, 46, 559-U3.

BANHART, J. & BAUMEISTER, J. 1998. Deformation characteristics of metal foams. *Journal of Materials Science*, 33, 1431-1440.

BENOUALI, A. H., FROYEN, L., DILLARD, T., FOREST, S. & N'GUYEN, F. 2005. Investigation on the influence of cell shape anisotropy on the mechanical performance of closed cell aluminium foams using micro-computed tomography. *Journal of Materials Science*, 40, 5801-5811.

BHATTACHARYA, S. & KIEFFER, J. 2005. Fractal dimensions of silica gels generated using reactive molecular dynamics simulations. *Journal of Chemical Physics*, 122.

BIANCHI, M., SCARPA, F. & SMITH, C. W. 2010. Shape memory behaviour in auxetic foams: Mechanical properties. *Acta Materialia*, 58, 858-865.

- BITZER, T (1997). Honeycomb Technology: Materials, Design, Manufacturing, Applications and Testing, London: Chapman & Hall
- BOROVINSEK, M. & REN, Z. 2008. Computational modelling of irregular open-cell foam behaviour under impact loading. *Materialwissenschaft Und Werkstofftechnik*, 39, 114-120.
- BRAKKE., K, [The Surface Evolver](#), *Experimental Mathematics* vol. 1 no. 2 (1992), 141-165.
- BRAKKE., K, 2009 <http://www.susqu.edu/facstaff/b/brakke/default.htm>
- BRILLIANTOV, N. V., ANDRIENKO, Y. A., KRAPIVSKY, P. L. & KURTHS, J. 1998. Polydisperse adsorption: Pattern formation kinetics, fractal properties, and transition to order. *Physical Review E*, 58, 3530-3536.
- BRINKER. C. J., SCHERER. G. W., *Sol-Gel Science. The Physics and Chemistry of Sol-Gel Processing*. Academic Press, NY, (1990)
- BOUAKBA, M., BEZAZI, A., SCARPA, F. 2012, *International journal of solids and structures*, 49(18) 2450-59
- JOHN BURKARDT, MAX GUNZBURGER, JANET PETERSON, AND REBECCA BRANNON, *User Manual and Supporting Information for Library of Codes for Centroidal Voronoi Point Placement and Associated Zeroth, First, and Second Moment Determination*, SAND2002-0099 Unlimited Release Printed February 2002
- CALLISTER., W., JR., *Materials science and engineering as introduction*, John Wiley and Sons, 6th edition, 2003
- CHEN, C., LU, T. J. & FLECK, N. A. 1999. Effect of imperfections on the yielding of two-dimensional foams. *Journal of the Mechanics and Physics of Solids*, 47, 2235-2272.
- CHEN, Y. J., SCARPA, F., LIU, Y. J. & LENG, J. S. 2013. Elasticity of anti-tetrachiral anisotropic lattices. *International Journal of Solids and Structures*, 50, 996-1004.
- CODY, J., *An Overview of Software Development for Special Functions*, *Lecture Notes in Mathematics*, 506, Numerical Analysis Dundee, G. A. Watson (ed.), Springer Verlag, Berlin, 1976

- COOPER, D. W. 1988. Random-Sequential-Packing Simulations in 3 Dimensions for Spheres. *Physical Review A*, 38, 522-524.
- DAWSON, J. R. & SHORTALL, J. B. 1982. The Microstructure of Rigid Polyurethane Foams. *Journal of Materials Science*, 17, 220-224.
- DESHPANDE, V. S., FLECK, N. A. & ASHBY, M. F. 2001. Effective properties of the octet-truss lattice material. *Journal of the Mechanics and Physics of Solids*, 49, 1747-1769.
- DESMOND, K. W. & WEEKS, E. R. 2009. Random close packing of disks and spheres in confined geometries. *Physical Review E*, 80.
- DESPETIS, F., BENGOURNA, N., LARTIGUE, B., SPAGNOL, S. & OLIVI-TRAN, N. 2012. Three-dimensional reconstruction of aerogels from TEM images. *Journal of Non-Crystalline Solids*, 358, 1180-1184.
- DEUTSCHER, G., MAYNARD, R. & PARODI, O. 1988. Simple-Model of the Elasticity of Heterogeneous Materials - Application to Silica-Gels. *Europhysics Letters*, 6, 49-54.
- DILLARD, T., N'GUYEN, F., MAIRE, E., SALVO, L., FOREST, S., BIENVENU, Y., BARTOUT, J. D., CROSET, M., DENDIEVEL, R. & CLOETENS, P. 2005. 3D quantitative image analysis of open-cell nickel foams under tension and compression loading using X-ray microtomography. *Philosophical Magazine*, 85, 2147-2175.
- DONEV, A., TORQUATO, S., STILLINGER, F. H. & CONNELLY, R. 2004. A linear programming algorithm to test for jamming in hard-sphere packings. *Journal of Computational Physics*, 197, 139-166.
- DORCHEH, A. S. & ABBASI, M. H. 2008. Silica aerogel; synthesis, properties and characterization. *Journal of Materials Processing Technology*, 199, 10-26.
- ELLIOTT, J. A., WINDLE, A. H., HOBDELL, J. R., EECKHAUT, G., OLDMAN, R. J., LUDWIG, W., BOLLER, E., CLOETENS, P. & BARUCHEL, J. 2002. In-situ deformation of an open-cell flexible polyurethane foam characterised by 3D computed microtomography. *Journal of Materials Science*, 37, 1547-1555.
- ELMOUTAOUAKKIL, A., SALVO, L., MAIRE, E. & PEIX, G. 2002. 2D and 3D characterization of metal foams using X-ray tomography. *Advanced Engineering Materials*, 4, 803-807.
- EMMERLING, A. & FRICKE, J. 1997. Scaling properties and structure of aerogels. *Journal of Sol-Gel Science and Technology*, 8, 781-788.
- EVANS, M., N. HASTINGS, and B. Peacock, *Statistical Distributions*, 2nd edition, John Wiley and Sons, 1993

- FAN, Z. G., WU, Y. G., ZHAO, X. H. & LU, Y. Z. 2004. Simulation of polycrystalline structure with Voronoi diagram in Laguerre geometry based on random closed packing of spheres. *Computational Materials Science*, 29, 301-308.
- FARR, R. S. & GROOT, R. D. 2009. Close packing density of polydisperse hard spheres. *Journal of Chemical Physics*, 131.
- FAZEKAS, A., DENDIEVEL, R., SALVO, L. & BRECHET, Y. 2002. Effect of microstructural topology upon the stiffness and strength of 2D cellular structures. *International Journal of Mechanical Sciences*, 44, 2047-2066.
- FORTES, M. A. & FERRO, A. C. 1985. Trivalent Polyhedra - Properties, Representation and Enumeration. *Acta Metallurgica*, 33, 1683-1696.
- GABBRIELLI, R., Foam geometry and structural design of porous material, A thesis submitted for the degree of Doctor of Philosophy, University of Bath, Department of Mechanical Engineering Submitted: April 2009 Revised: August 2009
- GAN, Y. X., KAMLAH, M. & REIMANN, J. 2010. Computer simulation of packing structure in pebble beds. *Fusion Engineering and Design*, 85, 1782-1787.
- GERVOIS, A., OGER, L., RICHARD, P. & TROADEC, J. P. 2002. Voronoi and radical tessellations of packings of spheres. *Computational Science-Iccs 2002, Pt Iii, Proceedings*, 2331, 95-104.
- GIBSON, L. J., ASHBY, M. F., SCHAJER, G. S. & ROBERTSON, C. I. 1982. The Mechanics of Two-Dimensional Cellular Materials. *Proceedings of the Royal Society of London Series a-Mathematical Physical and Engineering Sciences*, 382, 25-42.
- GIBSON, L.J., ASHBY, M.F., 1997. *Cellular Solids - Structure and Properties*. Cambridge University Press, Cambridge.
- GIBSON, L. N., Model of heterogeneous microscale in SOFI for Monte Carlo simulations, (2007),
<http://www.math.oregonstate.edu/~gibsonn/Teaching/MTH323-001S09/Supplements/SamplePaper.pdf>
- GIMEL, J. C., NICOLAI, T. & DURAND, D. 1999. 3D Monte Carlo simulations of diffusion limited cluster aggregation up to the sol-gel transition: Structure and kinetics. *Journal of Sol-Gel Science and Technology*, 15, 129-136.
- GITTUS, J. H. 1974. Theory of Irradiation-Induced Primary Creep in Crystalline Solids. *Philosophical Magazine*, 29, 679-683.
- GITTUS., J., ZARKA., J., NEMAT-NASSER., S., *Large Deformations of Solids: Physical Basis and Mathematical Modelling*, 1987

- GONG, L. & KYRIAKIDES, S. 2005. Compressive response of open cell foams - Part II: Initiation and evolution of crushing. *International Journal of Solids and Structures*, 42, 1381-1399.
- GONG, L., KYRIAKIDES, S. & JANG, W. Y. 2005. Compressive response of open-cell foams. Part I: Morphology and elastic properties. *International Journal of Solids and Structures*, 42, 1355-1379.
- GRAY, J. J., KLEIN, D. H., KORGEL, B. A. & BONNECAZE, R. T. 2001. Microstructure formation and kinetics in the random sequential adsorption of polydisperse tethered nanoparticles modeled as hard disks. *Langmuir*, 17, 2317-2328.
- GRENESTEDT, J. L. & TANAKA, K. 1998. Influence of cell shape variations on elastic stiffness of closed cell cellular solids. *Scripta Materialia*, 40, 71-77.
- GROSSE, J., DIETRICH, B., GARRIDO, G. I., HABISREUTHER, P., ZARZALIS, N., MARTIN, H., KIND, M. & KRAUSHAAR-CZARNETZKI, B. 2009. Morphological Characterization of Ceramic Sponges for Applications in Chemical Engineering. *Industrial & Engineering Chemistry Research*, 48, 10395-10401.
- GUEDES, J. M. & KIKUCHI, N. 1990. Preprocessing and Postprocessing for Materials Based on the Homogenization Method with Adaptive Finite-Element Methods. *Computer Methods in Applied Mechanics and Engineering*, 83, 143-198.
- HARDENACKE, V. & HOHE, J. 2009. Local probabilistic homogenization of two-dimensional model foams accounting for micro structural disorder. *International Journal of Solids and Structures*, 46, 989-1006.
- HARDER, J. M. & SILBERT, M. 1980. Binary Mixture of Hard-Spheres with Attractive Square-Well Interaction between Unlike Spheres. *Chemical Physics Letters*, 75, 571-574.
- HART, D. & RUDMAN, A. J. 1997. Least-squares fit of an ellipse to anisotropic polar data: Application to azimuthal resistivity surveys in karst regions. *Computers & Geosciences*, 23, 189-194.
- HASTINGS, J. K., JUDS, M. A., BRAUER, J. R., Accuracy and Economy of Finite Element Magnetic Analysis, 33rd Annual National Relay Conference, April 1985
- HE, D. & EKERE, N. N. 1998. Computer simulation of powder compaction of spherical particles. *Journal of Materials Science Letters*, 17, 1723-1725.
- HENCH, L. L., *Sol-Gel Silica, Properties, Processing and Technology Transfer*, 1998 William Andrew Inc. ISBN: 978-0-8155-1419-0, Electronic access through sciencedirect
- HILL, R. 1963. Elastic Properties of Reinforced Solids - Some Theoretical Principles. *Journal of the Mechanics and Physics of Solids*, 11, 357-372.

- HOHE, J. & BECKER, W. 2003. Geometrically nonlinear stress-strain behavior of hyperelastic solid foams. *Computational Materials Science*, 28, 443-453.
- Horrigan, E. J., Smith, C. W., Scarpa, F., Gaspar, N., Javadi, A. A., Berger, M. A., Evans, K. E., Simulated optimisation of disordered structures with negative Poisson's ratios, (2009), *Mechanics of Materials* 41 (8) 919-927
- HUBER, A. T. & GIBSON, L. J. 1988. Anisotropy of Foams. *Journal of Materials Science*, 23, 3031-3040.
- HUNT, A., AYERS, M., A Brief History of Silica Aerogels, Lawrence Berkeley Laboratories: Microstructured Materials Group, <http://eetd.lbl.gov/ecs/aerogels/>
- HUSING, N. & SCHUBERT, U. 1998. Aerogels airy materials: Chemistry, structure, and properties. *Angewandte Chemie-International Edition*, 37, 23-45.
- JANG, W. Y., KRAYNIK, A. M. & KYRIAKIDES, S. 2008. On the microstructure of open-cell foams and its effect on elastic properties. *International Journal of Solids and Structures*, 45, 1845-1875.
- JANG, W. Y., KYRIAKIDES, S. & KRAYNIK, A. M. 2010. On the compressive strength of open-cell metal foams with Kelvin and random cell structures. *International Journal of Solids and Structures*, 47, 2872-2883.
- JEBUR, Q., H., Characterisation and Modelling of Transversely Isotropic Flexible Viscoelastic Foam., A thesis for the degree of Doctor of Philosophy (PhD), Submitted to the School of Engineering, College of Science and Engineering, University of Glasgow, June 2013
- JOHN, M. & LI, G. Q. 2010. Self-healing of sandwich structures with a grid stiffened shape memory polymer syntactic foam core. *Smart Materials & Structures*, 19.
- KANAUN, S. & TKACHENKO, O. 2006. Mechanical properties of open cell foams: Simulations by Laguerre tessellation procedure. *International Journal of Fracture*, 140, 305-312.
- KANSAL, A. R., TORQUATO, S. & STILLINGER, F. H. 2002. Computer generation of dense polydisperse sphere packings. *Journal of Chemical Physics*, 117, 8212-8218.
- KISTLER, S. S. 1931. Coherent expanded aerogels and jellies. *Nature*, 127, 741-741.
- KISTLER, S. S. 1932. Coherent expanded aerogels. *Journal of Physical Chemistry*, 36, 52-64.
- KOLB, M. & JULLIEN, R. 1984. Chemically Limited Versus Diffusion Limited Aggregation. *Journal De Physique Lettres*, 45, L977-L981.

KOUZNETSOVA, V., BREKELMANS, W. A. M. & BAAIJENS, F. P. T. 2001. An approach to micro-macro modeling of heterogeneous materials. *Computational Mechanics*, 27, 37-48.

KRAYNIK, A. M. 1981. Rheological Aspects of Thermoplastic Foam Extrusion. *Polymer Engineering and Science*, 21, 80-85.

KRAYNIK, A. M. 1988. Foam Flows. *Annual Review of Fluid Mechanics*, 20, 325-357.

KRAYNIK, A. M. 2006. The structure of random foam. *Advanced Engineering Materials*, 8, 900-906.

KRAYNIK, A. M., REINELT, D. A. & VAN SWOL, F. 2003. Structure of random monodisperse foam. *Physical Review E*, 67.

KRAYNIK, A. M., REINELT, D. A. & VAN SWOL, F. 2004. Structure of random foam. *Physical Review Letters*, 93.

KUMAR. V. (2007), <http://faculty.washington.edu/vkumar/microcel/>

LETO ., J., Diffusion Limited Aggregation (DLA) version 0.03, Tested in Matlab 6.0 and 7.1, Sat Jan 06 00:27:21 EST 200 , <http://leto.net/math/dla.php>

LEVENTIS, N., SOTIRIOU-LEVENTIS, C., MULIK, S., PATIL, V., MOHITE, D., ZHANG, Y. L. & LU, H. B. 2008. POLY 165-Assemblies of nanoparticles as 3-D scaffolds for new materials design: From polymer crosslinked aerogels to polymer matrix composites. *Abstracts of Papers of the American Chemical Society*, 236.

LI, K., GAO, X. L. & SUBHASH, G. 2006. Effects of cell shape and strut cross-sectional area variations on the elastic properties of three-dimensional open-cell foams. *Journal of the Mechanics and Physics of Solids*, 54, 783-806.

LI, K., GAO, X. L. & WANG, J. 2007. Dynamic crushing behavior of honeycomb structures with irregular cell shapes and non-uniform cell wall thickness. *International Journal of Solids and Structures*, 44, 5003-5026.

LI, Q. M., MAGKIRIADIS, I. & HARRIGAN, J. J. 2006. Compressive strain at the onset of densification of cellular solids. *Journal of Cellular Plastics*, 42, 371-392.

LIU, Y., WANG, W. P., LEVY, B., SUN, F., YAN, D. M., LU, L. & YANG, C. L. 2009. On Centroidal Voronoi Tessellation-Energy Smoothness and Fast Computation. *Acm Transactions on Graphics*, 28.

LIVAGE, J. 1991. Vanadium Pentoxide Gels. *Chemistry of Materials*, 3, 578-593.

LLOYD, S. P. 1982. Least-Squares Quantization in Pcm. *Ieee Transactions on Information Theory*, 28, 129-137.

- LUBACHEVSKY, B. D. & STILLINGER, F. H. 1990. Geometric-Properties of Random Disk Packings. *Journal of Statistical Physics*, 60, 561-583.
- MA, H. S., PREVOST, J. H. & SCHERER, G. W. 2002. Elasticity of DLCA model gels with loops. *International Journal of Solids and Structures*, 39, 4605-4614.
- MA, H. S., ROBERTS, A. P., PREVOST, J. H., JULLIEN, R. & SCHERER, G. W. 2000. Mechanical structure-property relationship of aerogels. *Journal of Non-Crystalline Solids*, 277, 127-141.
- M. MALEKJAFARIAN, S.K. SADRNEZHAAD , M.S. ABRAVI , M. GOLESTANIPOUR , H. AMINI , MASHHADI; Manufacturing Aluminum Foams by Melt Gas Injection Process, 7th International Conference on Porous Metals and Metallic Foams
- MATZKE, E. B. 1946. The 3-Dimensional Shape of Bubbles in Foam - an Analysis of the Role of Surface Forces in 3-Dimensional Cell Shape Determination. *American Journal of Botany*, 33, 58-80.
- MCDONALD, S. A., RAVIRALA, N., WITHERS, P. J. & ALDERSON, A. 2009. In situ three-dimensional X-ray microtomography of an auxetic foam under tension. *Scripta Materialia*, 60, 232-235.
- MEAKIN, P. 1983. Formation of Fractal Clusters and Networks by Irreversible Diffusion-Limited Aggregation. *Physical Review Letters*, 51, 1119-1122.
- MEAKIN, P. 1999. A historical introduction to computer models for fractal aggregates. *Journal of Sol-Gel Science and Technology*, 15, 97-117.
- MEAKIN, P. & WASSERMAN, Z. R. 1984. Some Universality Properties Associated with the Cluster Cluster Aggregation Model. *Physics Letters A*, 103, 337-341.
- MEBATSION, H. K., VERBOVEN, P., VERLINDEN, B. E., HO, Q. T., NGUYEN, T. A. & NICOLAI, B. M. 2006. Microscale modelling of fruit tissue using Voronoi tessellations. *Computers and Electronics in Agriculture*, 52, 36-48.
- MERZBACHER, C. I., BARKER, J. G., SWIDER, K. E. & ROLISON, D. R. 1998. Effect of re-wetting on silica aerogel structure: a SANS study. *Journal of Non-Crystalline Solids*, 224, 92-96.
- MIEHE, C. & KOCH, A. 2002. Computational micro-to-macro transitions of discretized microstructures undergoing small strains. *Archive of Applied Mechanics*, 72, 300-317.
- MILLS, N. J., FITZGERALD, C., GILCHRIST, A. & VERDEJO, R. 2003. Polymer foams for personal protection: cushions, shoes and helmets. *Composites Science and Technology*, 63, 2389-2400.

MILLS, N. J., *Polymer Foams Handbook: Engineering and Biomechanics Applications and Design Guide*, 2007, Butterworth-Heinemann

MILTZ, J. & RAMON, O. 1990. Energy-Absorption Characteristics of Polymeric Foams Used as Cushioning Materials. *Polymer Engineering and Science*, 30, 129-133.

MIMIC., <http://biomedical.materialise.com/>

MONER-GIRONA, M., ROIG, A., MOLINS, E. & LLIBRE, J. 2003. Sol-gel route to direct formation of silica aerogel microparticles using supercritical solvents. *Journal of Sol-Gel Science and Technology*, 26, 645-649.

MONTMINY, M. D., TANNENBAUM, A. R. & MACOSKO, C. W. 2001. New algorithms for 3-D imaging and analysis of open-celled foams. *Journal of Cellular Plastics*, 37, 501-515.

MONTMINY, M. D., TANNENBAUM, A. R. & MACOSKO, C. W. 2004. The 3D structure of real polymer foams. *Journal of Colloid and Interface Science*, 280, 202-211.

MULCHRONE, K. F. & CHOUDHURY, K. R. 2004. Fitting an ellipse to an arbitrary shape: implications for strain analysis. *Journal of Structural Geology*, 26, 143-153.

NAKANO, A., BI, L. S., KALIA, R. K. & VASHISHTA, P. 1993. Structural Correlations in Porous Silica - Molecular-Dynamics Simulation on a Parallel Computer. *Physical Review Letters*, 71, 85-88.

NEIMARK, A. V. & VIGNESADLER, M. 1995. Variations from the Plateau Law in Foams. *Physical Review E*, 51, 788-791.

OKUBO, T. & ODAGAKI, T. 2004. Random packing of binary hard discs. *Journal of Physics-Condensed Matter*, 16, 6651-6659.

PAJONK, G. M., RAO, A. V., PARVATHY, N. N. & ELALOUI, E. 1996. Microstructural characterization of silica aerogels using scanning electron microscopy. *Journal of Materials Science*, 31, 5683-5689.

PAPKA, S. D. & KYRIAKIDES, S. 1994. Inplane Compressive Response and Crushing of Honeycomb. *Journal of the Mechanics and Physics of Solids*, 42, 1499-1532.

PATRICK, J. F., SOTTOS, N. R. & WHITE, S. R. 2012. Microvascular based self-healing polymeric foam. *Polymer*, 53, 4231-4240.

PAVLLOTIS., G., A., STUART., A., M., *Multiscale methods : averaging and homogenization*, New York, NY : Springer, c2008

PIERRE. A. A., *Introduction to Sol-Gel Processing*, Kluwer Academic Publishers, Boston, (1998)

- PLATEAU., J., *Statique Experimentale et Theorique des Liquids Soumis aux Seules Forces Moleculaires*, Gauthier-Villars, Paris, 1873.
- POHL, P. I., FAULON, J. L. & SMITH, D. M. 1995. Molecular-Dynamics Computer-Simulations of Silica Aerogels. *Journal of Non-Crystalline Solids*, 186, 349-355.
- RAHMANI, A., BENOIT, C., JULLIEN, R., POUSSIGUE, G. & SAKOUT, A. 1996. Dynamical properties of a diffusion-limited cluster-cluster aggregation model. *Journal of Physics-Condensed Matter*, 8, 5555-5567.
- RAPAPORT. D. C., *The art of molecular dynamics simulation / Second edition 2004*, Cambridge university press, 978-0-521-82568-9
- REDENBACH, C. 2009. Modelling Foam Structures Using Random Tessellations. *Ecs10: The10th European Congress of Stereology and Image Analysis*, 51-62.
- RICHARD, P., OGER, L., TROADEC, J. P. & GERVOIS, A. 2001. A model of binary assemblies of spheres. *European Physical Journal E*, 6, 295-303.
- ROBERTS, A. P. 1997. Morphology and thermal conductivity of model organic aerogels. *Physical Review E*, 55, R1286-R1289.
- ROUAULT, Y. & ASSOULINE, S. 1998. Modeling the disordered dense phase in the packing of binary mixtures of spheres. *Journal of Colloid and Interface Science*, 204, 87-92.
- SAADA. A. S. 1974, *Elasticity, theory and applications*. Pregamon unified engineering series, 16
- SAN MARCHI, C., DESPOIS, J. F. & MORTENSEN, A. 2004. Uniaxial deformation of open-cell aluminum foam: the role of internal damage. *Acta Materialia*, 52, 2895-2902.
- SCARPA, F., CIFFO, L. G. & YATES, J. R. 2004. Dynamic properties of high structural integrity auxetic open cell foam. *Smart Materials & Structures*, 13, 49-56.
- SENN. H. M. / online pdf lecture notes / University of Glasgow, Department of Chemistry <http://www.chem.gla.ac.uk/staff/senn/teaching.php>
- SHULMEISTER, V., VAN DER BURG, M. W. D., VAN DER GIESSEN, E. & MARISSSEN, R. 1998. A numerical study of large deformations of low-density elastomeric open-cell foams. *Mechanics of Materials*, 30, 125-140.
- SILVA, M. J. & GIBSON, L. J. 1997. The effects of non-periodic microstructure and defects on the compressive strength of two-dimensional cellular solids. *International Journal of Mechanical Sciences*, 39, 549-563.

SILVA, M. J. & GIBSON, L. J. 1997. The effects of non-periodic microstructure and defects on the compressive strength of two-dimensional cellular solids. *International Journal of Mechanical Sciences*, 39, 549-563.

SILVA, M. J. & GIBSON, L. J. 1997. Modeling the mechanical behavior of vertebral trabecular bone: Effects of age-related changes in microstructure. *Bone*, 21, 191-199.

SILVA, M. J., HAYES, W. C. & GIBSON, L. J. 1995. The Effects of Nonperiodic Microstructure on the Elastic Properties of 2-Dimensional Cellular Solids. *International Journal of Mechanical Sciences*, 37, 1161-1177.

Simpleware Ltd., ScanIp Image processing Software,
<http://www.simpleware.com/software/scanip.php>

SMIT, R. J. M., BREKELMANS, W. A. M. & MEIJER, H. E. H. 1998. Prediction of the mechanical behavior of nonlinear heterogeneous systems by multi-level finite element modeling. *Computer Methods in Applied Mechanics and Engineering*, 155, 181-192.

SONG, Y. Z., WANG, Z. H., ZHAO, L. M. & LUO, J. A. 2010. Dynamic crushing behavior of 3D closed-cell foams based on Voronoi random model. *Materials & Design*, 31, 4281-4289.

SURACE, R., DE FILIPPIS, L. A. C., NIINI, E., LUDOVICO, A. D. & ORKAS, J. 2009. Morphological Investigation of Foamed Aluminum Parts Produced by Melt Gas Injection. *Advances in Materials Science and Engineering*.

SURACE, R., DE FILIPPIS, L. A. C., (2010). Investigation and Comparison of Aluminium Foams Manufactured by Different Techniques, *Advanced Knowledge Application in Practice*, Igor Fuerstner (Ed.), ISBN: 978-953-307-141-1, InTech, Available from: <http://www.intechopen.com/books/advanced-knowledgeapplication-in-practice/investigation-and-comparison-of-aluminium-foams-manufactured-by-differenttechniques>

SWAN, C. C. 1994. Techniques for Stress-Controlled and Strain-Controlled Homogenization of Inelastic Periodic Composites. *Computer Methods in Applied Mechanics and Engineering*, 117, 249-267.

SYKULSKI, J. K. 2004. Reducing computational effort in field optimisation problems. *Compel-the International Journal for Computation and Mathematics in Electrical and Electronic Engineering*, 23, 159-172.

TAGARIELLI, V. L., DESHPANDE, V. S., FLECK, N. A. & CHEN, C. 2005. A constitutive model for transversely isotropic foams, and its application to the indentation of balsa wood. *International Journal of Mechanical Sciences*, 47, 666-686.

TANEMURA, M., Statistical Distributions of Poisson Voronoi Cells in Two and Three Dimensions, *Forma*, 18, 221-247, 2003

TAYLOR, J., E., The Structure of Singularities in Soap-Bubble-Like and Soap-Film-Like Minimal Surfaces (1976), *Annals of Mathematics, Second Series* 103 (3): 489-539

TIMOSHENKO AND GERE (1961), *Theory of elastic stability*, 2nd edition, McGraw Hill

THOMSON, W. "On the Division of Space with Minimum Partitional Area." *Philos. Mag.* 24, 503, 1887

TORQUATO, S., DONEV, A. & STILLINGER, F. H. 2003. Breakdown of elasticity theory for jammed hard-particle packings: conical nonlinear constitutive theory. *International Journal of Solids and Structures*, 40, 7143-7153.

VANDERBURG, M. W. D., SHULMEISTER, V., VANDERGEISSEN, E. & MARISSSEN, R. 1997. On the linear elastic properties of regular and random open-cell foam models. *Journal of Cellular Plastics*, 33, 31-40.

VISSCHER, W. M. & BOLSTERL. M 1972. Random Packing of Equal and Unequal Spheres in 2 and 3 Dimensions. *Nature*, 239, 504-506.

VORONOI, G., 1908. Nouvelles applications des paramètres continus à la théorie des formes quadratiques. *Journal für Reine und Angewandte Mathematik* 134, 198-312

WADLEY, H. N. G., FLECK, N. A. & EVANS, A. G. 2003. Fabrication and structural performance of periodic cellular metal sandwich structures. *Composites Science and Technology*, 63, 2331-2343.

WARREN, W. E. & KRAYNIK, A. M. 1988. The Linear Elastic Properties of Open-Cell Foams. *Journal of Applied Mechanics-Transactions of the Asme*, 55, 341-346.

WEAIRE, D. 1992. Some Lessons from Soap Froth for the Physics of Soft Condensed Matter. *Physica Scripta*, T45, 29-33.

WEAIRE, D., HUTZLER, S., 1999, Oxford University Press

WEAIRE, D. 2008. The rheology of foam. *Current Opinion in Colloid & Interface Science*, 13, 171-176.

WEAIRE, D. & PHELAN, R. 1994. A Counterexample to Kelvin Conjecture on Minimal-Surfaces. *Philosophical Magazine Letters*, 69, 107-110.

- WITTEN, T. A. & SANDER, L. M. 1981. Diffusion-Limited Aggregation, a Kinetic Critical Phenomenon. *Physical Review Letters*, 47, 1400-1403.
- WITTEN, T. A. & SANDER, L. M. 1983. Diffusion-Limited Aggregation. *Physical Review B*, 27, 5686-5697.
- WOIGNIER, T., PHALIPPOU, J. & VACHER, R. 1989. Parameters Affecting Elastic Properties of Silica Aerogels. *Journal of Materials Research*, 4, 688-692.
- WOIGNIER, T., PRIMERA, J., LAMY, M., FEHR, C., ANGLARET, E., SEMPERE, R. & PHALIPPOU, J. 2004. The use of silica aerogels as host matrices for chemical species - Different ways to control the permeability and the mechanical properties. *Journal of Non-Crystalline Solids*, 350, 299-307.
- WU, Y. G., FAN, Z. G. & LU, Y. Z. 2003. Bulk and interior packing densities of random close packing of hard spheres. *Journal of Materials Science*, 38, 2019-2025.
- YAO., N., *Focused ion beam systems, basic and applications*, Cambridge university press, 2007
- YOUSSEF, S., MAIRE, E. & GAERTNER, R. 2005. Finite element modelling of the actual structure of cellular materials determined by X-ray tomography. *Acta Materialia*, 53, 719-730.
- ZHANG, G. H., DASS, A., RAWASHDEH, A. M. M., THOMAS, J., COUNSIL, J. A., SOTIRIOU-LEVENTIS, C., FABRIZIO, E. F., ILHAN, F., VASSILARAS, P., SCHEIMAN, D. A., MCCORKLE, L., PALCZER, A., JOHNSTON, J. C., MEADOR, M. A. & LEVENTIS, N. 2004. Isocyanate-crosslinked silica aerogel monoliths: preparation and characterization. *Journal of Non-Crystalline Solids*, 350, 152-164.
- ZHANG, G. Q., WANG, B., MA, L., XIONG, J. & WU, L. Z. 2013. Response of sandwich structures with pyramidal truss cores under the compression and impact loading. *Composite Structures*, 100, 451-463.
- ZHENG, Z. J., YU, J. L. & LI, J. R. 2005. Dynamic crushing of 2D cellular structures: A finite element study. *International Journal of Impact Engineering*, 32, 650-664.
- ZHU, H. X., HOBDELL, J. R. & WINDLE, A. H. 2000. Effects of cell irregularity on the elastic properties of open-cell foams. *Acta Materialia*, 48, 4893-4900.
- ZHU, H. X., HOBDELL, J. R. & WINDLE, A. H. 2001. Effects of cell irregularity on the elastic properties of 2D Voronoi honeycombs. *Journal of the Mechanics and Physics of Solids*, 49, 857-870.
- ZHU, H. X., KNOTT, J. F. & MILLS, N. J. 1997. Analysis of the elastic properties of open-cell foams with tetrakaidecahedral cells. *Journal of the Mechanics and Physics of Solids*, 45, 319-&.

- ZHU, H. X. & MILLS, N. J. 2000. The in-plane non-linear compression of regular honeycombs. *International Journal of Solids and Structures*, 37, 1931-1949.
- ZHU, H. X., MILLS, N. J. & KNOTT, J. F. 1997. Analysis of the high strain compression of open-cell foams. *Journal of the Mechanics and Physics of Solids*, 45, 1875-1904.
- ZHU, H. X., THORPE, S. M. & WINDLE, A. H. 2001. The geometrical properties of irregular two-dimensional Voronoi tessellations. *Philosophical Magazine a-Physics of Condensed Matter Structure Defects and Mechanical Properties*, 81, 2765-2783.
- ZHU, H. X., THORPE, S. M. & WINDLE, A. H. 2006. The effect of cell irregularity on the high strain compression of 2D Voronoi honeycombs. *International Journal of Solids and Structures*, 43, 1061-1078.
- ZHU, H. X. & WINDLE, A. H. 2002. Effects of cell irregularity on the high strain compression of open-cell foams. *Acta Materialia*, 50, 1041-1052.
- ZINCHENKO, A. Z. 1994. Algorithm for Random Close Packing of Spheres with Periodic Boundary-Conditions. *Journal of Computational Physics*, 114, 298-307.